2010

Development of Multivariate Powder X-ray Diffraction Techniques and Total Scattering Analyses to Enable Informatic Calibration of Solid Dispersion Potential

Michael Moore

DEVELOPMENT OF MULTIVARIATE POWDER X-RAY DIFFRACTION TECHNIQUES AND TOTAL SCATTERING ANALYSES TO ENABLE INFORMATIC CALIBRATION OF SOLID DISPERSION POTENTIAL

A Dissertation

Submitted to the Graduate School of Pharmaceutical Sciences

Duquesne University

In partial fulfillment of the requirements for

the degree of Doctor of Philosophy

By

Michael D. Moore

December 2010

DEVELOPMENT OF MULTIVARIATE POWDER X-RAY DIFFRACTION TECHNIQUES AND TOTAL SCATTERING ANALYSES TO ENABLE INFORMATIC CALIBRATION OF SOLID DISPERSION POTENTIAL

By

Michael D. Moore

Approved August 10, 2010

Peter L. D. Wildfong, Ph.D
Associate Professor of Pharmaceutics
Graduate School of Pharmaceutical Sciences
(Committee Chair)

David A. Engers, Ph.D.
Research Director
SSCI, a division of Aptuit, Inc.
(Committee Member)

Carl A. Anderson, Ph.D.
Associate Professor of Pharmaceutics
Graduate School of Pharmaceutical Sciences
(Committee Member)

Ira S. Buckner, Ph.D.
Assistant Professor of Pharmaceutics
Graduate School of Pharmaceutical Sciences
(Committee Member)

Jennifer A. Aitken, Ph.D.
Associate Professor
Department of Chemistry and Biochemistry
Bayer School of Natural and Environmental Sciences
(Committee Member)

James K. Drennen, III, Ph.D.
Associate Professor of Pharmaceutics
Associate Dean for Graduate Programs and Research
Mylan School of Pharmacy
(Committee Member)

J. Douglas Bricker, Ph.D.
Dean, Mylan School of Pharmacy and the
Graduate School Pharmaceutical Sciences

ABSTRACT

DEVELOPMENT OF MULTIVARIATE POWDER X-RAY DIFFRACTION TECHNIQUES AND TOTAL SCATTERING ANALYSES TO ENABLE INFORMATIC CALIBRATION OF SOLID DISPERSION POTENTIAL

By

Michael D. Moore

December 2010

Dissertation supervised by: Peter L.D. Wildfong, Ph.D.

The objective of this work was to introduce a novel method for predicting solid dispersion potential enabled by the ability to differentiate phase-separated co-solidified products from amorphous molecular solid dispersions. The central hypothesis states that a combination of materials properties exists that defines the propensity of an active pharmaceutical ingredient to form a binary amorphous molecular solid dispersion with polyvinylpyrrolidone:vinyl acetate copolymer using a melt-quench procedure. Testing this hypothesis required execution of specific aims directed to address issues inherent to characterizing amorphous materials. The work herein is presented with respect to two separate subjects: (1) analytical development and (2) theoretical applications. In the first few chapters, advanced powder X-ray diffraction data processing techniques are explored and adapted to composite pharmaceutical systems. Specific emphasis will be placed on

total scattering data manipulations and their benefits over traditional practices. The concluding part of this work is devoted to illustrating the use of materials informatics in modeling solid dispersion potential, ultimately afforded by implementing the materials characterization methodologies developed in the initial stages. Molecular descriptors, commonly employed in quantitative structure-property relationship assessment, were tested for correlation to dispersion potential across a library of small molecule organic compounds. The final model accurately predicted dispersion potential for all 12 calibration compounds and three test compounds.

DEDICATION

I dedicate this dissertation to the memory of my late brother, Jonathan David Moore (1983 – 2005). Although it is not the role of a younger brother to look after the elder, thank you for watching over me until we meet again…

ACKNOWLEDGEMENTS

The transition from my early career in the pharmaceutical industry to the life of a graduate student at Duquesne University proved to be difficult, at best. The teetering of the balance between success and failure in graduate school often tilted in the direction of the former solely as a result of the following individuals; people so dear to my heart that a mere "thank you" does not do justice to their influence in my life. As a prelude to my acknowledgements, I can only offer my sincere gratitude to you, and pray that I'm able to mirror your benevolence.

I knew my advisor for some time prior to joining him at Duquesne; my choice to attend DU was ultimately a result of a promise I made to him as an undergraduate research assistant during his doctoral studies. My decision to join my old friend and mentor, though difficult at the time, turned out to be the most important and defining choice in my career. I am therefore thankful to my academic advisor, Dr. Peter Wildfong, for calling me on my promise, believing in me, and providing support when the journey seemed to be too difficult. The generosity that both he and his wife Karen have shown me will be forever remembered.

I attribute the quality of my work to the interactive group of individuals that comprise my committee. To my committee members, Drs. Carl Anderson, James Drennen, Ira Buckner, Jennifer Aitken, and David Engers, I am grateful for the genuine interest taken in my research. The critical assessments, external conversations, and extensive meetings resulted in research that I am sincerely proud and honored to have completed. A large portion of my research was made possible through a pre-doctoral

fellowship provided by the American Foundation for Pharmaceutical Education and a faculty development fund grant provided by Duquesne University; both are gratefully acknowledged.

The support and friendship of my fellow graduate students was imperative to completing my degree. Of the many influential individuals I've encountered at Duquesne, a few were vital to my success. I am truly grateful to my predecessor Yannan Lin, who helped to develop my analytical skills, made me feel welcome in the Wildfong lab, and participated in numerous technical discussions. I appreciate the assistance of Alison Steinbach, Colleen Hair, and Johanna Bezjak who served as undergraduate researchers, each involved with different aspects of my work. Ryanne Palermo, Brian Zacour, Bob Bondi, and Sameer Talwar are all acknowledged for great friendships and fruitful scientific discussions. Finally, I've had the honor and privilege of working with Dr. Steve Short, Dr. Zhenqi Shi, and Dr. Bob Cogdill, all of whom served as scientific mentors in addition to exceptional friends.

Although my mother, Penny, was not initially onboard with the idea of my quitting a job to return to school, her unwavering support throughout my entire life has shaped the person I am today. I personally thank her for all the sacrifices she made to afford opportunities to me. I am also thankful for the support of my father, John and sister, Megan, Jim and Peggy Higgins, my grandmother, Mary Moore, and countless others. Serving as my proverbial rock, I acknowledge the support of Darlene Monlish who has backed me in every facet of my life since we've met.

Kristin Armstrong once wrote: "*The more I thought about what I got to do, the less I realized I had to do. It was just a shift, just a new perspective, just a new and more*

grateful method for labeling the things in my life. Think about it -- if you stopped yourself every single time you were about to say, "I have to" and changed it to "I get to," it might change your entire experience." The paradigm shift resulting from the realization that graduate school was a privilege rather than a burden turned out to be a powerful driver in completing my work. I am thankful for the opportunity to study at Duquesne University and the ability to contribute to the growth of the graduate school of pharmaceutical sciences.

I ultimately thank God for the many blessings I've received throughout my life, including those enabling me to complete this journey.

TABLE OF CONTENTS

Page

Abstract iv

Dedication vi

Acknowledgements vii

List of Tables xiv

List of Figures xv

List of Abbreviations xx

Chapter 1: Introduction 1

1.1 Statement of Problem 1

1.2 Hypothesis and Objectives 6

1.3 Literature Survey 7

1.3.1 Powder X-ray Diffraction 7

1.3.1.1 Quantitative Powder X-ray Diffraction 14

1.3.1.2 Pair Distribution Function 21

1.3.2 Solid Dispersions 29

1.3.2.1 Structure 30

1.3.2.2 Manufacture 36

1.3.2.3 Stability 42

Chapter 2 : Chemometric Applications in Quantitative Powder X-ray Diffraction (PXRD) of Intact Multi-Component Consolidated Samples 48

2.1 Introduction 48

2.2 Materials and Methods 50

2.2.1 Powder X-ray Diffraction Analysis of the Four Component Compacts..... 51
2.2.2 Data Preprocessing..... 51
2.2.3 Inverse Least Squares (ILS) Regression..... 52
2.2.4 Classical Least Squares (CLS) Regression..... 53
2.2.5 Principal Components Regression (PCR)..... 54
2.2.6 Partial Least Squares (PLS) Regression..... 55
2.3 Results and Discussion..... 55
2.4 Conclusions..... 75
Chapter 3: A Structural Investigation into the Compaction Behavior of Pharmaceutical Composites Using Powder X-ray Diffraction and Total Scattering Analysis..... 76
3.1 Introduction..... 76
3.2 Materials and Methods..... 77
3.2.1 Powder X-Ray Diffraction (PXRD)..... 78
3.2.2 Pattern Separation..... 78
3.2.3 Pair Distribution Function (PDF)..... 80
3.2.4 Principal Components Analysis (PCA)..... 82
3.3 Results..... 83
3.3.1 Pure Theophylline Compaction..... 83
3.3.2 PDF of Mathematically Isolated Theophylline..... 89
3.3.3 PCA of PDF Transformed Data..... 91
3.4 Discussion..... 97
3.4.1 Pure Theophylline Compaction..... 97
3.4.2 PDF of Mathematically Isolated Theophylline..... 99

3.4.3 PCA of PDF Transformed Data 100
3.5 Conclusion 102
Chapter 4: Structural Interpretation in Composite Systems Using Powder X-ray Diffraction: Applications of Error Propagation to the Pair Distribution Function 104
4.1 Introduction 104
4.2 Materials and Methods 106
4.2.1 Solid Dispersion Preparation 106
4.2.2 Powder X-ray Diffraction (PXRD) 107
4.2.3 Differential Scanning Calorimetry (DSC) 107
4.2.4 Pair Distribution Function (PDF) 108
4.2.5 Error Propagation 109
4.2.6 Monte Carlo Simulation 110
4.3 Results 111
4.4 Discussion 119
4.5 Conclusion 124
Chapter 5: Informatics Calibration of a Molecular Descriptors Database to Predict Solid Dispersion Potential of Small Molecule Organic Solids 125
5.1 Introduction 125
5.2 Materials and Methods 128
5.2.1 Solid Dispersion and Amorphous Phase Preparation 130
5.2.2 Differential Scanning Calorimetry (DSC) 130
5.2.3 Powder X-ray Diffraction (PXRD) 131
5.2.4 Pair Distribution Function 132

5.2.5 Molecular Descriptors 133
5.2.6 Logistic Regression 134
5.3 Results 136
5.3.1 Co-solidified product characterization 136
5.3.2 Calibration 144
5.4 Discussion 149
5.4.1 Co-solidified product characterization 150
5.4.2 Calibration 154
5.5 Conclusion 158
Chapter 6: Summary 159
Appendix A: Eutectics 163
A.1 Structure 163
A.1.1 Structural Interpretation of Physicochemical Benefits 164
A.2 Manufacture 165
A.3 Physical Stability 173
Appendix B: PXRD and PDF Analyses 175
Appendix C: DSC Analyses 191
Bibliography 207

LIST OF TABLES

Page

Table 2.1 Sample composition design matrix 56

Table 2.2 Selected statistical values for the different quantitative PXRD calibrations relative to the collection geometry 58

Table 2.3 The effects of various powder pattern corrections on linearity and the standard error of prediction of the univariate and PLS calibrations for prediction of both crystalline and disordered components using data collected by reflectance geometry 64

Table 2.4 The effects of various powder pattern corrections on linearity and the standard error of prediction of the univariate and PLS calibrations for prediction of both crystalline and disordered components using data collected by transmission geometry 67

Table 4.1 Summary of DSC and PDF analyses 108

Table 5.1 Molecular structures and Cambridge Structural Database Codes for compounds used in this study 129

Table 5.2 DSC and PDF analyses results 137

Table 5.3 Calibration library generation results 143

Table 5.4 Model parameters for the seven best univariate models 145

LIST OF FIGURES

Page

Figure 1.1 Example PXRD focusing arrangements 9

Figure 1.2 Enthalpy:temperature phase diagram 31

Figure 1.3 Schematic showing various release modes of amorphous drug inclusions during dissolution of a solid dispersion 34

Figure 2.1 Calculated regression vectors for each multivariate calibration used in the prediction of anhydrous theophylline from data collected in reflectance geometry 60

Figure 2.2 Calculated regression vectors for each multivariate calibration used in the prediction of anhydrous theophylline from data collected in transmission geometry 61

Figure 2.3 Calculated regression vectors for each multivariate calibration used in the prediction of starch from data collected in reflectance geometry 63

Figure 2.4 Calculated regression vectors for each multivariate calibration used in the prediction of starch from data collected in transmission geometry 65

Figure 2.5 The effects of various corrections on the PLS calibration regression vectors as applied to data collected in transmission geometry 69

Figure 2.6 The effects of the number of samples in the calibration set on the standard error of prediction for both collection geometries 71

Figure 2.7 The effects of the number of samples in the calibration set on the starch and theophylline CLS regression vectors for data collected from reflectance geometry 73

Figure 2.8 The effects of the number of samples in the calibration set on the starch and theophylline CLS regression vectors for data collected from transmission geometry 74

Figure 3.1 Mean PXRD patterns for anhydrous theophylline compacted at 67 MPa and 503 MPa 84

Figure 3.2 Mean PDF patterns of theophylline compacted at 67 MPa and 503 MPa..... 85

Figure 3.3 (a) Experimental PDF pattern for theophylline compacted at 67 MPa, calculated PDF pattern from the crystal structure, and the difference plot; (b) Experimental PDF pattern for theophylline compacted at 503 MPa, a simulated PDF from reverse Monte Carlo refinement, and the difference plot 87

Figure 3.4 (a) PXRD pattern of a compact containing 75% MCC and 25% theophylline compressed at 67 MPa (sample 3) and the isolated diffraction attributable to theophylline; (b) The calculated PDF of anhydrous theophylline, the PDF of isolated theophylline from sample 3, and the difference between the calculated and experimental 90

Figure 3.5 (a) PXRD pattern of a compact containing 75% lactose and 25% theophylline compressed at 67 MPa (sample 19) and the isolated diffraction attributable to theophylline; (b) The calculated PDF pattern for anhydrous theophylline, the PDF pattern for isolated theophylline from sample 19, and the difference between the calculated and experimental..... 92

Figure 3.6 PCA scores plot corresponding to the first and second principal components for analysis of PDF patterns from pure theophylline samples and PDF patterns from theophylline mathematically isolated from binary compacts containing MCC..... 94

Figure 3.7 PCA scores plot corresponding to the first and second principal components for analysis of PDF patterns for pure theophylline samples and PDF patterns for theophylline mathematically isolated from binary compacts containing lactose 95

Figure 3.8 PCA scores plot corresponding to the first and second principal components for analysis of all samples..... 96

Figure 4.1 Structures for felodipine, ketoconazole, terfenadine, and PVPva 106

Figure 4.2 (a) The diffraction pattern for amorphous ketoconazole and ±3σ; (b) the PDF transform of (a), calculated ±3σ, and simulated ±3σ; (c) absolute representation of calculated 3σ and simulated 3σ..... 112

Figure 4.3 (a) The PDF of a 50 wt% physical mixture of amorphous felodipine and PVPva and the refined linear combination of the amorphous component PDFs; (b) the difference between the PDFs and ±3σ 114

Figure 4.4 (a) The PDF of a 75 wt% co-solidified product of felodipine and PVPva and the refined linear combination of the amorphous component PDFs; (b) the difference between the PDFs and ±3σ, where the green dots are indicative of the error interval not containing zero..... 116

Figure 4.5 (a) The PDF of a 75 wt% co-solidified product of terfenadine and PVPva and the refined linear combination of the amorphous component PDFs; (b) the difference between the PDFs and ±3σ 117

Figure 4.6 The DSC thermograms for felodipine:PVPva systems 118

Figure 4.7 The DSC thermograms for terfenadine:PVPva systems 119

Figure 5.1 (a) DSC thermogram for amorphous felodipine, PVPva, and 75 wt% co-solidified product; (b) PDF analysis 138

Figure 5.2 (a) DSC thermogram for amorphous quinidine, PVPva, and 75 wt% co-solidified product; (b) PDF analysis 139

Figure 5.3 (a) DSC thermogram for amorphous terfenadine, PVPva, and 75 wt% co-solidified product; (b) PDF analysis 141

Figure 5.4 Predicted dispersion potential probabilities for each of the 12 model compounds 147

Figure 5.5 Predicted dispersion potential probabilities for each of the three test compounds 148

Figure A.1 A schematic of lamellar growth for a binary eutectic behind a near-planar solid-liquid interface 164

Figure A.2 A T–χ diagram for a mixture of two mutually miscible liquids α and β 169

Figure B.1 The PDF assessment for felodipine:PVPva co-solidified product..... 176

Figure B.2 The PDF assessment for indomethacin:PVPva co-solidified product..... 177

Figure B.3 The PDF assessment for ketoconazole:PVPva co-solidified product..... 178

Figure B.4 The raw PXRD pattern for the itraconazole:PVPva co-solidified product... 179

Figure B.5 The PDF assessment for tolbutamide:PVPva co-solidified product..... 180

Figure B.6 The PDF assessment for chlorpropamide:PVPva co-solidified product 181

Figure B.7 The raw PXRD pattern for the nifedipine:PVPva co-solidified product..... 182

Figure B.8 The PDF assessment for quinidine:PVPva co-solidified product..... 183

Figure B.9 The raw PXRD pattern for the propranolol:PVPva co-solidified product.... 184

Figure B.10 The raw PXRD pattern for the cloperastine:PVPva co-solidified product. 185

Figure B.11 The PDF assessment for the terfenadine:PVPva co-solidified product..... 186

Figure B.12 The raw PXRD pattern for the sulfanilamide:PVPva co-solidified product 187

Figure B.13 The PDF assessment for the cimetidine:PVPva co-solidified product..... 188

Figure B.14 The PDF assessment for the melatonin:PVPva co-solidified product..... 189

Figure B.15 The PDF assessment for the bicalutamide:PVPva co-solidified product ... 190

Figure C.1 DSC thermograms showing the glass transition event for the felodipine:PVPva individual components and co-solidified product 192

Figure C.2 DSC thermograms showing the glass transition event for the indomethacin:PVPva individual components and co-solidified product..... 193

Figure C.3 DSC thermograms showing the glass transition event for the ketoconazole:PVPva individual components and co-solidified product 194

Figure C.4 DSC thermograms showing the glass transition event for the itraconazole:PVPva individual components and co-solidified product.....195

Figure C.5 DSC thermograms showing the glass transition event for the tolbutamide:PVPva individual components and co-solidified product 196

Figure C.6 DSC thermograms showing the glass transition event for the chlorpropamide:PVPva individual components and co-solidified product 197

Figure C.7 DSC thermograms showing the glass transition event for the nifedipine:PVPva individual components and co-solidified product 198

Figure C.8 DSC thermograms showing the glass transition event for the quinidine:PVPva individual components and co-solidified product..... 199

Figure C.9 DSC thermograms showing the glass transition event for the propranolol:PVPva individual components and co-solidified product..... 200

Figure C.10 DSC thermograms showing the glass transition event for the cloperastine:PVPva individual components and co-solidified product 201

Figure C.11 DSC thermograms showing the glass transition event for the terfenadine:PVPva individual components and co-solidified product..... 202

Figure C.12 DSC thermograms showing the glass transition event for the sulfanilamide:PVPva individual components and co-solidified product..... 203

Figure C.13 DSC thermograms showing the glass transition event for the cimetidine:PVPva individual components and co-solidified product..... 204

Figure C.14 DSC thermograms showing the glass transition event for the melatonin:PVPva individual components and co-solidified product..... 205

Figure C.15 DSC thermograms showing the glass transition event for the bicalutamide:PVPva individual components and co-solidified product..... 206

LIST OF ABBREVIATIONS

ANN	Artificial Neural Network
API	Active Pharmaceutical Ingredient
BCS	Biopharmaceutical Classification System
CLS	Classical Least Squares
CSD	Cambridge Structural Database
DSC	Differential Scanning Calorimetry
GETAWAY	GEometry Topology Atom Weights AssemblY
GLS	Generalized Least Squares
HPMC	Hydroxypropyl methylcellulose
HPMC-AS	Hydroxypropyl methylcellulose acetate succinate
ICDD	International Centre for Diffraction Data
ILS	Inverse Least Squares
IVIVC	*in vivo-in vitro* correlation
LOO	Leave-one-out
LOO CV	Leave-one-out cross-validation
LR	Likelihood Ratio
MCC	Microcrystalline cellulose
ML	Maximum Likelihood
MLR	Multiple Linear Regression
NBI	Non-bonded Interactions
NCE	New Chemical Entity

PC	Principal Component
PCA	Principal Component Analysis
PCR	Principal Component Regression
PDF	Pair Distribution Function
PEG	Polyethylene glycol
PLS	Partial Least Squares
PVP	Polyvinyl pyrrolidone
PVPva	Polyvinyl pyrrolidone:vinyl acetate
PXRD	Powder X-ray Diffraction
qPXRD	Quantitative Powder X-ray Diffraction
QSPR	Quantitative Structure-Property Relationship
R3m	atomic mass-weighted third-order R autocorrelation index
SCP	Supercritical fluid processing
SE	Solvent Evaporation
SEP	Standard Error of Prediction
SMO	Small Molecule Organic
TGA	Thermogravimetric Analysis
USP	United States Pharmacopeia

Chapter 1: Introduction

1.1 Statement of Problem

The development of small molecule organic (SMO) new chemical entities (NCE) for use in therapeutic products is a complex process involving effort from a diverse multidisciplinary scientific team. Charged with the formidable task of formulating chemically/physically stable, manufacturable, and bioavailable dosage forms, scientists have traditionally relied on highly empirical tactics for solving the most daunting developmental issues. Instances where first-principles approaches are not available for troubleshooting problematic materials-based deterrents seldom precipitate empirically-derived predictive models largely due to analytical limitations. As a result, innovation in the areas of pharmaceutical pre-formulation and formulation development are often precluded by advancements in materials characterization.

In the area of solid oral dosage form development, solubility of a solid material in the aqueous environment of the gastrointestinal fluid and subsequent permeability of active pharmaceutical ingredient (API) molecules through epithelial cellular membranes are two principal biopharmaceutical properties given significant consideration when deciding the fate of a NCE in the pharmaceutical development process. Molecules having acceptable aqueous solubility and permeability, *i.e.,* biopharmaceutical classification system[1] (BCS) I compounds, are desirable owing to typically higher *in vitro-in vivo* correlation (IVIVC), but are encountered less frequently among emerging NCEs. Therefore, modifications to APIs intended to improve biopharmaceutical properties inherent to successful development are becoming routinely necessary.

Tactics commonly employed in permeability enhancement of NCEs often require alteration of intramolecular functional groups, thereby manipulating properties, including reduction of ionization potential under physiological conditions and lipophilicity. These modified functional groups, however, often influence other physicochemical and pharmacological properties, such as aqueous solubility and receptor binding efficiency. Consequently, molecules that lack adequate permeability (BCS Class III, IV) are often dismissed as viable development candidates. As aqueous solubility enhancing approaches are developed, BCS Class II compounds (low aqueous solubility, high permeability) exhibit greater potential for successful development. With the decline in "blockbuster" drug development in the last decade, methods for optimizing biopharmaceutical properties of SMO compounds are becoming increasingly important.

The solubilization of a solid material in an aqueous medium is a complex, equilibrium process that can be broken down into three general steps. The first step involves removing a molecule from the bulk solute particle. This is achieved by breaking/overcoming the cohesive inter-molecular non-bonded interactions (NBI) responsible for maintaining the crystal lattice. Half of the work committed in this process is regained from "closing" the hole created from the departure of the molecule. The second step is called pre-solvation and is the work of breaking cohesive solvent:solvent interactions to create a "hole" sufficient to accommodate the solute molecule. The final step, solvation, is the insertion of the solute molecule into the solvent "hole" and subsequent formation of adhesive interactions. The final step represents an overall gain in work (or decrease in potential energy) due to: (1) the formation of adhesive

interactions between the solute molecule and surrounding solvent molecule(s); and (2) the "hole" created in step two is sealed.[2]

Techniques that may be used to enhance the aqueous solubility and/or dissolution rate of NCEs can be broken down into two subgroups: (1) chemical and (2) physical modifications. Conventional chemical modifications include prodrug development[3] and salt screening/selection.[4,5] Though successfully applied to commercially available therapeutic agents,[2] these methods have their shortcomings. Synthesizing an appropriate prodrug through the addition of an optimal physiologically cleavable functional group is not trivial. Further, chemical modifications also possess the potential to unpredictably alter other biopharmaceutical properties, such as permeability, toxicological potential and pharmacological action. Specifically, a molecular modification resulting in the greatest aqueous solubility enhancement may increase the toxicity of the molecule, *e.g.,* in the case of quaternary ammonium prodrugs of tertiary amine containing compounds.[6] Further, salt formation of a compound is only a viable option when the NCE possesses an ionizable group, and oftentimes results in a material that has sub-optimal physical properties for manufacturing and stability.

Physical modifications, on the other hand, are more generally applied in the pharmaceutical industry relative to their chemical counterparts. From classical dissolution theory, such as Noyes-Whitney,[7] various materials properties can be altered, theoretically resulting in enhanced aqueous dissolution. The inverse relationship between particle size and dissolution rate has enabled the exploitation of particle size reduction as a method of enhancing aqueous dissolution.[8] Impact mills and fluid-energy mills are commonly used for reduction of particle size, however, the high-energy input of these

methods imparts the ability to induce phase changes (*i.e.,* polymorphism,[9] amorphization,[10,11] *etc.,*) with implications of physical instability.[12]

Other physical strategies, such as the formation of non-covalent inclusion complexes using cyclodextrins, provide solubility advantages over the un-manipulated drug.[13] The prediction of solubilization potential with cyclodextrins, however, remains highly empirical, and is limited to appropriately sized, chemically compatible molecules. Solubility enhancement can be achieved through the use of formulation additives such as surfactants, however, drug:excipient compatibility becomes an issue.[14] Despite the extent of viable options described herein, it has still been estimated that more than 40% of highly potent NCEs fail to reach clinical trials owing to their poor aqueous solubility.[15] Therefore, alternative methods need to be rigorously explored, and more fundamentally understood.

Controlled solid state modifications comprise an additional tactic for aqueous solubility enhancement on the principle that different solid forms have different physicochemical properties. Adoption of metastable forms, however, is limited by their potential to convert to a more thermodynamically stable form in pharmaceutically-relevant time-frames.[12] Formation of binary amorphous molecular solid dispersions offers a method for physically stabilizing the amorphous phase of a drug substance. Generally speaking, amorphous molecular solid dispersions are formed by the co-solidification of a drug and polymer, in a specific ratio, producing an overall amorphous phase displaying short-range order unique from that of either amorphous component. These systems, coupled with other composite entities (*e.g.* eutectics and solid solutions) are commonly implemented in manufacturing in the areas of metallurgy,[16]

microelectronics, and superconductor technology, where their controlled formation is well understood in the optimization of specific materials properties (other than solubility enhancement).[17,18]

The application of composite systems to pharmaceuticals is highly empirical, where solid dispersion potential screening may involve multiple concentration points (*i.e.* drug to excipient ratios), various excipient (*e.g.* polymers) materials, and different methods of preparation. The raw material requirement involved with this assessment in early drug development stages remains an impediment for producing viable dosage forms from this technology. Given this, the commercial availability of these systems in currently marketed pharmaceutical dosage forms is limited.[8,19]

Predicting drug:polymer solid dispersion compatibility/stability presents a difficult task, which suffers from the absence of universally applicable rules describing the molecular requirements for physically stabilizing amorphous therapeutic agents. Attempts to empirically model solid dispersed systems have yielded conflicting accounts, which are seemingly due to the dependency of specific stabilization effects on the particular components in the system, as well as inconsistencies in analytical characterization. The insensitivity to structure at the short-range order level frequently impedes identification of miscible products from phase-separated products. Additionally, variable reports on the presence of adhesive drug:excipient interactions oftentimes prevents accurate modeling/calibration of dispersion potential.

The random orientation of molecules in a molecularly dispersed system, as well as the indiscriminate specific/non-specific bonding schemes, implies that miscibility-indicating features may be specifically related to properties of the individual molecules.

Through *in silico* modeling, various molecular properties and descriptors can be calculated from the compound's atomic crystallographic coordinates. With the enormous number of molecular properties available for modeling, a method for sorting through multi-dimensional data is required. Materials informatics provides a statistically-robust method for surveying multi-scale data to seek specific structure-property relationships through linear/non-linear modeling. Coupled with identification of successful amorphous molecular dispersion formation, this may ultimately provide an answer to determining molecular requirements for successful formation of amorphous molecular solid dispersions. The ability to predict the miscibility between a drug and polymer and thereby limit the overall resource burden would significantly enhance the appeal of solid dispersion technology.

1.2 Hypothesis and Objectives

The central hypothesis of this dissertation is that a combination of materials properties exists that defines the propensity of an API to form a binary amorphous molecular solid dispersion with polyvinylpyrrolidone:vinyl acetate (PVPva) copolymer using the melt-quench process. In order to test this hypothesis, the following specific aims were proposed and executed:

1. Due to the considerable complexity of composite materials relative to single component systems, the quantitative ability of multivariate PXRD techniques will be compared with traditional univariate methods to support the use of full-pattern analyses on composite samples.

2. The sensitivity of the PDF transform to subtle alterations in interatomic distances of an API:excipient composite mixture induced by high compaction pressures will be demonstrated with the goal of illustrating the potential of finite phase differentiation using the short-range structural order.
3. A statistically-relevant method for interpreting PDF difference plots based on the propagation of an initial PXRD error estimate will be derived and applied to classification schemes for solid dispersion systems.
4. An informatics calibration from a molecular descriptor database will be created to predict the potential of a compound to form an amorphous molecular solid dispersion with a given polymeric carrier using a single preparation method.

The purposes of the previous specific aims are: (1) to support the use of advanced analytical techniques to improve the characterization of complex pharmaceutical systems; and (2) to replace traditional empirical methodologies with advanced *in silico* modeling.

1.3 Literature Survey

1.3.1 Powder X-ray Diffraction

The discovery of X-radiation occurred in 1895 by W.C. Röntgen. It was not until 1912 when Max von Laue confirmed the wave character of X-rays from his single crystal diffraction experiments that the birth of the X-ray crystallography field commenced. Following von Laue's three-vector dot-product description of X-ray diffraction, William Henry Bragg and his son William Lawrence Bragg derived a simpler method for understanding and predicting this phenomenon, thereby arriving at the well-known Bragg equation (**Equation 1.1**):

$$\boldsymbol{n}\lambda = 2\boldsymbol{d}\ \mathbf{sin}\ \theta \qquad (1.1)$$

where λ is the wavelength of X-radiation, *n* is the integer value of wavelength displacement satisfying constructive interference criteria, *d* is the interplanar spacing between a pair of Miller indices, θ is equal to 2θ/2 and 2θ is the angle between incidence and diffracted beams.[20]

According to **Equation 1.1**, when a particular set of molecular planes is oriented toward an X-ray beam, X-rays will be diffracted at an angle (2θ) satisfying a particular distance between planes. Although initially derived for single crystal samples, applications of X-ray crystallography principles to powders (*i.e.* polycrystalline material) provide the ability to study structural order without isolating a single crystal specimen. The powder diffraction pattern arises from the assumption that a large number of polycrystalline aggregates have crystallites in all possible orientations permitting the X-ray beam to see all intermolecular planes. Powder X-ray diffraction (PXRD) has become particularly useful practically, as structure-sensitive analyses may be applied to samples obtained from all stages of various manufacturing unit operations.

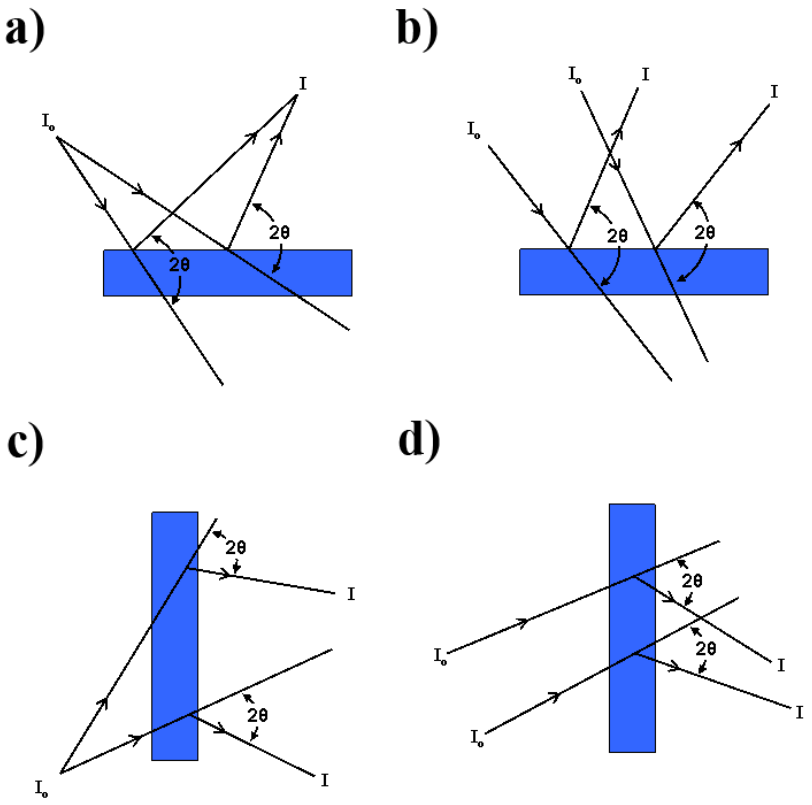

Figure 1.1. Example PXRD focusing arrangements (after Zevin and Kimmel[21], with modifications): (a) diverging incident radiation converges upon diffraction in reflectance geometry; (b) converging incident radiation diverges upon diffraction in reflectance geometry; (c) diverging incident radiation diverges upon diffraction in transmission geometry; and (d) converging incident radiation converges upon diffraction in transmission geometry.

Fundamentally, there are two primary geometric modes of PXRD analysis: (1) reflectance and (2) transmission. Differences between the two setups involve the convergence-divergence of the X-ray beam. In reflectance, the sample itself either: (a) changes a divergent beam into a convergent beam or (b) changes a convergent beam into a divergent beam. In transmission mode, an incident diverging beam remains divergent upon diffraction and *vise versa*. From these definitions, four types of focusing arrangements may be envisioned. The first scheme involves a reflectance orientation where incident X-rays diverge with subsequently diffracted convergence and is

commonly referred to as Bragg-Brentano parafocusing geometry (**Figure 1.1a**). The second reflectance setup produces converging incident X-radiation with subsequent diffracted divergence and is known as Seeman-Bohlin focusing geometry (**Figure 1.1b**). The first transmission mode produces converging X-rays that display convergence upon diffraction and is named for Guinier (**Figure 1.1d**). The second transmission mode, which is much less common relative to the Guinier geometry, is divergent incident radiation with subsequent divergent diffracted radiation (**Figure 1.1c**).[21] Both reflectance and transmission geometries have their own advantages and disadvantages that may be ultimately reconciled into instrumental and chromatic effects.

The most commonly employed focusing scheme, Bragg-Brentano reflectance, suffers from both instrumental and chromatic aberrations. Each error source has scattering angle dependence, where instrumental effects decrease with increasing scattering angle and chromatic effects increase with increasing scattering angle. There are four inherent instrumental errors of particular significance that are largely a consequence of the geometrically-imposed parafocusing circle. They include the axial-divergence error, flat specimen error, sample transparency error, and sample displacement error, where the latter two are closely related.

The axial-divergence error arises from the divergence of X-rays within the plane of the specimen, orthogonal to the theta angle. This anomaly produces asymmetric broadening of Bragg diffraction peaks in the low two-theta direction. Additionally, it introduces a decreasing negative error in two-theta up to 90°, then an increasingly positive error beyond. To combat this issue, collimator slits comprised of a metal (*i.e.* molybdenum for copper radiation), cut to a specific length, and evenly spaced apart are

placed in between the source and sample, as well as, the sample and detector, to axially focus the X-ray beam.[20]

The flat-specimen error, as indicated by the name, is due to the inability of the entire irradiated sample to be co-concentric with the parafocusing circle. The sample surface forms a tangent to the circle, where a different apparent irradiation distance for specimen extremities results in diffraction at an angle lower than expected. The overall pattern aberration is a broadening of Bragg peaks due to a distortion of the average radius of the parafocusing circle. Assuming a fixed incident divergence slit, the magnitude of the error is highly dependent on scattering angle, where decreasing divergent slit sizes result in smaller errors.[20]

The principles associated with errors from sample transparency and sample displacement are very similar, where both are a result of instances where the effective diffraction surface lies above/below the focusing circle. Pharmaceutically-relevant SMO compounds are effectively "transparent" to X-radiation, as the mass-attenuation of atoms comprising these molecules is relatively low. The specimen-transparency error arises when X-rays penetrate to layers below the surface with subsequent diffraction from planes well below the focusing circle. It has been reported that decreasing linear attenuation coefficients result in as much as a tenth of a degree peak shift and substantial angular asymmetry.[22] Practical difficulties associated with placing a specimen directly co-concentric to the focusing circle lead to sample-displacement errors. Pattern aberrations attributable to this error include low two-theta asymmetric peak broadening and absolute peak shifts equivalent to 0.01°2θ for every 15 μm displacement.[20]

To understand chromatic aberrations, an explanation of X-ray generation is warranted. The production of X-rays is a highly inefficient process with respect to both substantial heat generation and emission of polychromatic radiation. Copper X-radiation is produced as a result of the displacement of electrons from its inner electron shell and the concurrent replacement of those electrons from an outer electron shell. The demoted electron releases energy equivalent to the energy difference between each orbital, which is on the order of the wavelength of X-radiation. Typically, high current voltage is passed through a tungsten filament, which is encased in a glass housing that possesses an overall negative potential. As high current passes through the filament, electrons are generated and subsequently directed towards the copper anode. When they collide with the copper anode, electrons are displaced from the inner electron shell (normally 1s) and subsequently replaced by an electron from an outer shell (2p→1s). This particular transition produces K_α radiation. Also, a transition of electrons from the 3p shell (3p→1s) results in radiation (termed K_β) of shorter wavelength. Depending on the combination of the angular quantum number and spin quantum number of the electron which transitions from the outer shell, different wavelengths of radiation may be produced ($K_{\alpha1}$/ $K_{\alpha2}$ or $K_{\beta1}$/ $K_{\beta3}$).[23]

Nickel has an absorption edge at 1.488Å with mass attenuation coefficients for K_β and K_α radiation of 286 cm^2/g and 49.2 cm^2/g, respectively. By controlling the thickness of a Ni filter in the path of incident/diffracted X-rays, considerable attenuation of K_β radiation with minimal affect on K_α intensity is possible. It is common practice to use Ni filters, where 15 μm results in an integrated intensity ratio of K_α / K_β = 50:1.[20] Given this, the bulk of chromatic aberrations are due to the inability to discriminate between $K_{\alpha1}$ and

$K_{\alpha 2}$. At large scattering angles, the $K_{\alpha 1}/K_{\alpha 2}$ doublet results in significant Bragg peak broadening unless otherwise resolved. The use of a monochromator to remove $K_{\alpha 2}$ radiation is the most effective method; however, mathematical "stripping" may be carried out through data processing, having knowledge of each respective profile (*i.e.* shape, magnitude).[24] Inaccuracies associated with the estimation of each wavelength's contribution to the overall diffraction peak when mathematically stripping $K_{\alpha 2}$, however, may result in the introduction of substantial error into the data.

The transmission technique where a constant specimen-detector distance is employed creates an analog similar to the back-reflection of the aforementioned Bragg-Brentano scheme. Given the conceptual similarities, it may be envisioned that a certain likeness exists between errors encountered using Bragg-Brentano and transmission schemes. Generally speaking, both instrumental and chromatic aberrations are much lower in transmission geometry relative to reflectance, largely due to the focusing circle placement at θ - 90°. This emulates back-reflection characteristics, and as previously discussed, is approximately where instrumental aberrations decrease in Bragg-Brentano setups. Chromatic aberrations are largely eliminated due to competitive dispersion elements arising from the specimen and/or the mechanism used for incident X-ray convergence, *e.g.* elliptical mirror. These factors largely reduce the separation between the $K_{\alpha 1}$ and $K_{\alpha 2}$ components.[21] In addition to lower instrumental and chromatic aberrations, constant depth-of-penetration in transmission geometry results in increased robustness to particle size, preferred orientation, and stress/strain aberrations relative to traditional Bragg-Brentano reflectance, where depth of penetration varies with diffraction

angle thereby amplifying these effects. When significant sample absorption is not an issue, transmission geometry affords superior performance.

1.3.1.1 Quantitative Powder X-ray Diffraction

Ranging from univariate to full-pattern approaches, quantitative powder X-ray diffraction (qPXRD) techniques have long been plagued with errors attributable to the physical characteristics of the sample. Paramount to the list is the issue of sample absorbance, where the electron density of the atoms comprising the specimen may result in considerable radiation attenuation. The implementation of full-pattern multivariate quantitative modeling will be discussed, specifically in the context of the aforementioned instrumental and chromatic pattern aberrations.

The interaction between the radiation and matter is fairly complex, where "absorbed" radiation may have been subjected to various other transformations. Total absorption or energy loss as a function of passing through matter is due to a combination of scattering and the photoelectric effect. General scattering occurs when radiation interacts with matter, retains the initial energy/wavelength, but scatters at an angle not defined by Bragg's law (**Equation 1.1**). An instance where a decrease in energy of the radiation occurs in addition to the previously described situation is commonly referred to as Compton scattering. Radiation can be absorbed by atoms according to the photoelectric effect, where the atom is excited and an electron is ejected. When the atom returns to its ground state, another electron (Auger effect) or fluorescent radiation can be emitted.[25] The methods for absorption corrections in qPXRD applications range from first principles estimations to empirical assessments with respect to a reference material(s). The principles originally developed by Alexander and Klug[26] for quantitative

analysis of powder mixtures with respect to the absorptive properties of the sample are the foundation for the forthcoming discussion.

The oldest method for absorption correction in qPXRD applications is a univariate approach known as the internal standard technique.[21] The specimen is spiked with a known amount of a pure reference phase and subsequently analyzed as a mixture. The ratio of unknown phase intensity to the internal standard intensity can be used to determine the concentration of the unknown phase, as the ratio of intensity values are independent of sample absorption. Analyte concentration values are, therefore, obtained from a single experiment negating the need for a calibration. The weight fraction of a phase *j* is given by:

$$\boldsymbol{c}_j = \boldsymbol{H}\,\frac{\boldsymbol{I}_{ij}}{\boldsymbol{I}_{hs}} \tag{1.2}$$

where I_{ij} is the intensity value for the unknown phase, I_{hs} is the intensity value for the internal standard, and H is a constant determined from knowing the weight of the internal standard. In this analysis, intensity is taken as the peak height or integrated intensity.

In selecting an internal standard, a few considerations must be made. First, the standard is desired to possess high symmetry, thereby producing a small number of highly intense Bragg peaks. Additionally, sufficient isolation of the peak(s) used for the unknown phase from that of the standard is also a necessity. The density of the internal standard should be close to that of the unknown phase as to permit a homogeneous distribution upon mixing.[27] Finally, the standard material should be chemically stable in the analytical environment.

The internal standard method is insensitive to unknown phases and therefore may be implemented to analyze any crystalline material in a multiphase matrix. Lithium

fluoride was used to aid in simultaneously quantifying an enantiomeric material and racemic compound mixture of ibuprofen, where limits of quantification were around three percent.[28] A potential disadvantage involves the physical addition of an internal standard to the sample matrix. Errors in weighing and inhomogeneous distribution of the standard may increase the uncertainty associated with the measurement. Further, the methodology prevents analysis of composite samples intact, as the sample must be destroyed and blended with the standard.

The most direct method for absorption correction is afforded through knowledge of the mass absorption coefficient. This may be determined using a simple calculation from the chemical composition[23] or any direct experimental technique, provided the determination is independent of the diffraction measurement. Born from this approach is the diffraction-absorption method, where calibrations are created from correlating standard samples to corrected intensity(s). If it is assumed that the absorption coefficient for the unknown phase is the same as that for the entire sample matrix, the concentration of phase *j* is given by:

$$\boldsymbol{c}_j = \chi_{ij} \boldsymbol{I}_{ij} \tag{1.3}$$

where I_{ij} is a measured intensity value and χ_{ij} is a calibration constant obtained by analyzing any mixture with a known concentration of phase *j*. The use of a single intensity value in this application may introduce significant error into the analysis due to many of the systematic aberrations described previously. Variations in the lattice strain and particle size, which commonly influence Bragg peak shape, are avoided by using the integrated intensity.[27]

Adaptations for constant and variable absorption coefficients have been developed for multiphase analysis. Unfortunately, sources of nonlinearity other than absorption can introduce errors into this type of calibration, including microabsorption, extinction, and preferred orientation. The effect of preferred orientation may be substantially different in a composite system than that exhibited by the pure phase, as powder consolidation has been shown to induce preferred orientation.[29] A qPXRD study by Tiwari *et al.* to quantify polymorphs of a specific drug showed particle size and preferred orientation errors significantly affected the number of identifiable peaks and their respective integrated areas.[30] To increase the accuracy and precision of their method, substantial parameter and sample optimization was required beforehand, thereby increasing raw material demands and other costly resources.

Full pattern techniques are particularly useful when peak overlap between components occurs in a mixture. The most popular full pattern method for quantification of crystalline phases was introduced by Rietveld,[31,32] which was originally developed for crystallographic structure refinement using single-crystal neutron diffraction data. It was over ten years after its introduction before the Rietveld method was applied to X-ray data. Once accepted by crystallographers, the number of publications citing this method drastically increased.[33] Under the Rietveld method, a powder pattern is thought of as a collection of individual profiles the have a peak height, position, breadth, and an integrated intensity proportional to the square of the structure factor. Being a structure refinement technique, a starting structural model is refined to fit the experimentally determined intensity values. Calculated intensity values are determined from the structure factor (derived from a structural model) that sums neighboring Bragg reflection

contributions plus a background estimate. Adjustable parameters in the calculation of the structural model are iteratively altered as to obtain a least-squares minimization between the calculated and experimental intensity values. No specific effort is made by the Rietveld method to allocate an observed intensity to a particular Bragg peak or resolve overlapped peaks, thereby mandating accurate initial model estimation.[34] A central part of Rietveld's contribution stated information in overlapping peaks (unless coincident) is not entirely lost when the peak profile function is known.

It was realized some time after the Rietveld method was proposed that the scale factors derived from the analysis of multiphase diffraction data are proportional to crystal phase composition when the product of the mass and volumes of the unit cell of each phase are known.[35] This full-pattern analysis proceeds with structural parameters, experimental parameters, and scale values (weight fractions) that are simultaneously refined against the experimental pattern. The Rietveld method has been successfully applied to both inorganic and organic samples, where additional information concerning preferred orientation may be gained from the analysis.[36] This imposes a requirement of crystallographic structure solutions for all phases present and thus precludes its use for quantifying multiple amorphous phases, which is not to say that a collective amorphous content is unavailable through mass balance.

In all of the qPXRD methods mentioned thus far, the overarching limitation, with respect to pharmaceutical applications, is the inability to quantify multiple amorphous phases. Although each ostensibly permits the ability to back-calculate the collective amorphous element of a mixture, they all fail to address the individual contributions comprising the disordered component. This is particularly important, as an increasing

number of formulations contain amorphous excipients as well as disordered API, where differentiation is paramount for claiming sensitivity. In an effort to assert sensitivity to all components present in a mixture, other full pattern techniques that consider Bragg diffraction and diffuse scattering have been developed.

The term "full pattern" with respect to qPXRD applications has traditionally referred to two different types of analyses, one that solely solved the issue of overlapping peaks and the other addressing the additional issue of multiple amorphous components. The first approach is generally referred to as profile fitting, as clusters of overlapping peaks are decomposed into components (*i.e.* individual peaks). Unlike Rietveld's method, structural data is not needed; rather, knowledge of peak shape (*i.e.* profile) and, less importantly, position are used to decompose convoluted peaks. Once clusters are separated, integrated intensity values are assigned to each component.[21] These intensity values can then be used in a calibration-based method, such as the diffraction-absorption technique, or standard-based methods that do not require construction of a calibration, as previously described.

The second approach may be tailored to handle the quantification of multiple amorphous phases in a mixture. The entire powder pattern of a multiphase mixture is assumed to be the sum of the scaled patterns of the individual phases present. Linear combinations of each pure component pattern are used to create a simulated pattern that can be compared with the experimental pattern. The scaling constants serve as estimates of the mass fraction of each phase in the mixture. To date, it appears as though this method has only been applied to pharmaceuticals in an effort to quantify the amount of amorphous lactose in a multiphase mixture.[37] The technique, however, could be

theoretically extended to multiple amorphous phases, provided the diffuse scatter patterns of each individual disordered component were unique.

For the aforementioned method, the advantage in handling convoluted peaks and quantification of amorphous phase(s) without the creation of a calibration is contingent upon a few factors. Diffraction patterns must be obtained for each individual component comprising the mixture; impurities in the composite pattern or individual component patterns would introduce error into the analysis. Each pattern in the analysis should be collected using exactly the same parameters and conditions. Additionally, peak shape and intensity must be consistent for a given phase to give reliable predictions. Much of the success of implementing the latter full-pattern technique was attributable to invoking a pattern normalization method based on Vainshtein's law.[37] This states that total integrated diffraction intensity in reciprocal space is independent of phase, as total electron density does not change with solid form, given constant mass. An important interpretive assumption linked to this law imposes either: (1) the whole sample must be irradiated throughout the entire angular range of the diffraction experiment; or (2) the same mass of sample is irradiated throughout the entire angular range of the diffraction experiment. If violated, the total electron density interrogated between samples would vary. Issues with preferred orientation, particle size broadening, strain, and microabsorption, unless uniformly observed between samples, will all introduce error into the analysis.

From the preceding qPXRD discussion, it may seem apparent that an increased sensitivity to materials that diffract X-rays at a lower intensity (*e.g.* amorphous, disordered, nanocrystalline materials) is afforded through multivariate techniques.

Recent qPXRD literature has introduced multivariate chemometric linear algorithms as useful tools in pharmaceutical applications and demonstrated robust modeling capabilities using classical least squares regression, principal components regression, and partial least squares regression. The implementation of full-pattern analysis in combination with creating a calibration, avoids many of the preceding issues. This is the subject of **Chapter 2**.

1.3.1.2 Pair Distribution Function

The majority of pharmaceutical applications employing PXRD focus on analysis of Bragg diffraction peaks only. These diffraction data contain highly useful information pertaining to the global view of the structure (*i.e.* long range interatomic correlations). To be rigorous, one must recognize that structure occurs at a local level (*i.e.* short- and intermediate- range interatomic correlations), as well. When considering ideal crystalline systems, this distinction is rather irrelevant, as the global structure is indicative of the local structure. Lattice periodicity is a crucial element to the successful implementation of Bragg's law. If a material is not perfectly periodic, however, Bragg's law does not fully characterize the solid structure and researchers are forced to describe it in different ways. Therefore, when deviations from average crystallographic order are present, consideration of local structure packing becomes pertinent.

Given Bragg diffraction peaks contain information pertaining to global structure only, additional data is required to investigate local structure. Total scattering methods make use of the entire diffraction pattern and are sensitive to local level structure. The name "total scattering" comes from intensity values encompassing Bragg peaks (average structure), elastic diffuse scattering (static local structure) and inelastic scattering

(atom/molecular dynamics).[38] Total scattering analyses make use of the collection of the aforementioned sources without resolving or differentiating the individual contributions and are, therefore, sensitive to short- and intermediate-range interatomic correlations.

When an atom, *j*, is irradiated by an incident wave, the total scattering amplitude of the wave due to the sample is given by:

$$\psi(\boldsymbol{Q}) = \frac{1}{\langle \boldsymbol{f} \rangle} \sum_{j} \boldsymbol{f}_j \boldsymbol{e}^{i\boldsymbol{Q}\boldsymbol{R}_j} \tag{1.4}$$

where $\psi(Q)$ is the sample scattering amplitude, f is the atomic scattering factor, ‹› indicates the average, R_j is the position of the j^{th} atom, and Q is the diffraction vector or momentum transfer.[38] The momentum transfer is essentially equivalent to the change in momentum between the incident wavevector and the scattered wavevector. If it is assumed that only elastic scattering is considered, the wavelength of each respective vector would remain constant, and thus the magnitude of the momentum transfer is given by:

$$|\boldsymbol{Q}| = \frac{4\pi \sin\theta}{\lambda} \tag{1.5}$$

where λ is the wavelength of radiation used, $\theta = 2\theta/2$, and 2θ is the maximum scattering angle interrogated in the experiment. In deriving the sample scattering amplitude (**Equation 1.4**), the kinematic approximation was made, thereby only considering single scattering events.

Since the sample scattering amplitude can not be directly measured, it becomes highly advantageous that the square of its magnitude is directly related to the intensity of the diffracted beam. Although PXRD intensity data are collected in "reciprocal space" as a function of *Q*, a direct representation of the real structure (*i.e.* real space domain) may

be obtained by Fourier transform of scattered intensity. The pair distribution function (PDF) transform is a total scattering method that exploits the Fourier relationship between reciprocal space and real space. The basis of this method resides in the structure function, $S(Q)$, which is the normalized scattering intensity measured from a sample (*i.e.* normalized PXRD pattern). The magnitude of the structure function with respect to the wavevector will be highly dependent on the direction interrogated in Q-space. A simplification occurs when scattering becomes macroscopically isotropic, as only the magnitude of the scatter (and not direction) is important. Isotropic scattering is easily envisioned for liquids, gases, and glassy materials; however, it is also reasonably assumed for fine crystalline samples, where each individual crystallite is not isotropic, but the ensemble of scattering is.[38] The PDF, $G(r)$, is therefore obtained as follows:

$$\boldsymbol{G(r)} = \frac{2}{\pi}\int_0^{\infty} \boldsymbol{Q}\left[\boldsymbol{S(Q)} - 1\right]\mathbf{sin}(\boldsymbol{Qr})\boldsymbol{dQ} \tag{1.6}$$

$$= 4\pi\boldsymbol{r}\left[\rho(\boldsymbol{r}) - \rho_0\right] \tag{1.7}$$

$$\rho(\boldsymbol{r}) = \frac{1}{4\pi\boldsymbol{r}^2}\sum_{ij}\frac{\boldsymbol{f_i f_j}}{\langle \boldsymbol{f} \rangle^2}\delta(\boldsymbol{r} - \boldsymbol{r_{ij}}) \tag{1.8}$$

where r is the distance between two atoms, $\rho(r)$ is the microscopic pair density, ρ_o is the average number density, f and ‹› are defined above, and δ is a delta function. The PDF gives the probability of finding two atoms separated by a distance, r and is thus attributable to some atom-atom relationship, or interatomic correlation.[39]

From **Equation 1.6**, the integration of the function is taken from $Q = 0$ to $Q = \infty$ for an infinitely precise computation of the PDF. The PDF of a perfectly crystalline material would display constant-amplitude oscillations in $G(r)$ to infinity. In reality, however, Q can only be measured over a finite range (*i.e.* Q_{max}). The result is the

amplitude of the signal gradually falls off in $G(r)$, not due to the limitation of structural coherence, but rather a limitation in spatial coherence of the measurement. The finite Q-resolution of a PXRD experiment can be the source of termination ripples ($\lambda \sim 2\pi/Q_{max}$)[40] in the PDF, unless treated appropriately.

In a PXRD experiment, substantial corrections need to be made to intensity data prior to Fourier transformation. Generally speaking, a number of estimates and approximations are made when calculating the normalized structure function, thereby inducing some distortion(s) to the intensity data. Fortuitously, inadequacies in the data normalization result in long-wavelength distortions to the structure function that manifest as nonphysical features (ripples) at very low r values in the PDF.[41] These inadequacies are often dealt with through an arbitrary mathematical correction, including varying the sample density during scaling, varying the beam width, or scaling the structure function itself.

Although the sample density is fairly easy to determine with reasonable accuracy, it can be varied to produce a structure function consistent with its asymptotic requirements. Varying sample density applies a predominantly multiplicative correction to the structure function, as is strongly affects both intensity normalization and absorption correction. Although the beam size is known from the collimation of the instrument, the beam may not be homogeneous.[41] The effective beam width will be different from the physical dimensions due to varying intensity across the beam profile. Varying the beam size is primarily a multiplicative correction to the resulting structure function, as well. Both corrections can have additive components when multiple scattering manipulations

are applied. Finally, directly scaling the structure function itself using multiplicative, additive, or a combination of the two, may be used to optimize the Fourier transform.

The selection of the value(s) to vary is arbitrary if some sort of quality criteria is implemented to assess the validity of optimization. The PDF is highly sensitive to the asymptotic behavior of the structure function in the high *Q* region, which could ostensibly serve as a quality metric. The density, beam width, or scaling factors would be varied to produce a structure function that asymptotes one. Alternatively, the greatest manifestation of improper structure function correction is the introduction of ripples in the low *r* region of the PDF, and therefore, a quality criterion derived from this anomaly is more suitable. The ΔG_{low} metric is given by:

$$\Delta \boldsymbol{G}_{\boldsymbol{low}} = \frac{\int_{0}^{r_{low}} [\boldsymbol{rG}(\boldsymbol{r}) + 4\pi \boldsymbol{r}^2 \rho_{\boldsymbol{fit}}]^2 \, \boldsymbol{dr}}{\int_{0}^{r_{low}} (4\pi \boldsymbol{r}^2 \rho_{\boldsymbol{fit}})^2 \, \boldsymbol{dr}} \tag{1.9}$$

where r_{low} is a region in *r* before the appearance of the first physically possible peak, and ρ_{fit} is the average number density. From the **Equation 1.9**, the ΔG_{low} criterion is a measurement of the magnitude of ripples in the region between $r = 0$ and $r = r_{low}$. Parameters are varied, as described above, to effectively minimize the ΔG_{low} metric. A study by Peterson *et al.*[41] concluded the ΔG_{low} criterion was more robust than other options, and the choice of the parameter to vary during optimization (*i.e.* sample density, beam width), for all practical purposes, is inconsequential, as all seemingly yielded the same result.

Justification for using high energy synchrotron radiation for X-ray diffraction-based PDF studies is warranted in the mere definition of the magnitude of the momentum

transfer. The increase in spatial coherence of the measurement and decrease in nonsensical artifacts from the Fourier transform are as good a reason as any to use synchrotron radiation for all PDF studies. It is impractical, however, for the average researcher to perform all studies using this highly sought, expensive technology. Bruhne *et al.*[42] showed that PDF transforms obtained from both synchrotron and laboratory source data on three icosohedral alloys were qualitatively comparable and both suitable for least squares local structure refinement. This is ultimately attributable to the robust nature of the PDF transform with respect to errors in the structure function, as previously discussed.

The PDF has been extensively applied to inorganic-based materials assessment since its introduction into the literature. One of the largest applications involves material structure refinement, where successful structure elucidation for atomic amorphous materials[43,44] and intrinsically disordered materials[44-46] has been reported. In addition, size-dependent structure and strain of semiconductor nanoparticles[45] and assessment of thermal motions[46,47] in atomic structures are becoming more routine. Although the number of pharmaceutically-related PDF applications is substantially less, the increased exposure from recent publications is significantly advancing the interest among scientists in the field.

Pharmaceutical processing involving high-energy input is commonplace in the manufacture of solid oral dosage forms. Shear-intensive particle milling, powder consolidation, and thermal challenging (*i.e.* fluid bed drying) all have the potential to affect structural order in pharmaceutical powders. Of the PDF applications published in the pharmaceutical literature, the overwhelming majority have transformed standard

laboratory X-ray data. Sheth *et al*.[48,49] used PDF transforms to explain local structure differences in amorphous phases created from milling different polymorphic forms of piroxicam. Interestingly, residual long range order in cryogenically milled samples explained recrystallization habits of different polymorphic forms of the starting material. A study by Bates *et al.*[50] assessed the potential of the PDF transform to describe the nature of an amorphous substance. From their analysis, materials were classified as disordered nanocrystalline or amorphous. Disordered nanocrystalline materials exhibited peak broadening as a function of increasing introduction of disorder. The final X-ray amorphous halo had specific correlations to highly intense Bragg peaks displayed by the crystalline material. Additionally, a comparison between PDF transforms revealed interatomic probability peak correlations between the disordered nanocrystalline material and crystalline material. In contrast, PXRD patterns of amorphous materials did not display peak broadening as a function of continuous disordering. Further, the PDF of amorphous materials relative to crystalline material displayed significant differences. Again, from distinguishing different types of disordered materials, information concerning recrystallization behavior was gained.

Dehydration-initiated crystalline-to-amorphous conversions must be considered during high-temperature pharmaceutical processing, such as that observed for raffinose pentahydrate. Authors proposed a quasi-mechanism for this transition using PDF transforms obtained as a function of drying time.[51] The study revealed that a defect-mediated process led to the collapse of the crystalline structure, where retention of the crystalline order was accompanied by significant defect generation during the loss of the first two water molecules. Additional heating beyond this point resulted in a total

collapse of the intermediate- and long-rang order of material structure. The ability of the PDF transform to yield information concerning defect-generated disordering due to shear-intensive and high energy input processing, as illustrated in the previously discussed examples, foreshadows its potential use in investigating structural changes resulting from powder compaction, which is ultimately the subject of **Chapter 3**.

In addition to the lack of Bragg diffraction peaks exhibited by amorphous molecular solid dispersions, PXRD patterns have been shown to provide additional information pertaining to local structure in these systems. The sensitivity of the PDF transform to interatomic correlations makes it an obvious choice for studying pharmaceutical systems displaying order on only a short length scale. One of the most recent applications of the PDF transform to pharmaceutical systems is in the characterization of co-solidified products to aid in identifying miscibility between a drug and polymer (Section 1.3.2). Newman *et al*.[52] illustrated the principles behind the use of PDF transforms to distinguish co-solidified products possessing unique short-range order relative to the amorphous components that comprise the mixture. The method involved obtaining PXRD patterns of the amorphous phases comprising the co-solidified product, as well as, one for the co-solidified product itself. All PXRD patterns were subsequently transformed by the PDF algorithm and linear combinations of the amorphous component PDFs were compared to the PDF of the co-solidified product. If the calculated PDF exacted a "good fit" to the PDF of the composite, the co-solidified product was categorized as phase-separated, due to the absence of a unique packing pattern. If a good fit could not be obtained, the co-solidified product was categorized as completely

miscible, due to formation of unique short-range order (*i.e.* nearest neighbor and next-nearest neighbor correlations) not explained by the individual amorphous phases.

The power of this method is quickly realized by the scientist charged with the task of determining miscibility in drug:polymer products, an all too often intangible distinction. Upon first glance, an initial weakness is the necessity of obtaining amorphous phase samples for each of the pure components. As the purpose of forming a solid dispersion is to physically stabilize the amorphous form of a drug, the ability to isolate and physically maintain a sample to provide sufficient analysis time is not trivial. A second limitation was the ambiguity with which an assessment of "difference" was made between linearly combined PDF transforms and the transform of the co-solidified product. To make the analysis more robust, a method has been proposed to propagate error estimates for the calculated difference and is the subject of **Chapter 4**.

1.3.2 Solid Dispersions

Rigorous differentiation between the different composite systems, such as eutectics (**Appendix A**) and solid dispersions, is somewhat ambiguously presented across the breadth of the pharmaceutical literature. This leads to a systematic misclassification of these products, thereby founding fundamentally irrelevant conclusions from studies encompassing the subject area. A more accurate approach to defining and contrasting the individual composites can be realized through a strict materials-based structural assessment. Analogous to the way in which crystal symmetry defines a crystal system (and not *vice versa*) the microstructure of a binary solid composite defines its type. From these definitions, analytical techniques required for accurate product classification are

identified, a better fundamental understanding of aqueous solubility enhancement can be provided, and issues inherent to the underutilization of the technology is established.

1.3.2.1 Structure

The three types of symmetry defining long-range crystallographic order are translational, orientational, and conformational. Crystalline solids have all three, where mesophase materials possess one or two.[53] In amorphous materials, all three symmetry operators are characteristically absent; therefore the orientation and position of molecules relative to one another is random, as similarly observed in liquids, but short-range order over a few molecular dimensions is present.[54,55] The thermodynamic relationship between crystalline and amorphous phases is best rationalized schematically in the enthalpy-temperature phase diagram (**Figure 1.2**). Starting with a crystalline material, small changes in temperature correspond to minor changes in enthalpy response, where the slope defines the heat capacity of the solid at constant pressure. Upon further increase in temperature to T_f, a discontinuity in the diagram is encountered and a sharp increase in enthalpy is observed. This is the first-order fusion event representing the crystalline-to-liquid transition. If the melt is rapidly cooled, enthalpy may bypass the melting/freezing point producing a supercooled liquid. Upon further cooling the glass transition event is encountered, where a change in heat capacity is observed due to a higher-order transition from a supercooled liquid to a glass. Any additional cooling is thought to have very little influence on the microstructure of the material.[56] The Kauzmann temperature (T_K in **Figure 1.2**) represents the temperature at which the entropy of a supercooled liquid would fall below that of the stable crystalline material.

The change in heat capacity that occurs at the glass transition prevents the hypothetical decrease in entropy to permit this phenomenon.[57]

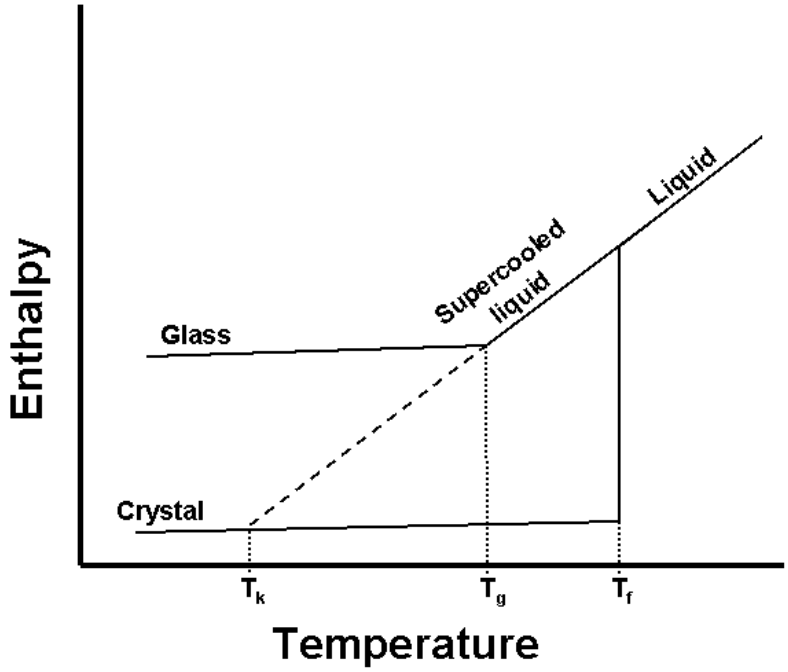

Figure 1.2. Enthalpy:temperature phase diagram.

From **Figure 1.2**, the glass is a higher free energy phase compared to its crystalline counterpart, and further deviates from equilibrium. The system is said to be kinetically "trapped" in the solid state, as it exhibits increased molecular mobility relative to the crystalline phase, but lower than that of the liquid state. The higher free energy provides for enhanced apparent aqueous solubility, as NBIs maintaining the solid-like viscosity are weaker than those responsible for crystalline counterpart.[58] A corollary of this solubility enhancement is the thermodynamic driving force to revert back to the lower energy, crystalline phase. To maintain the amorphous phase and sustain the solubility enhancements, solid dispersions are formed between an amorphous drug substance and a polymeric carrier material; although, the exact mechanism of physical stabilization is largely unknown.

A binary amorphous molecular solid dispersion is a material consisting of two components co-solidified such that the short-range order of the product is distinct from that intrinsic to the amorphous phases comprising the mixture. Since solid dispersions are macroscopically amorphous systems, it is worthwhile to note that this implies that they are also non-equilibrium phases. Many of the models founded on equilibrium thermodynamic principles may be highly inappropriate for solid dispersions. As a consequence, specific mechanistic explanations describing structural correlations between solid dispersion co-solidification and observed physicochemical and mechanical properties of these systems are lacking. This void is also an effect of the random orientations of the drug and carrier molecules, as well as the heterogeneity of the interactions between the two components, which ultimately differ between single- and two-phase systems. Both specific (*i.e.,* hydrogen bonding) and nonspecific (*i.e.,* van der Waals forces) intermolecular interactions, however, have been characterized in solid dispersed systems, and are well represented in the pharmaceutical literature.[59-62] The extent of the participation of these interactions in solid dispersion stabilization (or lack thereof) continues to be a matter of discussion.

The lack of periodic NBI schemes in amorphous materials results in a higher internal energy, which can provide enhanced physicochemical properties, such as increased apparent aqueous solubility and/or enhanced dissolution. The random structural framework of solid dispersed systems and the presence of various combinations of specific/non-specific bonding schemes, make direct correlations between structure and enhanced solubility less straightforward than other composite bodies (*e.g.* eutectics). The increase in dissolution rate of solid dispersions, however, has been attributed to three

factors: (1) reduction in drug particle size (*i.e.*, in molecular dispersions, the "particle size" of the amorphous inclusion is on the order of the dimensions of the API molecule), (2) decreased drug:water interfacial energy, and (3) establishment of weaker NBIs per unit volume material relative to the NBIs per unit volume of the drug's crystalline phase.[19,63] Given the number of possible structural variants, the degree to which each of these contributes to the optimized physicochemical properties may be dramatically different. It may seem apparent from the preceding discussion that more rigorous structural characterization will be required to model physicochemical benefits afforded through the directed design of solid dispersions. Furthermore, these benefits will vary with respect to individual systems; a universal model of solid dispersion structure-function correlation seems impractical.

A review by Craig[64] introduced a model that explained the release behavior of drug molecules from a solid dispersion as being either *carrier-mediated* or *drug-mediated*. A representation of these two schemes is illustrated in **Figure 1.3**, where drug release from a *two-phase* solid dispersion is shown. Initially, a polymer-rich diffusion layer is formed at the interface between the solid dispersion and the dissolution medium. The viscosity of this interfacial layer is assumed to be greater than that of the liquid phase. In carrier-mediated dissolution, the amorphous drug inclusions (assuming a biphasic solid dispersion) diffuse from the dispersion matrix into the polymer-rich phase, where they begin to dissolve. Drug is further released from this polymer-rich layer into the dissolution medium as either solvated molecules, or as amorphous particles having undergone size-reduction, at a rate dictated by the carrier.

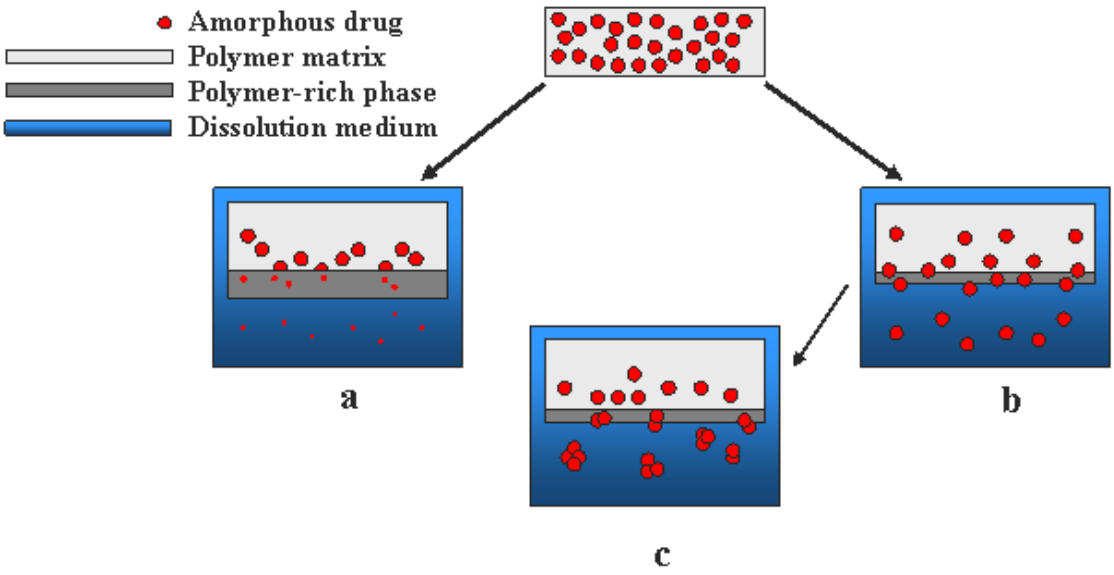

Figure 1.3. Schematic showing various release modes of amorphous drug inclusions during dissolution of a solid dispersion (after Craig,[64] with modifications); (a) carrier-mediated dissolution: the carrier forms a polymer-rich phase aiding in initial drug complex dissolution; (b) drug-mediated dissolution: high solubility of the carrier in the dissolution medium prohibits formation of a polymer-rich phase; dissolution of the drug occurs following diffusion of the amorphous complex from the dispersion to the dissolution medium; (c) Complex aggregation following drug-mediated dissolution: amorphous inclusions agglomerate upon diffusion into the dissolution medium, resulting in their higher propensity for devitrification.

In drug-mediated dissolution, the solubility of the polymer in the medium is considered to be much greater relative to the dissolution time-frame, ultimately resulting in a polymer-rich layer that is smaller relative to the polymer-rich phase observed in carrier-mediated dissolution. As the drug inclusions diffuse through the polymer-rich phase, the rate is sufficient to prevent their dissolution in the polymer layer. The amorphous drug is, therefore, released intact into the surrounding aqueous medium, and its dissolution rate is proportional to the aqueous solubility of the amorphous condensed phase. In both instances, solubility enhancement relative to crystalline materials is provided owing to either the total breakdown of drug inclusions prior to release in the medium (carrier-mediated), or to the release of amorphous complexes left to dissolve on

their own (drug mediated). Craig proposes the application of this model to aid in identifying the correct strategy to improve dissolution via solid dispersion formulation. More importantly, the model may assist in understanding the basis for formulation instability, as related to dissolution, and provide a scientific approach to dealing with such issues.

A route of physical instability occurring during dissolution that is directly related to the drug-mediated model for solid dispersions is depicted in **Figure 1.3c**. When the amorphous inclusions diffuse through the polymer-rich diffusion layer too rapidly, and their dissolution rate in the aqueous medium is relatively slow, a time-frame sufficient to promote recrystallization may be encountered. Nucleation and growth can be thought of as occurring by, (1) each individual amorphous complex begins the recrystallization process independent of other amorphous complexes, or (2) agglomeration of amorphous complexes creates high-energy interfacial boundaries, thereby driving the interfacial term of nucleation models to favorable values. The latter of these two conditions is expected to be more prevalent, as reduction in specific surface area upon formation of agglomerates would slow the dissolution rate even more, permitting a longer time-frame for recrystallization. This particular mechanism of physical instability illustrates the importance of excipient selection in solid dispersion formulation; notably, the relative aqueous solubility of the carrier component may induce physical instability during the dissolution process. Further, as will be discussed in greater detail, the relationship of manufacturing methods to resulting solid dispersion structure becomes an important variable when considering release behavior.

The review by Craig was an important step in correlating the release behavior of solid dispersions to formulation, stability issues, solid dispersion design, *etc*. However, the proposed model fails to address structurally-related bases for the proposed differences in release (*e.g.,* effects of intermolecular interactions between drug and carrier on drug release mechanism) and focuses specifically on biphasic systems, thereby neglecting molecularly dispersed solids. Karavas *et al*.,[65] more recently reported that the molecular interactions between felodipine:polyethylene glycol (PEG) & felodipine:polyvinylpyrrolidone (PVP) dictate the resulting physical state of felodipine (crystalline versus amorphous), as well as the size of inclusions in the dispersed matrix. The additional characterization of the solid dispersion enabled the authors to ascertain the release mechanism as related to the specific structure of the dispersion and to identify critical manufacturing attributes which altered the structure and release mechanism.

The preceding discussion demonstrates the size-dependence of the carrier matrix-dispersed inclusions on the release mechanism, and the additional implications concerning physical stability of the material during dissolution. Unfortunately, the structural heterogeneity of the solid dispersion variants often deters rigorous intrinsic correlation to physicochemical properties, creating an area having tremendous research potential.

1.3.2.2 Manufacture

The traditional methods for manufacturing solid dispersions can generally be broken down into two general categories: (1) fusion-based methods and (2) solvent-based methods. Sikiguchi and Obi[66] were the first to demonstrate the use of a hot-melt procedure in the production of pharmaceutically-relevant solid dispersions. Subsequently,

Tachibani and Nakumara[67] dissolved both a drug and carrier in a common solvent, which was then evaporated under vacuum to produce a solid dispersion. In the production of binary solid composites, each method has its own advantages and disadvantages stemming from production costs, ease of manufacture, scalability, and other critical areas. In the last decade, new techniques have emerged which address one or more of these deterrents. Some of the barriers that complicate the application of each individual binary composite to pharmaceuticals manifest through investigation of the manufacturing regimes.

Since solid dispersions are structurally aperiodic, methods not traditionally used in other solid composite production may be employed in their creation. Spray drying,[68,69] lyophilization,[63] fluid-bed coating,[70] and hot-melt extrusion[71,72] have all been used in pharmaceutically-related manufacturing of solid dispersions, as these processes are known to result in amorphous products. Current literature shows a trend in development of new schemes for solid dispersion formation that are fundamentally similar to traditional techniques; however, the newer methods have been shown to possess various benefits relative to their conventional counterparts, thereby deserving attention. It may be worthwhile to note that although these methods are common in the sense that an amorphous co-solidified product is formed, it has been shown that common manufacturing methods may, in fact, have an effect on the supersaturation of drug in polymer.[73]

In a recent study, Papadimitriou *et al*.,[74] used microwave irradiation in place of conventional heating to melt the drug and carrier mixtures and then compared the resulting dispersion with that prepared by the conventional fusion technique. In both

instances, the resulting dispersions were two-phase systems possessing an element of periodicity; therefore, neither product would be defined as a solid dispersion according to the criteria proposed in this paper. The authors claimed a reduction in production time by using microwave radiation with a slight enhancement in the dissolution profile. However, the biphasic dispersion produced using this method was shown to result in a smaller particle size, which may better explain the improvement in dissolution kinetics. Although the authors attributed the decrease in particle size to the use of microwave irradiation, this actually appears to be a consequence of the more rigorous mixing regime employed. The practicality of scale-up for this particular method may also limit its potential for adoption at the industrial level. In addition to the limitations imposed by capital investment, since pharmaceutical applications of microwave technology are relatively new to the industry, considerable attention to issues involving distribution homogeneity, implications of microwave energy on chemical stability, and other method-related topics is required.

Xu *et al*.,[75] developed a pulse combustion dryer system designed from the basic principles of spray drying. A combustion cycle is repeated at a specific frequency to produce consecutive high-temperature shock waves used to rapidly dry solutions of drug material and carrier. Advantages of the system include an increased rate of heat transfer, decreased drying time, and lower costs compared with conventional spray drying. Studies show an enhanced apparent dissolution rate for ibuprofen solid dispersions prepared using the pulse combustion dryer versus conventional spray drying. The authors failed to present structural characterizations for both products; therefore, the aforementioned dissolution advantage may be due to the decreased particle size of the

pulse combustion dryer final product relative to the conventional spray dryer product. Once again, the cost of developing a pulse combustion dryer system for large scale production may outweigh the benefits afforded by this technology.

Supercritical fluid processing was shown to be a valid alternative to the solvent-evaporation method resulting in lower residual organic solvent, co-precipitates possessing smaller particle sizes, and better flowability. In the work by Sethia and Squillante,[76] the authors showed that solid dispersions prepared by supercritical fluid processing (SCP) had an enhanced intrinsic dissolution rate relative to dispersions made via conventional solvent evaporation (SE) augmented with amphiphilic carriers, thereby eliminating the stability issues associated with lipid carriers. Powder X-ray diffraction analysis of products prepared by both SCP and SE augmented with an amphiphilic carrier revealed highly disordered materials; however, a closer look at the PXRD pattern of the SE product reveals some Bragg diffraction peaks attributable to the amphiphilic carrier. The solubility advantage of this material is most likely due to considerable amorphous content; however, the presence of phase-separated crystalline solid suggests incomplete preparation of an amorphous dispersion via the SE method. As with the other novel methods suggested above, although this technology holds some advantages, industrial scale-up may present a major cost-related barrier to its adoption.

Many of the authors presenting the manufacturing alternatives above advocate the cost-effectiveness of their respective processes in terms of efficiency (primarily decreased processing time) yet do not present a cost analysis to support their claims. As a supplement to structural and physicochemical comparisons, contrasts in small-scale

research costs as well as large-scale manufacture should be considered when suggesting the viability of a new manufacturing technology.

Typically, studies involving the structural characterization and assessment of the physicochemical properties of solid dispersions only consider solids produced by a single manufacturing scheme. In contrast, Dong *et al*.,[77] published results that compared the solid state properties of dispersions prepared both by hot-melt extrusion and solvent co-precipitation. In this study, a proprietary compound was evaluated for its potential development as a solid dispersion formulation. Dispersions were prepared using hypromellose acetate succinate (HPMC-AS) as the carrier molecule, via hot-melt extrusion and solvent co-precipitation. Both methods were observed to yield a single-phase (molecularly dispersed) amorphous dispersion. Differential scanning calorimetry (DSC) analysis of each product showed them to have a single glass transition event, occurring at comparable temperatures. The co-precipitation product, however, was determined to be more porous than the hot-melt extrusion product, thereby resulting in a larger specific surface area. The co-precipitation product had a faster dissolution profile, but a slower intrinsic dissolution rate relative to the hot-melt extrusion product. Though the authors did not suggest a reason for this observation and noted that it was unexpected, a possible explanation may be drawn from classical Noyes-Whitney dissolution theory:

$$\frac{dM}{dt} = \frac{DS}{h}(C_s - C) \tag{1.10}$$

where M is the mass of the drug dissolved in time t, D is the diffusion coefficient of the drug in the dissolution medium, S is the surface area of the exposed drug, h is the thickness of the diffusion layer, C_s is the solubility of the drug, and C is the concentration of the drug in the bulk solvent at time t.[2] Traditional dissolution profiles were generated

by suspending the product in an aqueous vehicle and transferring it to a United States Pharmacopeia (USP) type II apparatus (paddles). In these experiments, the co-precipitation product reached its plateau dissolution value possibly attributable to the increased value of S relative to the hot-melt extrusion product. Intrinsic dissolution studies were conducted by compressing each product at 2000 lbs. force to form a pellet having a constant exposed surface area. Given that one of the principle steps in consolidation is a reduction in void volume, or porosity, it is not unexpected that the surface area enhancement gained by employing the solvent co-precipitation method was lost. Normalization of the final compacted pellets to their solid fraction may explain the enhanced intrinsic dissolution observed for the hot-melt extrusion product.

The authors also showed an enhanced physical stability of the hot-melt extrusion product over the dispersion produced from the co-precipitation process, which once again, may be related to a specific surface area argument. The co-precipitation product, having a larger specific surface area, possesses more accessible sites for water molecules relative to the hot-melt extrusion product. The presence of water on the surface of amorphous materials can create supersaturated microenvironments which serve as nucleation sites. Additionally, water may act as a plasticizer,[78] thereby theoretically increasing the molecular mobility.

Though this study illustrates that the various physicochemical properties of solid dispersions may be dependent upon the manufacturing method, it fails to address specific structural differences which may contribute to these properties. For example, a powder X-ray diffraction pattern was shown for both products to illustrate an absence of Bragg diffraction peaks inherent of a crystalline material, which may be a result of the material

being truly X-ray amorphous or an artifact of inappropriate sensitivity to adequately detect diffraction. Advanced methods in diffraction pattern processing (*e.g.* pair distribution function transformation) may have been applied to delineate local structure differences between the two products, where a correlation to these differences may be established. Creation of models to explain and predict these types of phenomena will be imperative to understanding and applying these systems for commercial manufacturing and may ultimately result in the increased use of solid dispersions in pharmaceuticals.

1.3.2.3 Stability

The amorphous state possesses a higher free energy relative to its crystalline counterpart, which should result in enhanced thermodynamic properties (*i.e.* solubility) and molecular motion. A consequence of this increased molecular motion is the tendency to revert back to a stable crystalline phase (devitrification).[56] Thermodynamically, amorphous substances will inevitably devitrify; however, the time frame of this process is at the heart of research directed at stabilizing these materials. In addition to physical drivers for recrystallization, environmental factors, such as water, must be considered for dispersion systems, where the hygroscopicity of the polymeric carrier may be a significant factor.[79] Oftentimes strategies to deal with physical stability issues in pharmaceutical products do not require elimination of the source for the mechanism of instability; rather, the kinetics of the transformation are manipulated to prolong a product's shelf life.

Molecular mobility is frequently described as a key factor in the physical stability of amorphous phases.[80] The glass transition, commonly represented as a single value (T_g), actually occurs over a temperature range delineating high and low molecular mobility

within the material. Evidence of increased resistance to recrystallization in solid dispersions has been attributed to antiplasticization when polymeric carrier components having a higher T_g relative to that of the drug are used.[81] However, other reports show examples where differences in T_g values between carrier components and API were not correlated to the physical stability of the dispersions studied.[59,82] Both specific and nonspecific intermolecular bonds have been shown to occur in stable solid disperse systems. This includes direct bonding interactions between carrier and drug molecules and/or the disruption of drug:drug interactions (*e.g.* dimer formation)[48] by the carrier.[48,83] In conflicting reports, however, these interactions are shown unnecessary in the prevention of recrystallization.[81] Consequently, the preceding points illustrate the difficulties with identifying and the limited understanding of the physicochemical properties of the carrier necessary for inhibiting drug devitrification.

The Gordon-Taylor equation,[84] based on the mechanistic approach of free volume and related densities, has been successfully applied to predict T_g of molecular dispersions and is given by:

$$T_{g12} = \frac{w_1 T_{g1} + K w_2 T_{g2}}{w_1 + K w_2} \tag{1.11}$$

where w_1 and w_2 are the weight fractions of each component, T_{g1} and T_{g2} are the respective glass transition temperatures, and $K = (T_{g1}\rho_1)/(T_{g2}\rho_2)$, where ρ is the density of the component. A variation of **Equation 1.11**, where $K = \Delta C_{p1}/\Delta C_{p2}$ and derived from more thermodynamic assumptions, was later identified by Couchman and Karasz.[85] Although the Gordon-Taylor equation has been shown to be highly useful when both components are large polymeric materials, it has been shown to poorly predict SMO-polymer systems. Additionally, since many of the empirical parameters of each equation

are determined using thermodynamic techniques (*e.g.* DSC), it is somewhat more appropriate to use the Couchman-Karasz version of the equation.[86]

Recall that formation of solid molecular dispersions assumes complete drug:polymer miscibility in the liquid phase, which, as previously interpreted, means that adhesive interactions must be comparable to cohesive interactions (in the liquid phase). In the case of antiplasticization, some intermolecular interactions between the polymer and drug would be anticipated to decrease the molecular mobility of the amorphous system. This definition suggests a correlation between the two proposed mechanisms of stabilization, where this combination has been reported in studies as the underlying mechanism of stabilization.[83]

In order to maintain the advantage of drug substance solubility enhancement provided by its preparation in the amorphous state, methods to preserve its physical stability over a pharmaceutically-relevant time scale must be employed. Water-soluble polymers such as PEG, PVP, and cellulose derivatives (*e.g.* hydroxypropylmethyl cellulose) are commonly incorporated as carriers in pharmaceutical solid dispersions. Much of the current research investigates the specific stabilization mechanisms afforded by polymers in pharmaceutical solid dispersions. For amorphous molecular solid dispersions, it is recognized that devitrification is preceded by amorphous drug:polymer phase separation, in the case of nucleation and growth.[87] In a study by Konno and Taylor[59] the ability of three polymers to inhibit the recrystallization of felodipine was investigated. PVP, HPMC, and HPMC-AS were combined with felodipine to create molecularly dispersed systems. To study both antiplasticization effects and drug-polymer molecular interactions, the polymers were selected to span a range of T_g values and had

different potentials for hydrogen bonding. PVP showed both increased hydrogen-bonding interactions with felodipine as well as a greater antiplasticization effect relative to the other polymers. All three polymers, however, were found to prolong the time to nucleation of amorphous API to a similar extent, given an equivalent weight fraction. The mechanism proposed by the authors ascribed the increase in physical stability to result from the provision of a kinetic barrier to nucleation by the polymeric carriers, with the magnitude of the effect being related to the polymer concentration (w/w).

The important distinction between drug:polymer miscibility and physical stability needs to be drawn. The thermodynamic term "miscibility," in a strict sense, is taken out of context when applied to drug:polymer systems. Rather than associating miscibility to the equilibrium solubility between a drug and polymer, it more accurately describes the ability of a drug and polymer to form a supersaturated metastable phase. Although miscibility between a drug and polymer is indicative of the compatibility between a drug and polymeric material, it does not, however, give any insight into the timeframe (extent) of physical stability.

Predicting drug:polymer miscibility at various concentration ranges, as well as differentiation from partial miscibility,[88] has become the focus of recent studies. The use of interaction parameters (*e.g.* derived from group contribution theory) and Flory-Huggins theory to predict drug:polymer miscibility has recently appeared in the literature. One study[89] concluded that the majority of SMO compounds will be supersaturated with respect to solubility in a polymer, providing a thermodynamic driving force for recrystallization. Additionally, the physical stabilization was predominantly attributable to a kinetic barrier; however, molecular level miscibility was still shown to be an

important factor as molecularly dispersed systems have altered molecular level environments. In an unrelated report, an attempt to predict dispersion potential from physical properties (melting point, molecular weight, *etc.*) and functional groups of 20 compounds was described. Although none of the physical properties probed were predictive of miscibility, compounds with hydrogen bonding potential were shown to be favorable candidates.[90]

From the background supplied herein on the subject of PXRD structural and quantitative analyses, an appreciation for the necessity of accurately characterizing amorphous systems and the local structure deviations in a crystalline material is gained. The ability to successfully model predictability for overall aperiodic systems, such as amorphous molecular solid dispersions, will be discussed in great detail and ultimately hinged on the credibility of differentiating co-solidified products at the local structure level.

A general consensus among the pharmaceutical community concerning appropriate characterization methods for studying solid dispersions is sufficiently lacking. Characterization inconsistencies between research groups have yielded conflicting reports, thereby complicating the advancement in understanding of solid dispersion systems. Vibrational spectroscopy has been successfully used to identify specific/non-specific interactions developed between a drug and polymer in co-solidified systems.[59-62] Unfortunately, the level of mixing between materials is not available from spectral changes. Further, cohesive interactions are either so subtle or absent altogether that changes to molecular vibrations may not be detected.[81] Traditional PXRD analyses only confirm a lack of detectable crystallinity in a co-solidified product and fail to provide

information concerning the extent of mixing between the components, as well. Although DSC has served as the conventional method for identifying an overall phase-separated system, forthcoming sections will aim to illustrate instances where it is not sensitive to phase separation and the use of multiple characterization techniques is imperative. To this end, the successful completion of the theoretical portion of this dissertation (*i.e.* solid dispersion potential) was afforded by the analytical optimization comprising **Chapters 2, 3, and 4**.

Chapter 2: Chemometric Applications in Quantitative Powder X-ray Diffraction (PXRD) of Intact Multi-Component Consolidated Samples

2.1 Introduction

Powder X-ray diffraction (PXRD) of intact, consolidated samples is an important technique for pharmaceutical materials and drug product characterization. Quantitative PXRD methods are the most universal of the structure-sensitive methods for phase analysis of multi-phase systems.[20,23] The foundation of quantitative PXRD techniques for analyzing mixtures was originally developed by Alexander and Klug,[26] and some examples applied to pharmaceutical mixture analyses are reported in the literature.[52-57]

Traditional quantitative PXRD methods can be subcategorized into those which incorporate a standard and those which are standardless. Standardless techniques, such as whole-pattern fitting and Rietveld refinement, are particularly useful because they permit quantification without the use of specific calibration standards. These methods have the ability to assess and account for physical phenomena (such as preferred orientation); however, selecting an appropriate function, is not trivial.[36] Standardless quantification has also been limited to uses with crystalline materials. Further, they require a known crystal structure, which is often obtained from the literature/online databases.

Numerous quantitative PXRD methods exist to incorporate a standard material into mixtures for analysis,[21] the use of which permits correction for matrix absorption. The most commonly employed of these is the internal standard technique. Incorporation of a standard within a sample, however, prevents analysis of intact, marketable drug products, for which the inclusion of an analytical dopant would be prohibited. Moreover, finding a standard that is stable, has approximately the same absorption characteristics as

the sample, does not exhibit preferred orientation, and possesses isolated peaks which do not overlap with sample peaks are all potential barriers to using this method.[21]

Diffraction-absorption calibrations are created through empirical linear regression modeling of component concentration against single diffraction peak intensity, a few diffraction peak intensities, or the integrated area under diffraction peak(s). These techniques assume constant mass attenuation across the sample, and therefore, are susceptible to errors resulting from diffraction intensity attenuation. Anisotropic intensity reduction due to microabsorption and extinction often result in non-linearities observed in quantitative PXRD calibrations.[26,36] The largest contributor to intensity attenuation, however, is preferred orientation, which can be particularly problematic in consolidated samples.[36] Problems with preferred orientation in powdered samples are traditionally resolved by optimizing the particle size used for PXRD analysis, which may add significantly to method development and execution,[30] as well as the potential for induction of experimental artifact owing to conversions elicited by triturative particle sizing.[20]

By using only Bragg diffraction intensities, the traditional methods are limited to quantification of crystalline materials. Many solid oral dosage forms are developed using excipient materials having no long range order. The physicochemical benefits afforded by incorporating amorphous active pharmaceutical ingredients in formulations of solid oral dosage forms has resulted in increased interest in the use of these systems;[56] however, for PXRD to be sufficiently sensitive to quantify disordered materials, a method that models both diffuse scatter and Bragg diffraction is required.

Many of the aforementioned issues are addressed through the use of multivariate calibrations.[91] In quantitative chemometrics, a multivariate relationship is sought between input data (*e.g.*, diffraction patterns) and output data (*e.g.*, composition, various physical phenomena). Applications of chemometric-based analyses in PXRD are starting to surface in the literature. Examples of applications of partial least squares regression (PLS),[92] principal components analysis (PCA),[93,94] and advanced techniques such as artificial neural networks (ANN)[95,96] to PXRD data have all been reported. The possible benefits of incorporating entire diffraction patterns into empirical models include enhanced signal-to-noise, analyte sensitivity and selectivity.[97] The objective of this work was to investigate applications of different multivariate calibrations used to quantify both crystalline and amorphous components in consolidated samples. Intact compact analysis using PXRD was used to determine which algorithm was most suitable for intact quantification of multi-phase consolidated pharmaceutical systems.

Quaternary mixtures composed of two crystalline materials and two disordered materials were compressed at multiple compaction pressures and subjected to intact PXRD analysis using two different instrumental optics setups. Quantitative calibrations were created using the traditional (univariate) diffraction-absorption technique, and three multivariate algorithms commonly employed in spectroscopy. Calibration linearity, precision, and prediction error were calculated for assessing model suitability.

2.2 Materials and Methods

Four-component mixtures comprised of anhydrous theophylline (Lot No. 92577, Knoll AG, Ludwigshafen, Germany), Lactose 316 Fast Flo NF Monohydrate (Lot No. 8502113061, Hansen Labs, New Berlin, WI), microcrystalline cellulose (Avicel PH 200,

Lot No. M427C, FMC BioPolymer, Mechanicsburgh, PA), and soluble starch GR (Lot No. 39362, EMD Chemicals, Inc., Gibbstown, NJ) were prepared. The design matrix was fully balanced for compact concentration, having values ranging from 0 – 60% w/w. Approximately 800 mg of each mixture was compressed at 67.0 MPa, 117.3 MPa, 167.6 MPa, 217.8 MPa, and 268.1 MPa using a single station Carver Press (Carver, Inc, Model 3887.1SDOA00, Wabash, IN) equipped with a 13 mm flat-faced punch.

2.2.1 Powder X-ray Diffraction Analysis of the Four Component Compacts

PXRD data were collected using an X'Pert Pro MPD system (PANalytical B.V., Alemlo, the Netherlands) equipped with a copper anode (λ = 1.5406 Å), programmable divergence slit, and X'Celerator^{TM} detector. The operational voltage and amperage were set to 45.0 kV and 40.0 mA, respectively, and diffraction patterns were acquired using an angular step size of 0.02° 2θ over a range of 2 – 60° 2θ. Data were collected with the instrument set in both Bragg-Brentano reflectance geometry (equipped with a spinning sample stage) and transmission geometry (equipped with a vertical spinner sample stage with the sample sandwiched between Kapton® film), optically fitted with an auxiliary elliptical mirror used to expose the sample to quasi-parallel beam radiation.

All chemometric routines were performed in the Matlab programming environment (v7.1, MathWorks, Natick, MA) using the PLS_Toolbox (v3.0, Eigenvector Research, Manson, WA), together with several analysis routines developed in-house.

2.2.2 Data Preprocessing

Prior to the application of chemometric algorithms, sample diffraction patterns were corrected for anisotropic peak (axis) shift using an iterative program that tested for correlations between a reference pattern and the sample pattern as a function of

incremental calculated shifts. Corrected shifts that resulted in the highest correlation were ultimately selected. Additionally, the diffraction pattern of an empty sample holder (geometry dependent) was used to correct for scatter from that sample holder by pattern subtraction. Sample absorption correction was also performed according to published equations specific to the geometric setup of the instrument,[38] and finally, a modified version of the Rachinger method[98] was used to mathematically correct for $K_{\alpha 2}$ radiation.

2.2.3 Inverse Least Squares (ILS) Regression

Inverse least squares (ILS) regression assumes that component concentration is a function of diffraction intensity. The standard ILS univariate model for a single component is calculated by:

$$y = xb + e \tag{2.1}$$

where y is the reference concentration value, b is the regression coefficient, x is the diffraction value at a specific peak position (*i.e.* a single peak intensity, a calculated peak area, ratio of intensities, *etc.*), and e is the error, which is assumed to be attributed to the concentration values. One of the features of ILS regression is that quantitative analysis can be performed even when the concentration of only a single component is known in the calibration mixture. In multiple linear regression (MLR), several independent variables are used, and the regression vector is calculated as follows (in matrix notation):

$$\mathbf{B} = \frac{\mathbf{X'Y}}{\mathbf{X'X}} \tag{2.2}$$

where **Y** is a matrix of concentration values, **X** is a matrix of intensity values, **B** is an matrix of regression coefficients. MLR is limited, in that the number of variables selected can not exceed or equal the number of samples in the calibration set. For example, a calibration set having $n_{vars} = n_{samples}$ only possesses enough statistically-

independent information to estimate the mean; a larger sample set provides additional degrees of freedom to estimate other statistical parameters. Although statistical methods are available to assist with variable selection (*i.e.* stepwise regression), calibrations created with suboptimal selections can introduce modeling errors such as noise inflation from collinearity and over-fitting.[99]

2.2.4 Classical Least Squares (CLS) Regression

Classical least squares (CLS) regression is often used in spectroscopic quantitative modeling owing to its agreement with Beer's law. Under some conditions, PXRD intensity will be a linear function of the number of diffracting planes present, which qualifies the application of CLS regression in PXRD data modeling. CLS assumes a linear combination of pure component sensitivities, where each component is weighted by concentration. Unique to this technique is the feature that the regression vectors can be used as estimates of the pure component diffraction patterns. CLS regression models can be generated using PXRD data provided all reference constituent concentrations are known (**Equation 2.3**):

$$\mathbf{X} = \mathbf{KY} + \mathbf{E}_c \tag{2.3}$$

where **X** is a matrix of diffraction intensities, **K** is a matrix containing the regression vectors (pure component estimates), **Y** is a matrix of concentration values for all constituents, and $\mathbf{E_c}$ is the error matrix. Model error is attributed to diffracted intensities (*i.e.,* microabsorption, extinction, preferred orientation, *etc.*). The calculation of the regression vector (estimated pure components) is as follows:

$$\mathbf{K} = \mathbf{Y}^{+} \bullet \mathbf{X} \tag{2.4}$$

where the superscript "+" indicates the Moore-Penrose pseudoinverse. The effectiveness of CLS regression in multivariate modeling is limited when the concentrations of all constituents contributing to signal (in the case of PXRD, diffract or cause diffuse scatter) are not known, or when non-linearities are present.[99]

2.2.5 Principal Components Regression (PCR)

Principal components regression (PCR) is the ILS regression of "scores" calculated from principal components analysis (PCA) against a dependent variable(s). The objective of PCA is to maximize the variation contained in a data matrix with as few underlying "factors" as possible.[100] The PCA model has the form of:

$$\mathbf{X} = \mathbf{TP'} + \mathbf{E} \tag{2.5}$$

where **X** is a data matrix of *k* sample-independent variables (diffraction intensities), for *n* samples, **T** is a matrix of component "scores" in vector form for each component, **P** is a matrix of component "loadings," and **E** is a matrix containing the residuals (the prime indicates the transpose of the matrix). Principal component scores and loadings are calculated using singular value decomposition.[101] The algorithm proceeds through a least squares fit of a straight line through the data in a *k*-dimensional hyperspace.[102] New components are fitted to the data until an adequate amount of the variance has been explained. In PCR, the dependent variable(s) (*i.e.,* reference concentration values) are linearly regressed against the scores. The regression coefficients are calculated as follows:

$$\mathbf{B} = \frac{\mathbf{T'Y}}{\mathbf{T'T}} \bullet \mathbf{P} \tag{2.6}$$

where **Y** is a matrix of concentration values. A full-length regression vector is obtained by projecting the regression coefficients onto the loading vector(s). Calibrations may be

created with fewer samples than variables. Reviews of PCA and PCR can be found elsewhere.[99,102]

2.2.6 Partial Least Squares (PLS) Regression

The PLS and PCR algorithms, being factor-based analysis methods, have similar goals. The objective of PLS is to maximize the amount of co-variation explained between dependent variables and independent variables using the fewest number of factors. Contrary to PCA where only the independent variables are used to calculate the basis set, PLS incorporates both dependent and independent variables in the basis set calculation. It may be envisioned that this method is particularly powerful when the dependent variable set contains low noise. Generally speaking, PLS explains the total variance in fewer factors relative to PCR. In this study, the *SIMPLS* algorithm was used to directly calculate factors as linear combinations of the original variables, while constrained to orthogonality and normalization restrictions.[103] The PLS algorithm used herein,[104] and representative reviews can be found elsewhere.[99,102]

2.3 Results and Discussion

The fully balanced concentration design matrix used for this study is shown in **Table 2.1** and contains five concentration points (0,20,25,40,60% w/w) for each of the four constituents. The concentration points were added to the design matrix in a one-by-one fashion, followed by a calculation of the matrix covariance; each point was adjusted to minimize this covariance. It should be noted that separate experimentation concerning instrument sensitivity, selectivity, and signal-to-noise has been previously reported in Moore *et al.*,.[97] At each concentration point, mixtures were compacted using 5 different pressures (67.0 MPa, 117.3 MPa, 167.6 MPa, 217.8 MPa, and 268.1 MPa), resulting in a

calibration sample size of 145 compacts. Recognizing that consolidation may induce changes to diffraction intensity[105,106] and diffuse scatter, samples compacted at different pressures were included in the calibration set to incorporate pattern variability into the model approximation. An additional sample at each concentration point, compacted using a randomly-assigned pressure, was used to test the calibrations.

Table 2.1. Sample composition design matrix.

Tablet #	Theophylline wt/wt	Lactose wt/wt	MCC wt/wt	Starch wt/wt
1	0.600	0.200	0.200	0.000
2	0.400	0.400	0.200	0.000
3	0.200	0.600	0.200	0.000
4	0.400	0.200	0.400	0.000
5	0.200	0.400	0.400	0.000
6	0.200	0.200	0.600	0.000
7	0.600	0.200	0.000	0.200
8	0.400	0.400	0.000	0.200
9	0.200	0.600	0.000	0.200
10	0.600	0.000	0.200	0.200
11	0.400	0.200	0.200	0.200
12	0.200	0.400	0.200	0.200
13	0.000	0.600	0.200	0.200
14	0.400	0.000	0.401	0.200
15	0.200	0.200	0.400	0.200
16	0.000	0.400	0.400	0.200
17	0.200	0.000	0.600	0.200
18	0.000	0.200	0.600	0.200
19	0.400	0.200	0.000	0.400
20	0.200	0.400	0.000	0.400
21	0.400	0.000	0.200	0.400
22	0.200	0.200	0.200	0.399
23	0.000	0.400	0.200	0.400
24	0.200	0.000	0.400	0.400
25	0.000	0.200	0.400	0.400
26	0.200	0.200	0.000	0.600
27	0.200	0.000	0.200	0.600
28	0.000	0.200	0.200	0.600
29	0.250	0.250	0.250	0.250

Univariate calibrations were created by regressing a single intensity value for each individual component (*i.e.*, the largest Bragg peak for crystalline materials and the

largest overall intensity for the disordered materials) against constituent concentration (nominal value from the design). The PCR and PLS regression vectors for each constituent were estimated individually from a component-specific orthogonal basis set. Selection of the ideal number of principal components/latent variables (shown in **Table 2.2**) was performed through minimization of both the root mean square error of calibration (RMSEC) and the root mean square error of cross validation (RMSECV).

Table 2.2. Selected statistical values for the different quantitative PXRD calibrations relative to the collection geometry.

			Transmission			Reflectance		
Method	**Component**	**LV**	**R^2**	**SEP (%)**	**Precision (%)**	**R^2**	**SEP (%)**	**Precision (%)**
Univariate	**Theophylline**	N/A	0.961	3.79	0.00024	0.898	5.09	0.09491
	Lactose		0.927	5.70	0.00081	0.911	4.95	0.03195
	MCC		0.809	9.70	0.00324	0.940	5.81	0.04044
	Starch		0.292	15.30	0.00935	0.006	18.18	0.07608
CLS	**Theophylline**	N/A	0.972	2.90	0.00027	0.942	3.57	0.16771
	Lactose		0.963	3.48	0.00076	0.939	3.63	0.12726
	MCC		0.955	3.69	0.00237	0.958	5.47	0.07263
	Starch		0.946	5.24	0.00413	0.866	4.91	0.01797
PCR	**Theophylline**	1	0.972	2.92	0.00027	0.926	4.81	0.07780
	Lactose	3	0.968	3.16	0.00062	0.919	4.82	0.02580
	MCC	4	0.751	9.77	0.00346	0.875	7.49	0.03176
	Starch	5	0.941	4.98	0.00133	0.868	5.00	0.10102
PLS	**Theophylline**	1	0.972	2.91	0.00028	0.933	4.49	0.08007
	Lactose	3	0.978	2.48	0.00110	0.943	3.71	0.02915
	MCC	3	0.955	3.84	0.00210	0.937	6.23	0.03226
	Starch	3	0.950	4.88	0.00256	0.804	7.15	0.07829

Traditionally, it is not common to use a univariate PXRD calibration to predict the concentration of a disordered component in a mixture; however, it was performed in this study as a means to illustrate the practicality of different multivariate methods. In general, data collected in transmission geometry provided better linearity, precision and lower concentration prediction error relative to reflectance geometry for both the crystalline and disordered components. In transmission geometry, the entire sample volume is irradiated, whereas only a fraction of the sample is interrogated in reflectance analysis. Therefore, data collected in transmission mode is less susceptible to errors derived from analyzing inhomogeneous "regions" within a sample matrix.

The data in **Table 2.2** indicate that the standard error of prediction (SEP) for theophylline in most instances is greater when using data collected in reflectance geometry relative to that in transmission. This indicates a correlation between instrument geometry and prediction error; more than likely a result of the diffraction pattern anomalies related to specific analytical optics setup modes. Barring microabsorption, extinction, and other anomalies, regression vectors should mimic pure component diffraction patterns. In **Figure 2.1**, the pure component pattern and the calculated regression vectors for all three multivariate theophylline prediction models are shown for data collected in reflectance geometry. There is good agreement between all regression vectors and the pure component pattern, as would be expected. For PCR and PLS, negative correlations are observed at ~18º 2θ, which specifically corresponds with the location of Bragg peaks resulting from lactose monohydrate diffraction. Therefore, the PCR and PLS models are sensitive to the changes in both theophylline and lactose concentration at this angle. In **Figure 2.2**, the theophylline regression vectors calculated

from data collected using transmission geometry are identical to the pure component scan. Further, the negative correlations observed at ~18º 2θ in the reflectance geometry regression vectors are nearly absent from transmission data. The calculated regression vectors from the transmission geometry are, therefore, more highly correlated to only changes in theophylline concentration, thereby resulting in enhanced theophylline sensitivity and decreased prediction errors.

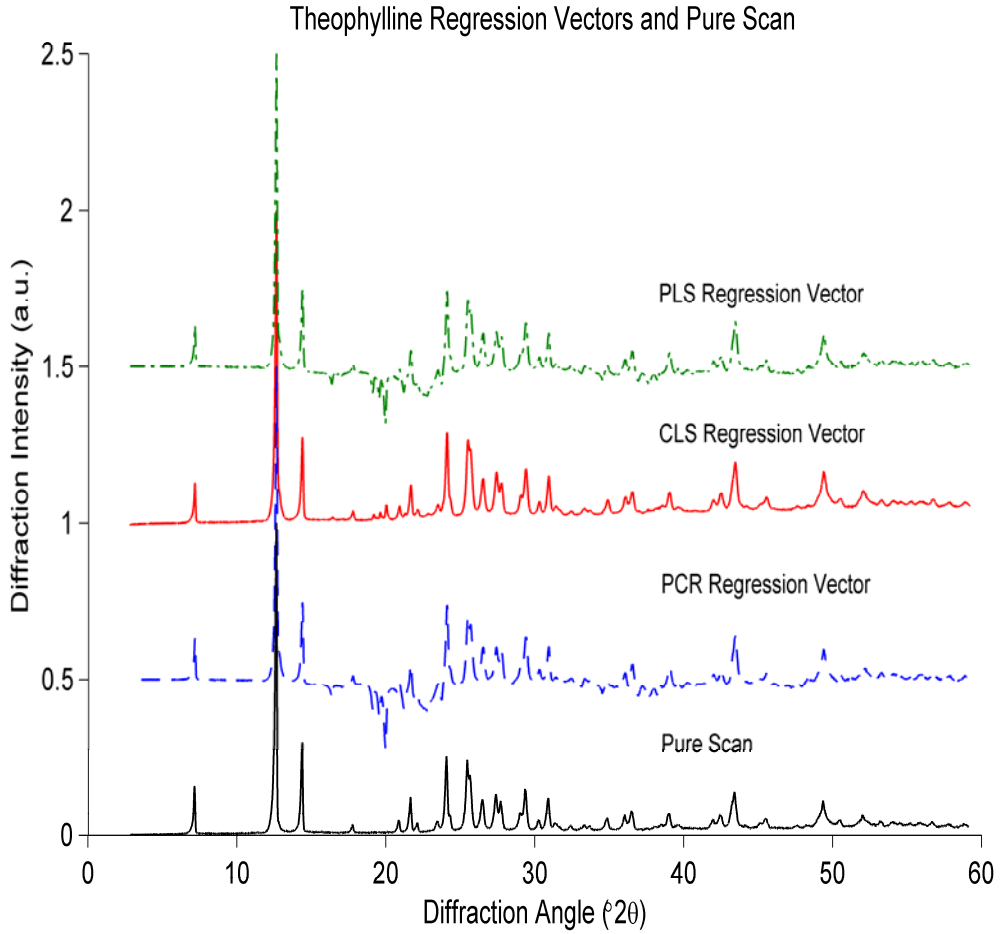

Figure 2.1. Calculated regression vectors for each multivariate calibration used in the prediction of anhydrous theophylline from data collected in reflectance geometry.

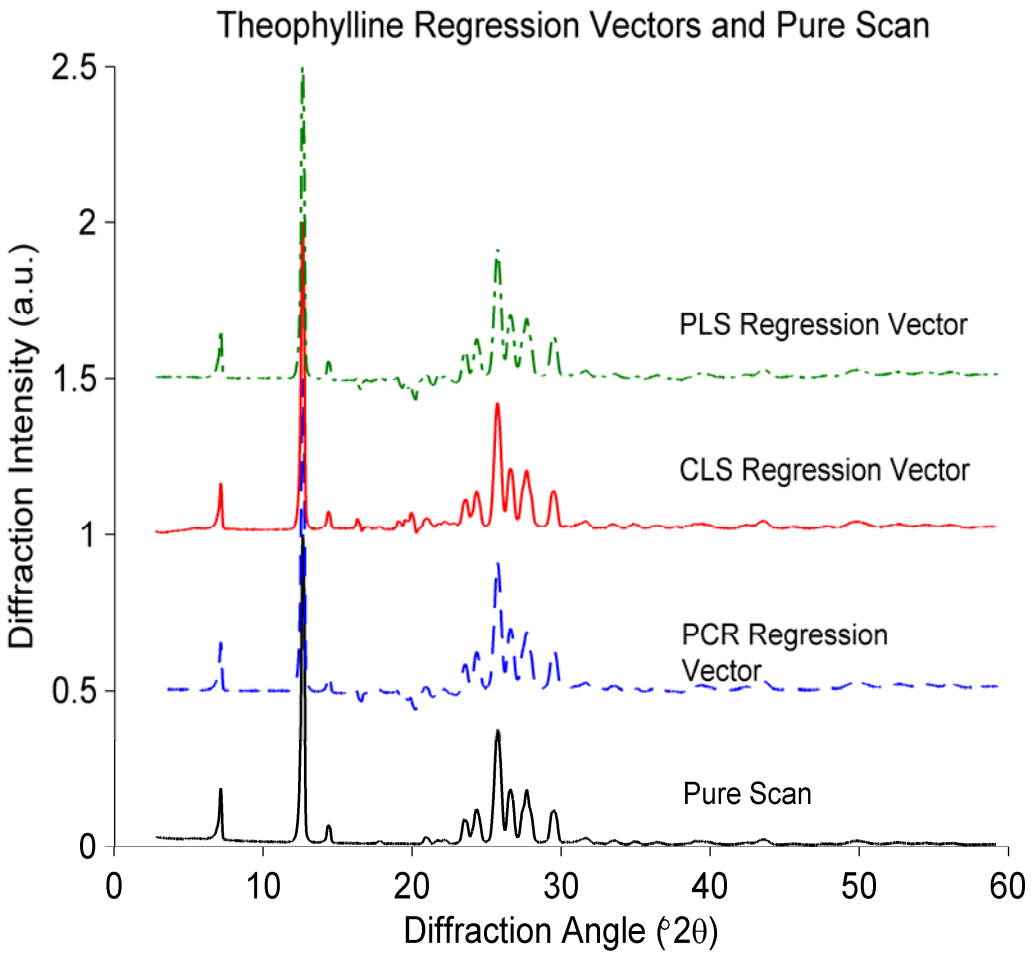

Figure 2.2. Calculated regression vectors for each multivariate calibration used in the prediction of anhydrous theophylline from data collected in transmission geometry.

When considering disordered materials, the diffuse scatter that produces the characteristic "amorphous halo" may not be linearly related to constituent concentration. Non-linear relationships may manifest as negative correlations in regression vectors as a result of modeling the decrease in concentration of other components. In **Figure 2.3**, the calculated regression vectors for the three multivariate starch prediction models and the corresponding pure component scan are shown for data collected in reflectance geometry. The CLS regression vector bears the highest correlation with the pure component diffraction pattern, thereby affording enhanced linearity and decreased prediction error

relative to PCR and PLS (from **Table 2.2**). Although they possess the same positive correlations as the starch pure component scan, the regression vectors from both PCR and PLS once again exhibit negative correlations attributable to changes in the concentrations of other mixture components at angles corresponding to their respective peaks of principal diffraction: theophylline (~12º 2θ), lactose (~18º 2θ) and MCC (~22º 2θ). This same trend is also observed for the transmission data, as shown in **Figure 2.4**, where both the PLS and PCR regression vectors exhibit the same negative correlations seen in reflectance. Additionally, the CLS regression vector of transmission data representing diffraction by the starch component possesses negative correlations at ~12º 2θ and ~18º 2θ. These regression vector similarities resulted in near-equal linearity and prediction error for the PCR, PLS, and CLS starch calibrations created from data collected in transmission. The negative correlations observed in the disordered component regression vectors, therefore, could quite possibly be a result of the non-linear relationship between constituent concentration and diffuse scatter intensity.

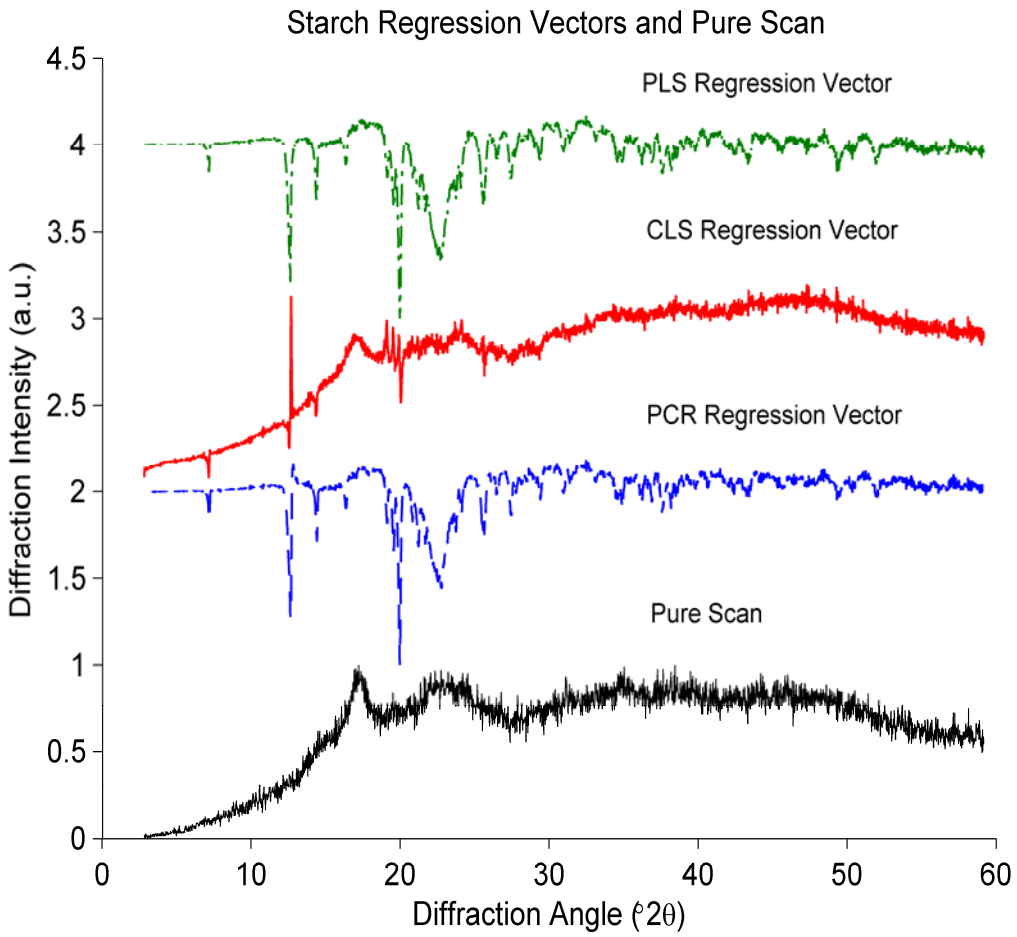

Figure 2.3. Calculated regression vectors for each multivariate calibration used in the prediction of starch from data collected in reflectance geometry.

Table 2.3. The effects of various powder pattern corrections on linearity and the standard error of prediction of the univariate and PLS calibrations for prediction of both crystalline and disordered components using data collected by reflectance geometry.

			No corrections	Axis shift	Kα2 subtraction	Absorption correction	Background subtraction	All
R^2	Univariate	Crystalline	0.723	0.898	0.759	0.729	0.723	0.904
		Disordered	0.493	0.489	0.484	0.486	0.493	0.473
	PLS	Crystalline	0.906	0.936	0.906	0.908	0.906	0.938
		Disordered	0.864	0.890	0.866	0.849	0.864	0.871
SEP (%)	Univariate	Crystalline	7.61	5.59	6.75	7.34	7.61	5.02
		Disordered	11.41	11.19	11.54	11.76	11.41	11.99
	PLS	Crystalline	4.39	4.45	4.40	4.11	4.39	4.10
		Disordered	5.97	6.40	5.98	6.42	5.97	6.69

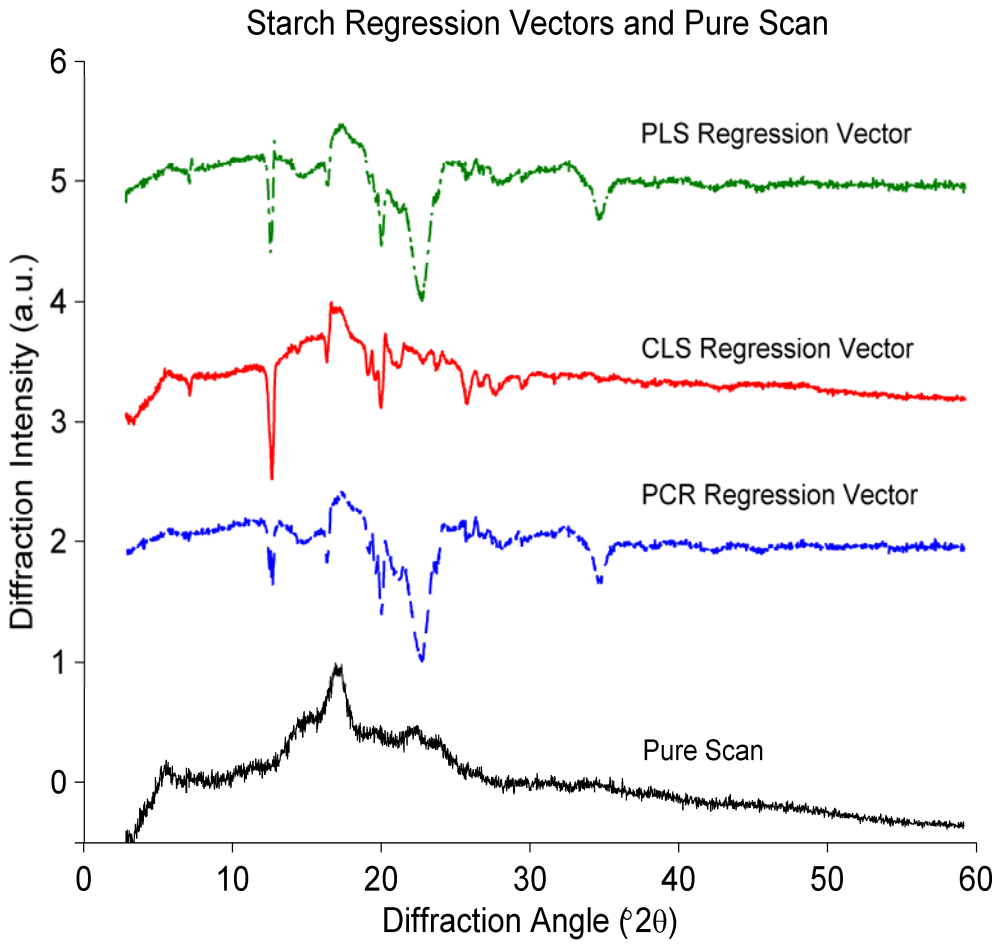

Figure 2.4. Calculated regression vectors for each multivariate calibration used in the prediction of starch from data collected in transmission geometry.

In **Table 2.3**, linearity and SEP are reported as a function of applied pattern corrections using data collected in reflectance geometry. Statistics are reported as an average of the two crystalline components and an average of the two disordered components. The importance of correcting for axis shift prior to creating a univariate calibration in the prediction of crystalline components is supported by the observed increased linearity and decreased prediction error. When modeling a single intensity, or the area of a single peak, anisotropic peak distortions may build errors into the calibration and result in inaccurate predictions. Interestingly, in multivariate calibrations (such as

PLS) the linearity and predictability are not significantly affected by corrections to the powder patterns relative to univariate modeling. By modeling multiple intensities having correlation with constituent concentration, the anisotropy of error-related variance is compensated for through increased correlation at unaffected variables. Further, through maximization of the explained covariance between diffraction intensity and constituent concentration, variability due to anisotropic peak aberrations is modeled in the regression vectors.

Table 2.4. The effects of various powder pattern corrections on linearity and the standard error of prediction of the univariate and PLS calibrations for prediction of both crystalline and disordered components using data collected by transmission geometry.

			No corrections	Axis shift	Kα2 subtraction	Absorption correction	Background subtraction	All
R^2	Univariate	Crystalline	0.940	0.947	0.937	0.939	0.941	0.944
		Disordered	0.260	0.590	0.260	0.186	0.260	0.551
	PLS	Crystalline	0.968	0.972	0.968	0.971	0.968	0.975
		Disordered	0.770	0.948	0.772	0.771	0.770	0.952
SEP (%)	Univariate	Crystalline	4.24	4.10	4.42	4.47	4.15	4.75
		Disordered	16.30	10.72	16.30	16.49	16.30	12.50
	PLS	Crystalline	3.07	2.89	3.07	2.96	3.07	2.70
		Disordered	8.07	4.17	8.10	8.17	8.07	4.36

Table 2.4 shows the effects of PXRD pattern corrections on linearity and prediction error using data collected in transmission geometry. Comparison with **Table 2.3** (reflectance geometry collection) indicates that performance statistics are superior for transmission data, particularly for disordered (weakly diffracting) materials. This is not unexpected, given that transmission experiments interrogate the entire compact sample volume. Although the low mass attenuation coefficients of pharmaceutical materials permit some sample penetration (on the order of mm), reflectance experiments interrogate a much smaller volume compared to transmission experiments. For the crystalline components, both models are invariant to all of the applied corrections. However, the SEP for the disordered components using PLS shows significant dependence on axis shift correction. **Figure 2.5** illustrates the effects of applied pattern corrections on the calculated PLS regression vectors. The calculated regression vectors of raw diffraction patterns, patterns corrected for absorption only, patterns corrected for $K_{\alpha 2}$ only, or background subtraction only are highly correlated to one another. Further, these regression vectors exhibit differences from the regression vector calculated from patterns corrected for axis shift. The dashed boxes highlight the main differences observed between the aforementioned group of regression vectors and those for which axis shift was corrected. These differences represent uncertainties correlated to peak aberrations and result in modeling concentration changes of other components. Ultimately, the prediction error was larger due to the error in modeling the concentration changes in multiple components.

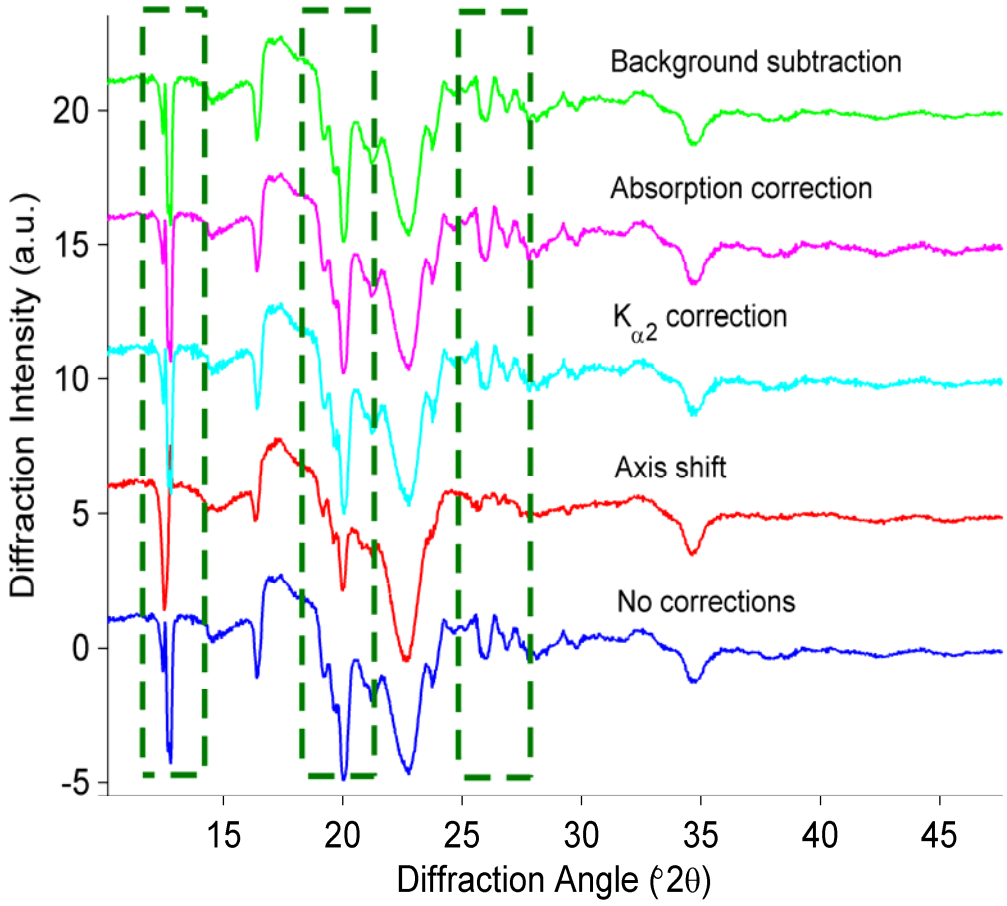

Figure 2.5. The effects of various corrections on the PLS calibration regression vectors as applied to data collected in transmission geometry.

For many spectroscopic methods, building quantitative models that include variability associated with compression force is imperative. However, the variability in diffraction intensity observed to have resulted from consolidation was minimal because the materials used in this study have low mass-attenuation coefficients and require few applied absorption corrections. Admittedly, creating a calibration and test sample matrix the size of the set presented in this work (n = 174) may be impractical in a multi-product industrial development group. Given the results of the present data, however, efficient calibrations could have been created using fewer samples. This was tested by

compressing a single sample from each concentration point (**Table 2.1**) at 268.1 MPa in order to re-create the calibrations (29 samples total), while the remaining samples (n = 145) were used to test the models generated from this reduced data set. The graph in **Figure 2.6** shows prediction error as a function of component, as modeled by each calibration method for differently sized calibration sets relative to the experimental optics utilized. Linearity statistics (not shown) were not affected by the reduction of the dataset used for calibration. The data in **Figure 2.6** illustrate that prediction error associated with transmission geometry is relatively unaffected by the size of the calibration set employed. Reflectance geometry, however, indicates that a slight increase in prediction error occurs when using the smaller calibration set, possibly due to the decreased signal-to-noise.

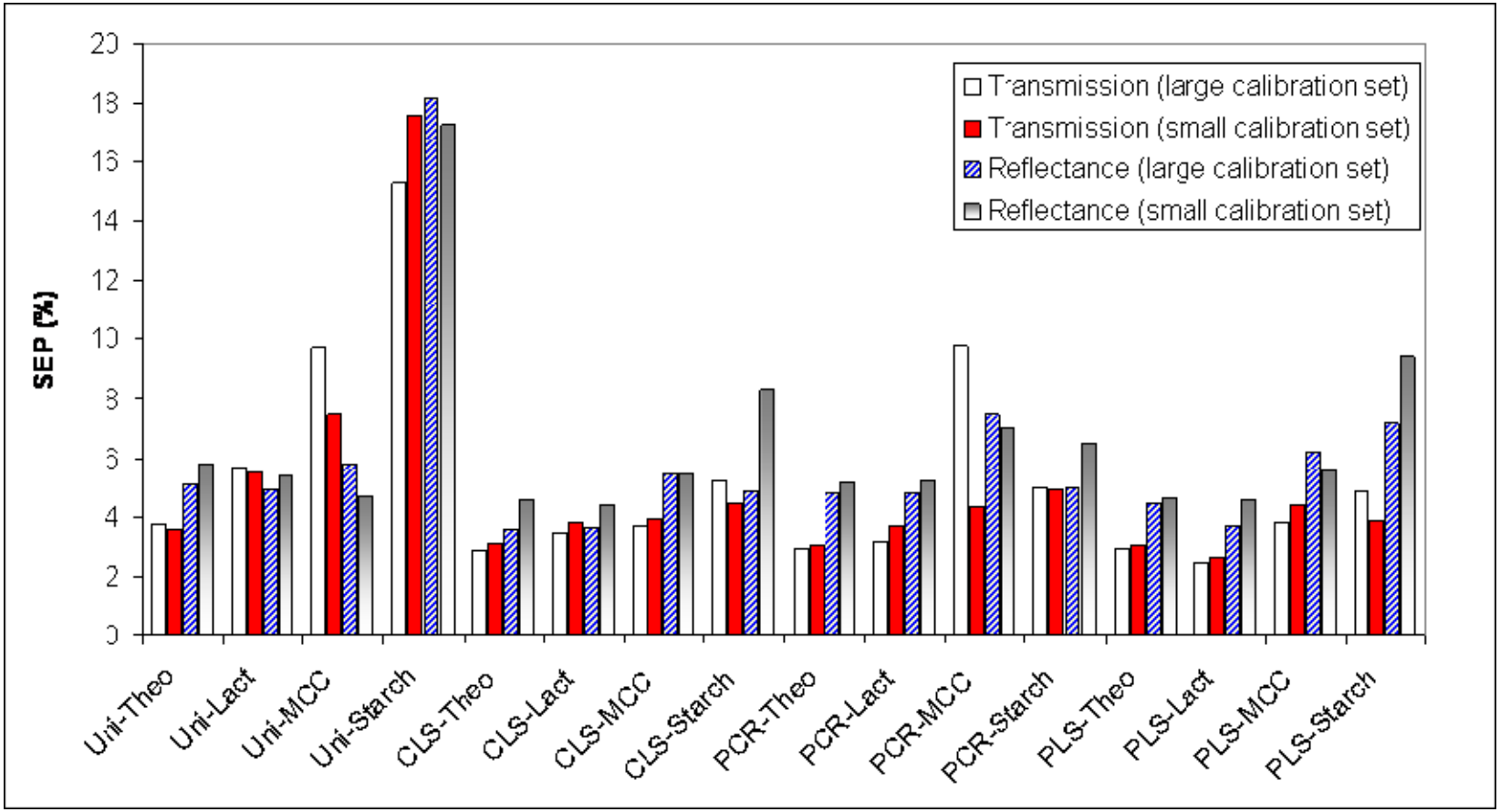

Figure 2.6. The effects of the number of samples in the calibration set on the standard error of prediction for both collection geometries.

The starch and theophylline calculated CLS regression vectors for reflectance and transmission geometry are shown in **Figure 2.7** and **Figure 2.8**, respectively. When comparing the starch regression vectors as calculated from data collected in reflectance geometry, the smaller calibration set vector exhibits increased noise (rougher) and larger peak/trough correlations ultimately attributable to increased uncertainty. Though the starch regression vector (as calculated from data collected in transmission geometry) for the smaller calibration set is "rougher" relative to the vector from the larger set, the overall shape is the same for both. The regression vectors calculated from the smaller calibration set using data collected in transmission mode demonstrated increased correlation to the regression vectors calculated from the larger calibration set relative to the reflectance data. Therefore, this enhanced correlation results in nearly identical error statistics independent of calibration sample size (shown in **Figure 2.6**).

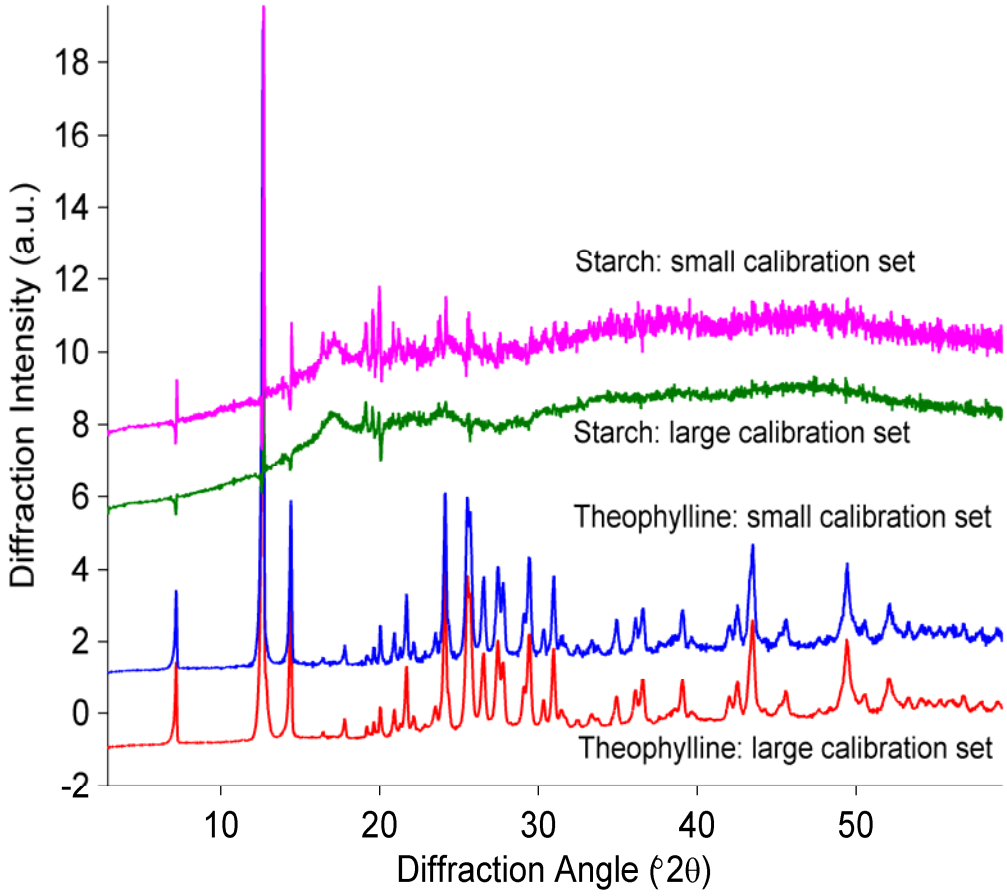

Figure 2.7. The effects of the number of samples in the calibration set on the starch and theophylline CLS regression vectors for data collected from reflectance geometry.

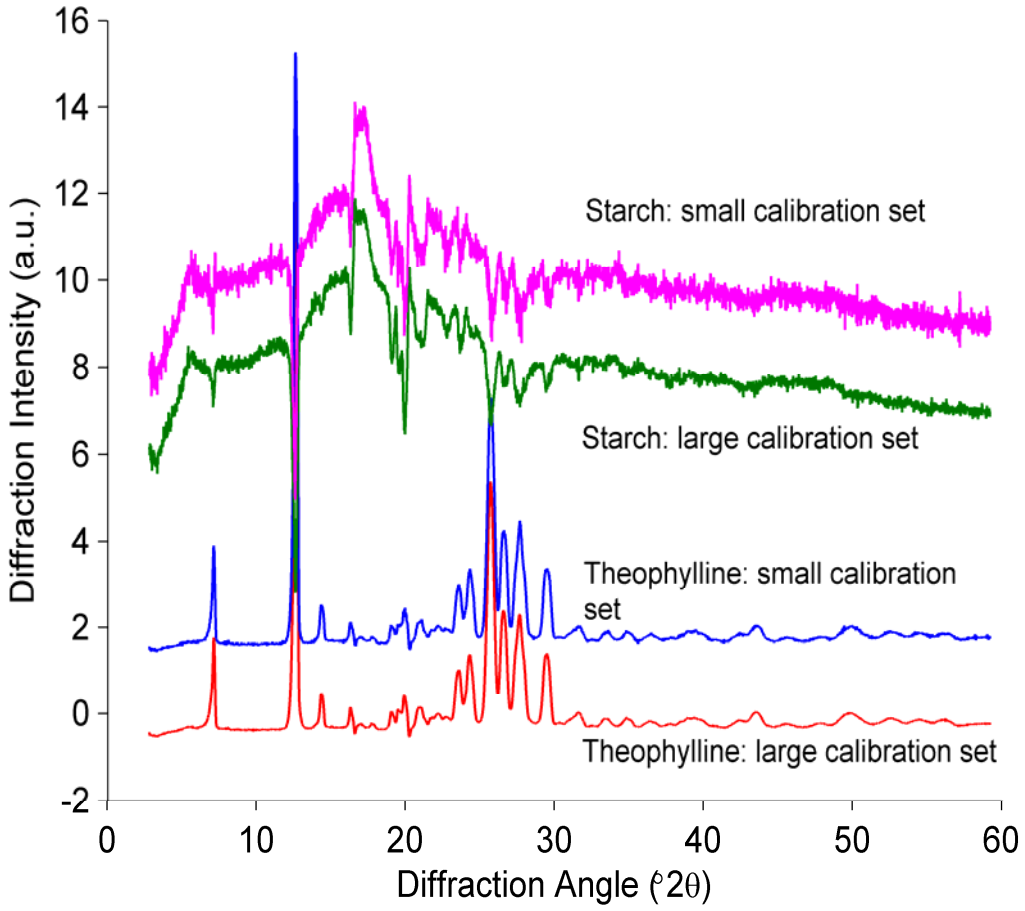

Figure 2.8. The effects of the number of samples in the calibration set on the starch and theophylline CLS regression vectors for data collected from transmission geometry.

Based on the results presented herein, calibrations via PLS, created from the data collected in transmission geometry can be recommended as optimal for quantitative PXRD of similar systems. The calibrations created using this algorithm exhibited optimal linearity values of 0.972, 0.978, 0.955, and 0.950 for theophylline, lactose, MCC, and starch, respectively. The calibrations created in the present work stem from a quaternary design using the design matrix concentration values. Given that each nominal design value is likely to differ slightly from the actual concentration, each component reference concentration value has some random error. Overall, a cumulative 2-3% error

in content uniformity of all the constituents may be anticipated; linearity values approaching 0.98 in this design are, therefore, statistically acceptable. Additionally, minimum prediction error and enhanced precision for both crystalline and disordered components in complex, intact compacts was achieved. Furthermore, PLS models were observed to be less susceptible to errors associated with diffraction pattern anomalies and effects related to the size of the calibration set.

2.4 Conclusions

The ability to analyze intact compacts makes PXRD an important analytical tool for non-destructive pharmaceutical characterization. The structure-sensitivity afforded by PXRD enables quantitative applications having the ability to discriminate between different chemical components, polymorphs, and other phase mixtures. It has been shown in this work that the traditional univariate calibrations are affected by peak distortion, variable selection, and applied powder pattern corrections. Multivariate calibrations, however, provided enhanced linearity, decreased prediction errors, and exhibited less susceptibility to errors attributable to peak distortions relative to single-point calibrations. Further, calibration errors related to pattern anomalies were minimized through empirical modeling of the entire diffraction pattern (*i.e.* both Bragg diffraction and diffuse scatter intensities). As an increased amount of mixed amorphous/crystalline systems are formulated into dosage forms, the need for discriminative and sensitive quantitative analytical tools for intact analysis will become more prevalent.

Chapter 3: A Structural Investigation into the Compaction Behavior of Pharmaceutical Composites Using Powder X-ray Diffraction and Total Scattering Analysis

3.1 Introduction

The US Food and Drug Administration's Critical Path Initiative to New Medical Products maintains the need for industry to continue investigation and development of analytical methods capable of fundamentally characterizing pharmaceutical systems. The availability of more effective analysis techniques will facilitate product and process understanding, and reduce drug product failures.[107] Challenges encountered during drug product development are often the result of unpredicted changes to the physicochemical and mechanical properties of materials used in manufacturing. Characterization during small-scale research should predict performance modifications that may occur at commercial scale. This goal is contingent upon accurate detection and quantification of specific changes in material structure that can be linked with product performance. Some such changes (*i.e.* dissolution rate, friability, etc.) can be traced to very subtle structure modifications, where the largest limitation in detection and quantification is inadequate analytical sensitivity, particularly in the context of complex mixtures of materials. At present, research in this area is heavily focused on active pharmaceutical ingredients (API), with substantially fewer reports concerning responses of excipients or composites to processing. As the pharmaceutical industry moves forward, it is imperative that the synergistic functions of both API and excipients be considered as the basis for claiming product understanding at the level of specifically engineered delivery platforms.

Powder X-ray Diffraction (PXRD) is universally applied for detecting phase changes and assessing material structure and order. Industrial applications of PXRD rest in the ability to analyze materials from all stages of powder processing, without prior destructive sample preparation. Traditional uses of this technique have focused on analysis of prominent, high-intensity Bragg diffraction peaks that are characteristic of a given crystalline phase. In addition to long-range order, the powder diffraction pattern contains information pertaining to intermediate and short-range order. Specifically, diffuse scatter, which occurs between and superimposed on Bragg diffraction peaks, offers additional information pertaining to the short- and intermediate-range structure of materials, when treated appropriately.

In the present work, the compaction behavior of anhydrous theophylline was investigated. Binary composite compacts were also prepared and analyzed, using either a common tablet filler (α-lactose monohydrate), or a common tablet compression aid (microcrystalline cellulose; MCC) in combination with anhydrous theophylline. PXRD, in combination with total scattering computational methods, was used to assess the effects of powder compaction without reversion of compacts to powders. Furthermore, the use of PCA as an alternative to the traditional weighted agreement factor in comparing PDF transformed diffraction data was explored.

3.2 Materials and Methods

Binary mixtures comprised of anhydrous theophylline (Lot No. 92577, Knoll AG, Ludwigshafen, Germany) and either crystalline α-lactose monohydrate, referred to as lactose for the remaining discussion, (Lot No. 125090020, Acros Organics, Geel, Belgium) or microcrystalline cellulose, referred to as MCC for the remaining discussion,

(Avicel PH 200, Lot No. M427C, FMC BioPolymer, Mechanicsburgh, PA) were blended and compacted using an automatic single-station Carver Press (Carver, Inc, Model 3887.1SDOA00, Wabash, IN) equipped with a 13 mm flat-faced punch. The approximate median particle size of theophylline was 90 μm. A circumscribed central composite experimental design[102] was used for sample preparation, in which both excipient concentration (0 – 75% w/w) and compaction pressure (67 – 503 MPa) were varied. Consolidation at each pressure resulted in composite solid fractions ranging from 0.85 – 0.98. The central point was repeated five times to build precision into the design.

3.2.1 Powder X-Ray Diffraction (PXRD)

PXRD data were collected using an X'Pert Pro MPD system (PANalytical B.V., Almelo, the Netherlands) equipped with a copper anode (λ = 1.5406 Å), an auxiliary elliptical mirror, and X'CeleratorTM detector. The operational voltage and amperage were set to 45.0 kV and 40.0 mA, respectively, and diffraction patterns were acquired using an irradiation time of 101.42 seconds per step and an angular step size of 0.017° 2θ over a range of 2 – 100° 2θ. Data were collected with the instrument set in transmission geometry, using intact compact samples, sandwiched between two layers of X-ray transparent kapton film and placed on a spinning vertical sample stage (16 rpm).

3.2.2 Pattern Separation

PXRD analysis of binary compacts produced diffraction patterns containing information from both components. To study the effects of powder compaction on a specific constituent, a method for accurately separating diffraction events attributable to each individual component was required. The pattern subtraction technique,[108] commonly reported for this purpose, often leaves residual artifact in separated patterns

attributable to diffraction by component(s) that are not of interest, or negative peak intensities as a result of overcompensation. An alternative approach for isolating single constituent diffraction patterns from multi-component data has been recently reported in the literature.[97]

Generalized Least Squares (GLS) pre-processing has been reported in the near-infrared spectroscopy literature as a multiplicative orthogonalization technique used to make spectra "blind" to interferants, while retaining sensitivity to the main analyte.[109] Signal pre-processing using this covariance-weighted technique reduces the dimensionality of final models by including prior knowledge. The scaling matrix, $\boldsymbol{T}$, is calculated as follows:

$$\Sigma_{\mathrm{L}} = d_{\boldsymbol{L}}^{2}\boldsymbol{L}\boldsymbol{L}'+\boldsymbol{I} \tag{3.1}$$

$$\boldsymbol{T} = inv(\Sigma_{\mathrm{L}}^{1/2}) \tag{3.2}$$

where d is a scalar covariance-scaling constant, $\boldsymbol{L}$ is an $m \times n$ noise matrix, $\boldsymbol{L}'$ is the transpose of $\boldsymbol{L}$, and $\boldsymbol{I}$ is an $n \times n$ identity matrix. In the case of PXRD, the matrix $\boldsymbol{L}$ would be comprised of diffraction information from material(s) that are not of interest to a given evaluation. The final scaling of the multi-component diffraction patterns, $\boldsymbol{X}$, is given by:

$$\boldsymbol{X}_{\boldsymbol{FIN}} = \boldsymbol{X}\boldsymbol{T} \tag{3.3}$$

where $\boldsymbol{T}$ multiplicatively suppresses diffraction in $\boldsymbol{X}$ displaying covariance with the noise matrix. A problem is encountered with this particular method when components that are not of interest (noise) diffract at the same angle (2θ) as the component of interest. This issue results in the suppression of diffraction events from the component being isolated.

The method was, therefore, modified to account for covariance between the "noise" component(s) and the component of interest by creating a second scaling matrix:

$$\Sigma_R = \boldsymbol{d}_{\boldsymbol{R}}^2 \boldsymbol{RR}' + \boldsymbol{I} \tag{3.4}$$

where $\boldsymbol{R}$ is an $m \times n$ matrix of the reference material (*i.e.* a pure component diffraction pattern of the constituent of interest) and the remaining variables are defined above. The scaling matrix, Σ_R, was used to suppress angular variables in the noise matrix, which are covariate with the component of interest as follows:

$$\Sigma_{FIN} = \Sigma_{\boldsymbol{L}} \bullet \boldsymbol{inv}(\Sigma_{\boldsymbol{R}}) \tag{3.5}$$

$$\boldsymbol{T} = \boldsymbol{inv}(\Sigma_{FIN}^{1/2}) \tag{3.6}$$

where $\boldsymbol{T}$ is substituted back into **Equation 3.3**. By compensating for angular variables (2θ) of the noise matrix that are covariate with those of the constituent of interest, a more accurate separation is obtained. All data manipulations in this study were performed using programs written in-house in the Matlab programming environment (v7.1, MathWorks, Natick, MA).

3.2.3 Pair Distribution Function (PDF)

The PDF is a total scattering method that exploits the Fourier relationship between X-ray diffraction intensity and the real-space arrangement of atoms, given appropriate data treatment. This method has received extensive attention in the inorganic literature;[39,43,44,110] however, few pharmaceutical applications have been reported.[48,51,52] In the present work, the PDF was calculated for (a) compacts formed from pure components, and (b) mathematically isolated diffraction attributable to a single component, detected from PXRD patterns of binary compacts. This provided a sensitive

method to assess the structure-specific compaction behavior of theophylline, individually as well as in a consolidated mixture. The PDF, *G(r)*, is defined as:

$$G(r) = 4\pi r\left[\rho(r) - \rho_o\right] \tag{3.7}$$

where $\rho(r)$ and ρ_o are the local and average atomic number densities, respectively, and r is the inter-atomic separation distance.[111] The PDF calculates the probability of finding atom pairs separated by a distance r, and is obtained by transformation of the reciprocal space structure function, $S(Q)$, according to:

$$G(r) = \frac{2}{\pi}\int_0^{Q_{max}} Q\left[S(Q) - 1\right]\sin(Qr)\,dQ \tag{3.8}$$

where $S(Q)$ is obtained from a diffraction experiment, and Q is the magnitude of the scattering vector.[41] The term Q_{max} is the resolution of the diffraction experiment, which is dependent on the wavelength of radiation used and the maximum diffraction angle (°2θ) of data collection. Corrections were made to the intensity data to obtain a structure function normalized to the total-scattering cross-sectional area, consistent with the assumptions of Egami and Billinge.[38]

For a crystalline material, a theoretical PDF may be calculated from a solved crystal structure. The mathematical corrections applied to a theoretical PDF, including compensations for limited Q-resolution and broadening of probability peaks as a result of thermal motion are detailed elsewhere.[38,47] Theoretical modeling of the PDF, $G(r)_c$, for a crystalline material is achieved by:

$$G(r)_c = \frac{1}{r}\sum_m \sum_n \frac{f_m f_n}{\langle f \rangle^2}\delta(r - r_{m,n}) - 4\pi r\rho_o \tag{3.9}$$

where f_m and f_n are the atomic form factors for the individual atoms, $\langle f \rangle$ is the mean atomic form factor for the structure, and $r_{m,n}$ is the separation distance between atoms m

and n (from the crystal structure), where the delta function is assessed out to a user-defined radial distance r_{max}.

Reviews of the PDF, both experimental and theoretical, are found elsewhere.[38,111] All intensity corrections and PDF calculations were performed using software developed in-house in the Matlab programming environment based on published equations. Theoretical PDF patterns for anhydrous theophylline were calculated using the solved Cambridge Structural Database (CSD) crystal structure, (refcode: BAPLOT01).

3.2.4 Principal Components Analysis (PCA)

PCA is a multivariate, bilinear decomposition technique used to identify the orthogonal basis set, which explains the maximum amount of variance in a data matrix, $\boldsymbol{X}$; where $\boldsymbol{X}$ is n observations of an m-dimensional vector. PCA decomposes data into loadings and scores, where loadings represent the weight of each variable for a given principal component (PC), and scores represent the weight of the PC for each sample. Vectors comprising a data matrix, $\boldsymbol{X}$, possessing comparable score values for a given PC are similar; dissimilar score values indicate differences between vector features. Reviews of principal components analysis may be found elsewhere in the literature.[99,112] PCA models were calculated in the Matlab programming environment using the PLS_Toolbox (v3.0, Eigenvector Research, Manson, WA).

Traditional comparison of PDF transforms have involved calculation of a weighted agreement factor, R_{wp}, between the properly scaled sample PDF and a reference, albeit a theoretically calculated or empirically derived pattern.[38] In this study, PCA was used to assess variations among PDF patterns as an alternative to the weighted agreement factor commonly employed for this purpose. This method may be preferable to the R_{wp}

calculation when there are a large number of PDFs to compare, as in this study. PCA is also applicable when a reference pattern is not available or comparison to a reference pattern is inappropriate for a given analysis.

3.3 Results

3.3.1 Pure Theophylline Compaction

In **Figure 3.1**, the PXRD patterns (average of 3 samples) for theophylline compacted at 67 MPa and 503 MPa are shown as blue and red solid lines, respectively. The original patterns were normalized and were corrected for absorption, Laue monotonic scattering, Compton scattering, *etc*.[38] to remove physical artifacts (i.e., sample thickness and solid fraction). The red and blue dashed lines in **Figure 3.1** respectively represent one standard deviation (n=3) for diffraction from theophylline compacts prepared at 67 MPa and 503 MPa. The Bragg peak positions of samples compacted at higher pressures occur at the same diffraction angle (°2θ) relative to the sample compacted at 67 MPa, indicating low probability of uniform residual strain. Moreover, additional PXRD peaks, which would be indicative of a polymorphic conversion, are not observed. One noticeable difference between the patterns, however, is increasing diffuse scatter over the 23-30 º2θ range for samples compacted at higher pressures.

Figure 3.2 (solid lines) shows the average PDF pattern (n=3) for each of the corresponding samples in **Figure 3.1**. The dashed lines represent one standard deviation as calculated from the three replicates. At lower radial distances in the PDF ($r < 30$ Å), peak positions and intensities are highly correlated, irrespective of compaction pressure. In contrast, the **Figure 3.2** inset, which focuses on $r > 40$ Å, shows a dampening of the

probability peaks, as well as peak shifts, which become significant with increased compaction pressure.

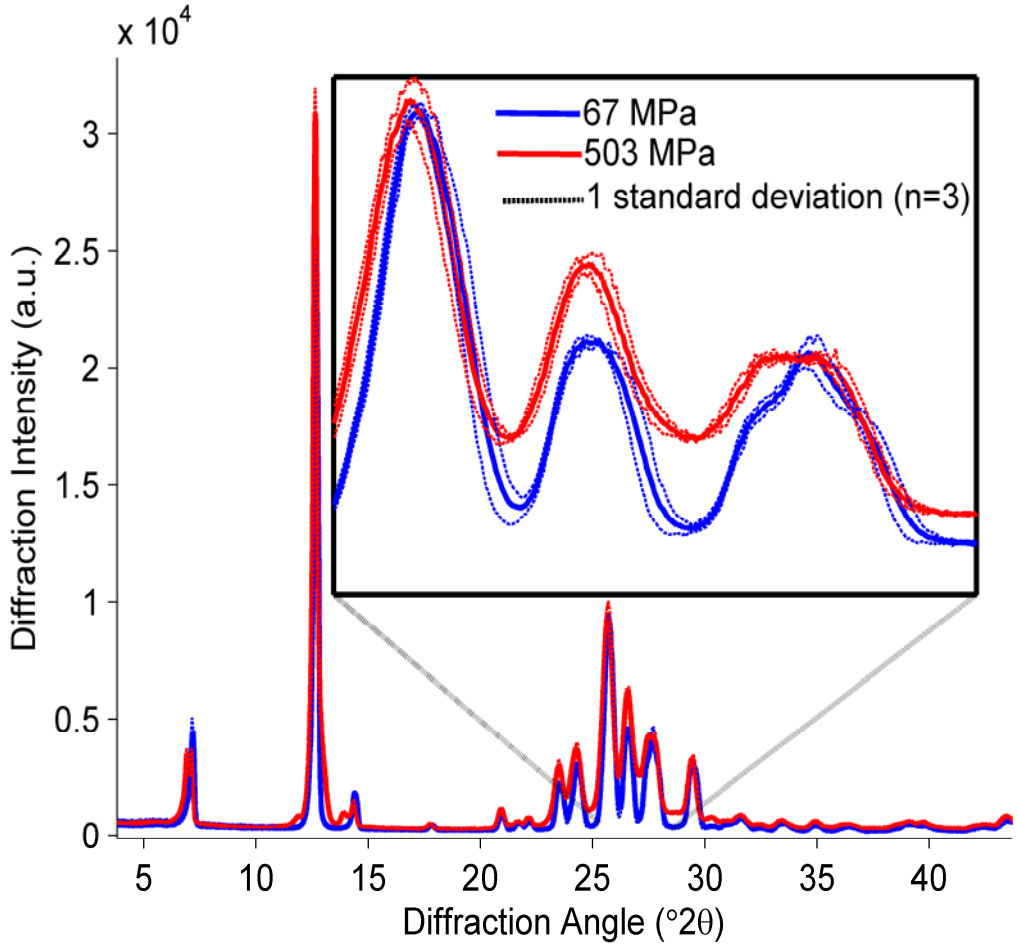

Figure 3.1. Mean PXRD patterns (average of n=3) for anhydrous theophylline compacted at 67 MPa (blue, solid line) and 503 MPa (red, solid line). The red and blue dashed lines correspond to 1 standard deviation from the mean of samples compacted at 67 MPa and 503 MPa, respectively.

In an attempt to arrive at a possible materials-based explanation for the alterations observed in the PDF of anhydrous theophylline upon compaction at high pressures, simulations based on reverse Monte Carlo[39,113] refinement were performed. Briefly, as unit cell translation and expansion was calculated from the crystal structure solution, spatial permutations were applied to randomly selected atomic coordinates. These

permutations included linear deviations from periodicity, as well as alterations to axial orientation (*e.g.*, the molecule may be rotated 120° with respect to the *c*-axis). The fully translated model, calculated to a defined r_{max}, therefore contained a certain percentage of atomic coordinates that varied from their original positions defined by the average structure. PDF patterns for computationally altered structures were subsequently calculated, and the data were mathematically compared with experimentally derived PDF patterns using an agreement factor.

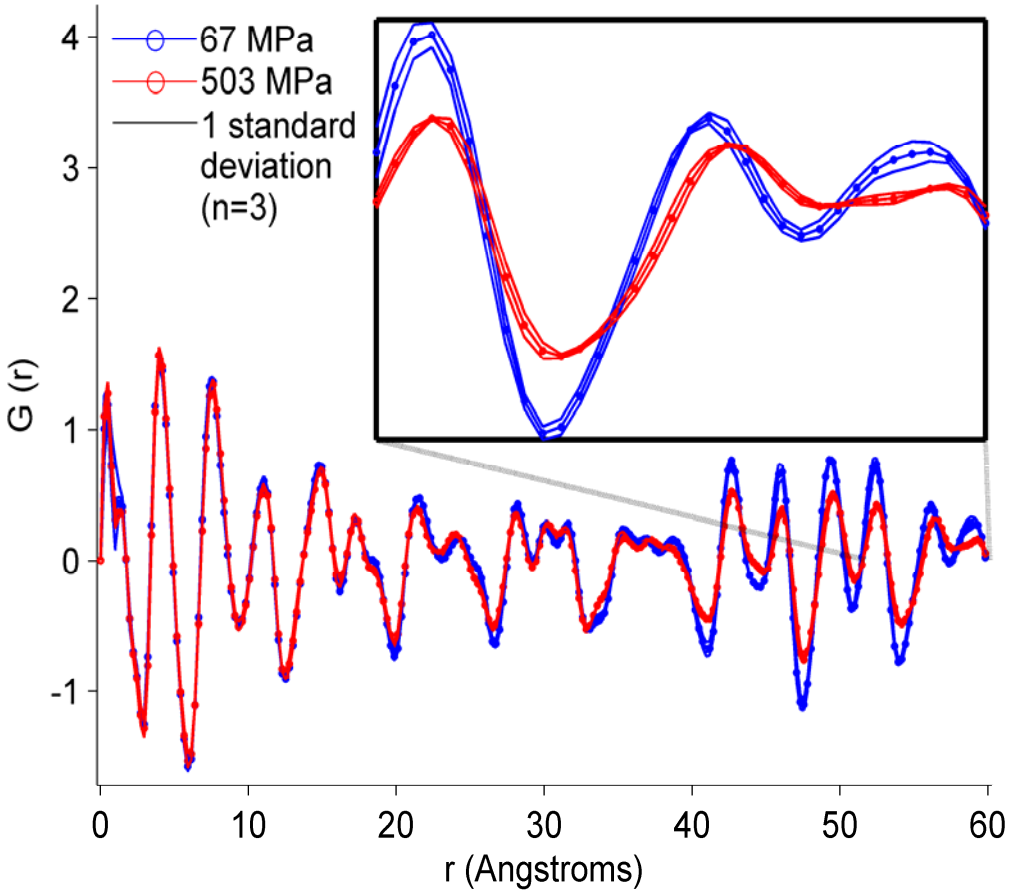

Figure 3.2. Mean PDF patterns (average of n=3) of theophylline compacted at 67 MPa (blue, solid line) and 503 MPa (red, solid line). The red and blue dashed lines correspond to 1 standard deviation from the mean of samples compacted at 67 MPa and 503 MPa, respectively.

When simulating atomic displacements from average structure, it is important to define the proper constraints to yield physically-meaningful simulations. One of the constraints incorporated in the models calculated for this study was the rigid body assumption; *i.e*, the molecule was held rigid such that permutations to atomic coordinates could not result in changes to intra-molecular bond distances, angles, or conformations. An additional constraint prevented atomic overlap of coordinates resulting from simulated displacements. The final constraint allowed only atomic coordinates residing at r values comprising long-range order ($r > 40$ Å) to be randomly selected for permutation, as this region defines the marked differences between the PDFs presented in **Figure 3.2**.

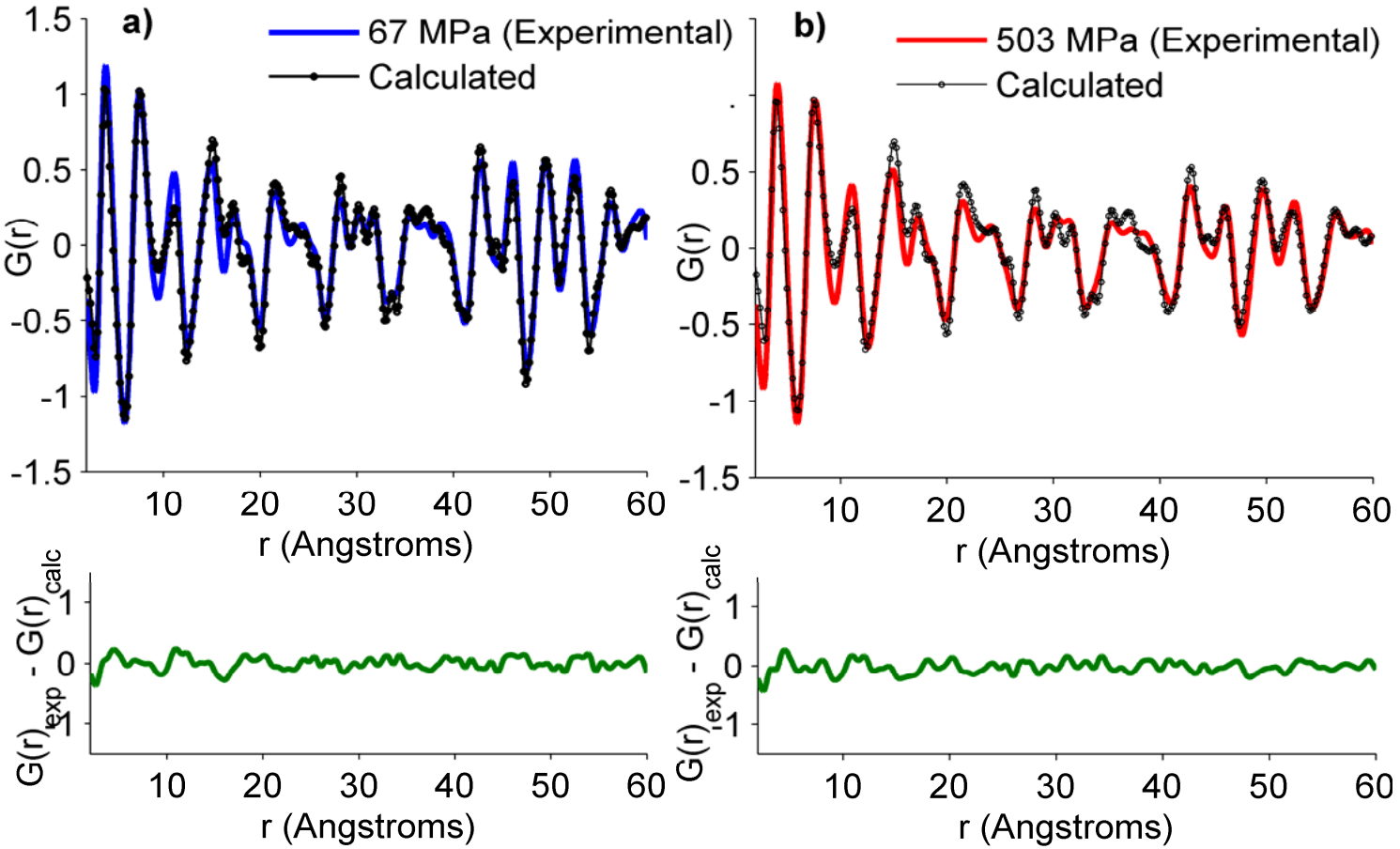

Figure 3.3. (a) Experimental PDF pattern for theophylline compacted at 67 MPa (black), calculated PDF pattern from the crystal structure (blue circles), and the difference plot (green, below); (b) Experimental PDF pattern for theophylline compacted at 503 MPa (red), a simulated PDF pattern from reverse Monte Carlo refinement (blue circles), and the difference plot (green, below).

The experimentally derived PDF pattern for theophylline compacted at 67 MPa (blue line) and the PDF pattern calculated from the crystallographic structure of theophylline (black circles) are shown in **Figure 3.3a**. Generally speaking, the difference plot indicates pattern similarity, especially at longer *r* values. This result is expected as the compaction pressure is insufficient to induce large deviations from the average crystallographic structure.

Recall from **Figure 3.2** that the PDF of the high pressure sample shows dampening and shifts in peak position relative to the lower pressure sample at $r > 40$ Å. An acceptable fit between the PDF of the sample compacted at high pressure and the theoretical PDF will require alterations to the original calculated PDF to accommodate the probability peak aberrations. **Figure 3.3b** shows the experimentally derived PDF for theophylline compacted at 503 MPa (red line), a refined PDF from the Monte Carlo simulation (black circles), and the difference between the two PDFs (green line, shown below **Figure 3.3b**). The simulated PDF shows the same probability peak shifts and dampening as the experimental PDF of the sample compacted at a high pressure. The goodness of fit between the calculated PDF and the experimental PDF can be seen in the difference plot (green) shown below **Figure 3.3b**. The simulated PDF was modeled by pseudo-randomly selecting molecules in the defined spherical volume (radius = 60 Å) and inducing a deviation from the average crystallographic structure. The number of molecular permutations was converted to a percentage of total molecules probed in the simulation. Therefore, the simulated PDF in **Figure 3.3b** (black circles) differs from the calculated PDF in **Figure 3.3a** (black circles) as a result of 0.928% of the molecules deviating from the defined average structure.

3.3.2 PDF of Mathematically Isolated Theophylline

Figure 3.4a shows the PXRD pattern of a sample (blue, circles) comprised of 25% w/w theophylline and 75% w/w MCC, compacted at 118 MPa. Diffraction data attributable only to theophylline (red) are superimposed over the diffraction pattern of the aforementioned sample. Most of the diffuse scatter observable in the diffraction pattern of the original binary sample (blue, circles) is absent when theophylline diffraction was isolated (red data). In **Figure 3.4b**, the PDF transform of the mathematically isolated theophylline (red) is shown superimposed with the calculated theoretical PDF pattern for theophylline (black, circles).

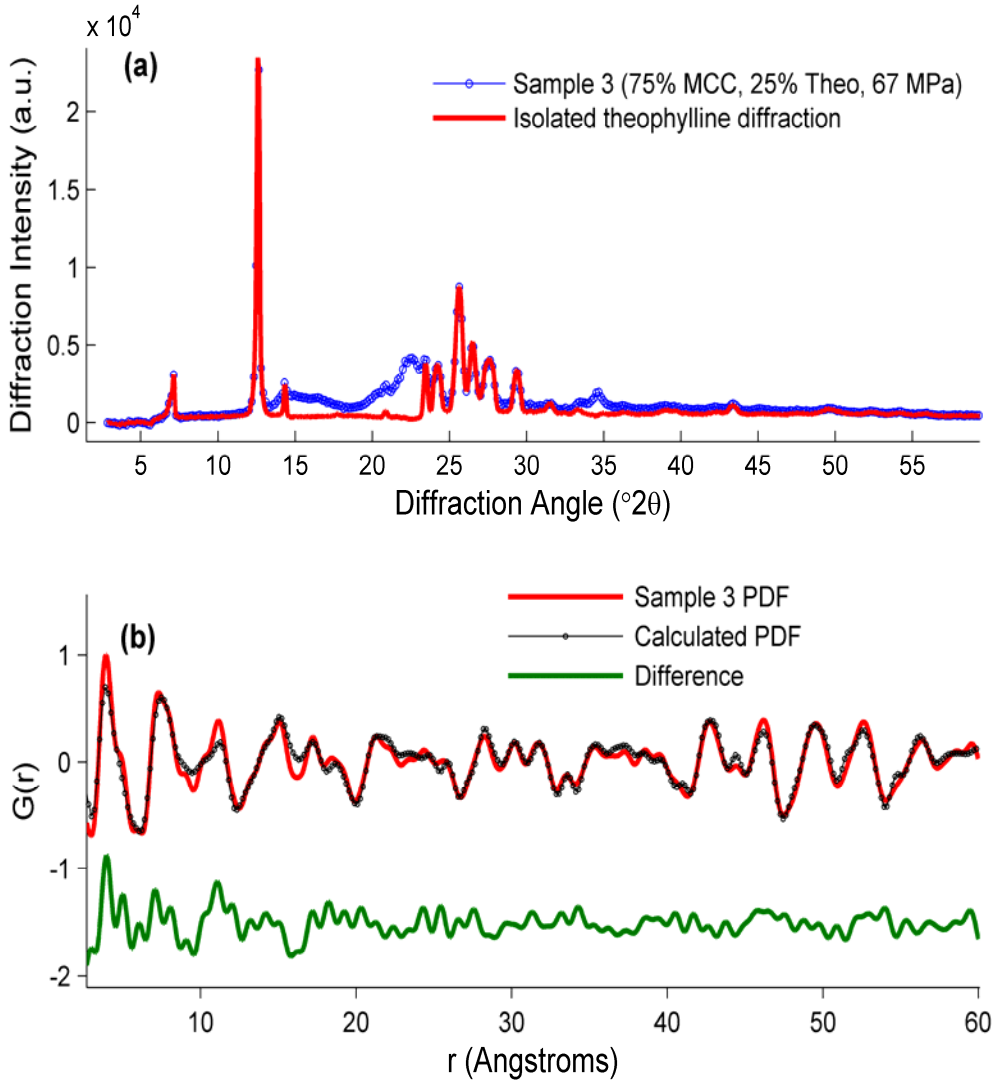

Figure 3.4. (a) PXRD pattern (zoomed) of a compact containing 75% MCC and 25% theophylline (sample3) compressed at 67 MPa (blue, circles) and the isolated diffraction attributable to theophylline (red); (b) The calculated pair distrubtion function of anhydrous theophylline (crystal structure ref: BAPLOT01) (black, circles), the pair distribution function of isolated theophylline from sample 3 (red), and the difference between the calculated and experimental (green).

Figure 3.5a shows the diffraction pattern of a sample (blue, circles) containing 25% w/w theophylline and 75% w/w lactose, compacted at 118 MPa. Mathematically isolated theophylline diffraction (red) is superimposed over the total diffraction data from this sample. Many of the Bragg diffraction peaks observed in the original sample pattern

(blue, circles), which are strictly attributable to lactose, are absent from the isolated theophylline diffraction pattern. In **Figure 3.5b**, the PDF transform of the isolated theophylline (red) is shown with the calculated PDF pattern for theophylline (black, circles).

3.3.3 PCA of PDF Transformed Data

As introduced, PCA is a bilinear decomposition method, where principle components (PCs) are calculated in a manner to explain the maximum amount of variance such that PC_n and PC_{n+1} are orthogonal. Similar PDF patterns will have similar scores for a given PC, while dissimilar PDF patterns will have drastically different score values for the same PC. Examples employing PCA score cluster analysis to ordinary PXRD patterns are found in the pharmaceutical literature;[45,114] however, the authors are unaware of the existence of previous applications of PCA cluster analysis to PDF data.

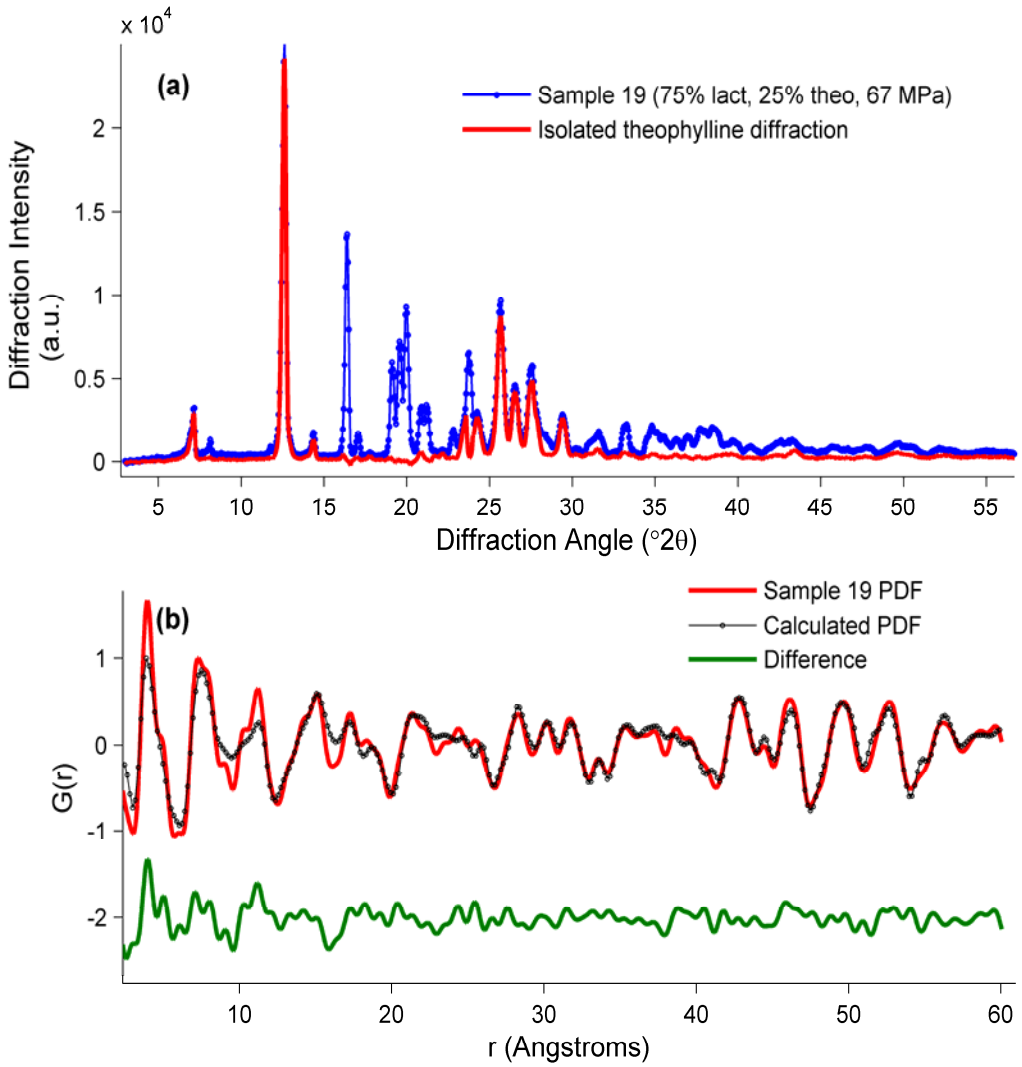

Figure 3.5. (a) PXRD pattern of a compact containing 75% lactose and 25% theophylline (sample 19) compressed at 67 MPa (blue, circles) and the isolated diffraction attributable to theophylline (red); (b) The calculated PDF pattern for anhydrous theophylline (crystal structure ref: *BAPLOT01*) (black, circles), the PDF pattern for isolated theophylline from sample 19 (red), and the difference between the calculated and experimental (green).

Three different PCA models were calculated, where each varied in the number/type of samples included. The first analysis incorporated PDF patterns for pure theophylline and theophylline mathematically isolated from binary mixtures with MCC. The resulting scores plot is shown in **Figure 3.6**. First, in the dimension of the first PC,

where 36.28% of the overall variance is explained, the score values for pure theophylline samples compacted at low pressures are drastically different than those for samples compacted at high pressures. The variance explained by the first PC, therefore, is weighed differently in PDF patterns for samples compacted at low pressures relative to samples compacted at high pressures. Secondly, PDF patterns for theophylline data mathematically isolated from binary samples containing MCC compacted at low pressures had similar score values for the first PC relative to those calculated for pure theophylline compacted at low pressures. This indicates that PDF patterns of samples compacted at low pressures were similar in the dimension of the first PC, regardless of MCC concentration. Additionally, all samples containing MCC compacted at higher pressures had score values similar to pure theophylline compacted at high pressures in the dimension of the first PC. Overall, it was observed that scores of PDF data from samples compacted at low pressures formed one general cluster, while those from samples compacted at higher pressures formed another cluster.

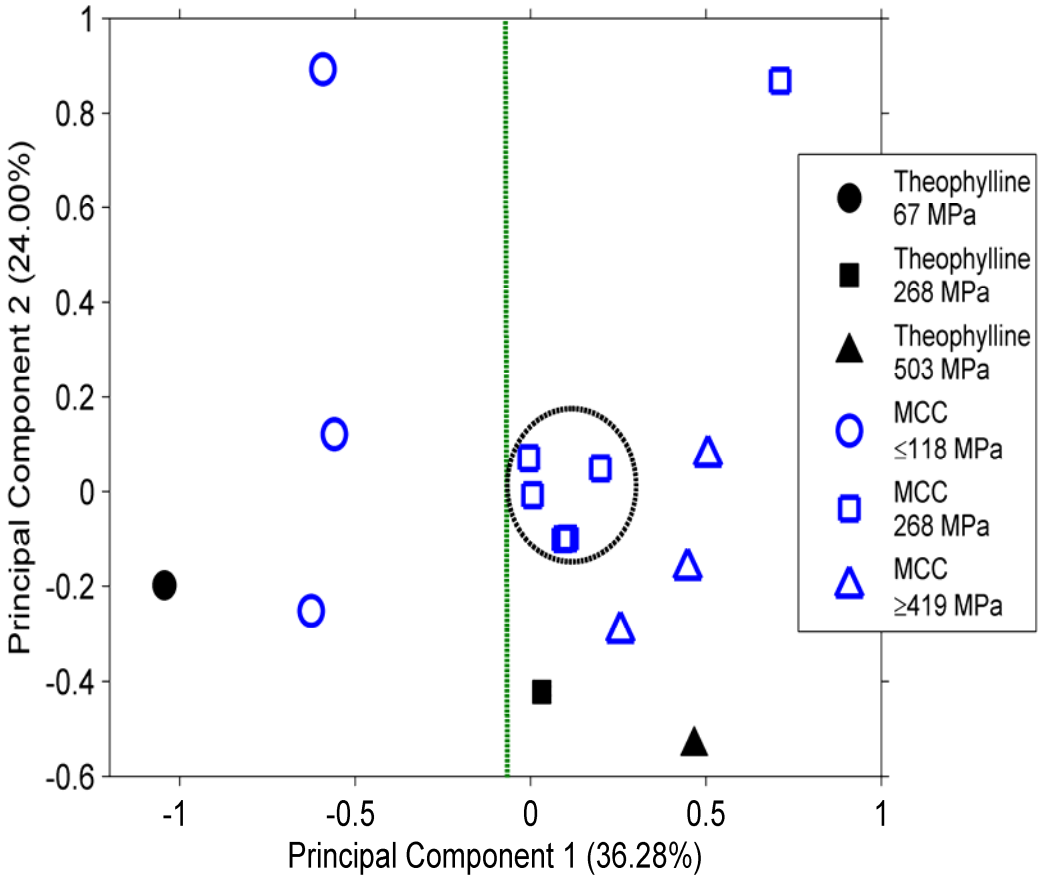

Figure 3.6. PCA scores plot corresponding to the first and second principal components for analysis of PDF patterns from pure theophylline samples (black, closed symbols) and PDF patterns from theophylline mathematically isolated from binary compacts containing MCC (blue, open symbols). Black, dashed line circles surround the replicate samples.

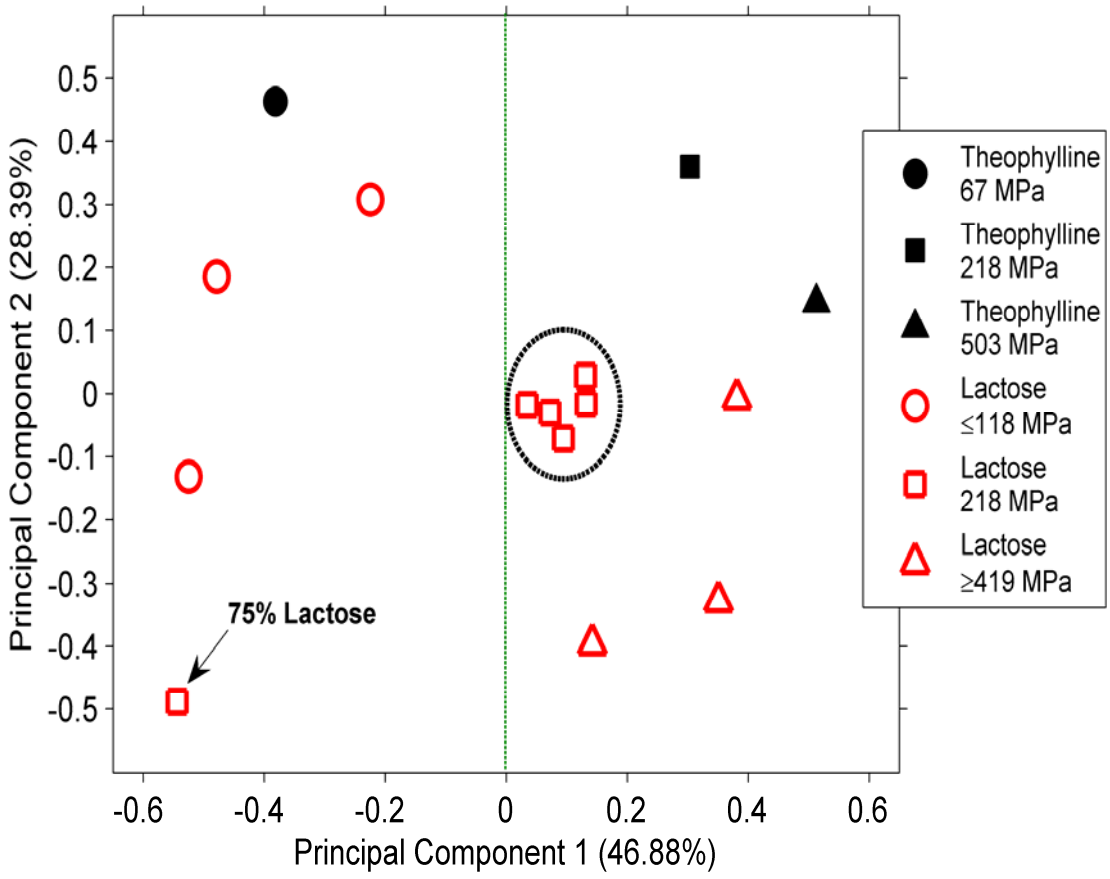

Figure 3.7. PCA scores plot corresponding to the first and second principal components for analysis of PDF patterns for pure theophylline samples (black, closed symbols) and PDF patterns for theophylline mathematically isolated from binary compacts containing lactose (red, open symbols). Black, dashed line circles surround the replicate samples.

The second PCA performed incorporated PDF data obtained from theophylline mathematically isolated from binary mixtures containing lactose, as well as pure theophylline compacts. The PCA scores plot for these data is shown in **Figure 3.7**, where the dimension of the first PC explained 46.88% of the overall variance. Score values for PDF patterns from pure theophylline samples compacted at low pressures were considerably different relative to PDF patterns from pure theophylline compacted at high pressures. Samples compacted at low pressures tended to cluster together, regardless of lactose content; as did samples compacted at high pressures. A particularly interesting

sample was the compact containing 75% w/w lactose compacted at 268 MPa, which clustered with the samples compacted at low pressures. These data indicate that the PDF pattern resulting from the isolated theophylline diffraction data of this sample is more similar to PDF data for samples compacted at low pressures than samples compacted at high pressures.

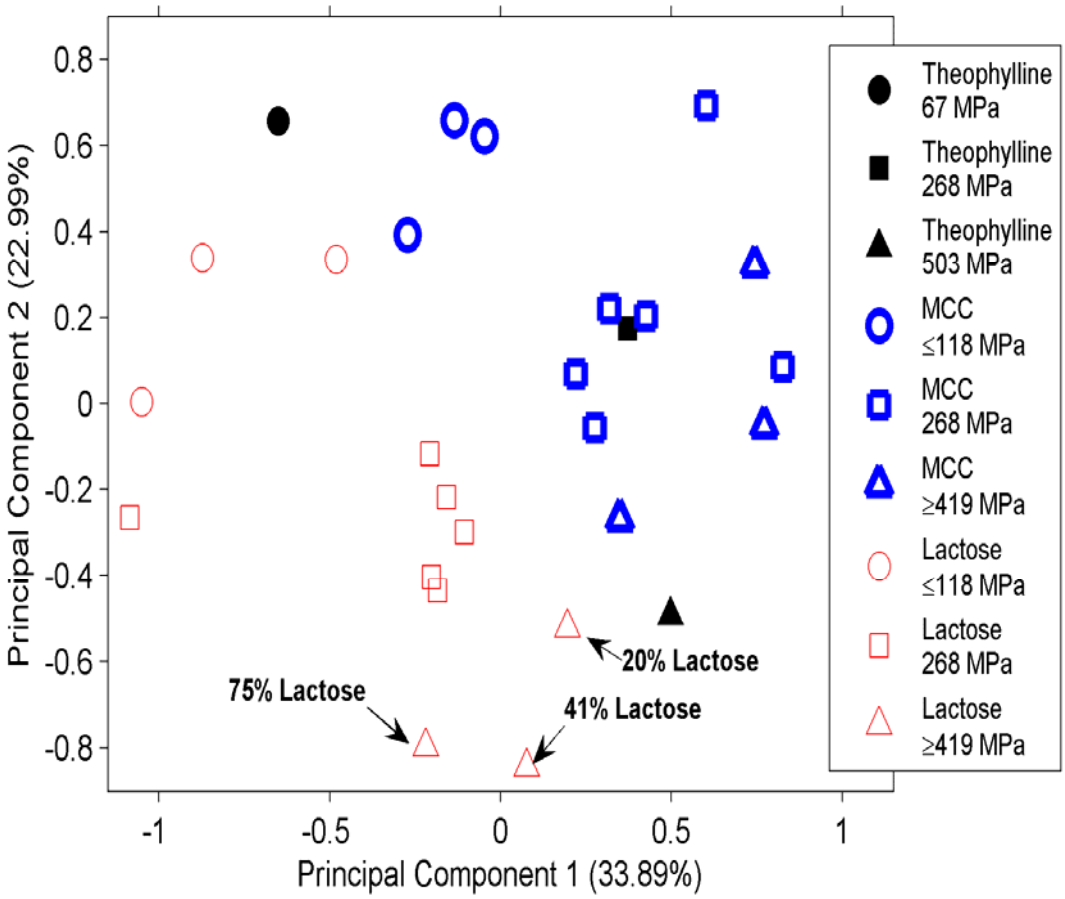

Figure 3.8. PCA scores plot corresponding to the first and second principal components for analysis of all samples, including: PDF patterns for pure theophylline samples (black, closed symbols), PDF patterns for theophylline mathematically isolated from samples containing MCC (blue, bold open symbols), and PDF patterns for theophylline mathematically isolated from samples containing lactose (red, un-emboldened open symbols).

The final PCA performed incorporated data from PDF patterns obtained from all samples in the circumscribed central composite experimental design, resulting in the

scores plot shown in **Figure 3.8**. In **Figures 3.6 and 3.7**, scores of samples compacted at low pressures formed one cluster while samples compacted at high pressures formed a separate cluster in the dimension of the first PC. In **Figure 3.8**, delineation between score values is not as obvious, and merit further explanation. Beginning with the pure theophylline compacts (filled symbols), the score values in the dimension of the first PC, where 33.89% of the overall variance is explained, are drastically different for samples compacted at low pressures versus those compacted at high pressures. The scores in the dimension of the first PC of PDF data from samples containing MCC (blue, unfilled symbols) again tended to cluster with pure theophylline samples compacted at similar pressures, irrespective of MCC concentration. Contrary to the previous analyses of PDF data for samples containing lactose, a clear-cut boundary delineating clusters of similarly compacted samples in the dimension of the first PC is not observed. Interestingly, almost all samples containing lactose (red, unfilled symbols) resulted in PDF patterns having score values (in the first PC) that were most similar to all other samples compacted at low pressures. The score values for all lactose samples compacted at the intermediate pressure (268 MPa) clustered around samples compacted at low pressures. Further, a lactose-containing sample compacted at 419 MPa clustered in the same area.

3.4 Discussion

3.4.1 Pure Theophylline Compaction

The PXRD patterns of pure theophylline compacted at different pressures exhibit an increase in diffuse scatter over the 23-30 º2θ range. With a median particle size of 90 μm, it is anticipated that the effects on pattern features and further mathematical manipulations will be minimal, as peak broadening and increased diffuse scatter tend to

occur for particle sizes in the nanometer scale. Replicate samples (n=3) of pure theophylline compacted at 67 and 503 MPa were analyzed to estimate contributions of sample variability to the PXRD patterns. At both compaction pressures, the standard deviation intervals (**Figure 3.1**, dashed lines) indicate that the increase in diffuse scatter is not attributable to random sample variations, as the magnitude of the standard error is not sufficient to explain the scattering deviations between the PXRD patterns of the samples compacted at two different pressures (**Figure 3.1**, solid lines).

The previously discussed pattern distortion can be associated with many different physical and structural anomalies;[45,111] however, a discussion of each is beyond the scope of this manuscript. Rather, it is proposed that the introduction of disorder into a crystalline material may result in the alterations observed in the average diffraction patterns (solid lines) in **Figure 3.1**. The PDF method is relatively sensitive to instances where materials exhibit long-range order; however, significant structural distortions may also be present that would not be representative of the average crystallographic structure. These "crystallographically challenged materials" result in dampened PDF features as a function of increasing radial distances relative to their pure crystalline counterparts.[39] It may, therefore, be suggested that the features observed as a function of increasing compaction pressure in **Figure 3.2** are the result of increasing deviations from the average crystallographic structure of anhydrous theophylline. Replicate samples at each compaction pressure were carried through the PDF transformation to assess the effect of sample variability on the resulting PDF patterns. As shown by the standard deviation intervals (**Figure 3.2**, dashed lines), the probability peak dampening and shifting can not be adequately explained by sample-to-sample variability, as the magnitude is not

sufficient to justify the pattern distortions. This is further supported by data in **Figure 3.3**. Key features in the experimental PDF and the pattern generated by simulating distortions to 0.928% of the molecules from their defined average position (**Figure 3.3b**), agree well with one another. This agreement further supports the observation that compaction-related structural distortions resulted in the types of probability peak changes observed in **Figure 3.2**.

It is worthwhile to note that the PDF is a one-dimensional representation of a three- dimensional structure; therefore, multiple simulated models may result in the same one-dimensional PDF representation. Though the simulations in this study were properly constrained to prevent physically meaningless solutions, other random structure permutations may give an acceptable or better answer than the one yielded in **Figure 3.3b**. The proposed model is presented only to show that the PDF differences associated with compaction are consistent with compaction-induced disorder.

3.4.2 PDF of Mathematically Isolated Theophylline

The significant disorder of MCC presents a potential problem with respect to separation of diffuse scatter specifically attributable to MCC from the diffuse scatter from theophylline introduced as a result of compaction. The green difference plot in **Figure 3.4b** shows that theophylline diffraction data mathematically isolated from the theophylline:MCC mixtures agrees well with the theoretical PDF of theophylline. Given the low compaction pressure used to prepare the samples for **Figure 3.4b**, significant changes to the anhydrous theophylline structure were not anticipated, and accurate mathematical isolation of theophylline diffraction was, therefore, expected.

Different issues with isolation of scattering from theophylline:lactose compacts occurs owing to the crystallinity of the excipient. Specifically, isolation of theophylline diffraction from regions in the PXRD pattern where both components have peak overlap may result in multiple anomalies with the isolated pattern, including inaccurate peak intensity values, peak shape distortions, and/or the disappearance of theophylline peaks altogether. The green difference plot in **Figure 3.5b** shoes that PDF-transformed theophylline diffraction data mathematically isolated from the theophylline:lactose mixtures agrees well with the theoretical PDF of theophylline. Again, considering the low pressure used to prepare compacts for **Figure 3.5b**, significant structural changes to anhydrous theophylline were not anticipated.

3.4.3 PCA of PDF Transformed Data

The circumscribed central composite design of experiments used in the present work directly built sample variability into each model through replication of the center point (n=5), which corresponded to a compaction pressure of 268 MPa and an excipient concentration of 48% w/w. The variance in the PDF attributable to sample variation is therefore susceptible to explanation by PCA. In the dimension of the first PC, however, the replicate samples are observed to cluster together (dashed circles in **Figures 3.6, 3.7**), thereby precluding sample variability from acting as the sole contributor to the data segregation observed in each plot.

The data-segregation correlated to compaction pressure observed in **Figure 3.6** occurred regardless of the concentration of MCC present. As described above, long-range atomic correlation dampening ($r \geq 40$ Å) was concluded to be most likely attributable to structural differences arising from compaction. Ultimately, these data

strongly support that the variance explained by the first PC is correlated to the probability peak dampening observed in PDF data (**Figure 3.2**).

The same data segregation observed in the first analysis (**Figure 3.6**) was also observed in the second PCA model (**Figure 3.7**), which suggests that clustering corresponds with the same probability peak dampening explained above. Recall that the point representing the binary sample containing 75% w/w lactose compacted at 268 MPa clustered with the samples compacted at low pressures. Interpretation of this behavior suggests that the presence of this much lactose may provide some degree of "protection" against the theophylline structural changes interpretable from the PDF; however, this warrants further investigation.

Almost all samples containing lactose (**Figure 3.8**, red, unfilled symbols) had PDF patterns with score values (in the dimension of the first PC) that were most similar to all other samples compacted at low pressures. The score values for all lactose samples compacted at 268 MPa clustered around samples compacted at low pressures, as did a lactose-containing sample compacted at 419 MPa. The clustering of this particular sample with others compacted at low pressures may not seem intuitive given that the remaining two lactose samples (containing less % w/w lactose) compacted at a high pressure did not. When sample composition is taken into consideration, however, a trend in the dimension of the first PC is observable. At a compaction pressure of 419 MPa, as the amount of lactose is decreased (**Figure 3.8**, red triangles), the sample score values became increasingly similar to the rest of the samples compacted at high pressure. Overall, every sample containing lactose (with the exception of the two compacted at 419 MPa having low % w/w concentrations), resulted in PDF patterns similar to all samples

compacted at low pressures. These PDF data, therefore, did not exhibit the probability peak dampening displayed by PDF-transformed data of (a) pure theophylline samples compacted at high pressures, and (b) PDF-transformed data of mathematically isolated theophylline from samples containing MCC compacted at high pressures. Hence, the samples containing > 50% w/w lactose did not demonstrate any detectable structural modifications as a function of compaction pressure in the range investigated.

3.5 Conclusion

In this study, the effects of powder consolidation on solid structure were examined. Simulated data suggest that the compaction-related changes observed in real-space analyses (PDF) of theophylline are primarily attributable to molecular deviations from average crystalline order. The analysis of pharmaceutically relevant, intact consolidated systems was performed using PXRD, which afforded structure-sensitive capabilities without the introduction of artifacts arising from traditional sample preparation (e.g. subsequent grinding to revert to powder samples). The application of the PDF transform to an individual constituent, in the presence of an excipient, was successfully accomplished as a result of a novel, accurate mathematical pattern separation technique. Ultimately, this permitted practical real-space structural analysis of a single component in the presence of another material, thereby enabling the investigation of compound consolidation effects (*i.e.* the affect a material has on the compaction behavior of another). The use of PCA as an alternative to the weighted agreement factor for comparing multiple PDF patterns was successfully demonstrated. Relative to binary compacts formed with microcrystalline cellulose, structural changes to theophylline in the presence of α-lactose monohydrate were not observed (except in the two samples

compacted with the least amount of lactose). This suggests the inclusion of lactose provides protection to theophylline from structural changes that would otherwise occur at high pressures. Further exploration of this particular conclusion, however, deserves additional attention and will be the focus of future experiments.

Chapter 4: Structural Interpretation in Composite Systems Using Powder X-ray Diffraction: Applications of Error Propagation to the Pair Distribution Function

4.1 Introduction

Advanced analytical techniques used to characterize pharmaceutically-relevant materials properties are becoming increasingly sensitive to changes in short-range order of material structure. At the forefront of these advancements is a total scattering powder X-ray diffraction (PXRD) method adapted from the inorganic materials science literature, commonly referred to as the atomic pair distribution function (PDF). The PDF transform exploits the Fourier relationship between powder diffraction intensity and the real space arrangement of atomic species. It has been used extensively to study crystalline, nanocrystalline, and amorphous inorganic materials, and its application in the pharmaceutical literature has increased substantially in the last decade.

Recent applications of the PDF in the pharmaceutical literature include the investigation of dehydration mechanisms in excipients,[51] phase differentiation,[48,115] assessing structural changes during pharmaceutical manufacturing,[116,117] and characterization of solid dispersions.[52,118,119] An unfortunate occurrence in recent analyses incorporating PDF transforms involves drawing subjective conclusions with little to no statistical support. Additionally, errors made to pre-Fourier transformed intensities manifest as pattern anomalies oftentimes mistaken for structural phenomena, thereby further detracting from the merit of the study. Deriving an error estimate for a PDF pattern would largely increase the value of PDF-related conclusions.

Experimental errors in the PXRD experiment may arise from quantum counting inefficiencies, experimental imprecision, sample inhomogeneities, etc. and should be

propagated and accounted for when interpreting PDFs. In addition to uncertainties in the PXRD experiment, the lack of infinite momentum transfer resolution, as well as inaccurate data corrections applied to intensity data affect the degree of uncertainty in the resulting PDF. The inherent artifacts incurred as a result of Fourier transforming lower energy X-ray source data to real-space representation are well known and when treated appropriately[41] are less significant contributors to errors in the PDF. An appropriate estimate of error at the outset of the experiment and subsequent propagation through the entire mathematical transformation would significantly aid in drawing meaningful conclusions from PDF studies.

The use of error propagation methods in assessing the fit between a theoretical PDF calculated from a known crystal structure and experimental PDF has been developed and applied in the materials sciences literature.[120,121] As it is becoming routine to compare two experimentally derived PDFs (i.e. two individual components versus composite materials), a question arises as to appropriate treatment of each individual error source in combined comparisons. In this study, the propagation of initial PXRD error estimates through the PDF transform is presented. Monte Carlo simulations were performed to assess the validity of applying traditional error propagation algorithms to accurately estimate uncertainty in the resulting PDF. The propagated error estimates for individual experimentally-derived PDFs were mathematically combined to define uncertainty intervals around difference plots. Statistical hypothesis inferences were drawn from these intervals to aid in identifying differences between experimental PDF patterns attributable to structure as opposed to those resulting from random error. The aforementioned principles were applied to co-solidified products in an attempt to assess

drug:excipient miscibility, an area where differentiation between structural information and error in the PDF is of the utmost importance.

4.2 Materials and Methods

Ketoconazole was purchased from Spectrum Chemicals (New Brunswick, NJ), polyvinyl pyrrolidone:vinyl acetate (PVPva) was purchased from BASF (Ludwigshafen, Germany), terfenadine was purchased from Sigma-Aldrich (St. Louis, MO) and felodipine was purchased from Tecoland (Edison, NJ). Molecular structures for the compounds used in this study are shown in **Figure 4.1**.

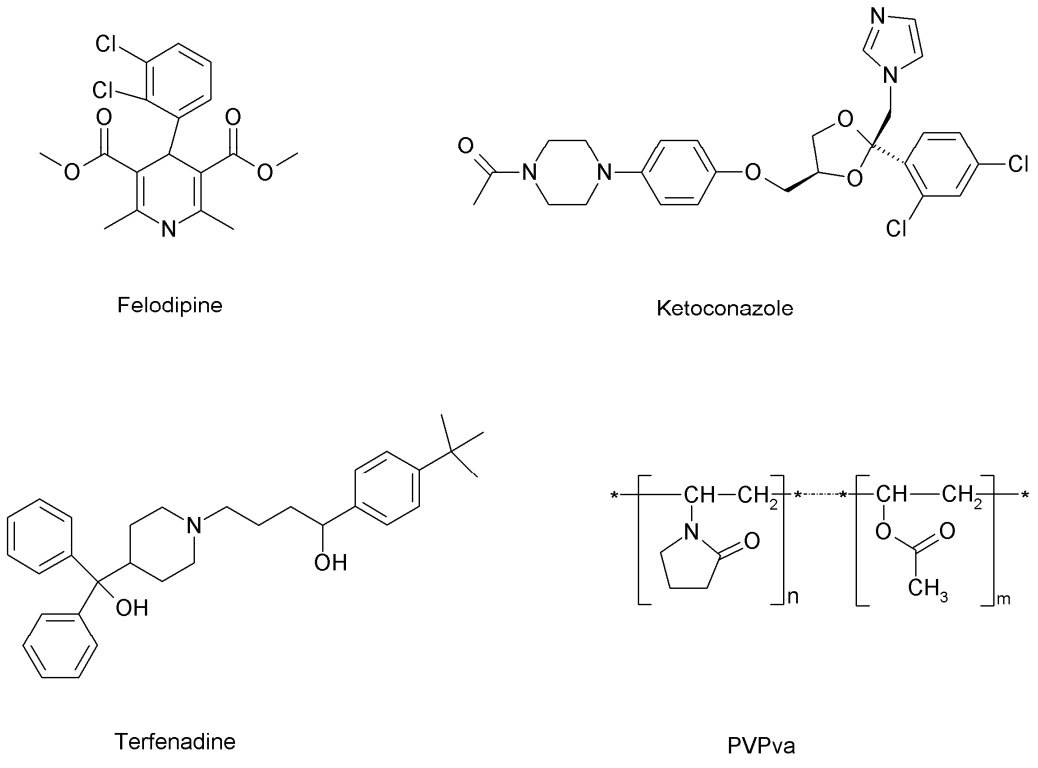

Figure 4.1. Molecular structures for felodipine, ketoconazole, terfenadine, and PVPva.

4.2.1 Solid Dispersion Preparation

Co-solidified products were prepared using the melt-quench method.[66] Briefly, the powdered components were physically mixed in a scintillation vial and added to a

crucible heated in a silicone oil bath at a temperature sufficient to melt the mixture. The molten mixture was held isothermally for 30 minutes. The molten mixture was quenched using an ice water bath. Individual amorphous phases were produced by holding the sample above the melting temperature for 10 minutes followed by quenching in an ice bath. All samples were removed from the bottom of the crucible intact for analysis.

4.2.2 Powder X-ray Diffraction (PXRD)

The PXRD data were collected in transmission geometry using an X'Pert Pro MPD system (PANalytical B.V., Almelo, the Netherlands) equipped with a copper anode (λ = 1.5406 Å), an auxiliary elliptical mirror, and X'Celerator^{TM} detector. The operational voltage and amperage were set to 45.0 kV and 40.0 mA, respectively. Diffraction patterns were acquired on intact samples, sandwiched between two layers of Kapton® film and subsequently placed on a spinning vertical sample stage (16 rpm). Experimental parameters include an irradiation time of 51.04 seconds per step and an angular step size of 0.02° 2θ over a 2-100° 2θ range.

4.2.3 Differential Scanning Calorimetry (DSC)

Glass transition temperatures (T_g) were measured using a Q100 DSC (TA Instruments, New Castle, DE) under constant nitrogen purge (~50mL/min). A three-point enthalpy and temperature calibration was performed at 20 °C/min using o-terphenyl, indium, and tin standards. In an attempt to avoid artifacts arising from grinding samples, approximately 5 mg intact "sample chips" were hermetically sealed in aluminum pans. To normalize thermal history, samples were first heated at 20 °C/min to 105 °C, held isothermally for 2 minutes, and subsequently cooled to -20 °C at 20 °C/min. Samples were then cycled through T_g at 20 °C/min for temperature determination. Ideal glass

transition temperatures for drug:polymer amorphous molecular solid dispersions were calculated using the Couchman-Karasz equation[85] and are listed in **Table 4.1**.

Table 4.1. Summary of DSC and PDF analyses.

	DSC Analysis		PDF Analysis			
	Ideal T_g (°C)	**T_g (°C)**	***R* value**	**Drug Conc. (w/w)**	**Polymer Conc. (w/w)**	**Conclusion**
felodipine:PVPva	62.1	66.9 (0.015)	0.2126	0.81	0.19	miscible
terfenadine:PVPva	77.48	60.7 (0.21)	0.0864	0.73	0.27	phase-separate

4.2.4 Pair Distribution Function (PDF)

The PDF is a total scattering method that exploits the Fourier relationship between X-ray diffraction intensity and the real-space arrangement of atoms, given appropriate data treatment.[38,111] This method has received extensive attention in the inorganic literature with an increasing number of pharmaceutical applications reported recently. The PDF, *G(r)*, is defined as:

$$G(r) = 4\pi r\left[\rho(r) - \rho_o\right] \tag{4.1}$$

where $\rho(r)$ and ρ_o are the local and average atomic number densities, respectively, and r is the inter-atomic separation distance. The PDF calculates the probability of finding atom pairs separated by a distance r, and is obtained by Fourier transform of the reciprocal space structure function, *S(Q)*, according to:

$$G(r) = \frac{2}{\pi}\int_0^{Q_{max}} Q\left[S(Q) - 1\right]\sin(Qr)\,dQ \tag{4.2}$$

where *S(Q)* is the structure factor obtained from a diffraction experiment and Q is the magnitude of the scattering vector. The term Q_{max} is the momentum transfer resolution of the diffraction experiment, which is dependent on the wavelength of radiation used and the maximum diffraction angle (°2θ) of data collection. Corrections consistent with those

outlined by Egami and Billinge[38] were made to the measured diffraction data leading to the calculation of the structure function. All intensity corrections (*e.g.* background due to Kapton® film scattering, absorption, *etc.*) and PDF calculations were performed using software developed in-house in the Matlab programming environment (v7.1, MathWorks, Natick, MA) based on published equations. The PDF transforms were optimized using the G_{low} quality criteria introduced by Peterson, *et al*.[41]

4.2.5 Error Propagation

The method of error propagation through the PDF transform has been derived and applied in previous work.[38,121] If it is assumed that the measurement of each individual observation is statistically independent of all others (*i.e.* the count intensity at a given diffraction angle is independent of all others), the covariance between observations is eliminated. It is worthwhile to note that the aforementioned assumption is appropriate in PXRD experiments provided the mathematical manipulations to the raw diffraction pattern do not introduce statistical correlation among individual data points (*i.e.* windowed smoothing, interpolation). When a quantity $\boldsymbol{T}$ is the sum of two independent observations, $\boldsymbol{X}_1$ and $\boldsymbol{X}_2$, each having their own error estimate, $\sigma(\boldsymbol{X}_1)$ and $\sigma(\boldsymbol{X}_2)$, the estimated error $\sigma(\boldsymbol{T})$ is:

$$\sigma(\boldsymbol{T}) = \sqrt{(\sigma(\boldsymbol{X}_1))^2 + (\sigma(\boldsymbol{X}_2))^2} \tag{4.3}$$

The quantity $\boldsymbol{T}$ calculated from the product of a constant value, $\boldsymbol{c}$, and $\boldsymbol{X}$ has an estimated error given by,

$$\sigma(\boldsymbol{T}) = \boldsymbol{c} \bullet \sigma(\boldsymbol{X}) \tag{4.4}$$

When a quantity $\boldsymbol{T}$ is the product of two independent observations, $\boldsymbol{X}_1$ and $\boldsymbol{X}_2$, each having their own error estimate, $\sigma(\boldsymbol{X}_1)$ and $\sigma(\boldsymbol{X}_2)$, the estimated error $\sigma(\boldsymbol{T})$ is:

$$\frac{\sigma(\boldsymbol{T})}{\boldsymbol{T}} = \frac{\sigma(\boldsymbol{X}_1)}{\boldsymbol{X}_1} + \frac{\sigma(\boldsymbol{X}_2)}{\boldsymbol{X}_2} \tag{4.5}$$

Error propagation was performed by setting up two data vectors. The first data vector contained the raw PXRD intensity values for a given powder pattern. The second vector contained the initial error estimates for each intensity value. The vectors were propagated side-by-side through to the calculation of the structure function using the principles outlined in **Equations 4.3**, **4.4**, and **4.5** for the mathematical manipulations to the error vector.

The final step of the PDF method involves the sine Fourier transform of the structure function, $S(Q)$, into real-space representation. Given accurate propagation of error up through calculation of the structure factor and no introduction of statistical correlation among the independent scattering events, a good estimate of the standard uncertainty in the PDF, $\sigma(G(r))$, is given by:

$$\sigma(\boldsymbol{G}(\boldsymbol{r}_j)) = \sqrt{\frac{4}{\pi^2} \sum_i (\boldsymbol{Q}_i \sin(\boldsymbol{Q}_i \boldsymbol{r}_j) \Delta \boldsymbol{Q}_i)^2 \sigma(\boldsymbol{S}(\boldsymbol{Q}_i))^2} \tag{4.6}$$

where $\sigma(S(Q))$ is the error estimate of the structure function.

4.2.6 Monte Carlo Simulation

The term Monte Carlo refers to a broad class of methods that employ generation of random numbers as a starting point for solving a complicated numerical problem. Monte Carlo methods are often used to simulate physical and mathematical systems. They are especially useful for modeling phenomena having significant uncertainty. The simulation typically begins with defining a distribution of possible inputs. An input generated from the distribution is used to perform deterministic computations to obtain an

individual result. Finally, the results from individual computations are compiled and interpreted.[122]

The raw PXRD counts go through a number of mathematical manipulations when transformed using the PDF algorithm; oftentimes optimized according to specific quality criteria.[41] In order to confirm the appropriate propagation of an initial raw count error estimate, Monte Carlo simulations were employed. The simulations began with a defined distribution of intensity values at each °2θ. The distribution at each specific scattering angle (°2θ) was formed by using the raw intensity (*i.e.* counts) as the distribution mean and the error estimate as the spread. Simulated PXRD patterns were formed by randomly selecting an intensity value from the previously defined distributions at each °2θ angle. Each simulated PXRD pattern was subsequently transformed into real-space representation using the PDF. After ten-thousand iterations, a matrix of PDF patterns spanning the variance of the simulated PXRD patterns was formed. The minimum and maximum *G(r)* at each *r*-value in the PDF was compared to the error vector calculated using the previously defined equations.

4.3 Results

The count of scattered intensity within a given time interval obtained from the PXRD experiment is subject to an unavoidable, random uncertainty due to statistical variation in quantum counting.[123] This stochastic variation best follows a Poisson probability density function a discrete distribution that possesses unique statistical properties. Assuming that *n* counts occur in a specific time interval, the distribution possesses a mean and variance equal to *n*, when *n* is a positive integer.[38] The standard

deviation for *n* counts at the scattering angle *x*° 2θ is, therefore, equal to the square-root of *n* and will serve as the initial error estimate.

Figure 4.2a shows the diffraction pattern for amorphous ketoconazole (black, solid line) and ±3 standard deviations (blue, solid line). The subsequent PDF transform of the PXRD pattern is shown in **Figure 4.2b** (zoomed, black, solid line). To confirm the appropriate propagation of error through the transform, Monte Carlo simulations were performed as previously described. The calculated error (blue, dashed lines) and simulated error (red, dashed lines) is shown as intervals in **Figure 4.2b** and as absolute error values in **Figure 4.2c**.

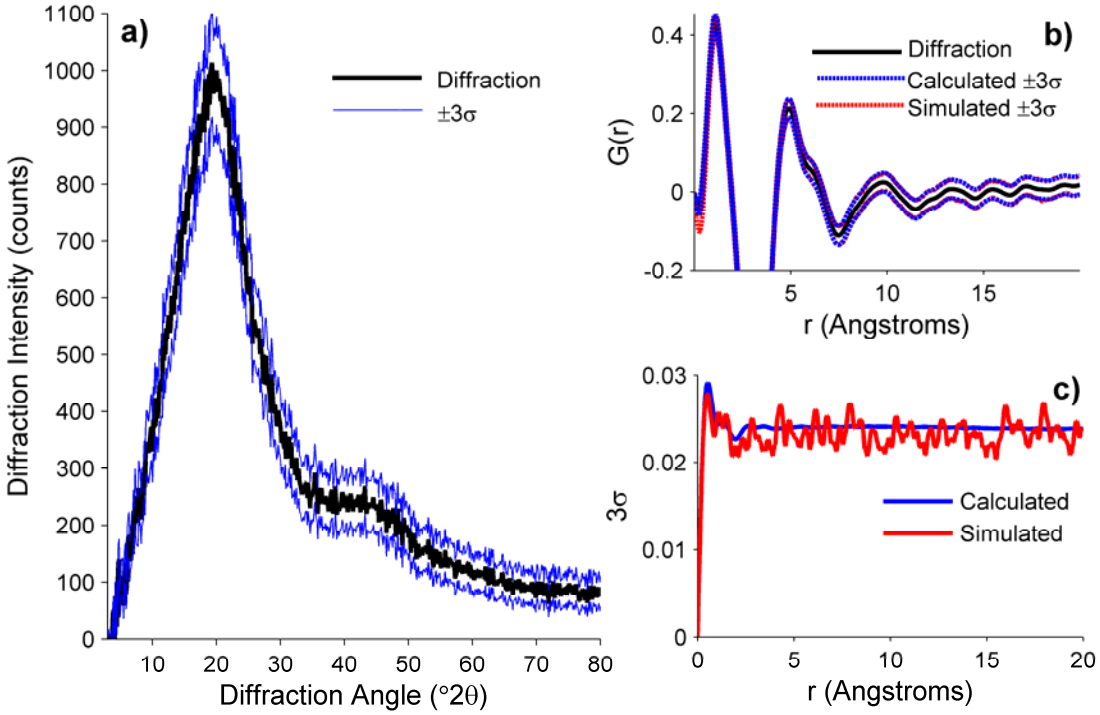

Figure 4.2. (a) The diffraction pattern for amorphous ketoconazole (black, thick line) and ±3σ (blue, thin line); (b) the PDF transform of (a) (black, thick line), calculated ±3σ (blue, dashed line), and simulated ±3σ (red, dashed line); (c) absolute representation of calculated 3σ (blue) and simulated 3σ (red).

It is common practice to compare an experimentally obtained PDF to one calculated from a structural model. Previous studies have illustrated the advantages of error propagation to this particular application. Recently, an increasing interest to compare multiple experimental PDFs has emerged. Difference plots with error intervals calculated from experimental PDFs may assist in delineating random errors from true, structural variations. **Figure 4.3a** shows the PDF transform of a 50 wt% physical mixture of amorphous felodipine and PVPva (black, solid line) with an overlay of a linear combination of PDFs from amorphous felodipine and PVPva (blue, line with circles). **Figure 4.3b** shows the difference plot (black, solid line) obtained from the two traces in **Figure 4.3a**. Additionally, the estimated combined error contribution ($\pm 3\sigma$) calculated from the propagation through each transform is also shown as an interval around the difference (red, dashed lines). That is to say, an interval calculated from the combination of the two amorphous component PDFs comprising the blue trace and the physical mixture PDF represented by the black trace.

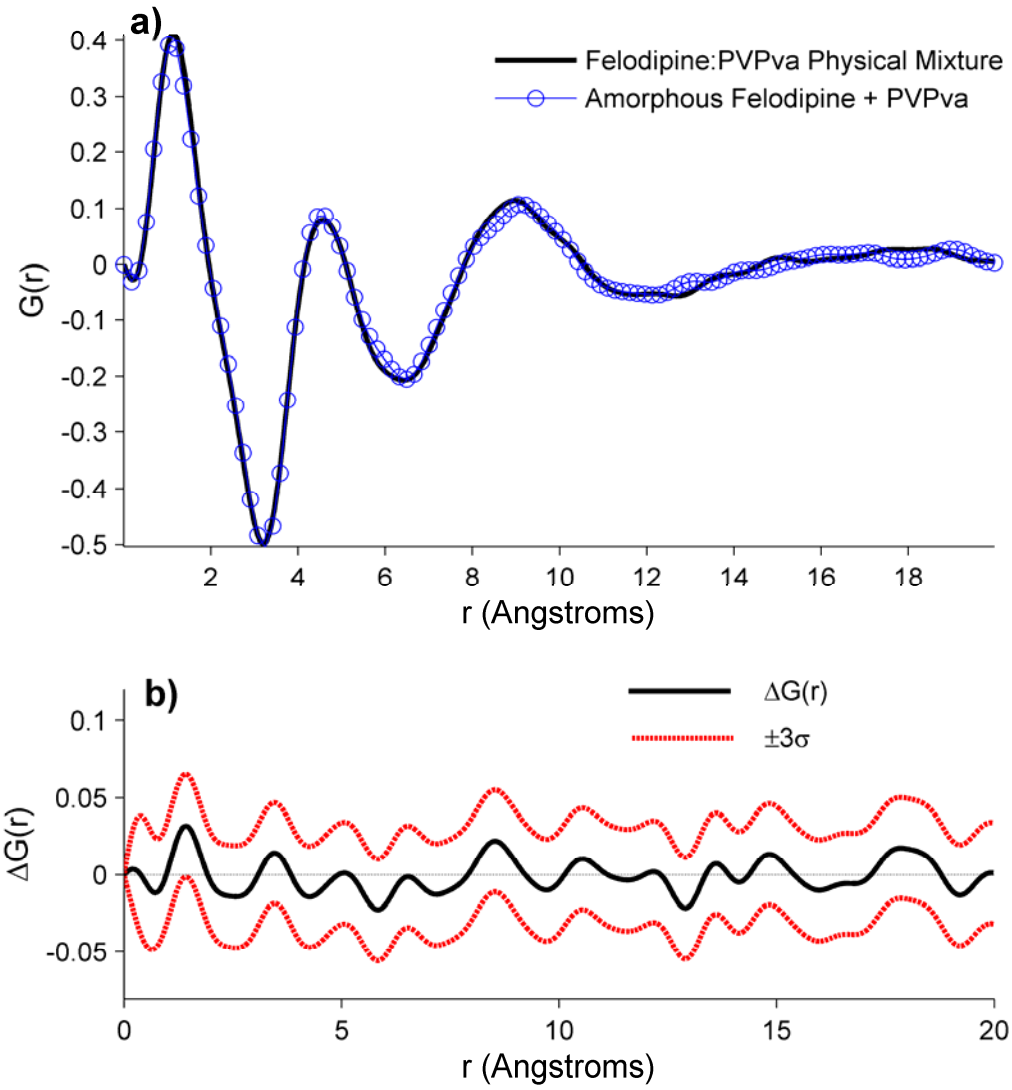

Figure 4.3. (a) The PDF of a 50 wt% physical mixture of amorphous felodipine and PVPva (black) and the refined linear combination of the amorphous component PDFs (blue, circles); (b) the difference between the PDFs (black) and ±3σ (red, dashed line).

To illustrate the potential to differentiate random error from true structural differences, the error propagation principles were applied to the method outlined by Newman *et al.*[52] that was proposed to identify miscibility between a drug and excipient. Briefly, the PDF of a co-solidified product is compared to the linear combination of the PDFs obtained from the amorphous components comprising the mixture. The scaling

constants serve as concentration estimates for each amorphous phase in the co-solidified mixture. If the linear combination of the PDF for each amorphous component describes the PDF of the co-solidified sample, it is reasonable to conclude that the system is at least partially phase-separated as the short-range order (*i.e.* the static local structure) of the co-solidified product can be described by the intrinsic distances found in the amorphous API and polymer. Substantial differences between the PDF calculated from linear combination of the individual amorphous component PDFs and the PDF of the co-solidified sample are indicative of short-range order not presented in the individual components, (*i.e.* that of a unique packing pattern). **Figure 4.4a** shows the PDF transform (black, solid line) for a 75 wt% felodipine and PVPva co-solidified product. The superimposed trace (blue, circles and line) is the best refined linear combination of the amorphous component PDFs. **Figure 4.4b** shows the difference between the two PDFs (black, solid line) with the calculated $\pm 3\sigma$ error estimates.

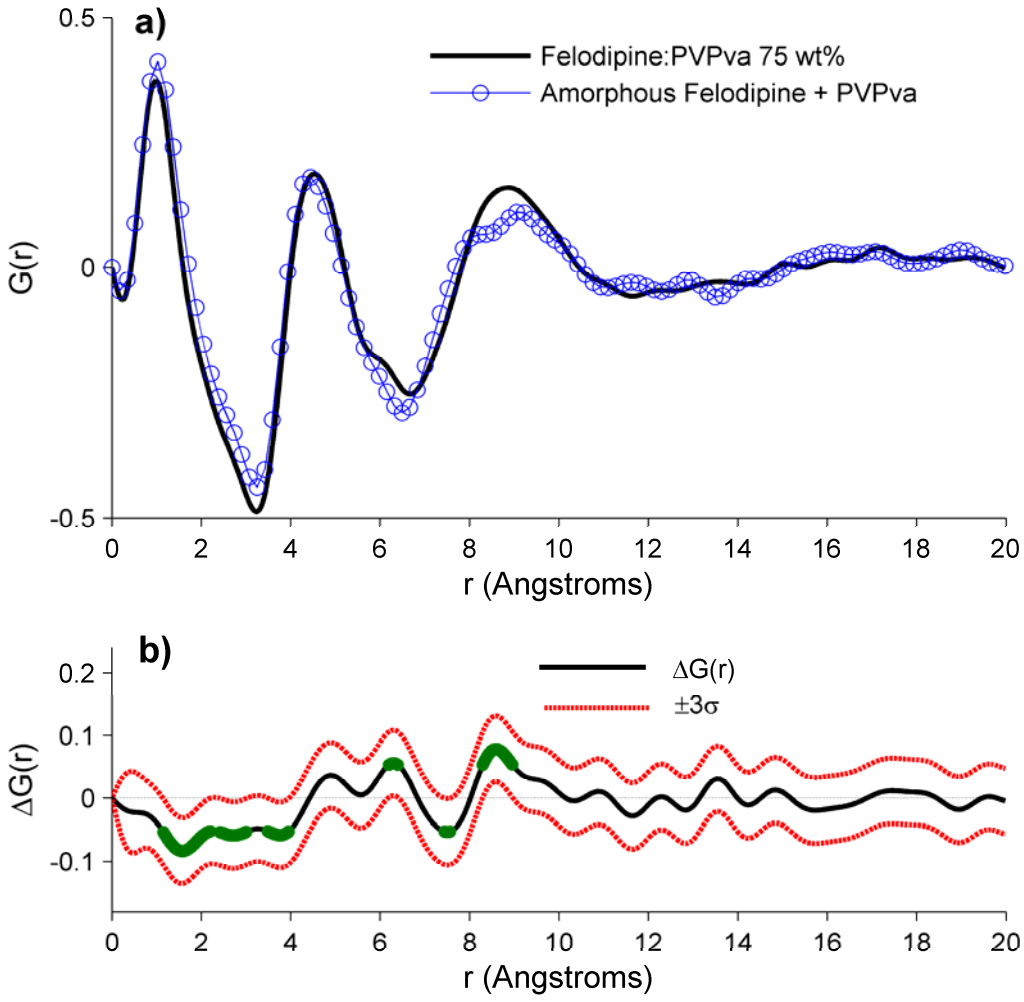

Figure 4.4. (a) The PDF of a 75 wt% co-solidified product of felodipine and PVPva (black) and the refined linear combination of the amorphous component PDFs (blue, circles); (b) the difference between the PDFs (black) and ±3σ (red, dashed line), where the green dots are indicative of the error interval not containing zero.

As a point of comparison, **Figure 4.5a** contains the PDF (black, solid line) for a 75 wt% terfenadine and PVPva co-solidified product. Superimposed is the best refined linear combination of the amorphous component PDFs. **Figure 4.5b** shows the difference between the two PDF traces (black, solid line) with the calculated ±3σ error estimates. The T_g for the co-solidified products in **Figure 4.4** and **Figure 4.5** are shown in **Figure 4.6** and **Figure 4.7**, respectively. In both products, a single T_g event is

observed (middle traces in **Figure 4.6** and **4.7**) intermediate to the T_g observed for the pure components (top and bottom traces in **Figure 4.6** and **4.7**). **Table 4.1** summarizes the DSC and PDF results.

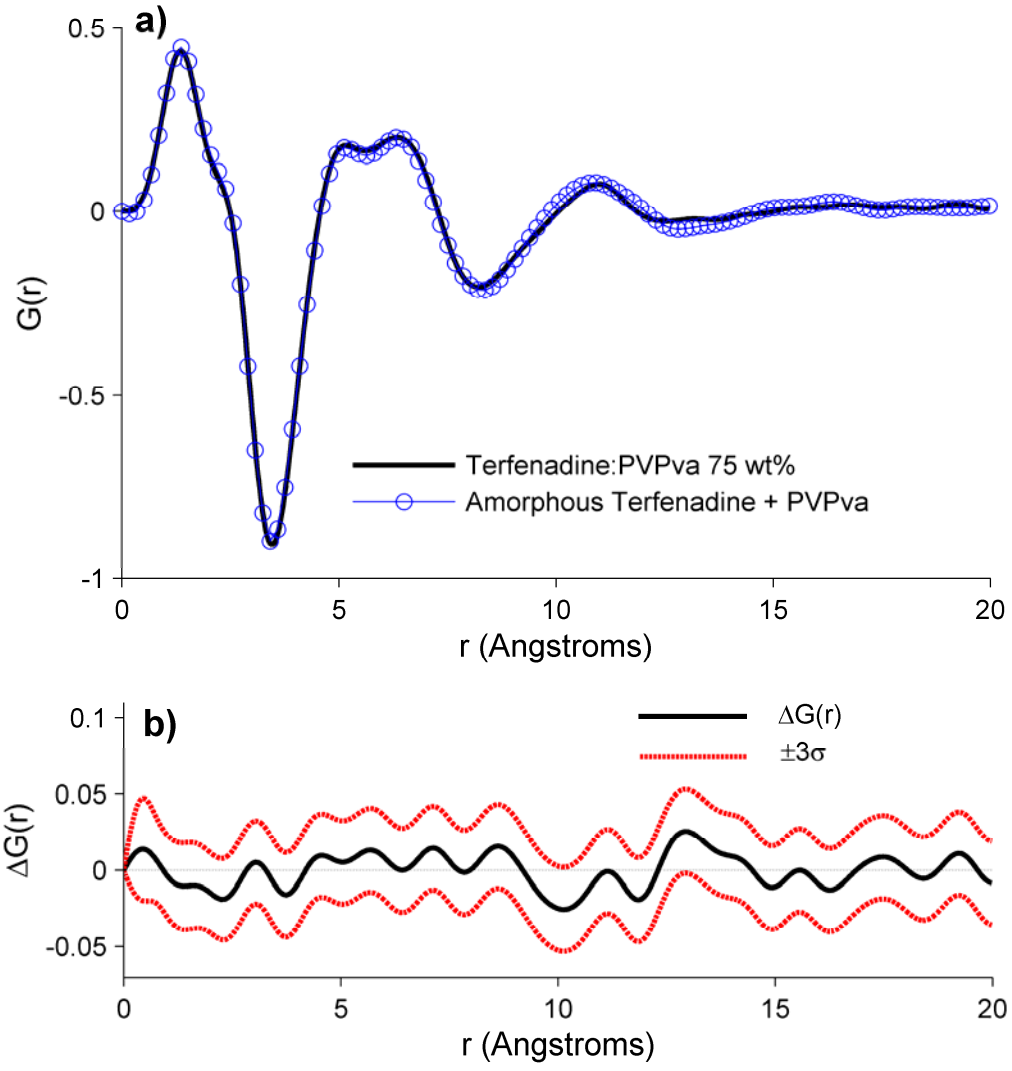

Figure 4.5. (a) The PDF of a 75 wt% co-solidified product of terfenadine and PVPva (black) and the refined linear combination of the amorphous component PDFs (blue, circles); (b) the difference between the PDFs (black) and ±3σ (red, dashed line).

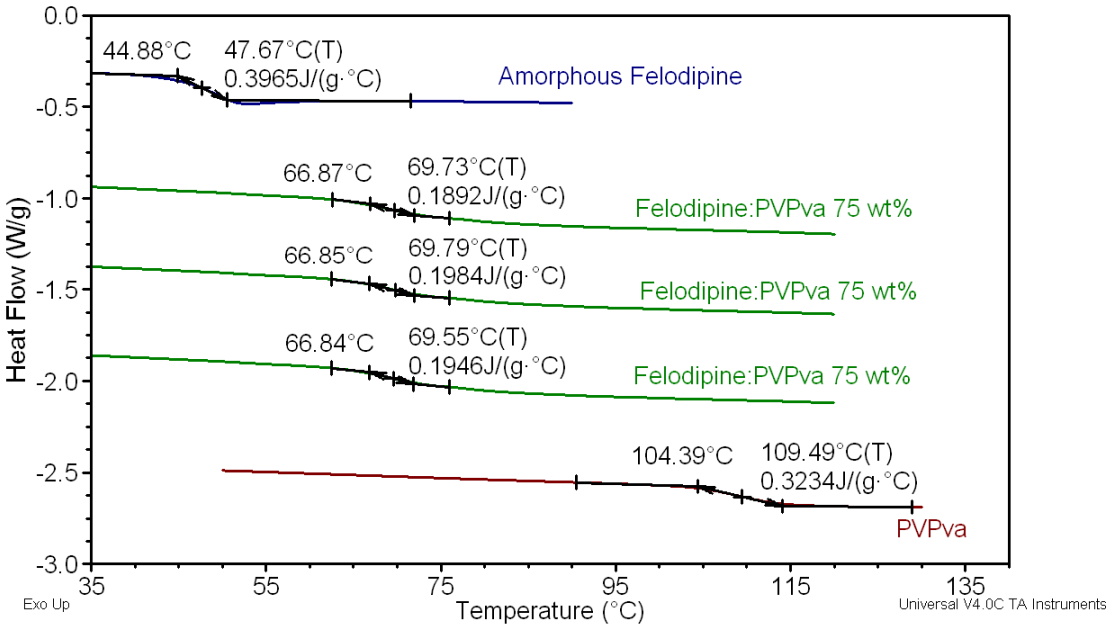

Figure 4.6. The DSC thermograms for felodipine:PVPva systems (as labeled).

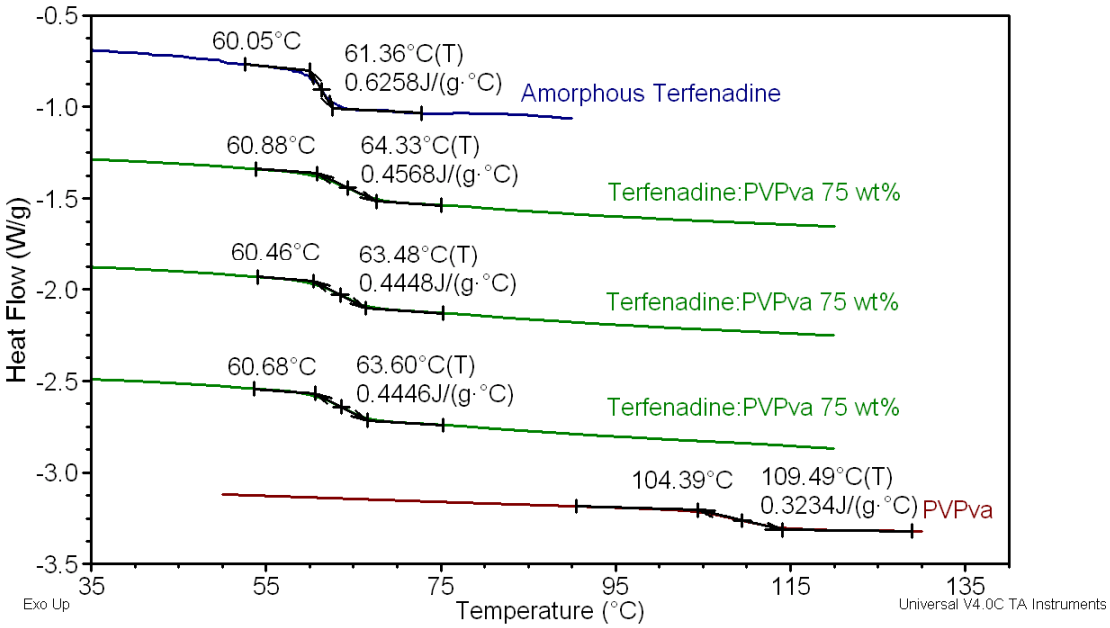

Figure 4.7. The DSC thermograms for terfenadine:PVPva systems (as labeled).

4.4 Discussion

The PXRD experiment is traditionally regarded as robust. Fluctuations in scattering intensity attributable to experimental geometry (Lorentz factor) and radiation polarization are assumed to be insignificant contributors to the overall variance due to their precision.[23,123] The uncertainty due to statistical variation in quantum counting, therefore, serves as an appropriate initial error estimate (**Figure 4.2a**). Although this estimate does not contain all possible sources of error, it does enable the ability to rule out changes that are too small to be taken seriously.

By randomly selecting scattering intensities spanning the defined error interval for each scattering angle (°2θ) over ten-thousand iterations, the Monte Carlo simulation creates a matrix of diffraction patterns that possess the overall variance contained within

the initial uncertainty estimate. The simulated patterns were individually transformed using the PDF algorithm. Since the simulated PXRD patterns span the total variance of the estimated uncertainty in reciprocal space, the resulting PDF patterns span that same variance in real-space. The propagated PDF uncertainty interval (**Figure 4.2b**, blue, dashed lines) is in good agreement with the simulated PDF uncertainty interval (**Figure 4.2b**, red, dashed lines). For a point of reference, the absolute PDF errors derived from propagation and simulation are given in **Figure 4.2c**. The agreement between simulated and propagated errors confirms the appropriate propagation of the initial error estimate through the PDF transform.

Comparisons and modeling between multiple experimentally obtained PDFs is becoming increasingly common. Similar to comparing an experimental PDF to a calculated PDF from a structural model, the premise in these analyses is to identify correlations between PDFs while maintaining the ability to differentiate pattern dissimilarities attributable to structural differences from those attributable to random error. To do this, it is proposed that error intervals are estimated for the difference plot calculated between experimental PDFs of interest. In **Figure 4.3a**, the PDF transform of a PXRD pattern obtained from a 50 wt% physical mixture of amorphous felodipine and PVPva is represented by the black, solid line. The blue line with circles in **Figure 4.3a** represents the refined linear combination of amorphous component PDFs. The difference between the calculated and physical mixture PDF is given in **Figure 4.3b** (black, solid line). The uncertainty interval around the difference plot was obtained from the combined propagated error of the two PDF patterns. The PDF transform of a PXRD pattern of an amorphous felodipine:PVPva physical mixture would be expected to be the

same as a linear combination of a PDF transform of a PXRD pattern of pure amorphous felodipine and a PDF transformed of a PXRD pattern of pure PVPva. This expectation is founded on the principle that a physical mixture of two amorphous materials would not alter the short-range order intrinsic to the two materials comprising the blend.

A null hypothesis may be formed stating that the difference between the two PDFs is equal to zero (h_o: $\mu_a - \mu_b = 0$). The alternative to the null hypothesis states the difference between the two PDFs is not equal to zero (h_A: $\mu_a - \mu_b \neq 0$). If, at any value of *r*, the ±3σ interval around the difference plot contains zero, then the null hypothesis is accepted. If, however, the ±3σ interval at a value *r* does not contain zero, then the difference between the two PDFs can not be explained simply by random error and the null hypothesis is rejected. The ±3σ interval shown in **Figure 4.3b** contains zero for every value of *r*, and therefore, reflects that all differences between the two PDFs is attributable to random error. Defining a threshold below ±3σ would lead to conclusions of structural differences between the two PDFs, as the entire range of *r* would not contain zero. As a result of this finding, ±3σ difference plot intervals that do not include zero are assumed to be indicative of statistically significant structural dissimilarities between experimental PDFs for the remainder of this manuscript.

It is worthwhile to point out that the aforementioned conclusion concerning the ±3σ threshold is not universal; rather, it is dependent on the PXRD experimental parameters. Longer irradiation times or different experimental geometries may result in better counting statistics, hypothetically producing relative initial error estimates orders of magnitude less than the ones illustrated herein. The principles surrounding error propagation and the conclusions drawn from statistical hypotheses testing outlined

previously, however, are valid and warrant application when drawing inferences from differences between multiple analytical results.

The DSC data for 75 wt% felodipine and PVPva co-solidified product, as well as 75 wt% terfenadine and PVPva co-solidified product are shown in **Figure 4.6** and **4.7**, respectively. From **Table 4.1**, the calculated ideal T_g for a 75 wt% felodipine:PVPva amorphous molecular solid dispersion is 62 °C. The experimentally determined T_g for the co-solidified product, cycled through the event three times, was 67 ± 0.02 °C and in good agreement with the ideal value. The ideal T_g for a 75 wt% terfenadine:PVPva (**Table 4.1**) is 77 °C. The experimentally determined T_g for the co-solidified product was 60 ± 0.2 °C. In both instances, a single T_g intermediate to the individual amorphous phase T_g that remains constant upon cycling was observed for the co-solidified products (**Figures 4.5** and **4.6**). From purely thermal analyses, both co-solidified products may be classified as amorphous molecular solid dispersions due to the presence of only a single T_g intermediate to the pure amorphous phase T_g events.

In **Figure 4.4a**, the PDF of the PXRD pattern for the felodipine:PVPva co-solidified product (black, solid line) is shown with the refined linear combination of the amorphous component PDFs. The scaling constant-derived concentrations of 81 % and 19 % drug and polymer, respectively (**Table 4.1**) deviate substantially from the theoretical values of 75 % drug and 25 % polymer. The sum-of-squares agreement factor (R) shows an error estimate of 21 % between the calculated PDF and the co-solidified product PDF. From the difference plot in **Figure 4.4b**, variations between the two patterns are observed within the range of 6 – 9Å that are not explained by random error as indicated by portions of the error interval not encompassing zero (green dots). As

previously suggested, this result would be indicative of a true amorphous molecular solid dispersion, as the product would have short-range order (*i.e.* nearest neighbor and next nearest neighbor interatomic distances) not explained by either pure component PDF.

The PDF for the terfenadine:PVPva co-solidified product (black, solid line) is shown with the calculated PDF in **Figure 4.5a**. The scaling constant-derived concentrations of 73 % and 27 % drug and polymer, respectively (**Table 4.1**) are close to the theoretical values of 75 % drug and 25 % polymer. The sum-of-squares agreement factor (R) shows an error estimate of only 8 % between the calculated PDF and the co-solidified product PDF (**Table 4.1**). Upon inspection of the difference plot uncertainty interval in **Figure 4.5b**, it was found that zero is contained within the $\pm 3\sigma$ interval over the entire range of r. The short-range order displayed in the PDF of the co-solidified product is well explained by that found in the individual amorphous components and thereby negates formation of a unique packing pattern. The terfenadine:PVPva dispersion product, therefore, is phase-separated.

A plausible explanation as to why a second T_g was not observed for the terfenadine co-solidified product was extrapolated from Newman, *et al*.[52] Close inspection of **Figure 4.7** shows the T_g of the dispersion product to be nearly equal to the T_g of amorphous terfenadine. Since terfenadine represents the major phase of the dispersion (75%), PVPva only constitutes 1.25 mg of a 5 mg sample. As the concentration of the PVPva amorphous domain decreases with respect to that of the amorphous terfenadine, the heat capacity change at the PVPva glass transition becomes so subtle relative to that of amorphous drug that it is not detectable using standard DSC.

4.5 Conclusion

The successful propagation of an initial error estimate through the PDF transform enabled statistically-based conclusions to be drawn from multiple pattern comparisons. It was found that difference plots calculated from linear combinations of amorphous phase PDFs and co-solidified product PDFs could be used to differentiate between phase-separated systems and amorphous molecular solid dispersions. The calculation of error intervals on the difference plot assisted this classification scheme by providing statistical thresholds to define structural dissimilarities as opposed to subjective interpretation. Though this study does not define a universal threshold for differentiation of random errors and structural dissimilarities, the principles developed herein may be adapted and applied accordingly.

Chapter 5: Informatics Calibration of a Molecular Descriptors Database to Predict Solid Dispersion Potential of Small Molecule Organic Solids

5.1 Introduction

The aqueous solubility of a small molecule organic (SMO) solid is one of the principle physicochemical properties considered when evaluating the developability of a new chemical entity (NCE) for pharmaceutical use. Although a number chemical- and physical-based approaches are available for enhancing the apparent aqueous solubility of active pharmaceutical ingredients (API), it is still estimated that more than 40% of highly potent compounds fail to reach clinical trials due to the inability to overcome poor aqueous solubility.[15] It is proposed that this statistic is somewhat inflated, not necessarily due to the inefficacy of available methods, but rather the raw material requirements associated with empirically assessing the potential of each. Formulation scientists are ultimately forced to investigate only a fraction of the existing technology, where unsuccessful outcomes may deem a therapeutically efficacious API undevelopable. The development of predictive models to optimize these methods in an attempt to preserve early stage raw material supplies is thus imperative.

Stabilization of an API as an amorphous solid phase through the formation of binary amorphous molecular solid dispersions has received increasing attention yielding up to a four-fold enhancement of apparent aqueous solubility relative to the crystalline form.[58] Binary amorphous molecular solid dispersions are created through the rapid co-solidfication of an API and a pharmaceutically acceptable excipient, such as a polymer, at loadings sufficient to achieve a physically stable amorphous API. Due to the kinetic nature of the formation, spray drying,[69] super-critical fluid processing,[76] lyophilization,[63]

and hot-melt extrusion[72] have all been successfully implemented in the preparation of amorphous molecular solid dispersions. Successful formation has been attributed to the presence of specific and/or nonspecific adhesive interactions,[62,83] as well as antiplasticization effects intended to reduce molecular mobility.[81]

Predictive models for API:polymer miscibility have been introduced and are largely derived from solution thermodynamics. Lattice based solution models, such as Flory-Huggins theory, can be used to assess miscibility in API:polymer blends. In addition to developing methods for estimating the Flory-Huggins interaction parameter, Marsac *et al*.[89] developed a model that predicted the solubility of an API in a polymer based on a combination of interaction variables and Flory-Huggins theory. Janseens *et al*.[73] applied the similar theory to model solid dispersion preparation method effects on the solubility of API in polymer. Friesen *et al*.[68] showed physical properties of APIs, such as hydrophobicity (*i.e.* log P), thermodynamic parameters (*e.g.* melting temperature) and kinetic parameters (*e.g.* glass transition temperature) to provide insight concerning formulation strategies for solid dispersion systems. In addition to ionic interactions, when applicable, Yoo *et al*.[124] also observed a correlation between hydrophobicity values of APIs and miscibility with a given polymer. Despite the recent advances, explicit universal criteria for API:polymer miscibility are still lacking.

Quantitative structure property relationships (QSPR) were derived from the fundamental concept that a compound's behavior is a result of its chemical structure. In QSPR models, molecular descriptors, single integer indices that encode specific structural information for a given compound, are typically regressed against some physical, chemical, or mechanical property. Applications of molecular descriptors in QSPR

modeling include predicting pharmacokinetic performance,[125] describing physical properties of alkanes,[126] and prediction of soil sorption coefficients of pesticides.[127] Coupled with characterization techniques to classify the co-solidified composites containing a given API, molecular descriptors have the potential to provide insight to API:polymer miscibility using a materials informatics approach.

In this study, 12 model compounds were prepared by a melt-quench procedure using polyvinylpyrrolidone:vinyl acetate (PVPva) copolymer as a stabilizing agent with useful thermoplastic properties and the potential (*i.e.* miscibility) for generating an amorphous molecular solid dispersion. Each co-solidified sample was characterized by thermal analysis, powder X-ray diffraction (PXRD). and a pair distribution function (PDF) method recently introduced into the literature.[52] Rather than attempting to quantify the extent of miscibility between API and polymer to afford a continuous dependent variable, each sample was classified as a successful formation (*i.e.* completely miscible) or an unsuccessful formation (*i.e.* partially miscible or immiscible) based upon conclusions drawn from the analyses. Molecular descriptors were calculated for each of the 12 model compounds comprising the library and tested for correlation to dispersion potential using logistic regression. A univariate model was created that predicted solid dispersion potential from a single molecular descriptor and challenged using three compounds not included in the calibration.

At the outset, it should be noted that the model developed herein is not proposed to be universally applicable across all SMO compounds nor is it predictive of the time course of physical instability (*i.e.* devitrification). Rather, a significant portion of the discussion will attempt to highlight the limitations associated with the model and define

the pertinent variance space for its applicability. The central objective of this work was to illustrate the potential of *in silico* calculations to create models that may one day provide the means for intelligent selection of stabilizing agents in the design of amorphous molecular solid dispersions. This possibility is ultimately afforded by the ability to classify co-solidified samples to compliment the interpretation that is possible from solid-state characterization methods alone.

5.2 Materials and Methods

Cloperastine, terfenadine, propranolol, chlorpropamide, nifedipine, melatonin, and quinidine were all purchased from Sigma-Aldrich (St. Louis, MO). Ketoconazole and itraconazole were purchased from Spectrum (Gardena, CA). Indomethacin, cimetidine, and tolbutamide were purchased from MP Biomedicals (Solon, OH). Felodipine was purchased from Tecoland Corporation (Edison, NJ), sulfanilamide was purchased from Acros Organics (Geel, Belgium), bicalutamide was purchased from Altan (Orange, CT), and Kollidon VA64 (PVPva) was a gift from BASF (Ludwigshafen, Germany). All model and test compounds are shown in **Table 5.1**.

Table 5.1. Molecular structures and Cambridge Structural Database Codes for compounds used in this study.

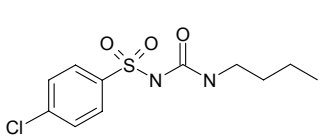

Chlorpropamide
BEDMIG02
Model

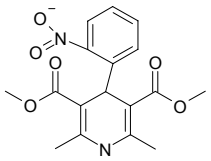

Nifedipine
BICCIZ
Model

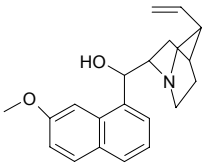

Quinidine
BOMDUC
Model

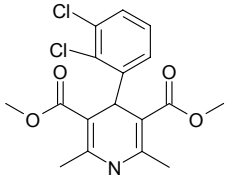

Felodipine
DONTIJ
Model

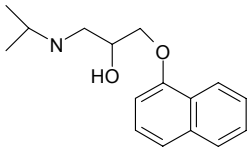

Propranolol
FIDGAB
Model

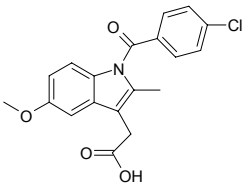

Indomethacin
INDMET03
Model

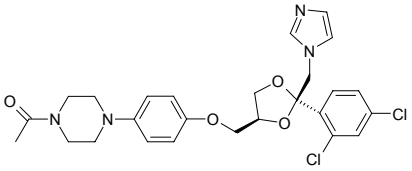

Ketoconazole
KCONAZ
Model

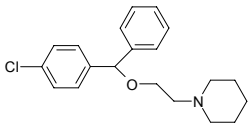

Cloperastine
QAWNAD
Model

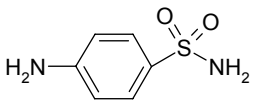

Sulfanilamide
SULAMD06
Model

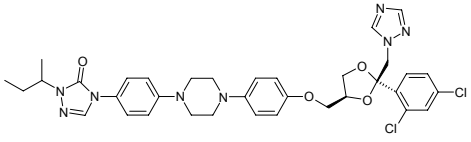

Itraconazole
TEHZIP
Model

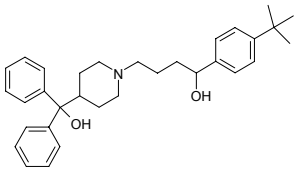

Terfenadine
XUHTID
Model

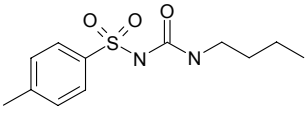

Tolbutamide
ZZZPUS02
Model

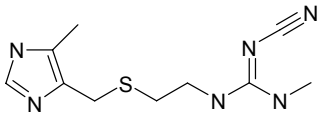

Cimetidine
CIMETD
Test

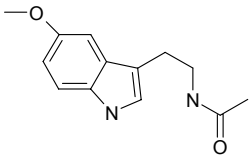

Melatonin
MELATN01
Test

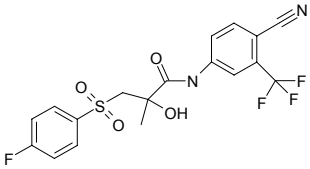

Bicalutamide
JAYCES
Test

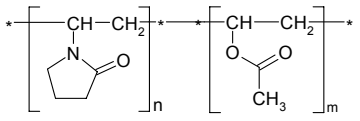

PVPva

5.2.1 Solid Dispersion and Amorphous Phase Preparation

Solid dispersion samples were manufactured using a melt-quench method.[66] Briefly, each API and PVPva was weighed and dispensed into a scintillation vial at 75 wt% API loading. The powders were physically mixed for a period of 5 minutes by manual agitation. To avoid sub-sampling, the entire mixed sample was added to a crucible heated in a silicone oil bath. The oil bath was maintained at a temperature equal to the fusion temperature of the API ($T_{f,API}$) + 10°C. In the instance where $T_{f,API}$ was less than 150 °C (*e.g.* the temperature at which PVPva liquefies), the mixture was held isothermally at 160 °C. The isothermal hold time was between 10-20 minutes to provide sufficient time for mixing. The hold time was determined using thermogravimetric analysis and was defined as the time (at a given preparation temperature) where ≥2% weight loss occurred. The molten mixture was subsequently quenched in an ice water bath. Amorphous samples of each component were produced by holding the crystalline API above its melting temperature for approximately 10 minutes followed by quenching in an ice bath. The melt-quench samples were removed from the crucible intact and examined. All preparations were repeated twice (n=3).

5.2.2 Differential Scanning Calorimetry (DSC)

Glass transition temperatures (T_g) for amorphous preparations of each model compound, PVPva, and the co-solidified samples were measured using a Model Q100 DSC (TA Instruments, New Castle, DE) under constant nitrogen purge (~50 mL/min). A three-point enthalpy and temperature calibration was performed at 20 °C/min using o-terphenyl, indium, and tin standards. In an attempt to reduce artifacts arising from sample preparation procedures (*i.e.* grinding), approximately 5 mg intact "sample chips"

were hermetically sealed in aluminum pans. To normalize thermal history, samples were first heated at 20 °C/min to 105 °C, held isothermally for 2 minutes, and subsequently cooled to -20 °C at 20 °C/min. Samples were then cycled from -20 °C to 120 °C at 20 °C/min for T_g determination.

The expected T_g assuming an intimate mixture was calculated using the Couchman Karasz[85] equation given by:

$$T_g = \frac{w_{API} T_{g_{API}} + K w_p T_{g_p}}{w_{API} + K w_p} \tag{5.1}$$

where w_{API} and w_p and the weight fractions of API and polymer, respectively, T_{gAPI} and T_{gp} are the glass transition temperatures of amorphous API and polymer, respectively, and $K = \Delta C_{pAPI}/\Delta C_{pp}$, where ΔC_{pAPI} and ΔC_{pp} are the heat capacity step change through the glass transition region of the API and polymer, respectively. Experimental T_g values were determined from the measured DSC heat flow signal as the onset of the step change in heat capacity.

5.2.3 Powder X-ray Diffraction (PXRD)

The PXRD data were collected in transmission geometry using an X'Pert Pro MPD system (PANalytical B.V., Almelo, the Netherlands) equipped with a copper anode (λ = 1.5406 Å), an auxiliary elliptical mirror, and X'Celerator™ detector. The operational voltage and amperage were set to 45.0 kV and 40.0 mA, respectively. Diffraction patterns were acquired on intact samples, sandwiched between two layers of Kapton® film and subsequently placed on a spinning vertical sample stage (16 rpm). Experimental parameters include an irradiation time of 51.04 seconds per step and an angular step size of 0.017° 2θ over a 2-100° 2θ range.

5.2.4 Pair Distribution Function

The PDF is a total scattering method that exploits the Fourier relationship between X-ray diffraction intensity and the real-space arrangement of atoms, given appropriate data treatment.[38,111] The PDF gives the probability of finding atom pairs separated by a distance *r*, and is obtained by Fourier transform of the reciprocal space structure function, *S(Q)*, according to:

$$G(r) = \frac{2}{\pi} \int_0^{Q_{max}} Q\left[S(Q) - 1\right]\sin(Qr)\,dQ \tag{5.2}$$

where *S(Q)* is the structure function obtained from a diffraction experiment and *Q* is the magnitude of the scattering vector. The term Q_{max} is the momentum transfer resolution of the diffraction experiment, which is dependent on the wavelength of radiation used and the maximum diffraction angle (°2θ) of data collection. Corrections consistent with those outlined by Egami and Billinge[38] were made to the measured diffraction data leading to the calculation of the structure function. All intensity corrections (*e.g.* background due to Kapton® film scattering, absorption, *etc.*) and PDF calculations were performed using software developed in-house in the Matlab programming environment (v7.1, MathWorks, Natick, MA) based on published equations.[38,111] The PDF transforms were optimized using the G_{low} quality criteria introduced by Peterson, *et al*.[41]

The PDF has been shown to be useful in characterizing co-solidified composite samples in differentiating phase-separated from completely miscible systems.[52,118] Briefly, the PDF transform for a co-solidified sample is compared to the linear combination of the PDF transforms obtained for each amorphous component comprising it. Scaling coefficients are multiplied by the amorphous component PDFs and serve as estimates of each component concentration in the co-solidified product. If the linear

combination of the PDF for each amorphous component describes the PDF of the co-solidified sample, it is reasonable to conclude the system is at least partially phase-separated, as short-range order (*i.e.* the static local structure) of the co-solidified product can be described by the intrinsic distances found in the amorphous API and polymer. Large deviations between the calculated PDF determined by linear combination of the PDFs for the individual amorphous components and the PDF of the co-solidified sample are indicative of short-range order not presented in the individual components, (*i.e.* that of a unique packing pattern). A statistically-founded protocol based on principles of error propagation has recently been introduced to aid in drawing conclusions from the aforementioned method (**Chapter 4**). A sum-of-squares difference, *R*, between the calculated PDF and PDF of co-solidified sample was also determined for comparative purposes.[123]

5.2.5 Molecular Descriptors

The term molecular descriptor refers to a broad class of indices calculated under the principal objective of representing a 3-dimensional molecule as a simple number(s). Their successful use in QSPR studies, relating the structure of a compound to how it behaves, provides impetus to modeling amorphous molecular solid dispersion potential. By employing graph theory,[128] a branch in discrete mathematics dealing with the way objects are connected and the consequences of connectivity, single integer indices may be calculated that encode structural information for a given molecule. Molecular graphs are a 2-dimensional depiction of molecules, where atoms are represented by vertices and bonds by edges. Two molecular graphs are isomorphic if there is a one-to-one correspondence between their vertex sets and edge sets. For a given molecular graph, *U*,

a graph invariant is a quantity that has the same value for any graph that is isomorphic with U.[128]

From the molecular graph, important theoretical matrices may be calculated. The vertex-adjacency matrix is a square symmetric matrix having off-diagonal values of one for adjacent vertices and zero for non-adjacent vertices. Similarly, the edge-adjacency matrix is a square symmetric matrix having off-diagonal values of one for adjacent edges and zero for non-adjacent edges. The distance matrix is a square symmetric matrix having off-diagonal values describing the shortest topological distance between two vertices. Single integers may be obtained from the mathematical manipulation of these matrices, thereby generating a class of molecular descriptors called topological indices. These indices are graph invariants and do not possess atom identities, thereby lacking heteroatom differentiation and stereochemical features of the molecule.[126]

To combat this issue, indices are calculated from weighted graph invariants, where atomic mass, atomic number, van der Waals volumes, and atomic polarization constants have all been implemented. These descriptors are much more powerful and have seen an increasing exposure to structure-property relationships studies. In this study, molecular descriptors were calculated using the EDRAGON online program.[129-131] Three-dimensional coordinates and atom connectivity was obtained from the Cambridge Structural Database (CSD),[132,133] where the CSD code for each model and test compound are listed in **Table 5.1**.

5.2.6 Logistic Regression

The intent of this study was to introduce a novel method for modeling the potential of a compound to successfully form an amorphous molecular solid dispersion

with PVPva using a common method of preparation. Attempting to define and quantify the extent of miscibility between API compounds and PVPva would likely confound the results of the analysis, as errors in this determination would propagate into the regression modeling. Therefore, the response in this analysis is a discrete, dichotomous variable taking a value of 1 for successful formation of an amorphous molecular solid dispersion (*i.e.* completely miscible) or a value of 0 for unsuccessful formation (*i.e.* partially miscible or immiscible) based upon conclusions drawn from the analyses. The inclusion of a dichotomous dependent variable unfortunately violates many of the assumptions of general linear regression.[134] Logistic regression was, therefore, used for modeling purposes in this study.

Logistic regression was performed using maximum likelihood (ML) estimation to calculate the regression coefficient for each molecular descriptor. Initial regression coefficients are estimated and the ML is calculated. The regression coefficient is iteratively adjusted until the maximum value of the ML (**Equation 5.3**) is achieved. To avoid multiplication of probabilities, the natural logarithm of the ML function is used and given by:

$$\ln(ML) = \sum [Y_i * \ln P_i] + [(1 - Y_i) * \ln(1 - P_i)] \tag{5.3}$$

where Y_i is the observed value (*i.e.* 0 or 1) and P_i is the estimated probability as obtained by:

$$P_i = \frac{e^{b_0 + b_1 X_i}}{1 + e^{b_0 + b_1 X_i}} \tag{5.4}$$

where $b_0 + b_1 X_i$ is the general linear model.[134-136] The effect of individual variables on model significance was tested by comparing the change in deviance (D), which is

Equation 5.3 multiplied by -2. The likelihood ratio (LR) test statistic, corresponds to the arithmetic difference between the deviance values for two models (*e.g.*, with and without a particular variable included), and follows a χ^2 distribution. The significance of the calculated regression coefficient for each molecular descriptor was evaluated by comparing the reduction of deviance value of the full model against using only the model intercept.

The error of cross-validation was assessed using the leave-one-out (LOO) method. Briefly, one of the compounds comprising the calibration library was removed from the data set. The remaining compounds were used to construct a calibration and a subsequent prediction on the compound removed from the library was performed. This was iteratively repeated for all compounds, where the sum of the total error was reported.

5.3 Results

5.3.1 Co-solidified product characterization

Amorphous molecular solid dispersions are formed as a result of the miscibility between the components comprising the sample. To enable model estimation, DSC and PDF analyses were used to characterize and classify the co-solidified samples according to the extent of miscibility. To achieve this, both DSC and PDF analyses were employed. To support the implementation of multiple characterization methods, three examples will be examined. The first example will illustrate a co-solidified sample categorized as an amorphous molecular solid dispersion, the second will detail identification of a phase-separated system according to both DSC and PDF results, and the final will showcase a phase-separated system identified by PDF results. A compilation of calculated parameters associated with each example are given in **Table 5.2**.

Table 5.2. DSC and PDF analyses results.

	DSC Analysis			PDF Analysis			
	Ideal T_g (°C)	**T_{g1} (°C)**	**T_{g2} (°C)**	***R* value**	**Drug Conc. (w/w)**	**Polymer Conc. (w/w)**	**Conclusion**
felodipine:PVPva	63.4	64.9	--	0.213	0.81	0.19	miscible
quinidine:PVPva	76.8	59.7	81.9	0.069	0.73	0.27	phase-separated
terfenadine:PVPva	77.2	60.6	--	0.086	0.73	0.27	phase-separate

The DSC thermogram for amorphous felodipine, PVPva, and the 75 wt% co-solidified sample is shown in **Figure 5.1a**. A single T_g at 64.9 ºC was observed for the co-solidified sample. The PDF analysis and respective difference plot for this system is shown in **Figure 5.1b**. From **Table 5.2**, the calculated T_g for an ideal 75 wt% mixture is 63.4 ºC, which is in good agreement with the experimentally determined 64.9 ºC shown in **Figure 5.1a**. The difference plot for the PDF analysis (**Figure 5.1b**) exhibits regions in *r* where the confidence intervals do not contain zero. An *R* of 0.2126 (**Table 5.2**) corresponds to 21% error between the two PDF patterns. Refined API and polymer concentrations (scaling coefficients) of 0.81 and 0.19 (**Table 5.2**) deviate substantially from theoretical concentrations of 0.75 and 0.25, respectively. Based on a single T_g and the large deviations between the calculated and measured PDF of the co-solidified sample, the system is an amorphous molecular solid dispersion.

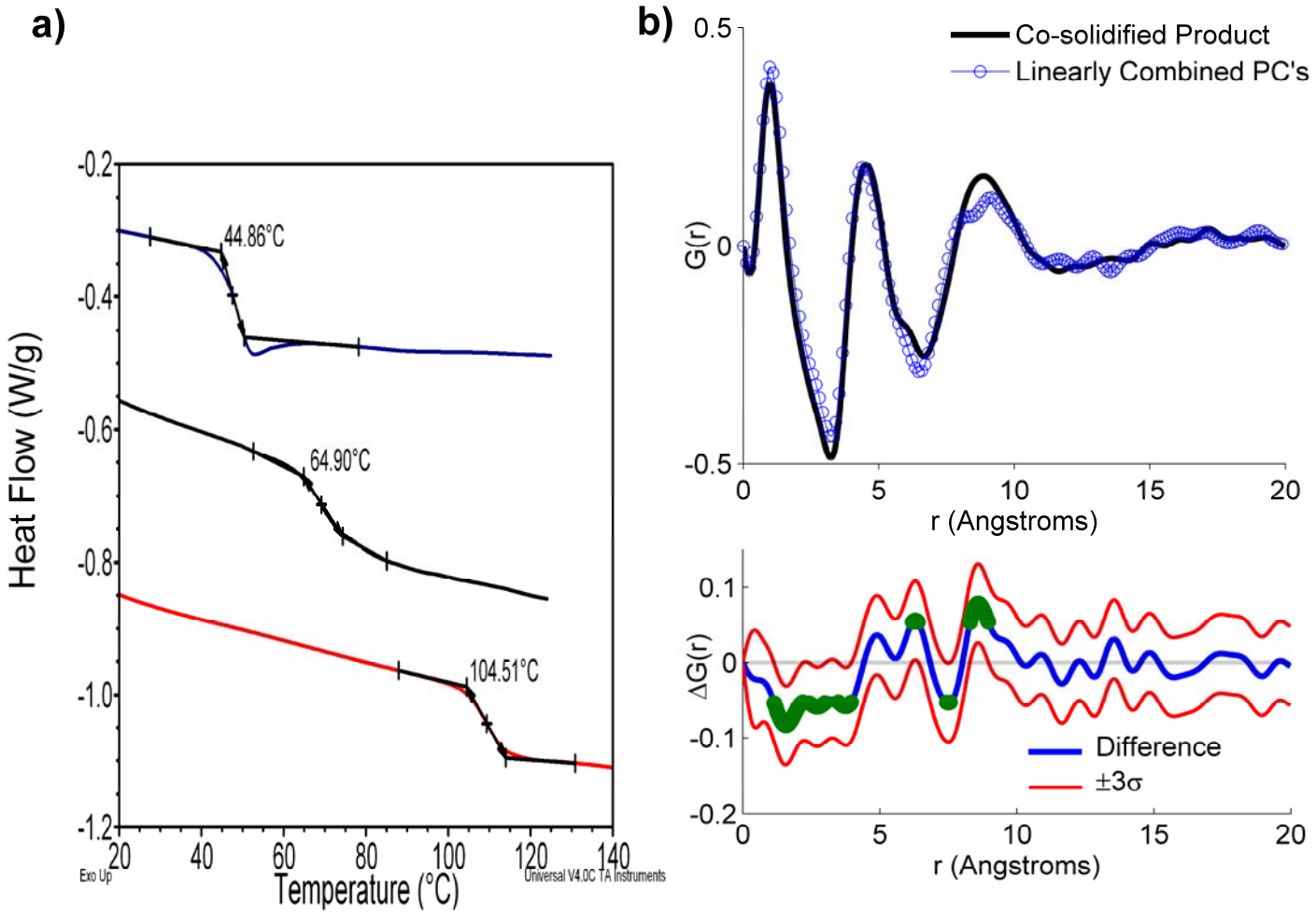

Figure 5.1. (a) DSC thermogram for amorphous felodipine (blue), PVPva (red), and 75 wt% co-solidified product (black); (b) PDF analysis (as labeled).

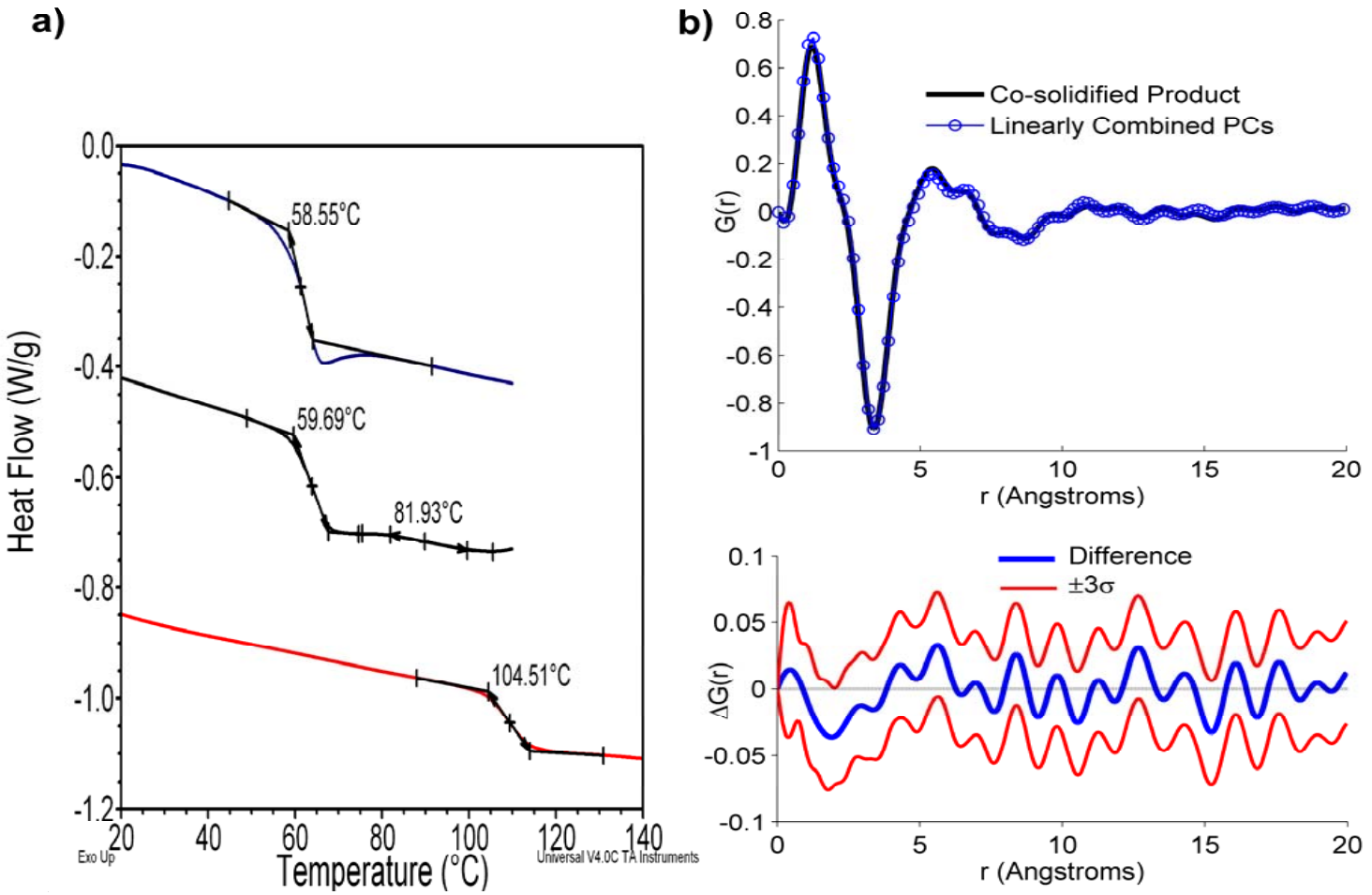

Figure 5.2. (a) DSC thermogram for amorphous quinidine (blue), PVPva (red), and 75 wt% co-solidified product (black); (b) PDF analysis (as labeled).

The DSC thermogram for amorphous quinidine, PVPva, and the 75 wt% co-solidified sample is shown in **Figure 5.2a**. Glass transition events at 59.7 ºC and 81.9 ºC were observed for the co-solidified sample. Although the DSC results alone provide conclusive evidence of phase-separation, the PDF analysis was performed and is shown in **Figure 5.2b**. The difference plot (**Figure 5.2b**) for the PDF analysis shows confidence intervals that contain zero through the entire *r* region. In addition to this, a satisfactory *R* value of 0.0689 and refined API and polymer concentrations of 0.73 and 0.27 (**Table 5.2**), respectively, were also observed. The system is phase-separated based on evidence of two T_g events and the agreement between the calculated and measured PDF for the co-solidified sample.

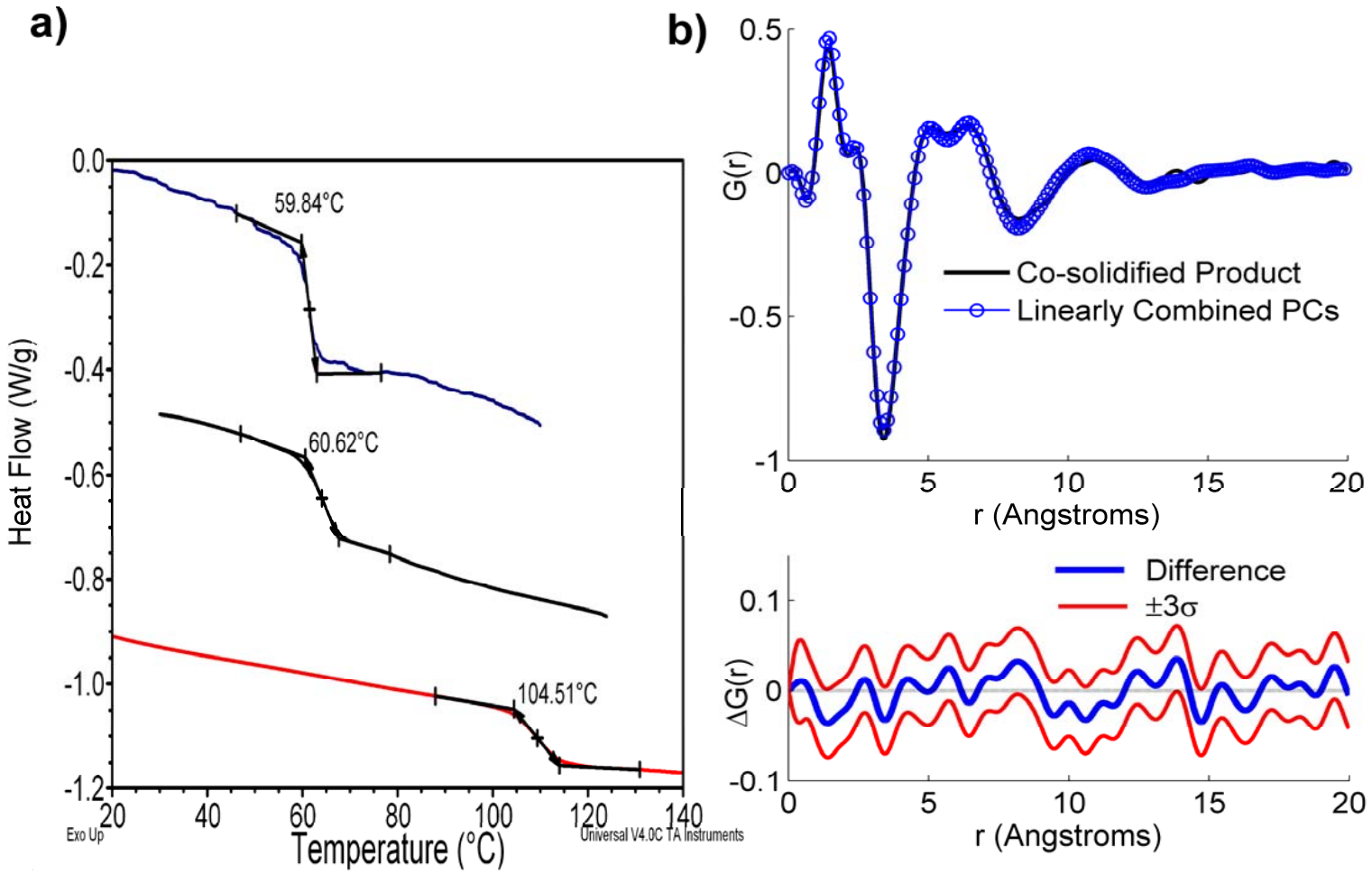

Figure 5.3. (a) DSC thermogram for amorphous terfenadine (blue), PVPva (red), and 75 wt% co-solidified product (black); (b) PDF analysis (as labeled).

The DSC thermogram for amorphous terfenadine, PVPva, and the 75 wt% co-solidified sample is shown in **Figure 5.3a**. A single T_g event at 60.6 ºC was observed for the co-solidified sample, albeit relatively close to the T_g observed for the amorphous terfenadine. The difference plot (**Figure 5.3b**) for the PDF analysis shows confidence intervals that ultimately contain zero through the entire *r* region. In addition to this, a low *R* and refined concentration values (**Table 5.2**) that are close to the theoretical concentrations were also observed. It is concluded that the system is phase-separated as a result of a single, T_g value near that of the amorphous API and the good agreement between the calculated and measured PDF for the co-solidified sample.

The final results of the co-solidified sample analyses are listed in **Table 5.3**. Of the 12 compounds comprising the calibration library, DSC and PDF analyses revealed six successfully formed an amorphous molecular solid dispersion (*i.e.* miscible with PVPva) and six formed phase separated systems. Propranolol, cloperastine, and sulfanilamide all exhibited Bragg diffraction peaks (PXRD analysis), a clear indication of phase separation, following preparation. Nifedipine and terfenadine both displayed a single T_g but were shown to be phase-separated using the PDF analyses.

Table 5.3. Calibration library generation results.

Compound	Miscible?	Comments
Felodipine	YES	--
Indomethacin	YES	--
Ketoconazole	YES	--
Itraconazole	YES	Could not obtain amorphous itraconazole; No PDF test
Tolbutamide	YES	--
Chlorpropamide	YES	--
Nifedipine	NO	PDF confirmation only; crystallinity day 1 for repeats
Quinidine	NO	Detectable phase separation from DSC and PDF
Propranolol	NO	Detectable crystallinity (PXRD) on day 1
Cloperastine	NO	Detectable crystallinity (PXRD) on day 1
Terfenadine	NO	PDF confirmation only; crystallinity day 1 for repeats
Sulfanilamide	NO	Detectable crystallinity (PXRD) on day 1

5.3.2 Calibration

Univariate logistic regression was performed by estimating regression coefficients for each of the calculated molecular descriptors. Subsequently, a model containing the regression coefficient for a given molecular descriptor was compared with a model containing only the mean using the LR test statistic. From this metric, the significance of the descriptor was determined. Molecular descriptors with a significance ≥ 0.999 (*i.e.* $\alpha = 0.001$) were retained for further analysis. The results of the univariate screening are given in **Table 5.4**. Along with the regression equation, deviance, LR, and error of cross-validation are shown. From each of these parameters, the atomic mass-weighted third-order R autocorrelation index, R3m, appears to be the most significant. Other significant molecular descriptors include the topological distance between oxygen and chlorine atoms (T(O…Cl)), the sum of the eigenvalues of an atomic number-weighted distance matrix (SEigZ), the sum of the eigenvalues of an atomic mass-weighted distance matrix (SEigm), first-order H autocorrelation weighted by atomic mass (H1m), the total H autocorrelation weighted by atomic mass (HTm), and the maximum of the fourth-order R autocorrelation weighted by atomic mass (R4m+). The R3m index will be described in detail later; however, an explanation of other indices is beyond the scope of the paper and interested readers are directed elsewhere.[137]

Table 5.4. Model parameters for the seven best univariate models.

Molecular Descriptor	**Regression Equation**	**Deviance**	**LR**	**LOO CV**
T(O..Cl)	logit P(Y) = -1.927 + 0.208**T(O…Cl)**	6.513	10.86	0.3841
SEigZ	logit P(Y) = -12.33 + 7.37**SEigZ**	4.889	12.49	0.4208
SEigm	logit P(Y) = 12.57 + 7.50**SEigm**	4.813	12.56	0.4199
H1m	logit P(Y) = -17.78 + 12.31**H1m**	6.314	11.06	0.3964
HTm	logit P(Y) = -13.25 + 1.14**HTm**	5.992	11.39	0.3720
R3m	logit P(Y) = -88.54 + 135.18**R3m**	0.039	17.34	0.0565
R4m+	logit P(Y) = -15.2 + 346.22**R4m+**	3.253	14.12	0.2637

Following univariate screening, both forward and backward elimination multivariate screening were performed at a significance level of 0.8 (*i.e.* $\alpha = 0.2$). The R3m index was the only remaining variable, and therefore, served as the final model. Predicted probabilities of amorphous molecular solid dispersion potential using the R3m model are shown graphically in **Figure 5.4**. The results from testing the R3m model with three compounds not used in the calibration are shown schematically in **Figure 5.5**. A description of the R3m index and explanation of its potential significance will be addressed in the discussion section.

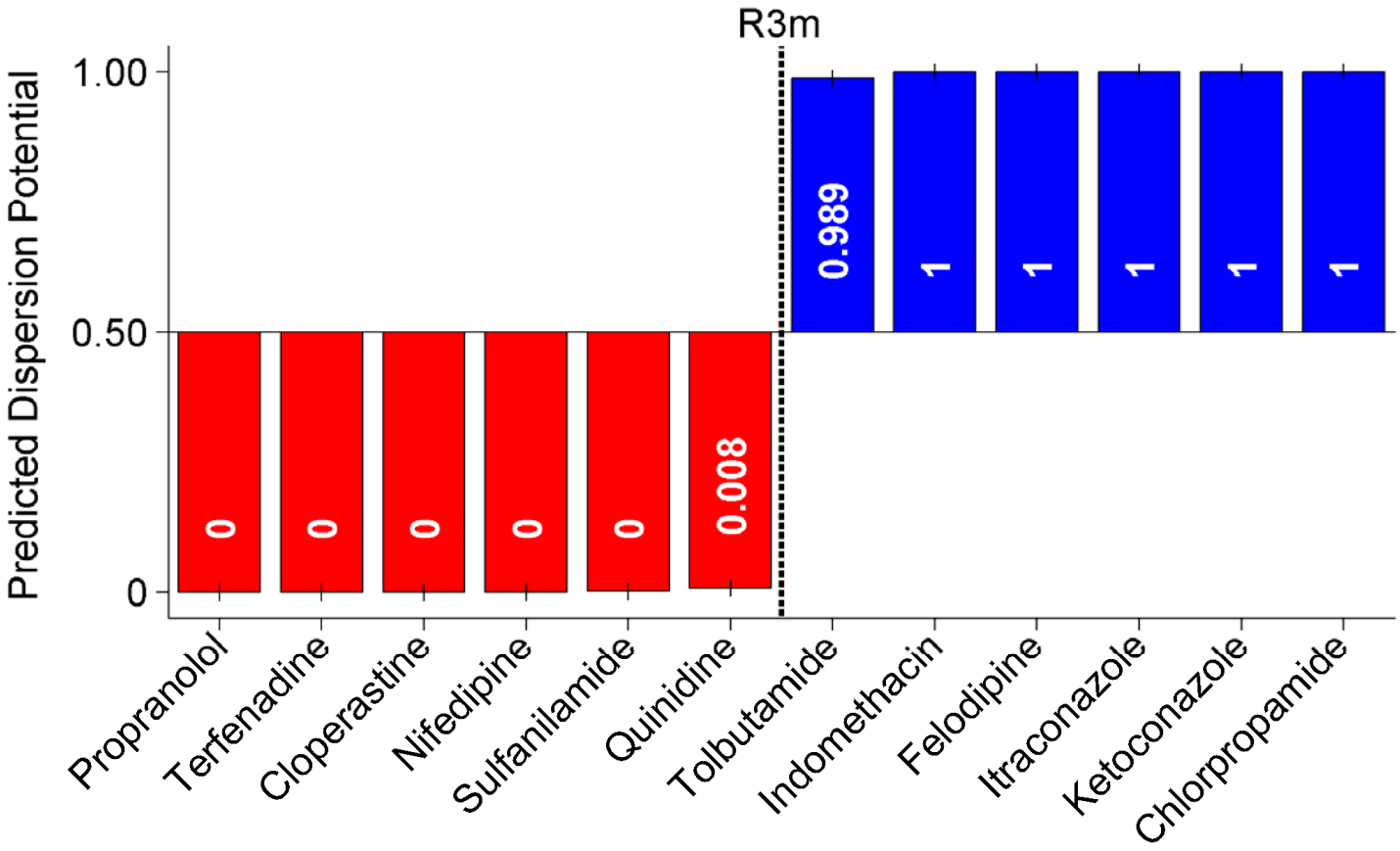

Figure 5.4. Predicted dispersion potential probabilities for each of the 12 model compounds. Red indicates a correct prediction for unsuccessful formation and blue indicates a correct prediction for successful formation.

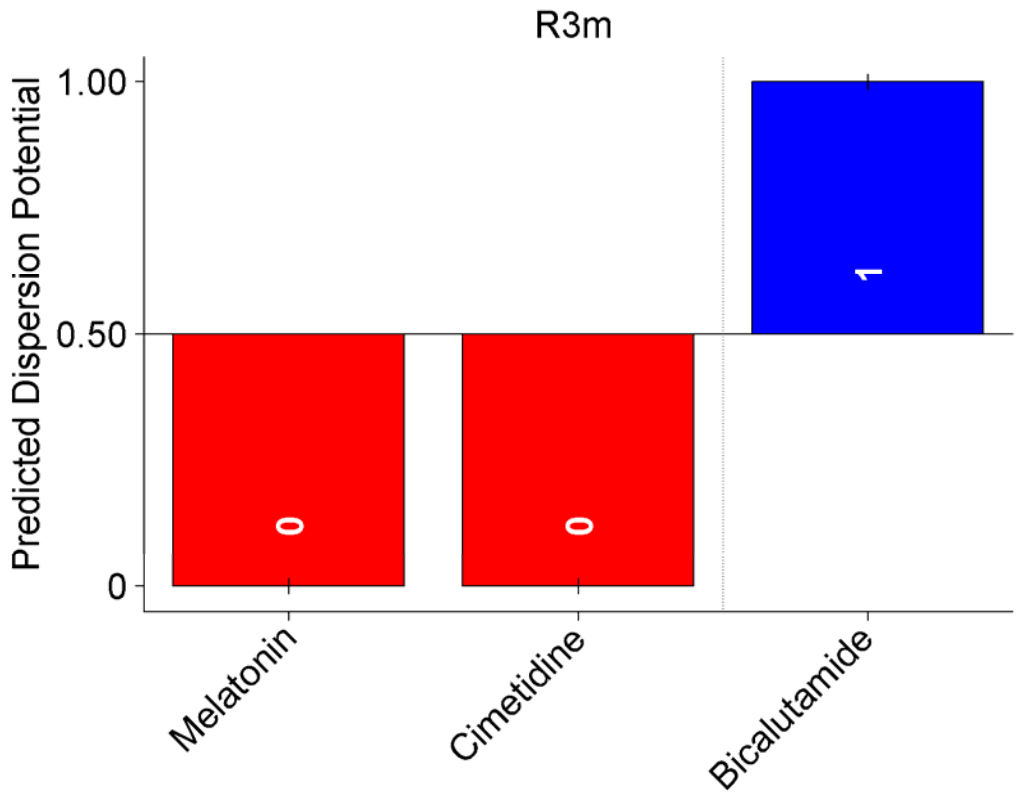

Figure 5.5. Predicted dispersion potential probabilities for each of the three test compounds. Red indicates a correct prediction for unsuccessful formation and blue indicates a correct prediction for successful formation.

5.4 Discussion

As stated in the introduction, the central objective of this research was to illustrate the potential of using *in silico* molecular calculations to create predictive models for assessing miscibility between a compound and polymeric material, afforded by the ability to classify co-solidified samples using advanced solid-state characterization methods. A further interpretation of this hypothesis states that some underlying molecular property is responsible for its ability to form a unique phase when intimately mixed with a carrier material. It is assumed that API:polymer miscibility is represented by the formation of short range order possessing physical, structural, and other intrinsic properties distinct from either individual amorphous component. It is further assumed that a completely miscible system will need to undergo phase separation as a pre-requisite to crystallization.

The extent of miscibility between a given compound and polymer is sensitive to many different variables. The method of preparation, drug loading, and environmental factors may all affect the outcome of this determination. The process of heating the materials to prepare co-solidified may introduce chemical impurities into the system. As shown elsewhere,[138] the presence of impurities can provide resistance to crystallization in co-solidified products by itself. This is recognized as a potential confounding factor to the analysis presented herein, where TGA impurity assessment limits quantification to volatile degradants only. It is assumed that the identification of miscible co-solidified products is a result of the compatibility between the API and polymer and not a consequence of thermal degradation. Therefore, conclusions concerning miscibility in this study will be with reference to the melt-quench method used, the fixed concentration

range interrogated, and assumptions derived from direct observation of characterization data.

5.4.1 Co-solidified product characterization

The purpose of showing the three examples was to illustrate the requirement for using multiple solid-state characterization techniques in order to classify the co-solidified samples. Although the two techniques are often complimentary, instances occur when results are contradictory. In the first example, a single T_g (**Figure 5.1a**, black line) intermediate to each of the amorphous component T_g events was observed for the co-solidified felodipine:PVPva sample. Since the experimental T_g of 64.9 ºC is relatively close to the predicted 63.4 ºC (**Table 5.2**), this may support classification as an amorphous molecular solid dispersion on its own accord.

Instances arise where DSC may not be sensitive to the presence of multiple T_g events. Possible explanations include convolution of two T_g events into a single T_g, the magnitude of the heat capacity change associated with an additional phase(s) is below the sensitivity of the instrument, the T_g event is superimposed over some other thermal transition, or the glass transition event unexpectedly occurs outside of the temperature range interrogated. In addition, heating the sample during the measurement may consequently force miscibility in a phase separated system. Each instance warrants the application of an alternative characterization technique, such as the PDF method using error propagation estimates, to examine the co-solidified sample.

For the felodipine:PVPva co-solidified sample, the high R value of 21.26%, concentrations inconsistent with theoretical values, and the presence of confidence intervals for r-values not containing zero (**Figure 5.1b** and **Table 5.2**) all serve as

indicators that the co-solidified product exhibits a packing pattern different than that produced by the local structure of each individual amorphous component. From **Figure 5.1b**, the difference plot indicates a significant difference between the calculated PDF and the co-solidified PDF around 8-9Å.

From **Equation 5.2**, the integration of the PDF is taken to Q_{max}, which ostensibly serves as the resolution of the calculation. In this study, Cu K_α radiation was used as the source in the PXRD experiments, which produces a Q_{max} of approximately 7Å^{-1}. Fully resolved PDFs require a Q_{max} much greater than 7Å^{-1}, often achieved using synchrotron radiation sources. Due to the limited Q-resolution afforded by laboratory source X-ray data, each probability peak in the PDF represents a convolution of many different delta peaks. With infinite Q-resolution, the formation of a new phase in the co-solidified sample would result in the appearance of unique delta peaks representing newly formed interatomic distances. The limitations imposed by using Cu K_α radiation call for considering the distributions of delta peaks in the convoluted probability peaks. Distribution changes manifest as alterations to the shape of the probability peak, as observed for the felodipine:PVPva co-solidified sample **(Figure 5.1b**, black line) relative to the combine amorphous components (**Figure 5.1b**, blue circles). It may be concluded that this sample has unique interatomic distances formed around 8-9Å not found in either amorphous component, and therefore, is an amorphous molecular solid dispersion. This conclusion is consistent with those found elsewhere.[79]

In the second example, the thermogram of the quinidine:PVPva co-solidified sample (**Figure 5.2a**, black line) displays a T_g event near that of the amorphous quinidine (**Figure 5.2a**, blue line) and a second intermediate to each amorphous component. Given

the detection of two T_g events, it is reasonable to conclude that the co-solidified sample has phase-separated. In an effort to illustrate an instance where the PDF method supports the conclusions drawn from DSC, an analysis was performed on the quinidine:PVPva system. From **Figure 5.2b**, agreement between the calculated PDF and the co-solidified sample was obtained as evidenced in the difference plot. The inclusion of zero throughout the entire *r* range, low *R* value, and experimentally determined concentration values close to theoretical (**Table 5.2**) all support the conclusion of phase separation.

The final example is unique due to the disagreement in conclusions drawn from each characterization technique. In **Figure 5.3a**, the thermogram for the terfenadine:PVPva co-solidified sample (black line) shows a single detectable T_g of 60.6 ºC close to the T_g of 59.8 ºC for amorphous terfenadine (blue line). Although this is likely indicative of the presence of amorphous terfenadine, unfortunately, a definitive conclusion is not readily available. Deeming this analysis as inconclusive, an additional characterization technique is required.

In **Figure 5.3b**, the linearly combined amorphous component PDF patterns are superimposed over the co-solidified sample PDF. From the difference plot, it is shown that the confidence intervals include zero throughout the entire range of *r* values. Additionally, the refined concentration values and low *R* value (**Table 5.2**) indicate a good fit between the two PDF patterns. The aforementioned PDF data supports the conclusion that the terfenadine:PVPva co-solidified sample is phase-separated.

Table 5.3 summarizes miscibility determination between the 12 model compounds comprising the calibration library and PVPva, where a few noteworthy points deserve some discussion. Propranolol, cloperastine, and sulfanilamide all exhibited

Bragg diffraction peaks in PXRD patterns obtained following co-solidification, thereby indicating phase separation. Nifedipine and terfenadine were identified as phase-separated using the PDF method, where their respective co-solidified sample thermograms displayed single T_g events. This conclusion was indirectly confirmed when the repeat co-solidification samples were analyzed. In their subsequent preparations, PXRD patterns from both compounds displayed Bragg diffraction peaks immediately following sample preparation, thereby corroborating the previous conclusions.

Itraconazole was deemed to successfully form an amorphous molecular solid dispersion. From **Table 5.3**, amorphous itraconazole was not obtained thereby preventing the PDF analysis; a definite shortcoming of the PDF method. It may be expected that making conclusions solely on DSC data increases the probability of a misclassification. In the previous discussion, terfenadine and nifedipine were classified as phase separated by PDF analysis. It was shown that subsequent preparations were prone to different levels of devitrification as evidenced in PXRD analyses. The inability to procure amorphous itraconazole was attributable to the tendency for instantaneous crystallization upon quench cooling. Given this characteristic, phase-separated itraconazole would be expected to instantaneously crystallize upon quenching. Three different itraconazole:PVPva preparations consistently produced a single T_g event with PXRD patterns lacking any detectable Bragg diffraction. The combination of all information supports a classification of complete miscibility between itraconazole and PVPva, which is further founded on conclusions drawn elsewhere.[139]

5.4.2 Calibration

From **Table 5.4**, the most promising molecular descriptor appears to be the R3m index. Deviance is the natural logarithm of the likelihood value multiplied by negative two and serves as an estimate of error. As the deviance is minimized (approaches zero), therefore, the predictions approximate experimental values and the model becomes more significant. With a deviance of 0.039 for the R3m model, it is two orders of magnitude lower than that of the next best index. The LR approximates a χ^2 statistic, where a larger value is indicative of greater significance. The R3m index has the greatest LR value for all molecular descriptors tested. Finally, the error of cross-validation (LOO CV) is a metric for determining the robustness of the model. By iteratively removing a compound from the library, creating a calibration, make a prediction on the compound removed, and calculating the error, the extent to which each sample influences the calibration is assessed. The LOO CV for the R3m is an order of magnitude less than that of the next best value, thereby confirming the robustness of the R3m model.

It is important to consider the possibility of over-saturating a model constructed from only 12 samples. With this in mind, multivariate logistic regression at a significance level of $\alpha = 0.2$ was performed. Both forward- and backward-elimination yielded the same conclusion; the R3m index was the single most significant descriptor. Shown in **Figure 5.4** are the R3m predicted probabilities for each calibration sample with an estimated confidence interval in bar graph form. Interestingly, 10 of the 12 compounds were predicted perfectly, while quinidine and tolbutamide only slightly deviated. The estimated confidence intervals ($\alpha = 0.05$) for all 12 predictions indicated the predictions are reliable.

The R3m index is part of a class of molecular descriptors known as GETAWAY (Geometry, Topology, and Atom-Weights AssemblY).[140,141] The GETAWAY indices link 3-D geometry to atom relatedness, while retaining specific chemical information. The first part of calculating any GETAWAY descriptor is to calculate the molecular influence matrix, **H**, given by:

$$\mathbf{H} = \mathbf{M} \bullet \mathbf{inv}(\mathbf{M}'\mathbf{M}) \bullet \mathbf{M}' \tag{5.5}$$

where **M** is the molecular matrix comprised of A rows (number of atoms in molecule) and three columns (Cartesian atomic coordinates). The molecular influence matrix is equivalent to a leverage matrix, ostensibly describing the Euclidean distance of atoms from the geometric center of the molecule. The diagonal elements of **H**, h_{ii}, are called leverages and represent the "influence" of each atom in determining the whole shape of the molecule. Interestingly, lower leverages are found for atoms in molecules of spherical shape, while higher leverages for atoms in more linear compounds. Each off-diagonal element of **H** represents the accessibility of the i^{th} atom to interactions with the j^{th} atom, where negative elements represent a low degree of accessibility. From the molecular influence matrix, various R-GETAWAY descriptors can be calculated, including the w-weighted k^{th} order autocorrelation index, $R_k(w)$, given by:

$$\boldsymbol{R_k(w)} = \sum_{i=1} \sum_{j>i} \frac{\sqrt{\boldsymbol{h_{ii}h_{jj}}}}{\boldsymbol{r_{ij}}} \bullet \boldsymbol{w_i} \bullet \boldsymbol{w_j} \bullet \delta(\boldsymbol{k};\boldsymbol{d_{ij}}) \quad \boldsymbol{k} = 1,2\ldots\boldsymbol{d} \tag{5.6}$$

where h is the element of the molecular influence matrix, r is the geometric interatomic distance, w is the chemical weighting, k is the path length, d is the topological interatomic distance, and δ is equal to 1 when $k = d$ and 0 when $k \neq d$. From this equation, the R3m

descriptor may be interpreted as follows: "*R*"-GETAWAY "3rd"-order autocorrelation index weighted by the atomic mass, "*m*".[140]

A direct physical interpretation of the correlation between the R3m index and amorphous molecular solid dispersion potential is not readily apparent. From **equation 5.6**, some key conceptual attributes of this index are evident. Larger values are obtained for two peripheral atoms (*i.e.* further from the geometric center of the molecule) that are in close proximity to each other (r_{ij}). Additionally, as the atomic masses of the two atoms increase, so does the index; ultimately attributable to a larger number of electronegative atoms (*i.e.* oxygen, sulfur, chlorine) in SMO compounds. In this study, it was observed that as the index increases, the probability of successful solid dispersion formation increases, as well. From the previous discussion of the R3m index, it is reasonable to state that a molecule having electronegative atoms along its periphery that are conformationally positioned such that their interatomic distances are minimized results in an increased probability of dispersion formation.

One of the most intriguing comparisons is that of felodipine and nifedipine. Commonly prescribed calcium channel blockers, their structural similarities are readily apparent in **Table 5.1**. It has been previously reported that the nucleation rate in amorphous nifedipine, both as a pure phase and as a 3 wt% amorphous molecular solid dispersion with PVP, is substantially greater than that of felodipine in the equivalent state.[142] In this study, felodipine was shown to be completely miscible with PVPva, whereas the co-solidified product of nifedipine and PVPva exhibited detectable phase separation. The benzene flanking the dihydropyridine in nifedipine contains a nitro group, where the same benzene contains two chlorine atoms in felodipine (**Table 5.1**).

This substituent change causes a marked increase in the R3m index from 0.579 for nifedipine to 0.813 for felodipine.

Since the R3m includes specific information concerning 3D molecular geometry provided by the molecular influence matrix, atom relatedness by molecular topology, and chemical information by using the atomic mass weighting scheme, it's difficult to simplify the relationship between this sophisticated index and the mechanism of API:polymer miscibility. The mere increase in the R3m index can be attributable to multiple molecular features (*i.e.* increasing amount of electronegative atoms, large number of atoms distant to the geometric center, or intramolecular interactions three topological units apart). Any further extrapolation, at present, concerning this correlation would be unfounded and is the subject of ongoing research.

The R3m model was challenged with three compounds not used in the calibration. The results are shown in **Figure 5** as a bar plot. Both cimetidine and melatonin were accurately predicted to not form an amorphous molecular solid dispersion with PVPva. Bicalutamide, however, was accurately predicted and identified to be completely miscible with the polymer. It was important, when selecting compounds to test the model, that molecular attributes did not exceed the variance space of the molecules used to construct the calibration. For example, the fusion temperature for compounds included in the calibration fell in the range of 120-180°C. Predictions for molecules with fusion temperatures substantially deviating from this range tended to be incorrect.

As with any materials informatics calibration, the power of the model increases with the variance spanned by the samples comprising it. Since this calibration only contained 12 compounds, it may seem apparent that the variance space is relatively small.

It is anticipated that as more compounds are added to this library, predictions will become more accurate over a wider range of molecular attributes. Additionally, an expanded library may identify different/additional molecular descriptors that are correlated to dispersion potential. This may shed further light onto the specific structural properties responsible for the correlation to dispersion potential.

5.5 Conclusion

The ability to identify phase-separated co-solidified samples was afforded by implementing a combination of standard DSC and PDF transforms of PXRD patterns. Classification of co-solidified samples based on extent of miscibility enabled construction of a 12 compound library to model amorphous molecular solid dispersion potential. Logistic regression analysis of a molecular descriptor database identified a GETAWAY index highly correlated to solid dispersion potential. When the model was tested with external compounds possessing materials-properties spanning an appropriate variance space, successful predictions were made. The model developed herein is not universally applicable across all SMO compounds. The methodology presented outlines a novel approach to solving the complex issues surrounding API:polymer miscibility, where pharmaceutical sectors having large compound libraries at their disposal are poised to benefit from these materials-based models. Future work aims to increase interpretability of molecular indices to aid in understanding the complex phenomena associated with API:polymer miscibility requirements.

Chapter 6: Summary

The plethora of recent pharmaceutical literature devoted to the topic of solid dispersion technology is a testament to its appeal for enhancing aqueous solubility/dissolution rate of poorly soluble NCEs. Despite the large amount of work focused on the miscibility between a drug and polymer, there remains a lack of consensus concerning specific properties underlying this phenomenon. As an alternative to case-by-case studies of specific intermolecular interactions to arrive at an explanation for miscibility, it was hypothesized that some structural characteristic(s) of a compound may be indicative of dispersion potential, when the polymer, concentration, and manufacturing method are all held constant. The approach to testing this hypothesis, calibrating a material informatics database of molecular descriptors, is novel to the best of the author's knowledge.

One of the central themes to this dissertation work, mentioned in the introduction, states that "innovation in the areas of pharmaceutical pre-formulation and formulation development are often precluded by advancements in materials characterization." As illustrated in this work, the types of materials used as/in medicinal products and inherent issues surrounding their implementation in pharmaceutical dosage forms are becoming increasingly complex. Although PXRD as an analytical method serves as the mainstay for assessing material structure, traditional data processing techniques neglect to benefit from the information in the entire diffraction pattern and, therefore, are unable to provide the scale of scrutiny required for analyzing highly disordered systems.

To accommodate sensitivity to "local" environments, full pattern PXRD techniques have emerged. Total scattering analysis coupled with multivariate

chemometric linear modeling was successfully shown to provide enhanced quantitative selectivity to multiple amorphous/disordered components in composite samples over traditional univariate diffraction-absorption processing. Additionally, the selection of transmission geometry, combined with multivariate modeling, further enabled a reduction in calibration size with little effect on standard error of prediction.

The pertinence of using PDF transformed PXRD data to study short-range structure in complex materials was described in great detail. The sensitivity of PDF transforms of laboratory PXRD data to local order of material structure deviations in composite pharmaceutical materials was successfully investigated. It was shown that high-energy input processing, such as powder compaction, induced structural alterations to average crystallographic molecular location and orientation relative to the raw crystalline material as evidenced by changes in PDF transforms. Additionally, these structural modifications were modeled using reverse Monte Carlo simulations and were shown to be consistent with deviations to long range order. Further, composite diffraction data was accurately separated permitting PDF transform of component-specific isolated diffraction. The conclusions drawn from this work are significant because they show the minor PXRD pattern aberrations resulting from subtle structural changes manifest as substantial modifications to interatomic correlations. Ultimately, this was important in supporting the use of our X-ray data to study solid dispersion systems, as low-frequency features in PXRD patterns of amorphous/disordered pharmaceutical materials that may not be interpretable as-is, become considerable in the PDF transform.

The published method for using PDF transforms to detect phase-separated co-solidified products was scientifically rigorous in its inception; however, it failed to provide a statistically-robust approach for drawing conclusions. As the actual PDF transform itself was adapted from the inorganic materials science literature, principles of error propagation using initial error estimates from the PXRD experiment were, as well. The novelty of the approach is the application of these algorithms to comparing multiple experimental PDF patterns. By developing a characteristic threshold to distinguish significant differences between experimental PDF transforms from insignificant, the conclusions drawn from analyses were consistent.

An alternative to circumvent one of the aforementioned limitations to the PDF method is possible. As previously described, the requirement of producing an amorphous standard of the drug substance to use in the analysis can be a difficult task. With the increasing power of structural simulations, akin to those used in some of the preceding work, and the knowledge of local structure in disorder systems, a simulated amorphous PDF transform for drug substances may be possible to model. This would be advantageous as it would bypass the difficulty in producing an amorphous phase of the drug, as well as decrease the raw material supplies associated with the task.

The final segment of this work tied together all of the analytical development to support a study to predict solid dispersion potential from *in silico* modeling. Given the ability to identify phase-separated co-solidified systems from true amorphous molecular solid dispersions, a compound library was generated for calibration. The ability to calculate molecular descriptors from the 3-dimensional coordinates of the atoms comprising the compound affords a wealth of information with no raw material costs.

The implementation of a material informatics calibration for correlating dispersion potential to structural attributes (via molecular descriptors), to the best of the author's knowledge, is the first attempt at this approach. A significant correlation between dispersion potential and the R3m GETAWAY index was observed. A direct physical meaning of the correlation between R3m and dispersion potential, however, was not readily identifiable or interpretable.

The informatics calibration largely suffered from an inadequate sample size, as accuracies in screening a large number of multi-scale independent variables increase as the sample size increases. The addition of compounds to the library that span further variance space may result in other selected significant molecular indices. These additional molecular descriptors may further provide information into structural characteristics responsible for dispersion potential. Analysis of molecular-level interactions, as by vibrational spectroscopy, may supplement some of the conclusions drawn from future work. Coupling structural features with information pertaining to local interactions may yield a complete picture of these complex systems.

The ability to optimize NCE properties, dosage form selection, and formulation characteristics using little-to-no raw material supplies is highly imperative to decreasing escalating development costs. The principles outlined throughout this dissertation may be adapted within the pharmaceutical setting, where the large libraries of drug compound information and advanced technological capabilities render them imminent. With the push for complete product understanding by the Food and Drug Administration, pharmaceutical companies are set to benefit from adapting and applying these computational methodologies to their standard development programs.

Appendix A: Eutectics

The distinction between solid dispersions and eutectics is important, as the structural, physicochemical, and other intrinsic properties are vastly different. A large number of pharmaceutical references inappropriately use these terms interchangeably; therefore, the following sections develop the materials properties of eutectics and how they limit preparation methods, enhance physicochemical performance, and induce physical instability.

A.1 Structure

A eutectic solid is a condensed phase formed when a specific composition (χ_e) of two miscible liquid phases is co-solidified at a specific temperature (T_e), resulting in a crystalline microstructure that has a lower melting temperature relative to that of either pure constituent. For eutectic solidification to occur, the components must be mutually miscible as liquids. From a molecular perspective, this implies that the NBIs between unlike components must be similar to interactions between like components, in the liquid phase.

Binary eutectic crystallizations typically proceed as first-order phase transitions, which mechanistically advance through several stages (*i.e.* appearance of nuclei, nuclei growth without replication, Ostwald ripening, *etc.*).[143] Eutectic solid products are, therefore, crystalline materials. Further, eutectics possess a microstructure-level component of periodicity different than that of either pure crystalline phase. Without the microstructural element, the system cannot be accurately classified as a eutectic. This particular concept is often neglected in the pharmaceutical literature, where accounts of

eutectic formation are reported without proper supporting thermal and structural characterization.[144-147]

An important part of the aforementioned definition of a eutectic surrounds the newly-formed eutectic microstructure. The effective entropy change and the volume fraction of the eutectic phase are inter-related during solidification, where the relationship between them may be used to characterize the microstructure (neglecting kinetics).[148] According to Hunt and Jackson,[149] the entropy of fusion of the individual pure components controls the resulting eutectic microstructure. When two materials possess equivalent entropy of fusion values, both phases grow simultaneously behind a planar solid/liquid interface resulting in a normal eutectic microstructure **(Figure A.1)**. In contrast, large differences in entropy of fusion result in faceted growth, producing an anomalous structure. In normal structures, the phases appear as alternating lamellae or rods of one phase embedded in the other; anomalous structures, however, exhibit many variants.[16]

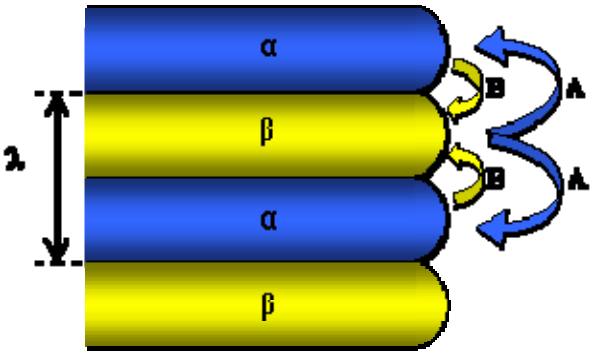

Figure A.1. A schematic of lamellar growth for a binary eutectic behind a near-planar solid-liquid interface (from Porter and Easterling, 1981, with modifications).

A.1.1 Structural Interpretation of Physicochemical Benefits

The enhanced aqueous solubility gained through eutectic formation is often attributed (in the pharmaceutical literature) to the lower temperature of fusion of the

solidified material.[150] A more fundamental reason for this lower fusion temperature, and the resulting increased aqueous solubility, exists. In **Figure A.1**, a schematic representation of normal eutectic solidification is shown. As the saturated α phase (composed of component A) and β phase (composed of component B) solidify, excess B and A diffuse laterally to the tips of the β phase and α phase, respectively, promoting further growth. In this figure, λ represents the interlamellar spacing between the α-phase and the β-phase and is directly related to the rate of growth (*i.e.,* rapid growth rate results in small λ). The unique eutectic solid microstructure, which results in incoherent interphase boundaries (the line between the α-phase and β-phase in **Figure A.1**), provides a less thermodynamically stable interface relative to the normal coherent interactions that comprise the individual crystalline phases. This boundary possesses a higher free energy because its structural makeup consists of NBIs between different molecules (*i.e.,* a drug and its carrier, or two different drugs) where these interactions are typically not energetically equivalent to those between like molecules. Further, the number of unfulfilled bonds at the interphase boundary is greater relative to either pure component phase, and the NBIs formed between unlike molecules are not as stable relative to those involved in maintaining the pure component crystal lattice resulting in an increase in internal energy. These bonds are, therefore, energetically easier to overcome.

A.2 Manufacture

Application of the fusion technique in the production of eutectics[151-156] requires that a mixture of the two components be heated above the melting temperature of the highest melting component. The two miscible liquids are mixed until homogenous, and controlled solidification is facilitated by cooling the liquid mixture through T_e. The

resulting solid may be further processed (*e.g.* sizing, blending) depending upon the specific downstream application. Although the fusion method is commonly applied, additional consideration to temperature must be given when using with pharmaceutically relevant materials. The temperature at which the onset of thermal degradation occurs relative to the fusion temperature must be taken into account, as alternative methods of preparation exist for thermally labile drugs and carriers. Further, the molten state of the component having the lower melting temperature may adversely affect the fusion kinetics of the other material. In particular, non-specific and specific interactions between the molten state of one material and the solid state of the other material during the fusion process may lead to effective dissolution of the higher melting component in the lower melting material's molten phase.[157]

Solvent-mediated co-precipitation is most commonly used to manufacture pharmaceutical eutectic solids, serving as the choice for temperature-sensitive products.[158-160] In this process two components are dissolved at the eutectic composition either in a single medium in which they are mutually soluble, or in separate media that are eventually mixed together in proportions representing the eutectic composition. The solvent is then removed in either a controlled or uncontrolled fashion, and the co-precipitated solid is subjected to further processing as above.

Although common, solvent-mediated co-precipitation has several practical disadvantages. Given a candidate NCE having sufficient hydrophobicity to merit exploration of solubilization strategies such as eutectic formation, and a second hydrophilic component, it is may be difficult to find a common solvent capable of dissolving both solutes. Many organic solvents are highly toxic to humans, imposing

additional concern with residual solvent levels following precipitation and processing. Further, the amount of solvent required to perform such a process on a commercial scale poses a tremendous production cost. Additionally, the method and rate of evaporation both have implications on the resulting solid microstructure, which may, therefore, alter product performance. Finally, the amount of time required to evaporate the solvent to acceptable levels places a constraint on the efficiency of this application. Given these impracticalities, the fusion method seems to hold an apparent advantage relative to the solvent technique.

Eutectic growth velocity holds considerable influence on the mechanical properties of the resulting binary solid material,[161] which is of concern particularly if the eutectic is to be formulated as part of a solid oral dosage form. During growth of a phase-pure single crystal, the principal faces governing morphology will grow at the slowest rate, and correspond with planes having the highest intraplanar density and greatest interplanar spacing (*i.e.* lowest Miller indices).[162] A crystalline lattice is often weakest coplanar with one of its largest faces, as high *d*-spacing correlates with weak interplanar bonding, establishing these as the most likely sites for plastic deformation to occur.[163] The interphase boundary in a eutectic solid represents the source of its weakest intermolecular interactions. If it is assumed that the interphase boundary has comparable mechanical implications to weak interplanar bonding in single crystal systems, then these interphase regions become likely sites for mechanical failure to occur. If it is further assumed that this boundary becomes weaker as the interlamellar spacing (λ) increases, then experimental parameters affecting the interlamaller spacing also affect the

mechanical properties of the material. A binary system co-solidified at its eutectic composition will display a growth rate (v):

$$v = k_2 D \Delta T \frac{1}{\lambda}\left(1 - \frac{\lambda^*}{\lambda}\right) \quad \text{(A.1)}$$

where λ is the interlamellar spacing, k_2 is a proportionality constant, D is the liquid diffusivity, λ^* is the minimum possible lamellar spacing and ΔT is the degree of undercooling below T_e.[16] Therefore, exacting control over the temperature at which a eutectic solid is grown holds implications for the interlamellar spacing and mechanical properties of the material.

As addressed above, the eutectic composition (χ_e) represents the specific mole/mass fraction concentrations of two mutually miscible liquids at which co-solidification without prior phase separation will result in a microstructure that melts at a lower temperature than the T_m of either pure component. In **Figure A.2**, a typical temperature-composition (T-χ) binary phase diagram is shown. Compositions falling to the left or right of χ_e will result in a product having a mixed microstructure, where the excess phase, will solidify prior to cooling below T_e **(Figure A.2b)**. In order to maximize predictable physicochemical benefits afforded by the unique microstructure, explicit control of growth parameters at χ_e and T_e is essential, although not easily established.

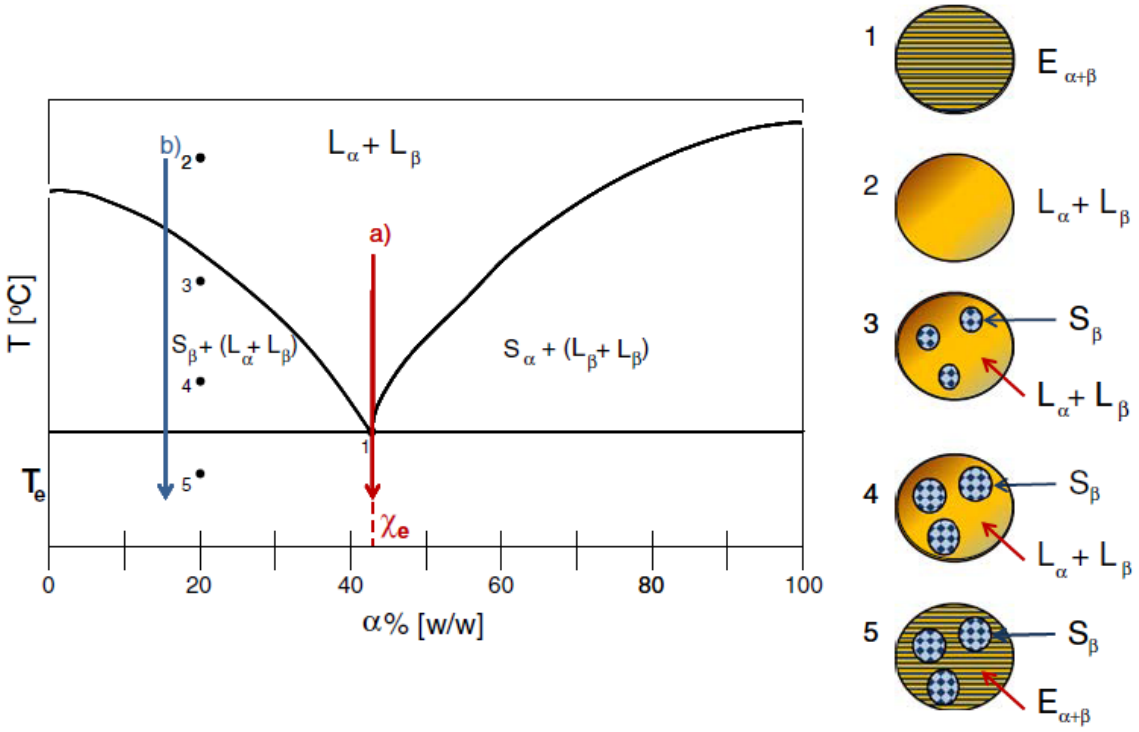

Figure A.2. A T–χ diagram for a mixture of two mutually miscible liquids α and β. **a)** Cooling the homogeneous mixture along this trajectory results in eutectic solidification below T_e, resulting in lamellar microstructure (1). **b**) For $\chi \neq \chi_e$, cooling the homogeneous liquid mixture (2) along the trajectory indicated results in precipitation of β (3). Continued cooling allows growth of crystalline β (4). At $T \leq T_e$, the remaining liquid ($\chi = \chi_e$) solidifies as eutectic (5) resulting in a mixed microstructure

Currently, χ_e for simple binary systems is determined empirically, first requiring assessment of the compatibility of the two components. Eutectic formation requires complete miscibility of the two components in the liquid state and immiscibility in the solid state. In the traditional method employed for χ_e determination, samples spanning the entire concentration range of the two materials are co-solidified, employing the fusion-based method discussed above. Samples are subjected to thermal analysis (*i.e.,* DSC, hot stage microscopy, *etc.,*) and the fusion temperature(s) of the co-solidified mixture is determined and plotted as a function of composition, thereby creating the *T*- χ phase diagram. This is where prior characterization of thermal interactions becomes

critical, as this may affect the accuracy in determination of the true melting temperature.[164] The thermal interactions between components upon heating may complicate the signal from thermal analysis of mixtures, thus warranting care when interpreting data. Further, phase-purity must be considered, as this will also affect the fusion temperature.

Two problematic issues associated with eutectic composition determination via *T*-χ phase diagram construction are anticipated: (1) the process of creating a *T*- χ phase diagram is laborious and (2) phase diagram construction requires the sacrifice of relatively large amounts of both components. Considering the amount of material typically available during the early stages of investigating a NCE, determining the eutectic point via phase diagram is often prohibitive. As a result, a great deal of current research focuses on the development of methods aimed at determining eutectic compatibility and eutectic composition in few-to-no experiments.

Law *et al*.,[165] developed a dimensionless index (I_c) used as a screening tool for predicting PEG-drug eutectic composition based on the van't Hoff equation:

$$I_c = \frac{T_d^f - T_p^f}{R(T_d^f)^2 / \Delta H_d^f} \qquad \text{(A.2)}$$

where T_d^f is the fusion temperature of the drug, T_p^f is the fusion temperature of the polymer, R is the ideal gas constant, and ΔH_d^f is the enthalpy of fusion of the drug. Though the authors claim to have successfully predicted the eutectic composition for eight model drug compounds, the index only provided an estimate of $\chi_e \pm$ 10-15%. Further, this index does not consider racemization, phase transitions, decomposition, incompatibility, *etc*., as these characteristics would affect the co-solidification process.

Approximation of χ_e is, however, not without merit. First, the approach adopted by Law *et al*.,[165] accurately predicted whether or not a eutectic would form between two components. During eutectic development, *T*- χ phase diagrams are created for two components which occasionally are not able to form a eutectic. The index, therefore, prevents this costly and time-consuming event from occurring. Also, when the approximate eutectic point is known, an abbreviated *T*- χ phase diagram may be prepared, thereby decreasing initial material requirements.

Two additional details concerning the aforementioned index deserve some attention: (1) the order of material structure of the carrier PEG and (2) applications of the van't Hoff equation. Much of the pharmaceutical literature reports the formation of eutectics between a drug and the water soluble, synthetic polymer PEG, as is the case in this example. From a structural standpoint, the formation of a classic eutectic microstructure between these two components may be difficult to envision, owing to the fact that the long-chain PEG molecules do not crystallize in the rigorous sense of the word. Furthermore, the considerable size difference between PEG and any small molecule is expected to result in significant dimensional mismatch. To visualize the formation of a eutectic microstructure between PEG and a small molecule drug compound, PEG needs to be considered in terms of both micro- and macroscopic structural features. In the solid state PEG molecules are arranged as repeating lamellar units bridged by tie molecules (molecules arranged in a disordered state). Therefore, PEGs exhibit a defined T_g due to the tie molecules, as well as having repeating ordered regions, termed spherulites, which may be conceptualized as a crystalline. Consequently, PEGs are considered "semicrystalline," where the relative amount of crystallinity is

determined by the molecular weight of the PEG chain.[166] The crystal lattice for PEG is often defined as encompassing only portions of the polymeric chains, where the unit cell dimensions are proportional to that of medicinal organic molecular crystals.

The second issue identified above considers that the index is constructed using the van't Hoff equation as its foundation. Models incorporating this equation are typically bounded by assumptions that may not be rigorously true for real systems (*i.e.,* equivalent interactions, no change in volume, *etc.*). The highly idealized assumption of equality of interactions is invalidated when the incoherent phase boundaries between layers of the eutectic structure are considered. These boundaries are less thermodynamically stable relative to bulk lattice regions, specifically due to the difference in interactions between unlike components across the solid-solid interface. These difficulties may ultimately detract from the practicality of such tools, limiting their universal application.

The financial and raw material resources required to determine the eutectic composition appear to represent deterrents of eutectic application in pharmaceutical systems. Therefore, a key avenue for future eutectics research should include development of methods designed to decrease the amount of experimentation necessary for determination of χ_e and T_e, as well as moving towards accurate, predictive determination of these parameters. Analytical tools used to characterize drug:carrier compatibility and models designed to predict compatibility are paramount to minimizing experimental consumption of API, thereby making this strategy more attractive as an early development tool. Further, as a better understanding of the relationship between eutectic microstructure and material function is gained, more efficient methodologies for predicting eutectic composition may result. Characterization of the incoherent

boundaries formed in eutectics may aide in achieving a better understanding of the aforementioned relationship. Through characterization, some questions concerning this boundary need to be investigated: 1) What is the composition at this boundary (*i.e.* a single layer of molecules of each phase, multiple, interspersed layers)? 2) Is the boundary both macroscopically and microscopically isotropic, or does anisotropy exist? and 3) Does the boundary become increasingly isotropic as the eutectic composition is approached? If these interfacial boundaries can be modeled structurally through defining specific intermolecular orientations and interactions, it may enable the macroscopic composition to be determined theoretically.

A.3 Physical Stability

Eutectics are the most thermodynamically stable of the binary composite materials covered in this dissertation. Structurally, eutectics are crystalline; the increased free energy, enthalpy, and entropy are manifestations of the incoherent phase boundaries formed upon solidification. At χ_e, the number of incoherent, higher energy regions is maximized. As explained previously, this is the source from which the enhanced aqueous solubility of these materials is derived. These high energy regions also result in the decreased melting temperature that is observed relative to those of each individual component. If T_e is close to ambient temperatures, a limit of physical stability is represented where the system disproportionates into a mixture of individual phases (*i.e.,* phase separation). On the contrary, a lower temperature limit of stability may also be observed in eutectic solids. In this case, eutectics held at temperatures well below the eutectic temperature decompose into a mixture of the two phases.[167] This most likely results from the higher energy associated with the interphase boundaries. These regions,

over a period of time, are likely to proceed from a metastable state to a more ordered phase. As a result, the eutectic decomposes into a mixture of the two individual phases. Both sources of physical instability may ultimately alter the physicochemical properties of the product, thereby negating the enhanced aqueous solubility that provided the impetus to engineer the eutectic at the outset of development. Unfortunately, there is a paucity of literature sources pertaining to the stabilization of eutectics, which may be due to: (1) the increased thermodynamic stability of eutectics relative to other solid binary composite systems results in rare occurrences of the aforementioned routes of instability, (2) traditional stabilizing methods are not applicable to eutectics and alternative techniques do not exist, (3) research concerning eutectic-based pharmaceutical formulations is limited relative to their solid-dispersion counterparts, or (4) a combination of the preceding points.

Appendix B: PXRD and PDF Analyses

All powder X-ray diffraction (PXRD) patterns were obtained using an X'Pert Pro MPD system (PANalytical B.V., Almelo, the Netherlands) equipped with a copper anode (λ = 1.5406 Å), an auxiliary elliptical mirror, and X'Celerator^{TM} detector. The operational voltage and amperage were set to 45.0 kV and 40.0 mA, respectively. Diffraction patterns were acquired on intact samples, sandwiched between two layers of Kapton® film and subsequently placed on a spinning vertical sample stage (16 rpm). Experimental parameters include an irradiation time of 51.04 seconds per step and an angular step size of 0.017° 2θ over a 2-100° 2θ range. From raw powder patterns, if co-solidified products displayed Bragg diffraction peaks, no PDF analysis was carried out due to the obvious indication of partial crystallinity. Indexed PXRD patterns only are shown for compounds exhibiting this level of phase separation.

A number of corrections are made to raw diffraction data to obtain a structure function consistent with those outlined by Egami and Billinge.[38] All intensity corrections and PDF calculations were performed using software developed in-house in the Matlab programming environment (v7.1, MathWorks, Natick, MA) based on published equations. The PDF transforms were optimized using the G_{low} quality criterion introduced by Peterson, *et al*.[41]

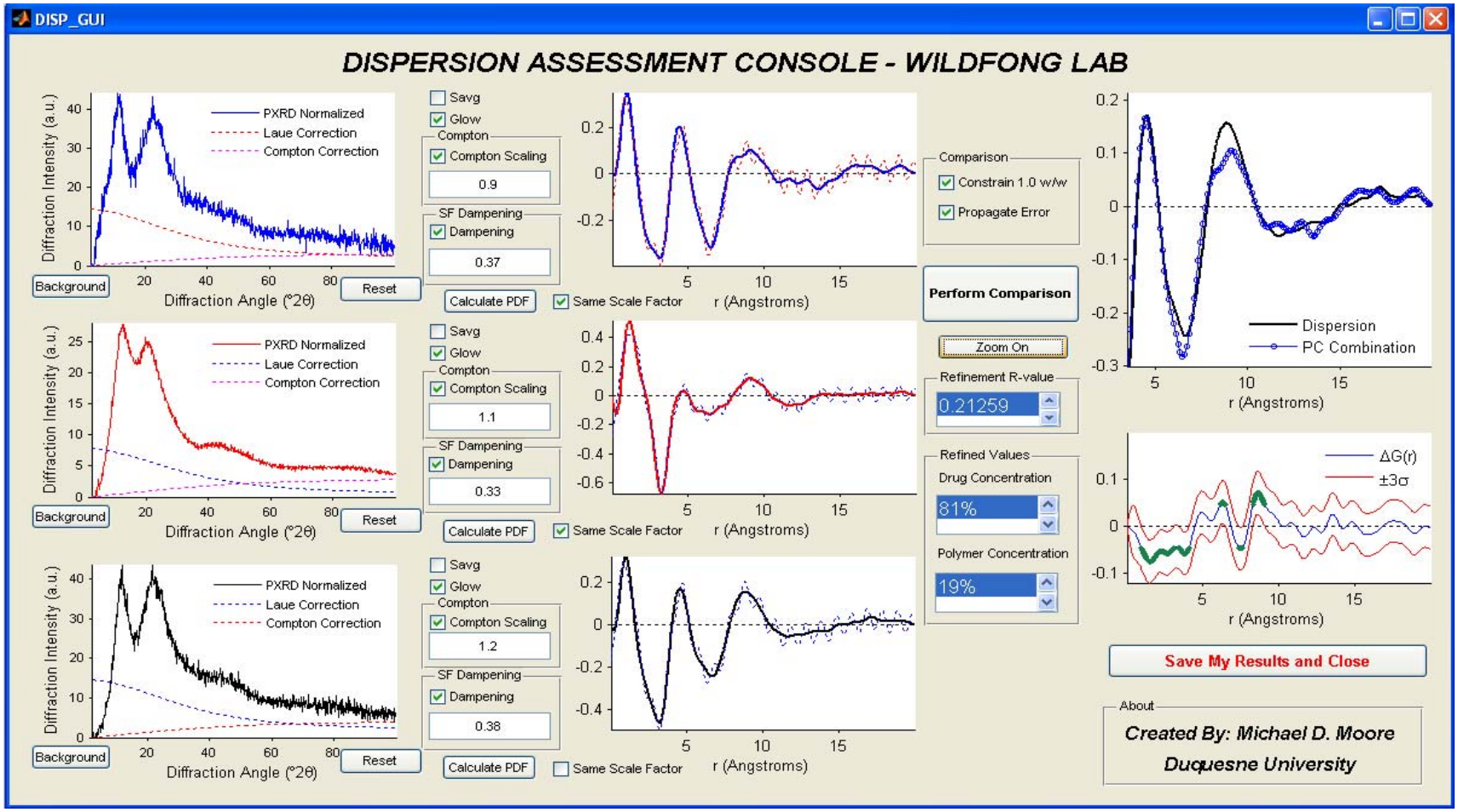

Figure B.1. The PDF assessment for felodpine:PVPva co-solidified product; left three graphs are corrected PXRD patterns for: (top to bottom) drug, polymer, and co-solidified product; center three graphs are the respective PDF transformations; right portion of illustration is the actual analysis, as labeled. Due to the lack of agreement between the calculated PDF and co-solidified product PDF as evidenced by the high R-value, drug and polymer concentration values that deviate from theory, and the regions in *r* where zero is not contained in the confidence interval, felodipine and PVPva are concluded to be completely miscible.

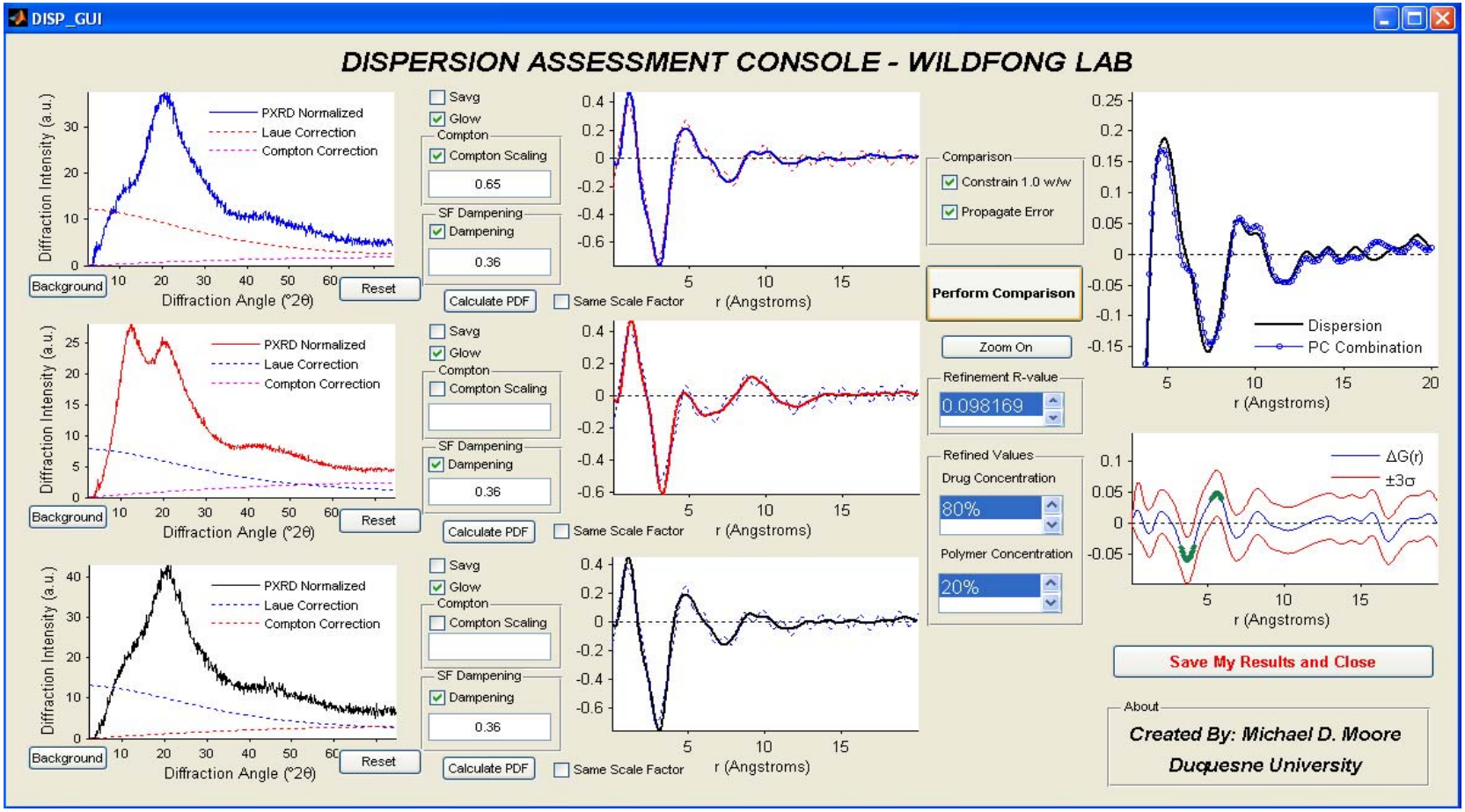

Figure B.2. The PDF assessment for indomethacin:PVPva co-solidified product; left three graphs are corrected PXRD patterns for: (top to bottom) drug, polymer, and co-solidified product; center three graphs are the respective PDF transformations; right portion of illustration is the actual analysis, as labeled. Due to the lack of agreement between the calculated PDF and co-solidified product PDF as evidenced by drug and polymer concentration values that deviate from theory and the regions in *r* where zero is not contained in the confidence interval, indomethacin and PVPva are concluded to be completely miscible.

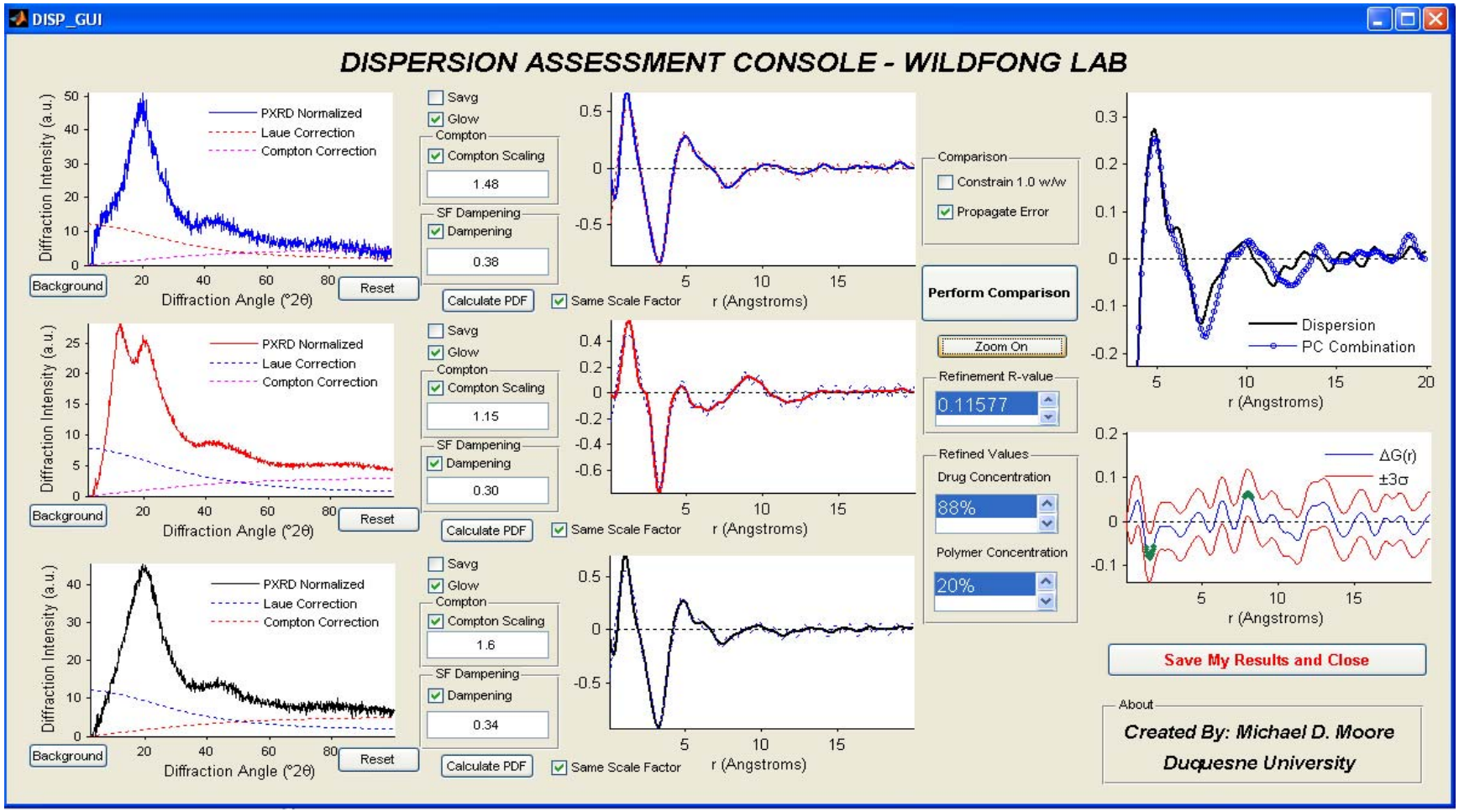

Figure B.3. The PDF assessment for ketoconazole:PVPva co-solidified product; left three graphs are corrected PXRD patterns for: (top to bottom) drug, polymer, and co-solidified product; center three graphs are the respective PDF transformations; right portion of illustration is the actual analysis, as labeled. Due to the lack of agreement between the calculated PDF and co-solidified product PDF as evidenced by the high R-value, drug and polymer concentration values that deviate from theory, and the regions in *r* where zero is not contained in the confidence interval, ketoconazole and PVPva are concluded to be completely miscible.

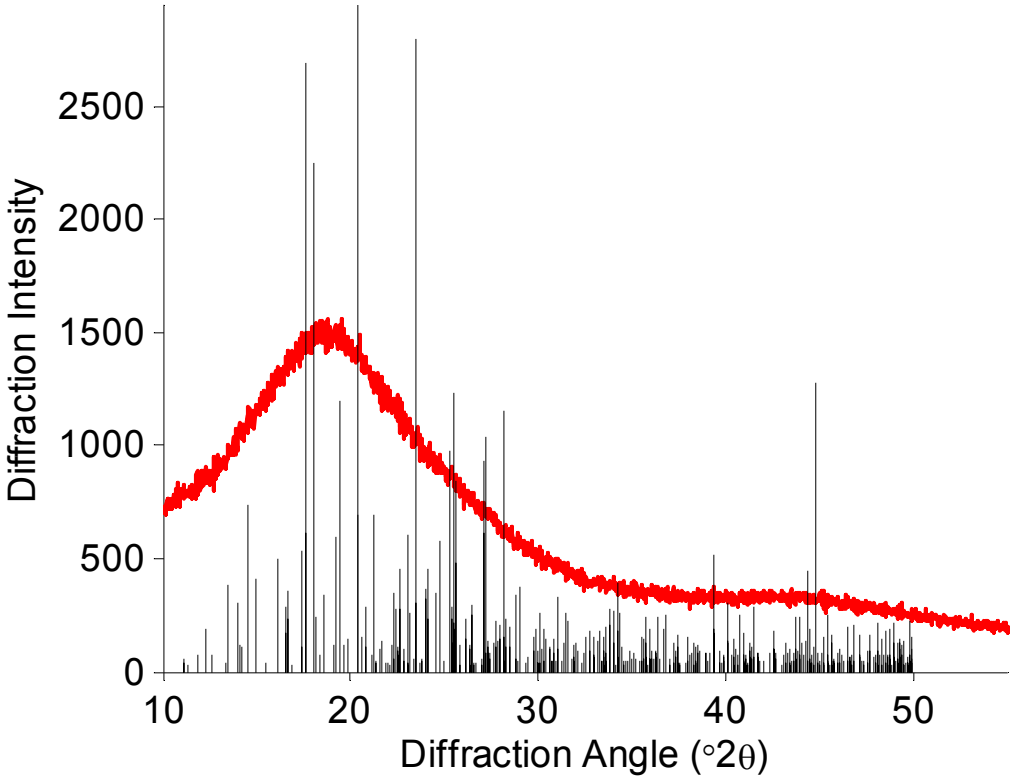

Figure B.4. Raw powder X-ray diffraction pattern for the itraconazole:PVPva co-solidified product. Black delta peaks are indicative of the referenced Bragg intensity values for itraconazole (CSD reference code: TEHZIP). The PXRD pattern of the co-solidified product does not contain any Bragg peaks attributable to crystalline itraconazole. Since the PDF analysis was not performed due to inability to produce amorphous itraconazole, conclusions were made from PXRD and DSC data (**Appendix C**) only. Itraconazole was concluded to be completely miscible with PVPva due to lack of detectable crystallinity in PXRD data and a single detectable T_g from DSC.

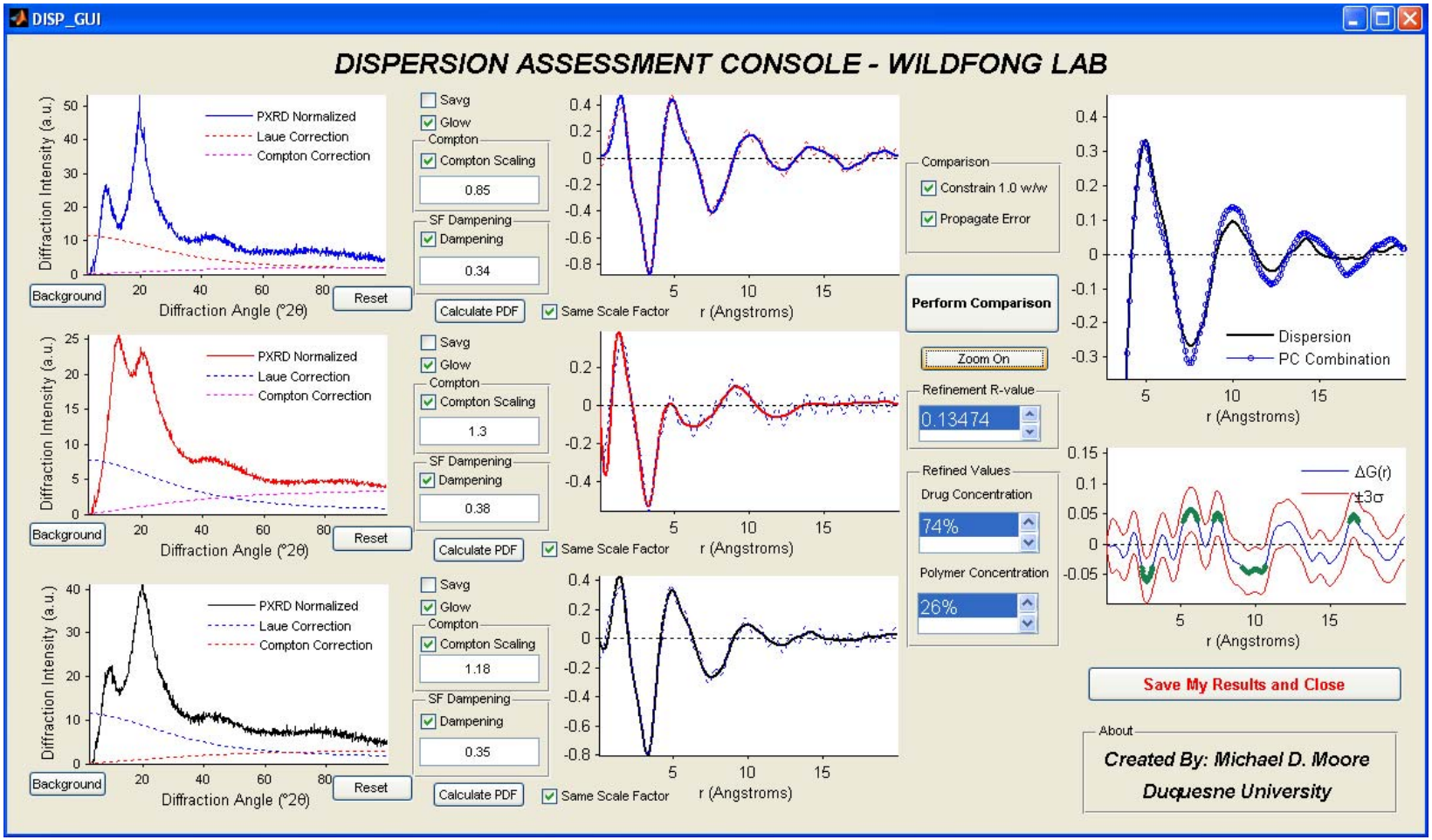

Figure B.5. The PDF assessment for tolbutamide:PVPva co-solidified product; left three graphs are corrected PXRD patterns for: (top to bottom) drug, polymer, and co-solidified product; center three graphs are the respective PDF transformations; right portion of illustration is the actual analysis, as labeled. Due to the lack of agreement between the calculated PDF and co-solidified product PDF as evidenced by the high R-value and the regions in *r* where zero is not contained in the confidence interval, tolbutamide and PVPva are concluded to be completely miscible.

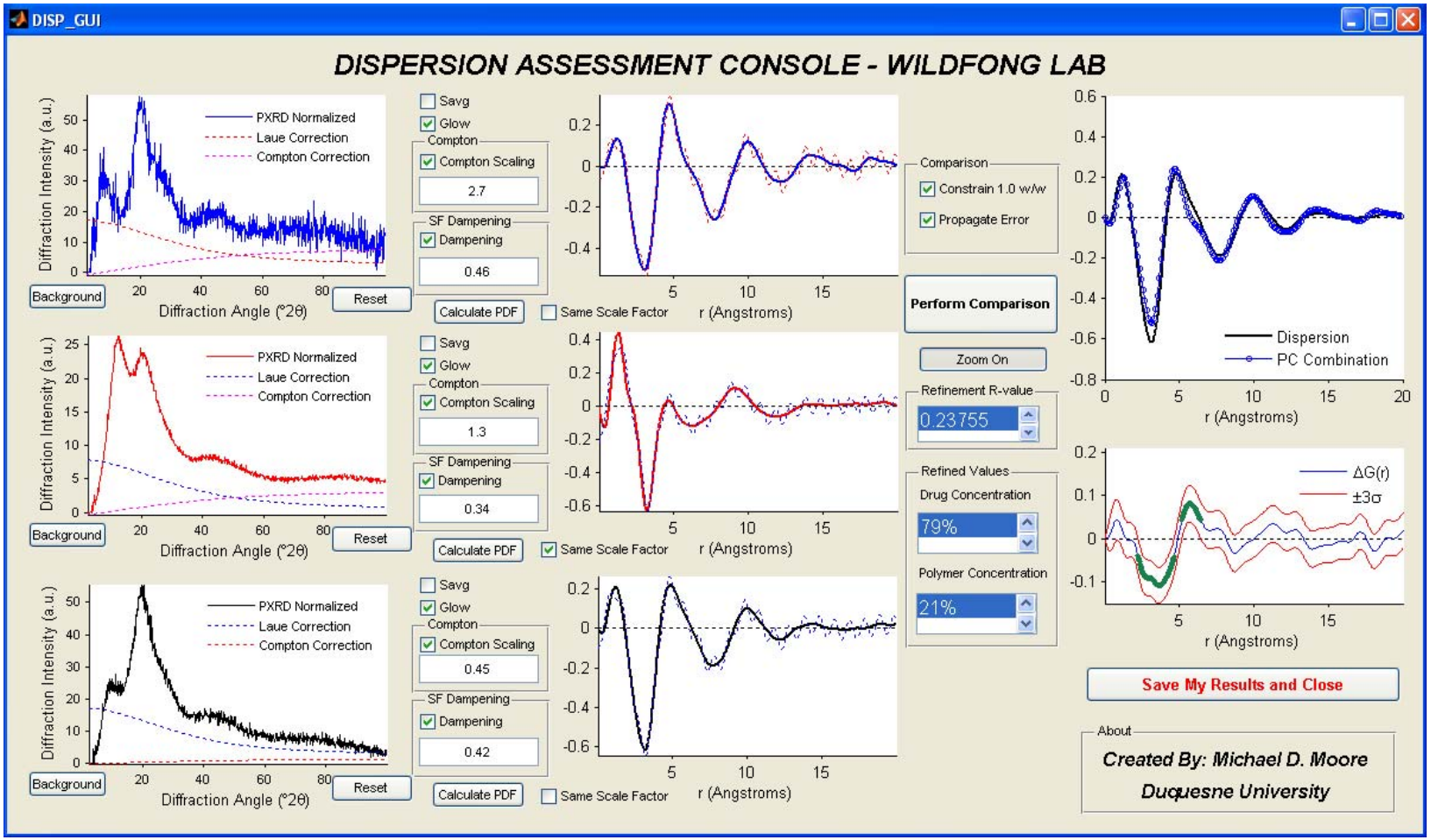

Figure B.6. The PDF assessment for chlorpropamide:PVPva co-solidified product; left three graphs are corrected PXRD patterns for: (top to bottom) drug, polymer, and co-solidified product; center three graphs are the respective PDF transformations; right portion of illustration is the actual analysis, as labeled. Due to the lack of agreement between the calculated PDF and co-solidified product PDF as evidenced by the high R-value, drug and polymer concentration values that deviate from theory, and the regions in *r* where zero is not contained in the confidence interval, chlorpropamide and PVPva are concluded to be completely miscible.

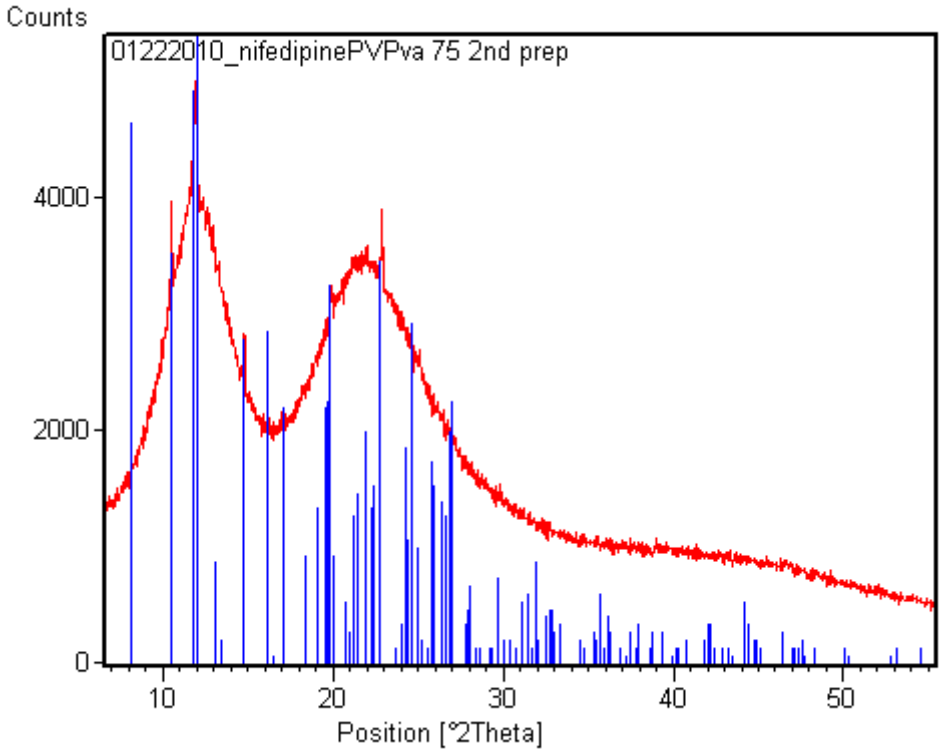

Figure B.7. Raw powder X-ray diffraction pattern for the nifedipine:PVPva co-solidified product. Blue delta peaks are indicative of the referenced Bragg intensity values for crystalline nifedipine (ICDD reference code: 00-052-2175). As shown, detectable partial crystallinity attributable to crystalline nifedipine is present in the co-solidified product.

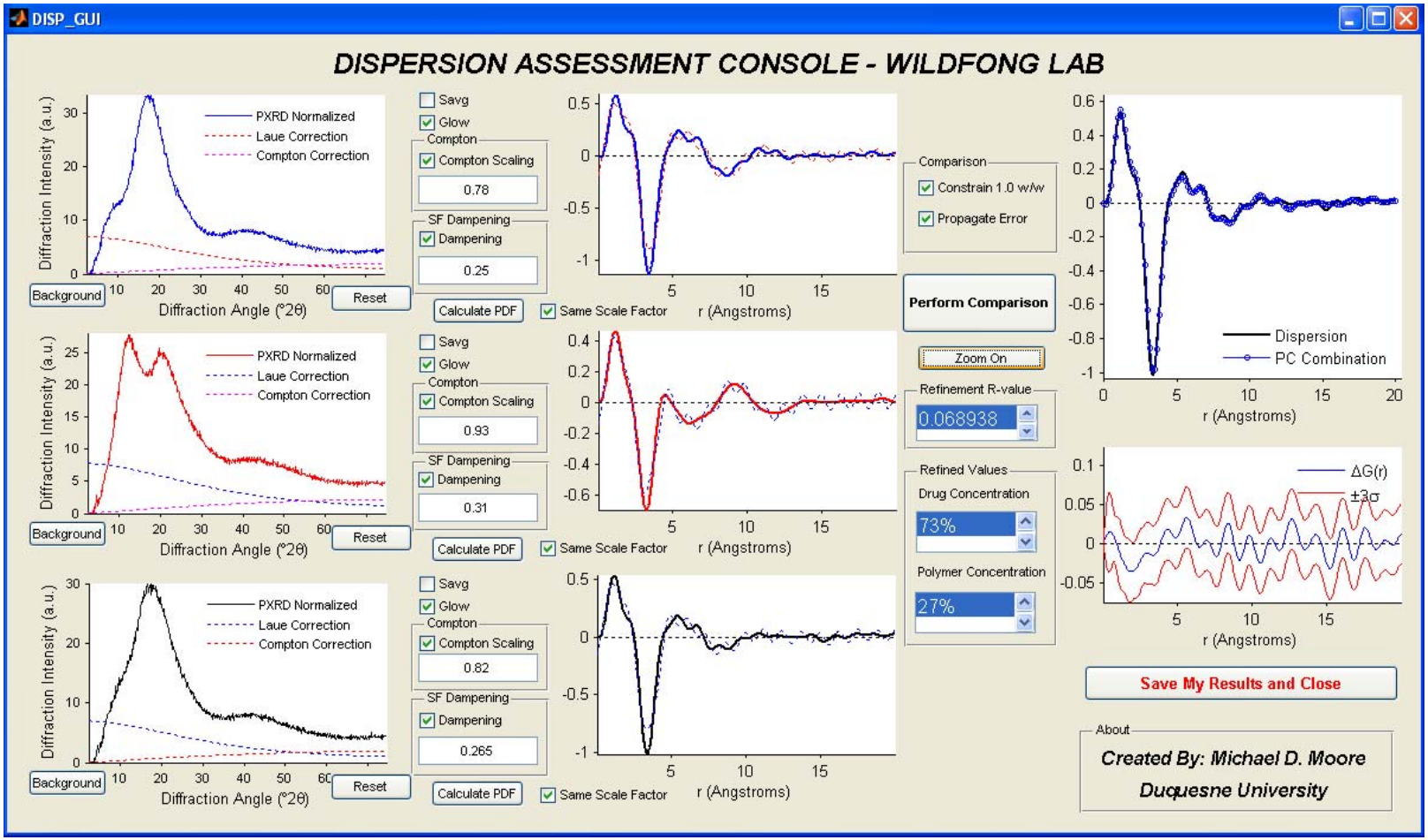

Figure B.8. The PDF assessment for quinidine:PVPva co-solidified product; left three graphs are corrected PXRD patterns for: (top to bottom) drug, polymer, and co-solidified product; center three graphs are the respective PDF transformations; right portion of illustration is the actual analysis, as labeled. Due to the agreement between the calculated PDF and co-solidified product PDF as evidenced by the low R-value, drug and polymer concentration values that are close to theory, and confidence intervals that contain zero for all values of *r*, quinidine and PVPva are concluded to be phase-separated.

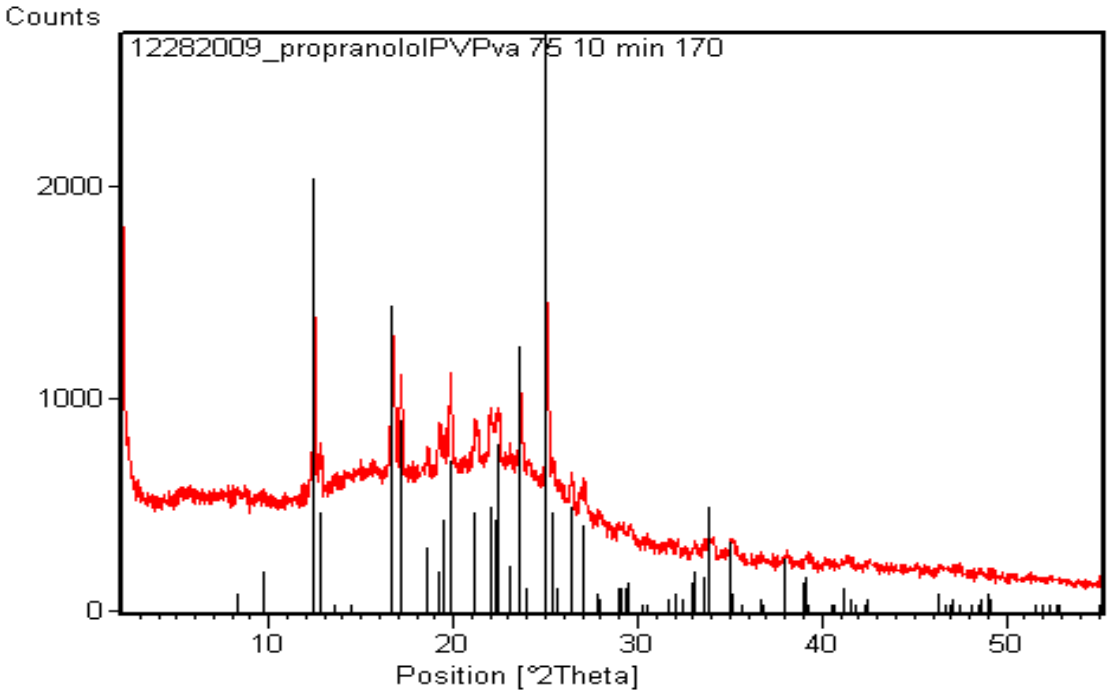

Figure B.9. Raw powder X-ray diffraction pattern for the propranolol:PVPva co-solidified product. Black delta peaks are indicative of the referenced Bragg intensity values for dl-propranolol hydrochloride (ICDD reference code: 00-051-2107). As shown, detectable partial crystallinity attributable to crystalline propranolol is present in the co-solidified product.

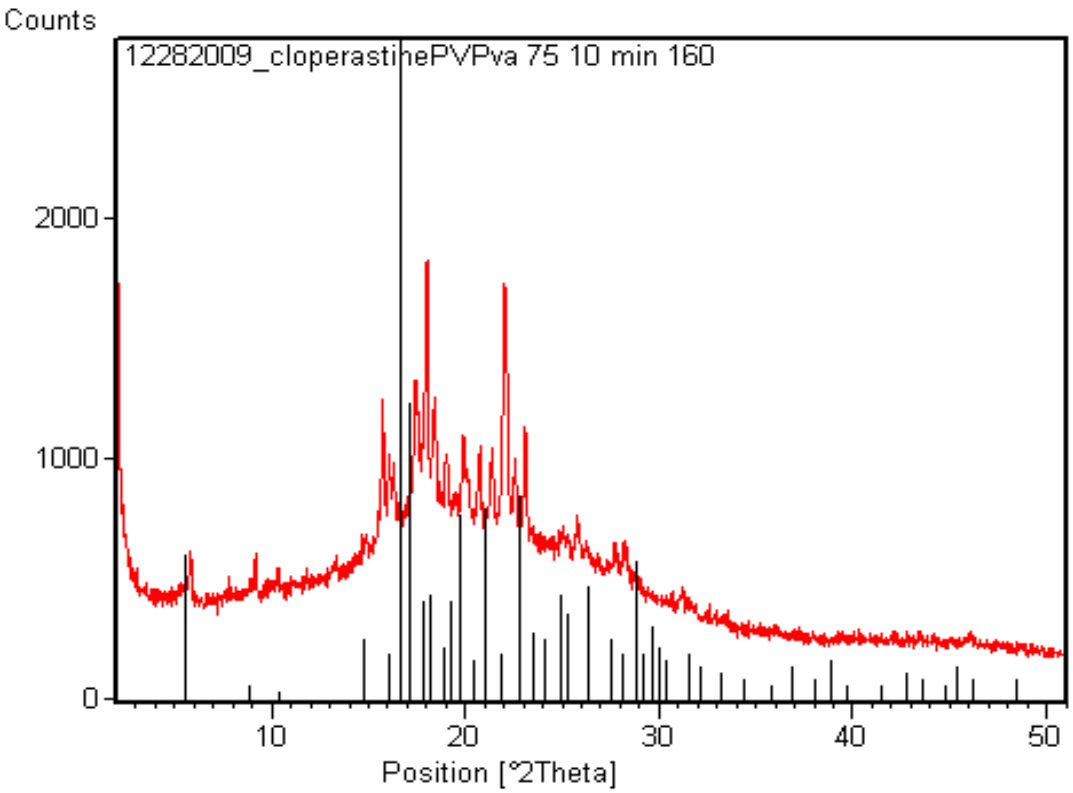

Figure B.10. Raw powder X-ray diffraction pattern for the cloperastine:PVPva co-solidified product. Black delta peaks are indicative of the referenced Bragg intensity values for crystalline cloperastine hydrochloride (ICDD reference code: 00-046-1967). As shown, detectable partial crystallinity, although not indexed to the crystal structure shown, is present in the co-solidified product.

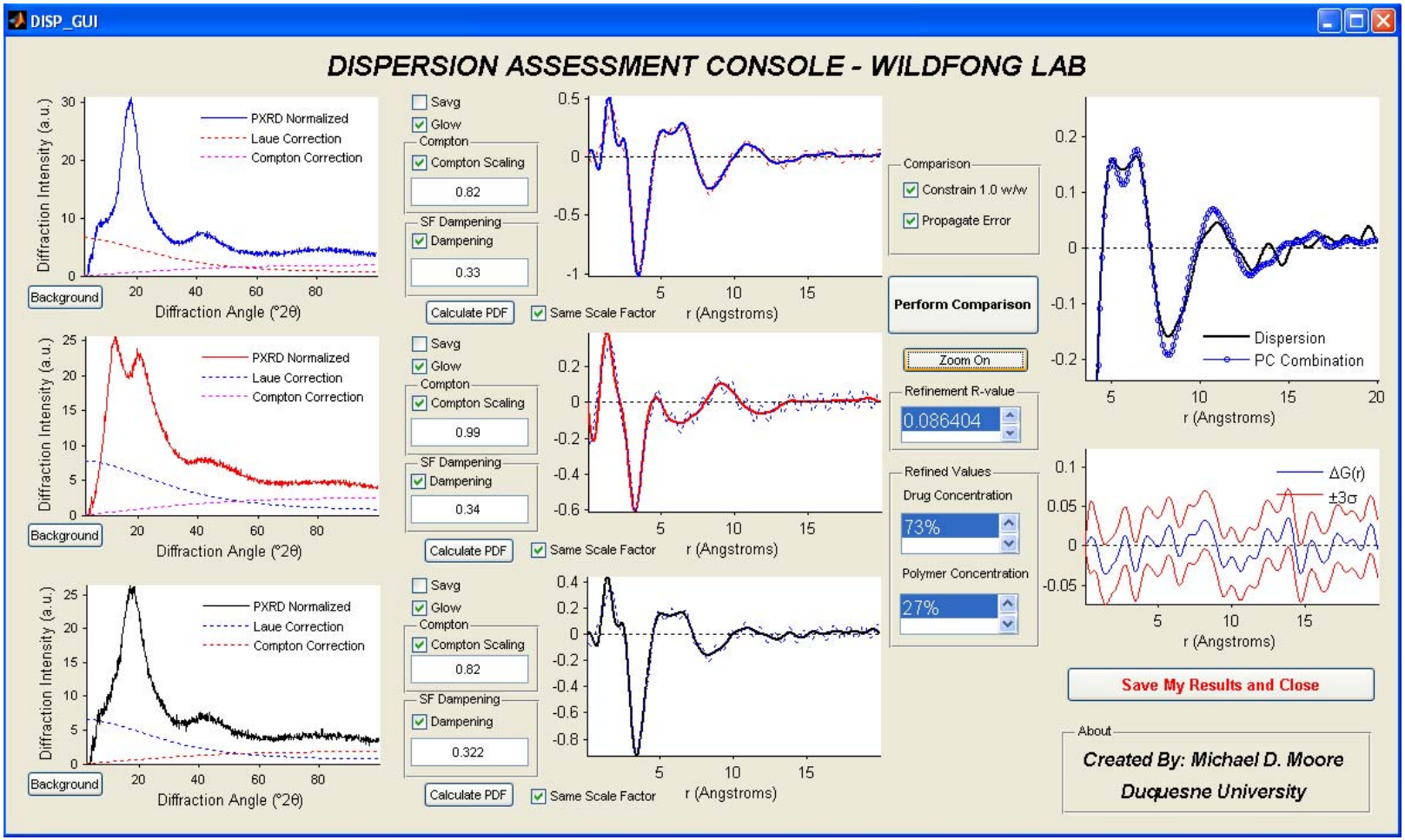

Figure B.11. The PDF assessment for terfenadine:PVPva co-solidified product; left three graphs are corrected PXRD patterns for: (top to bottom) drug, polymer, and co-solidified product; center three graphs are the respective PDF transformations; right portion of illustration is the actual analysis, as labeled. Due to the agreement between the calculated PDF and co-solidified product PDF as evidenced by the low R-value, drug and polymer concentration values that are close to theory, and confidence intervals that contain zero for all values of *r*, terfenadine and PVPva are concluded to be phase-separated.

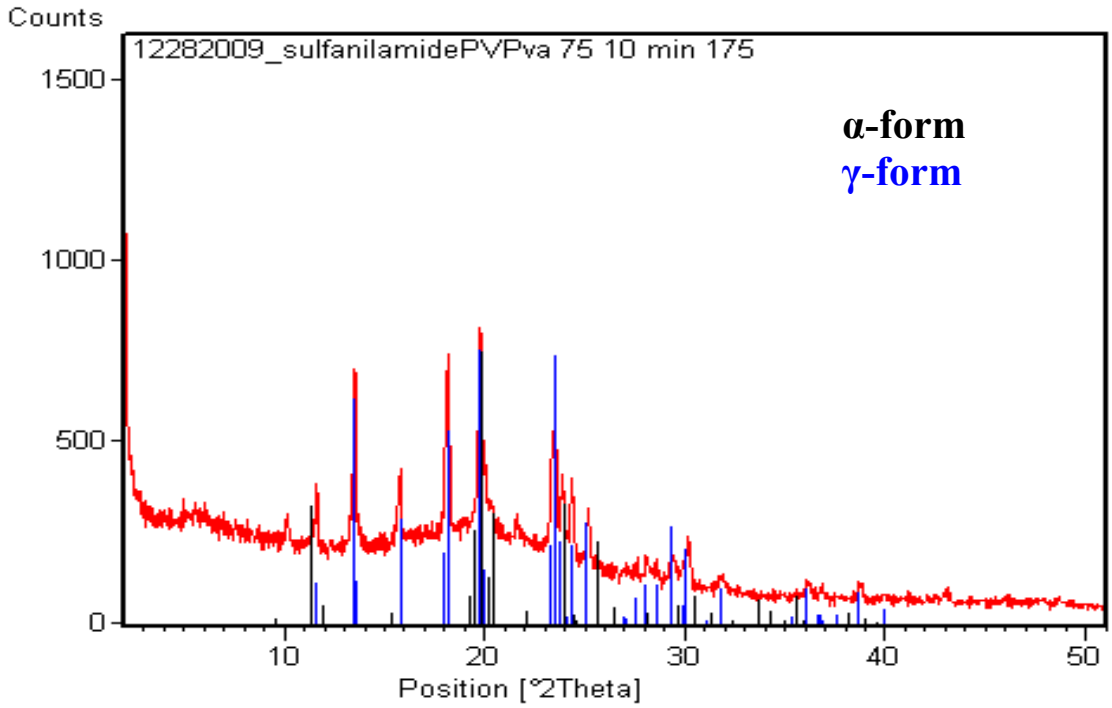

Figure B.12. Raw powder X-ray diffraction pattern for the sulfanilamide:PVPva co-solidified product. Black delta peaks are indicative of the referenced Bragg intensity values for α-sulfanilamide (ICDD reference code: 00-038-1709) and blue delta peaks are for γ-sulfanilamide (ICDD reference code: 00-038-1710). As shown, detectable partial crystallinity attributable to crystalline sulfanilamide is present in the co-solidified product.

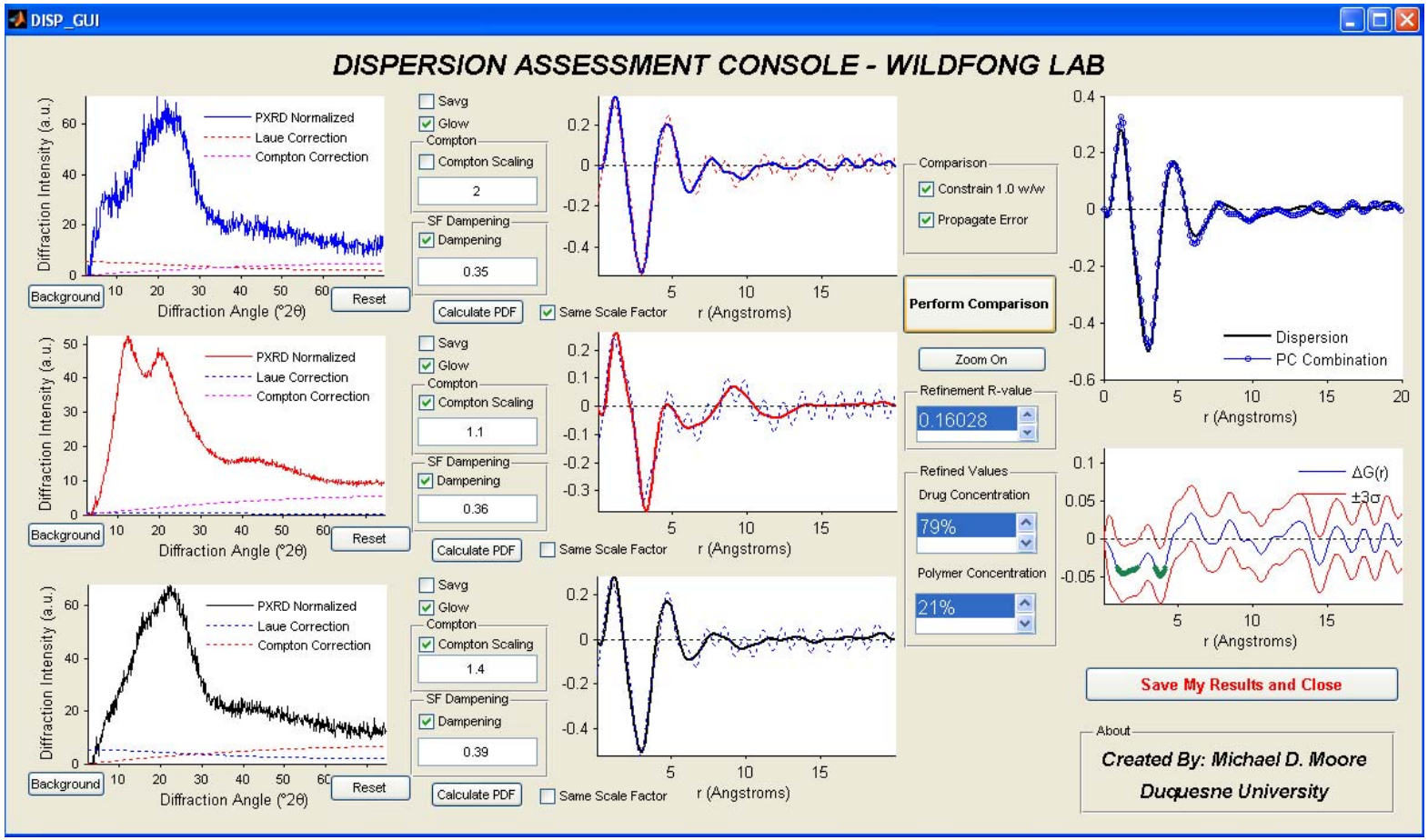

Figure B.13. The PDF assessment for cimetidine:PVPva co-solidified product; left three graphs are corrected PXRD patterns for: (top to bottom) drug, polymer, and co-solidified product; center three graphs are the respective PDF transformations; right portion of illustration is the actual analysis, as labeled. Although the larger *R*-value and regions in *r* where zero is not contained in the confidence interval may indicate a poor fit between the calculated PDF and co-solidified product PDF, the portion of the PDF likely to contain information pertaining to structure (*i.e.* $r \geq 5$Å) exhibits a good fit between the two PDFs and therefore leads to the conclusion that terfenadine and PVPva are phase-separated.

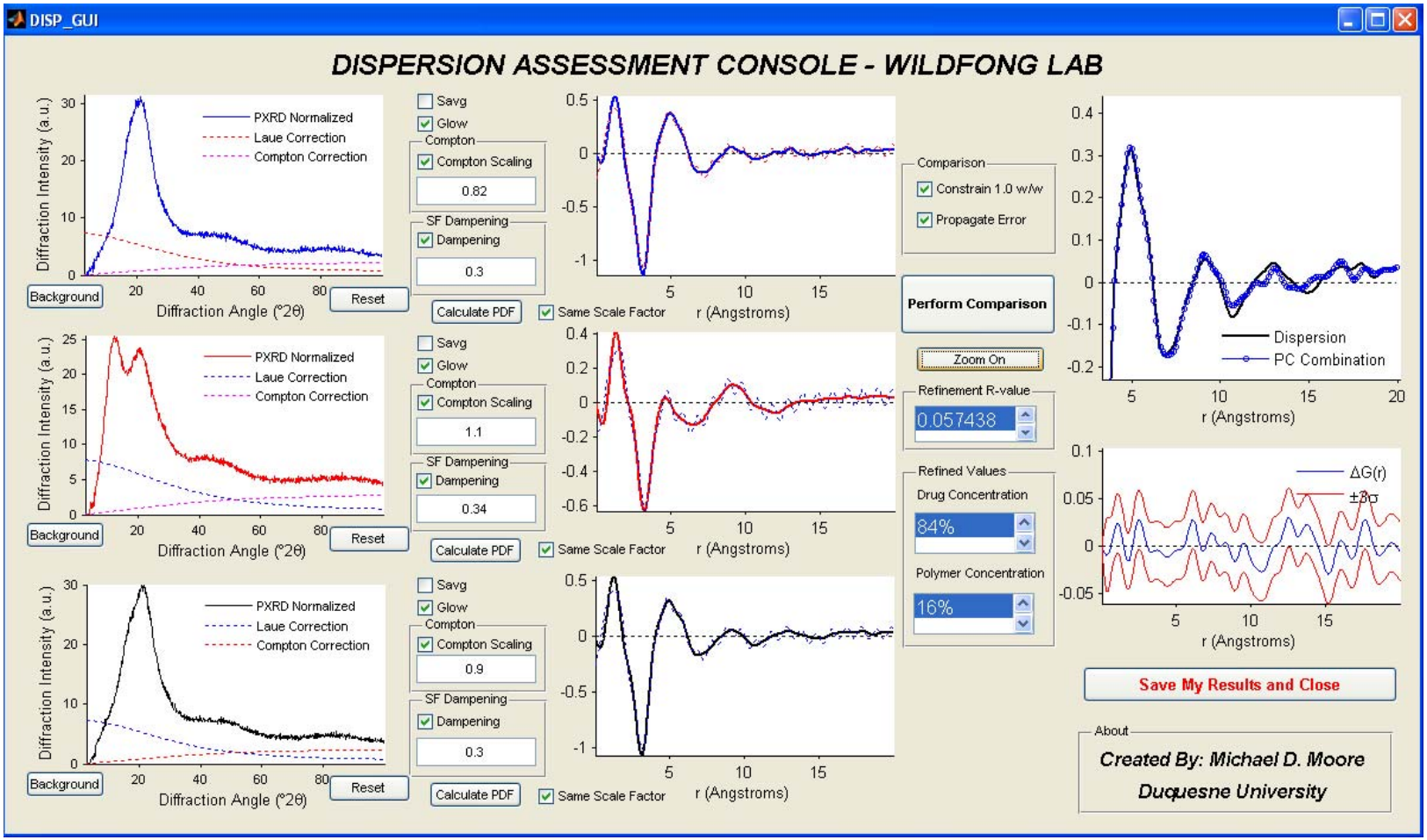

Figure B.14. The PDF assessment for melatonin:PVPva co-solidified product; left three graphs are corrected PXRD patterns for: (top to bottom) drug, polymer, and co-solidified product; center three graphs are the respective PDF transformations; right portion of illustration is the actual analysis, as labeled. Due to the agreement between the calculated PDF and co-solidified product PDF as evidenced by the low R-value, drug and polymer concentration values that are close to theory, and confidence intervals that contain zero for all values of *r*, melatonin and PVPva are concluded to be phase-separated.

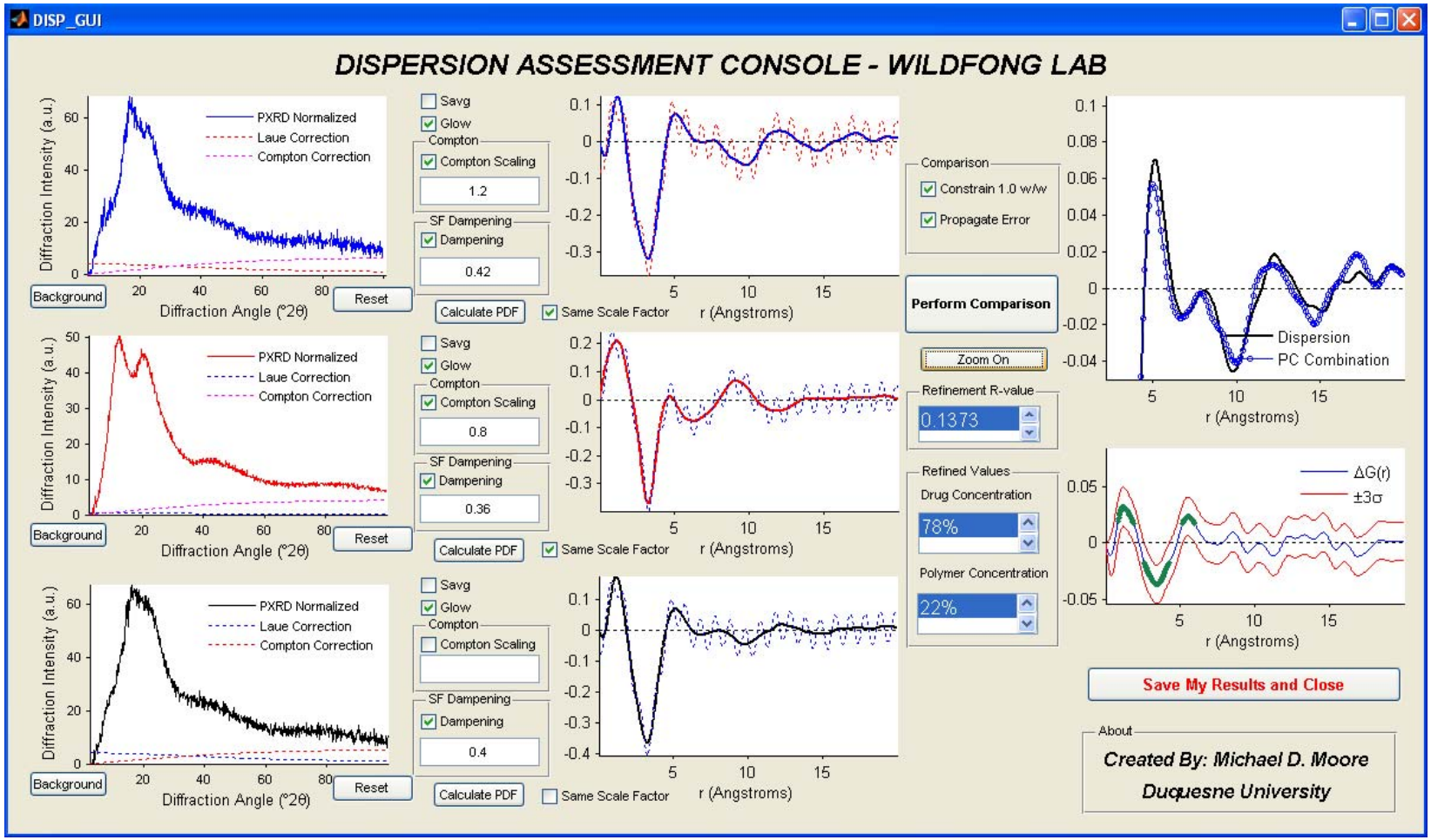

Figure B.15. The PDF assessment for bicalutamide:PVPva co-solidified product; left three graphs are corrected PXRD patterns for: (top to bottom) drug, polymer, and co-solidified product; center three graphs are the respective PDF transformations; right portion of illustration is the actual analysis, as labeled. Due to the lack of agreement between the calculated PDF and co-solidified product PDF as evidenced by the high R-value, drug and polymer concentration values that deviate from theory, and the regions in *r* where zero is not contained in the confidence interval, bicalutamide and PVPva are concluded to be completely miscible.

Appendix C: DSC Analyses

Glass transition temperatures (T_g) for amorphous pure components and co-solidified samples were measured using a TA Q100 DSC (TA Instruments, New Castle, DE) under constant nitrogen purge (~50mL/min). A three-point enthalpy and temperature calibration was performed at 20°C/min using o-terphenyl, indium, and tin standards. In an attempt to avoid artifacts arising from grinding samples, approximately 5 mg intact "sample chips" were hermetically sealed in aluminum pans. To normalize thermal history, samples were first heated at 20 °C/min to 105 °C, held isothermally for 2 minutes, and subsequently cooled to -20°C at 20 °C/min. Samples were then cycled through T_g events at 20 °C/min for temperature determination. In each of the following thermograms, the T_g event for each pure component and T_g for the co-solidified product is shown. For the co-solidified products, only a single cycle is shown, unless otherwise noted. The ideal T_g as calculated using the Couchman-Karasz equation,[85] $T_{g,CK}$, is given in the figure captions where applicable.

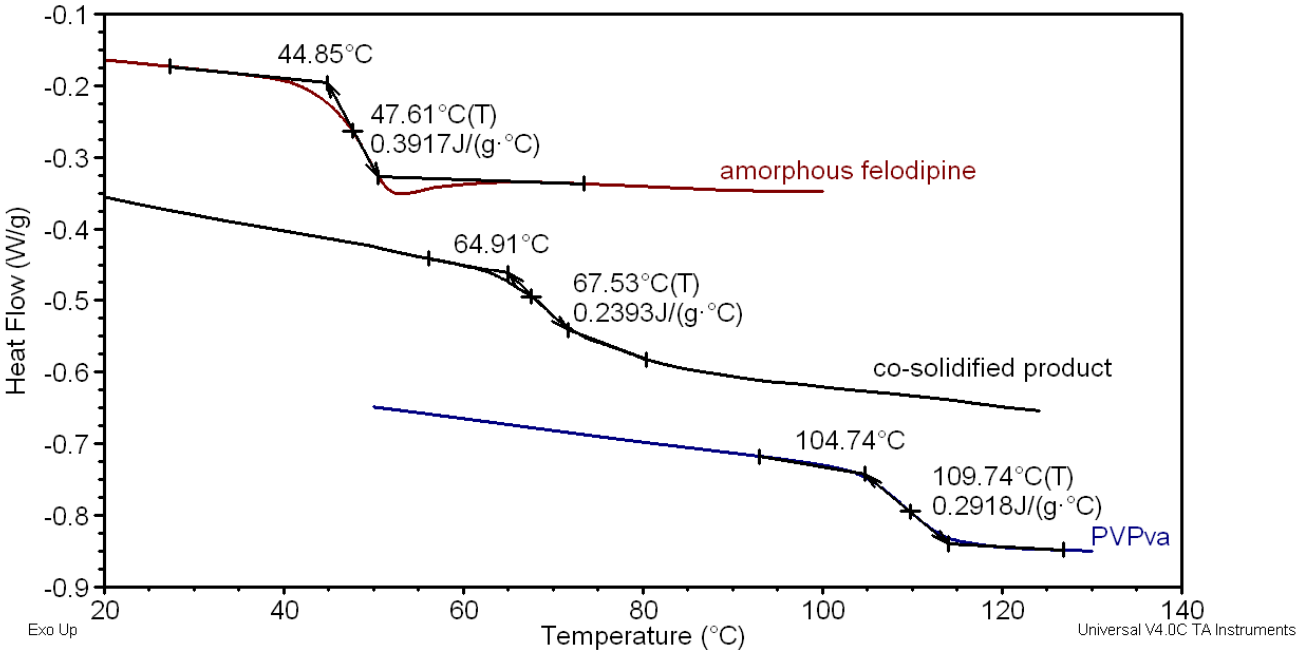

Figure C.1. The DSC thermograms of felodpine:PVPva systems showing the glass transition event for the individual components and co-solidified product (as labeled), where $T_{g,CK}$ = 63.4 °C. The presence of a single T_g in the co-solidified product is indicative of miscibility between felodpine and PVPva.

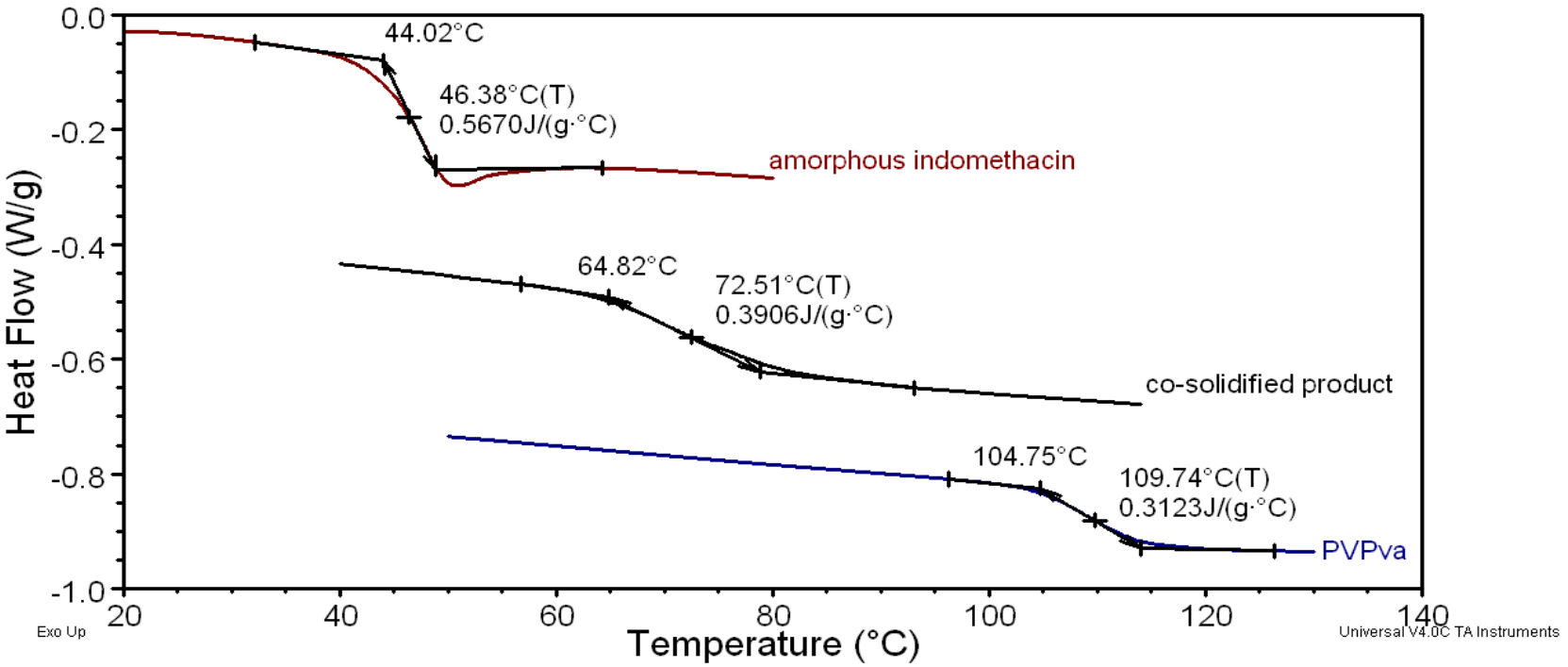

Figure C.2. The DSC thermograms of indomethacin:PVPva systems showing the glass transition event for the individual components and co-solidified product (as labeled) , where $T_{g,CK}$ = 66.9 °C. The presence of a single T_g in the co-solidified product is indicative of miscibility between indomethacin and PVPva.

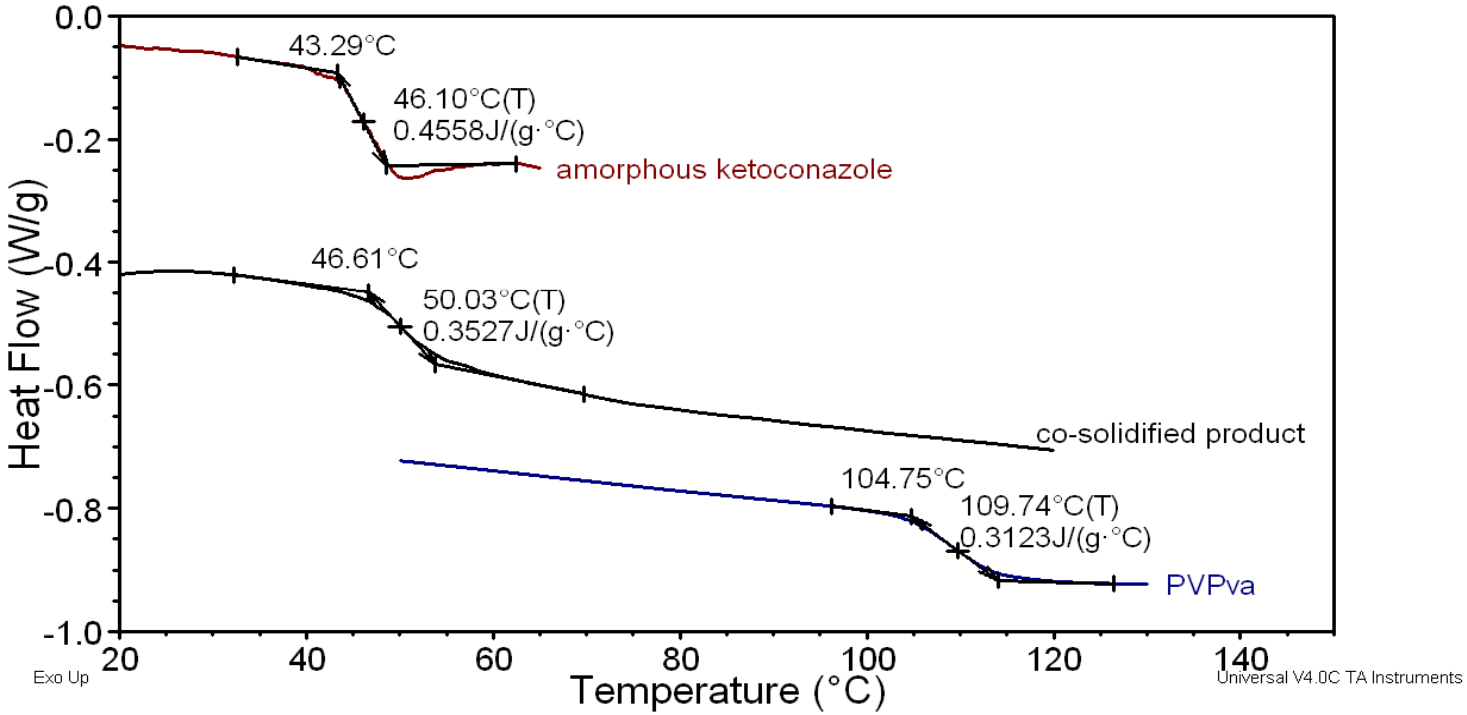

Figure C.3. The DSC thermograms of ketoconazole:PVPva systems showing the glass transition event for the individual components and co-solidified product (as labeled) , where $T_{g,CK}$ = 63.4 °C. The single, detectable T_g in the co-solidified product is similar to that of amorphous ketoconazole and therefore, not definitively interpretable.

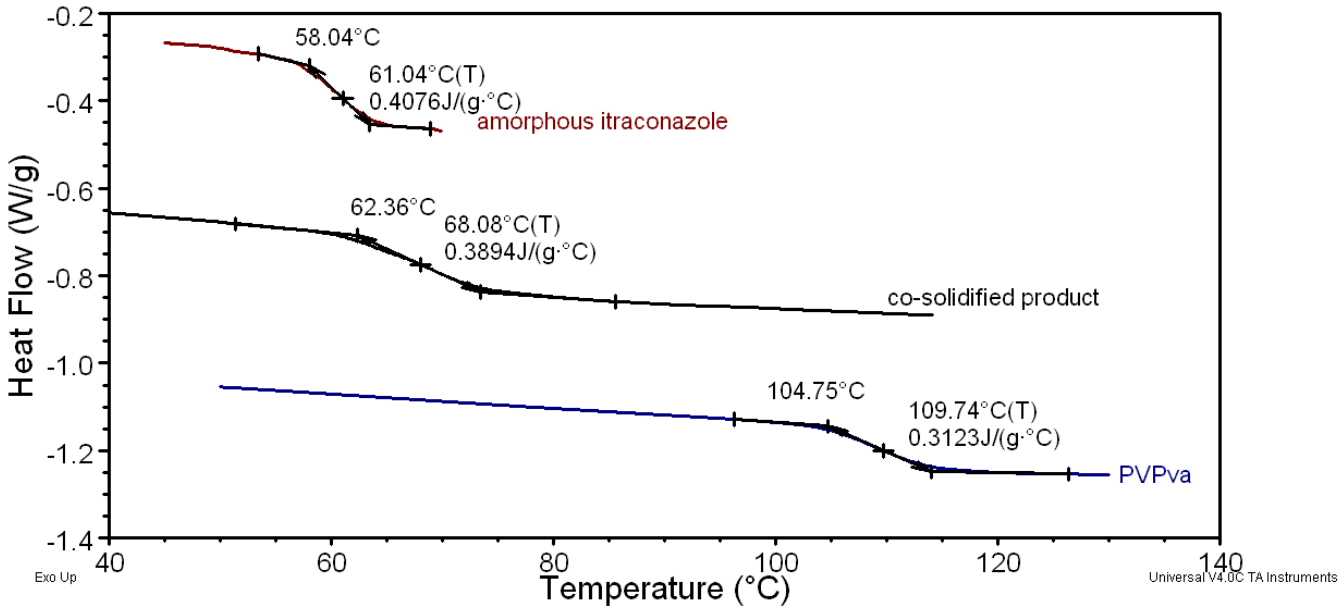

Figure C.4. The DSC thermograms of itraconazole:PVPva systems showing the glass transition event for the individual components and co-solidified product (as labeled) , where $T_{g,CK}$ = 72.2 °C. The single, detectable T_g in the co-solidified product is similar to that of amorphous itraconazole and therefore, not definitively interpretable. Due to the inability to perform a PDF analysis, the repeatability of the T_g across three preparations combined with the lack of detectable Bragg peaks in PXRD patterns provides basis for concluding miscibility between itraconazole and PVPva.

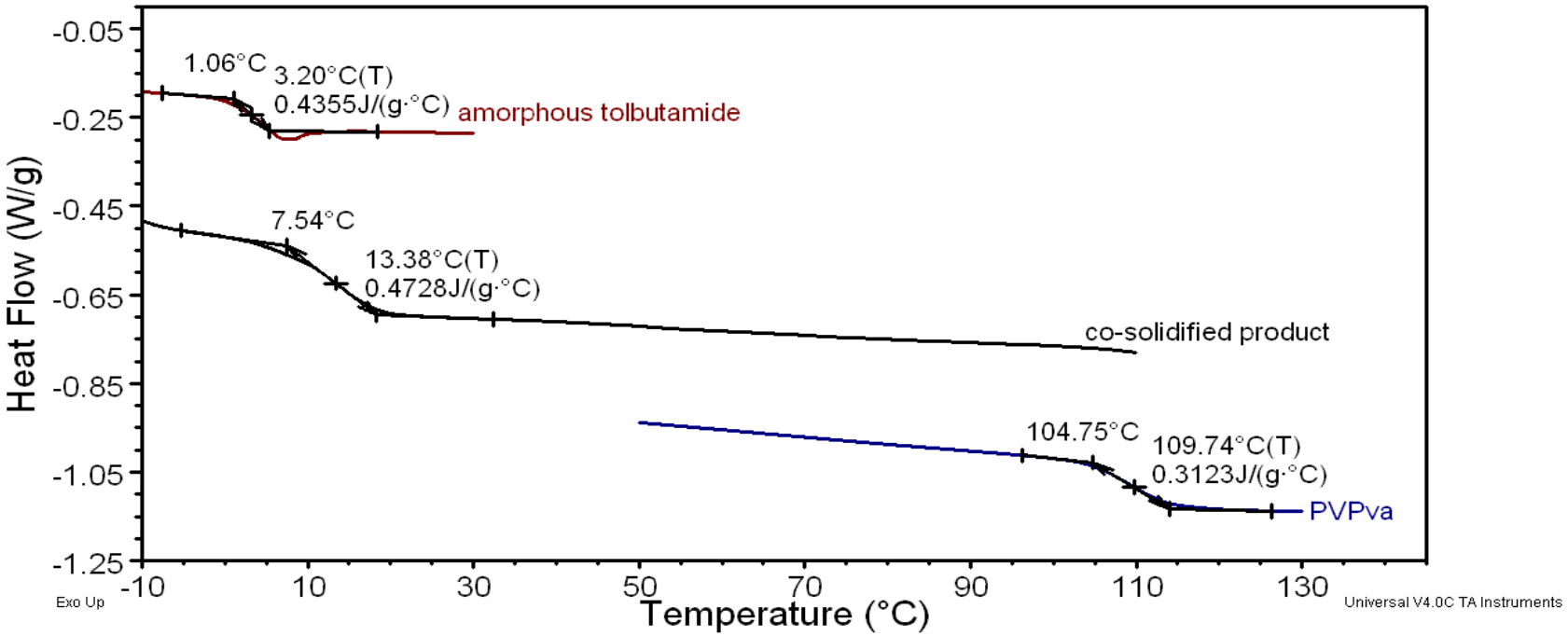

Figure C.5. The DSC thermograms of tolbutamide:PVPva systems showing the glass transition event for the individual components and co-solidified product (as labeled) , where $T_{g,CK}$ = 34.0 °C. The presence of a single, detectable T_g in the co-solidified product is indicative of miscibility between tolbutamide and PVPva.

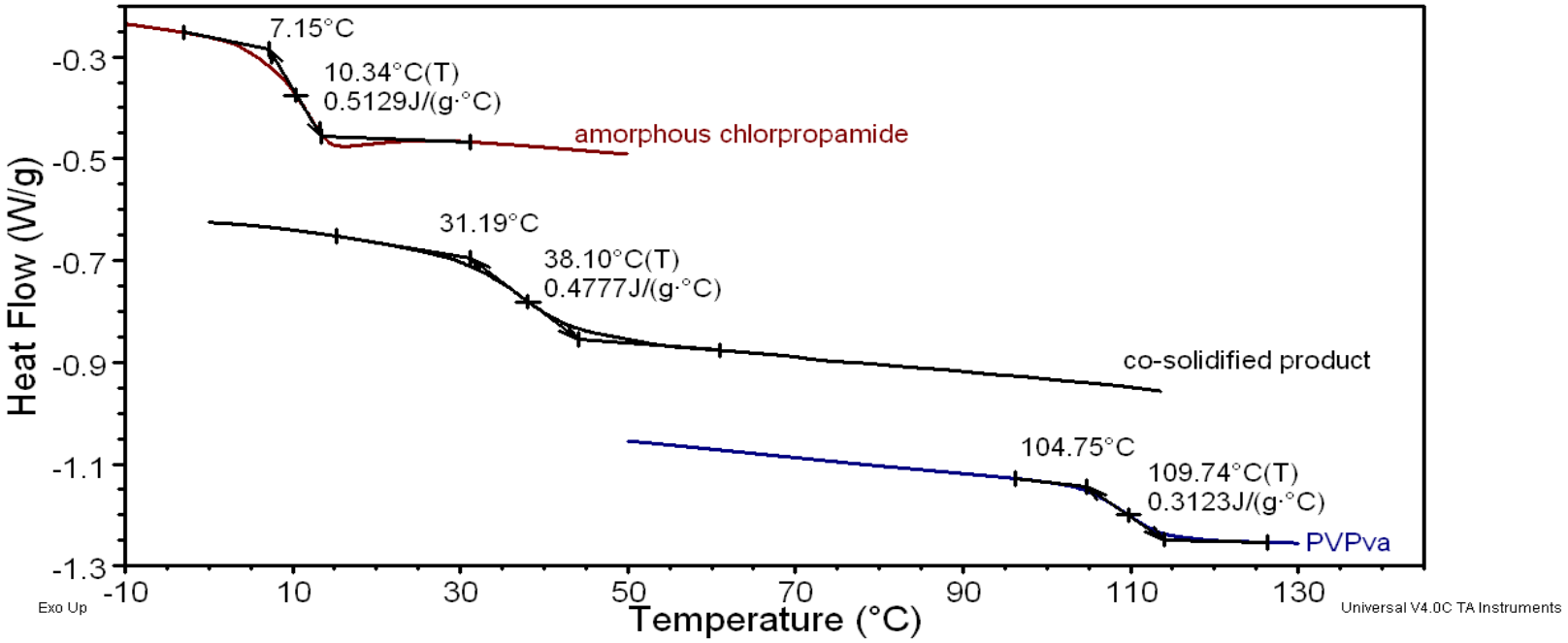

Figure C.6. The DSC thermograms of chlorpropamide:PVPva systems showing the glass transition event for the individual components and co-solidified product (as labeled) , where $T_{g,CK}$ = 41.7 °C. The presence of a single, detectable T_g in the co-solidified product is indicative of miscibility between chlorpropamide and PVPva.

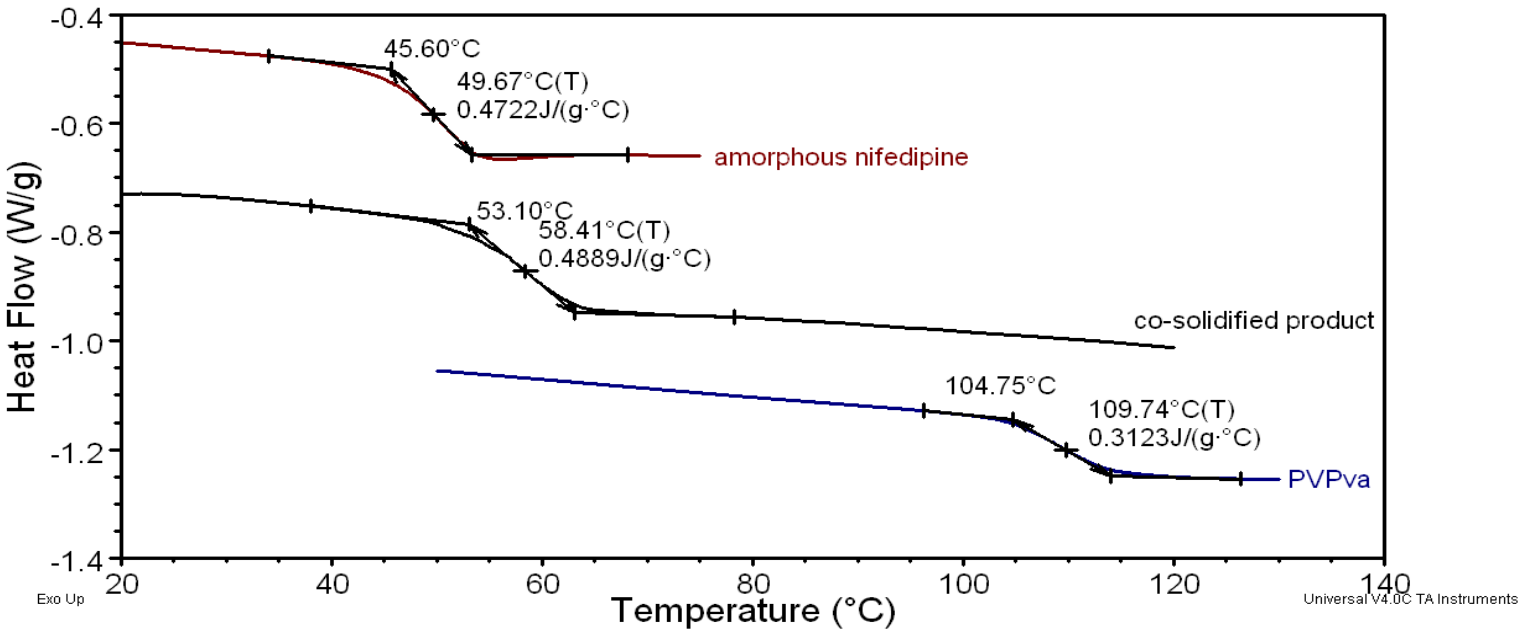

Figure C.7. The DSC thermograms of nifedipine:PVPva systems showing the glass transition event for the individual components and co-solidified product (as labeled) , where $T_{g,CK}$ = 65.4 °C. The presence of a single, detectable T_g in the co-solidified product is indicative of miscibility between chlorpropamide and PVPva; however, the PXRD pattern of the co-solidified product (**Appendix B**) revealed detectable crystallinity attributable to nifedipine.

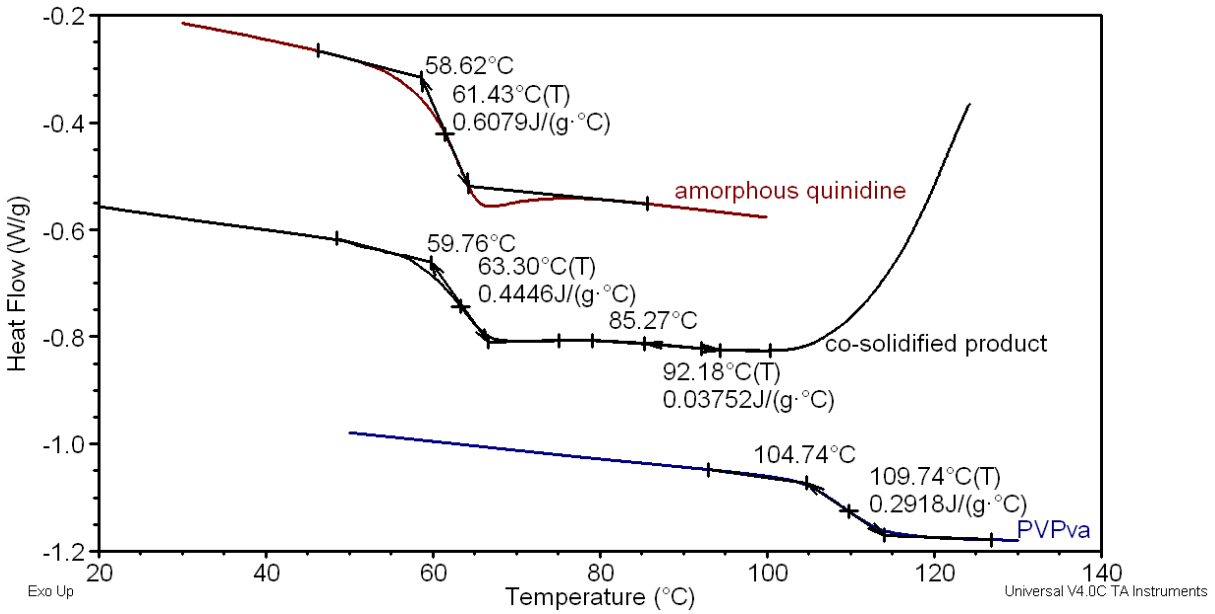

Figure C.8. The DSC thermograms of quinidine:PVPva systems showing the glass transition event for the individual components and co-solidified product (as labeled) , where $T_{g,CK}$ = 76.8 °C. The presence of two T_g events in the co-solidified product is indicative of phase separation.

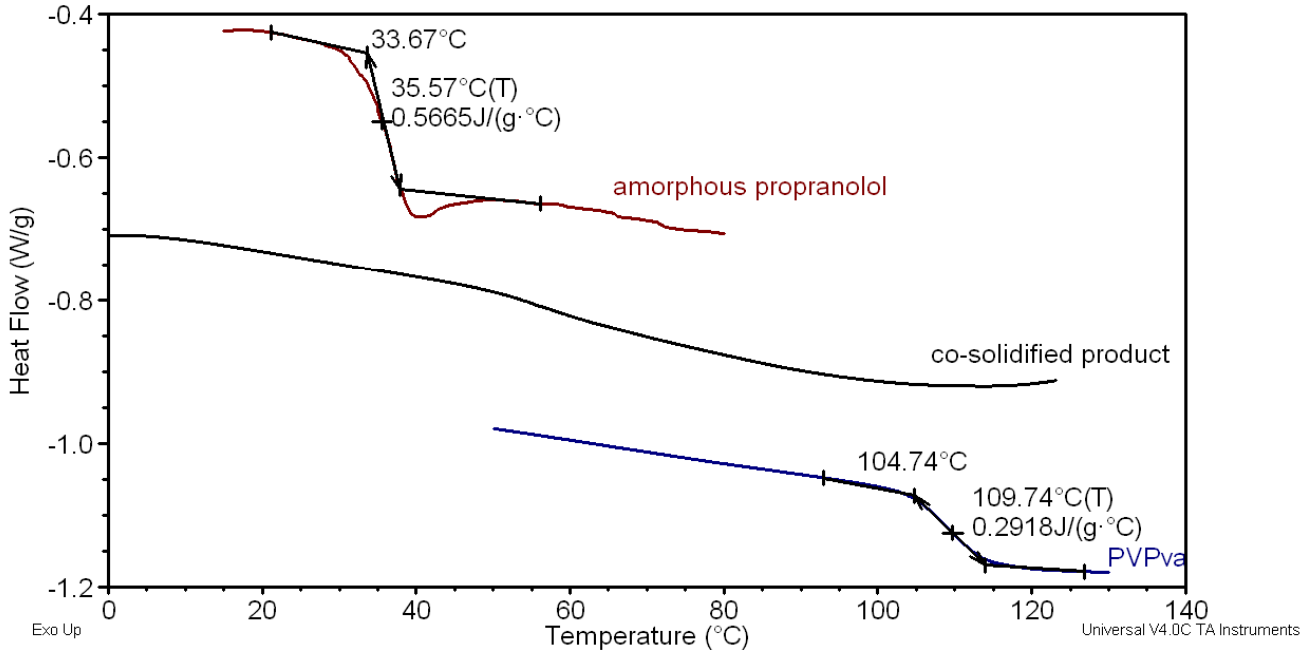

Figure C.9. The DSC thermograms of propranolol:PVPva systems showing the glass transition event for the individual components and co-solidified product (as labeled) , where $T_{g,CK}$ = 60.5 °C. The lack of a detectable T_g in the co-solidified product is indicative undetectable amorphous phase.

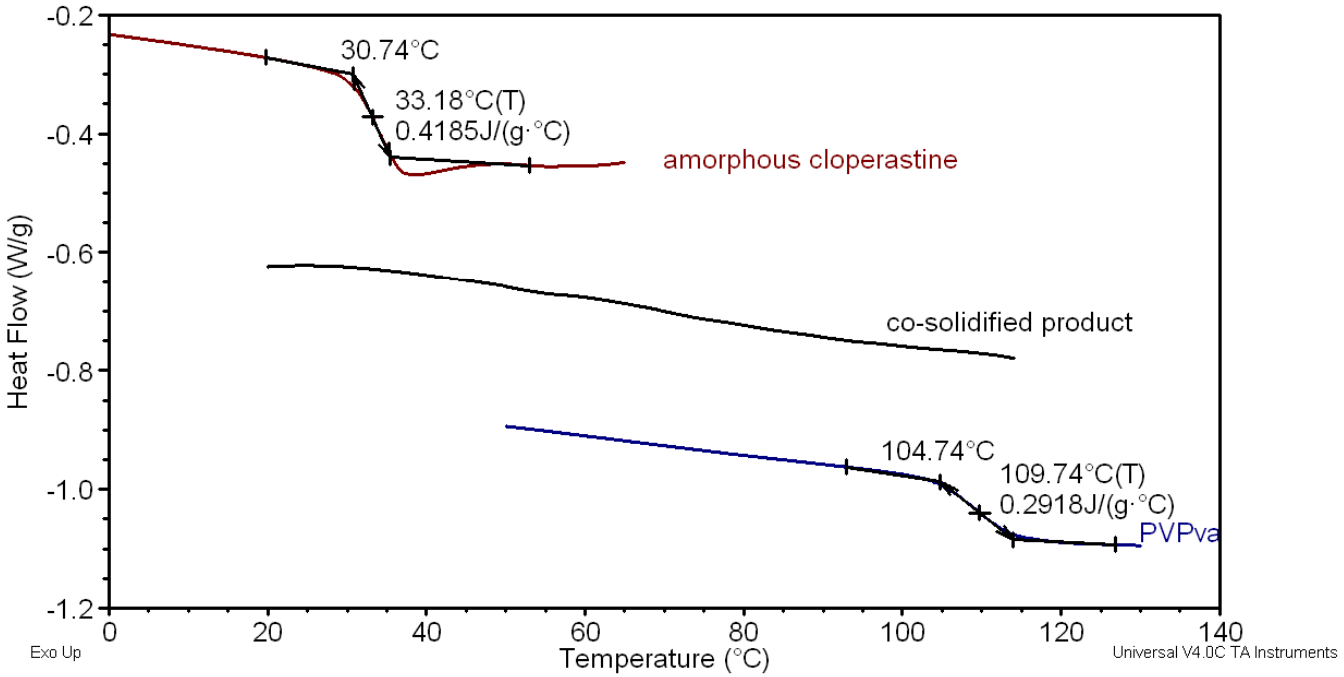

Figure C.10. The DSC thermograms of cloperastine:PVPva systems showing the glass transition event for the individual components and co-solidified product (as labeled) , where $T_{g,CK}$ = 53.6 °C. The lack of a detectable T_g in the co-solidified product is indicative undetectable amorphous phase.

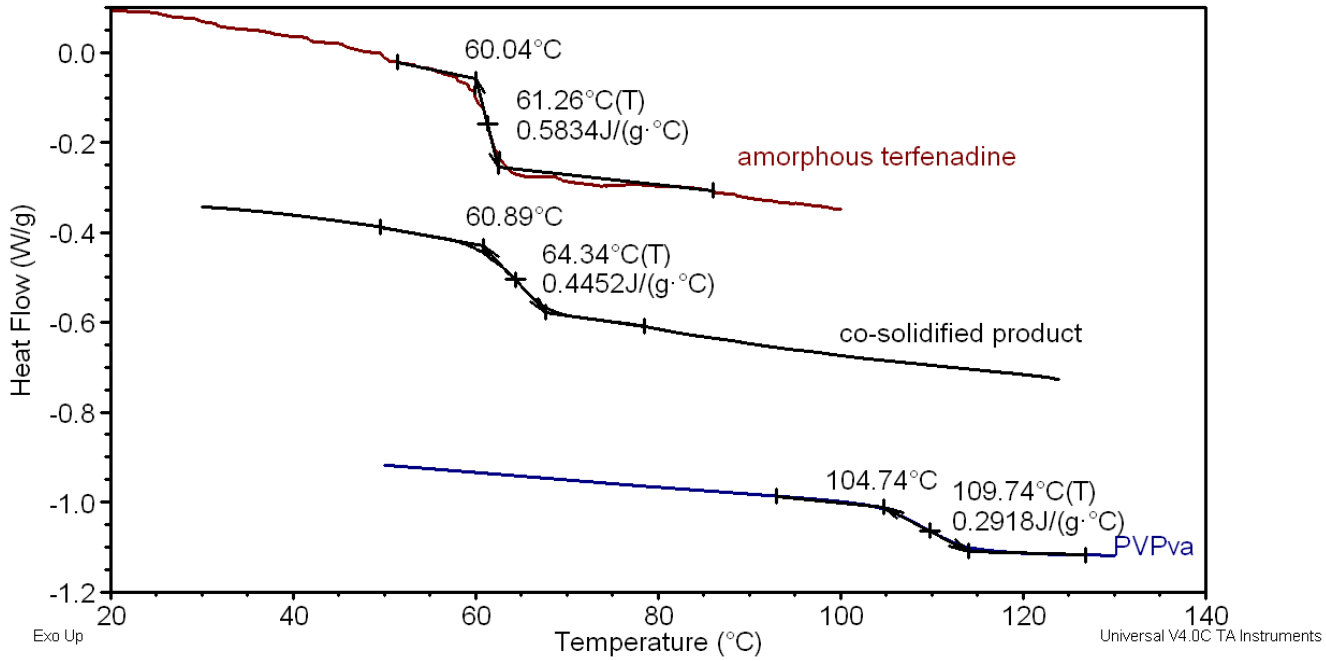

Figure C.11. The DSC thermograms of terfenadine:PVPva systems showing the glass transition event for the individual components and co-solidified product (as labeled) , where $T_{g,CK}$ = 77.2 °C. The single, detectable T_g in the co-solidified product is similar to that of amorphous terfenadine and therefore, not definitively interpretable.

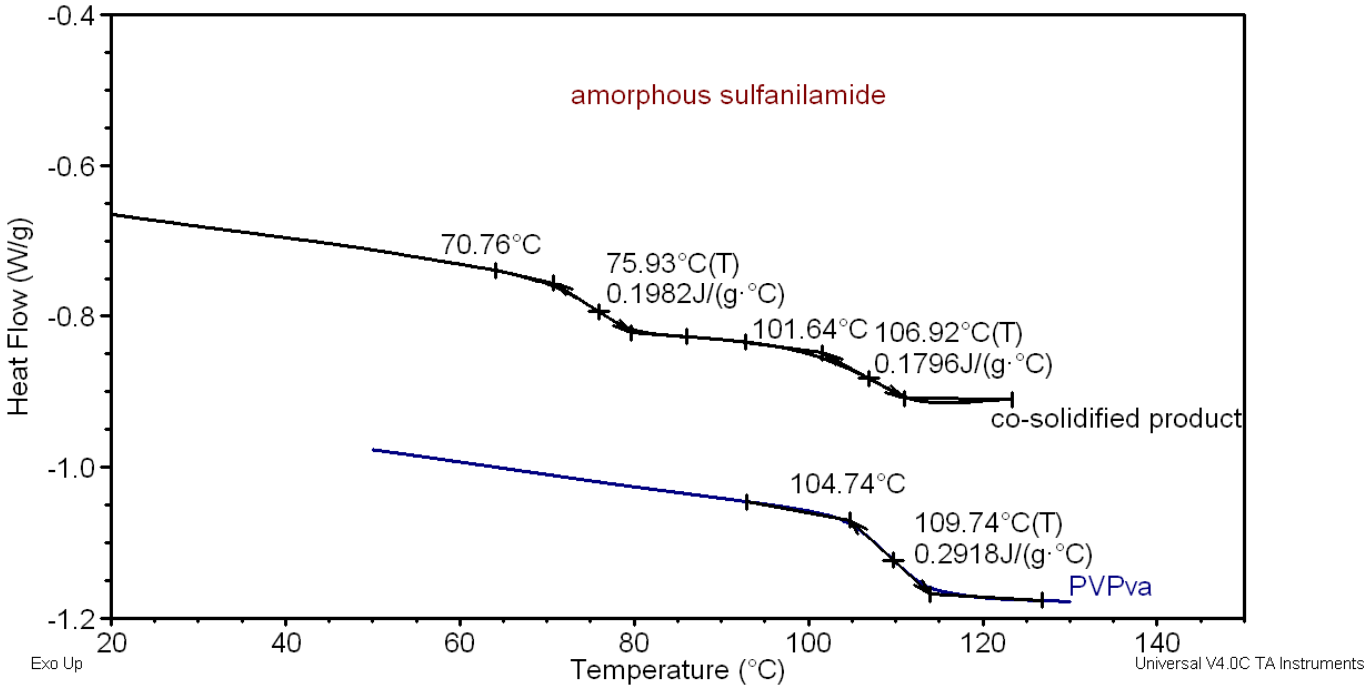

Figure C.12. The DSC thermograms of sulfanilamide:PVPva systems showing the glass transition event for the individual components and co-solidified product (as labeled) , where $T_{g,CK}$ = not obtainable. A thermogram for amorphous sulfanilamide is not shown due to the inability to produce the amorphous phase. The two T_g events in the co-solidified product is indicative of phase separation in the amorphous component of the system. Additionally, detectable crystallinity indexed to sulfanilamide was observed in the PXRD pattern (**Appendix B**) of the co-solidified product.

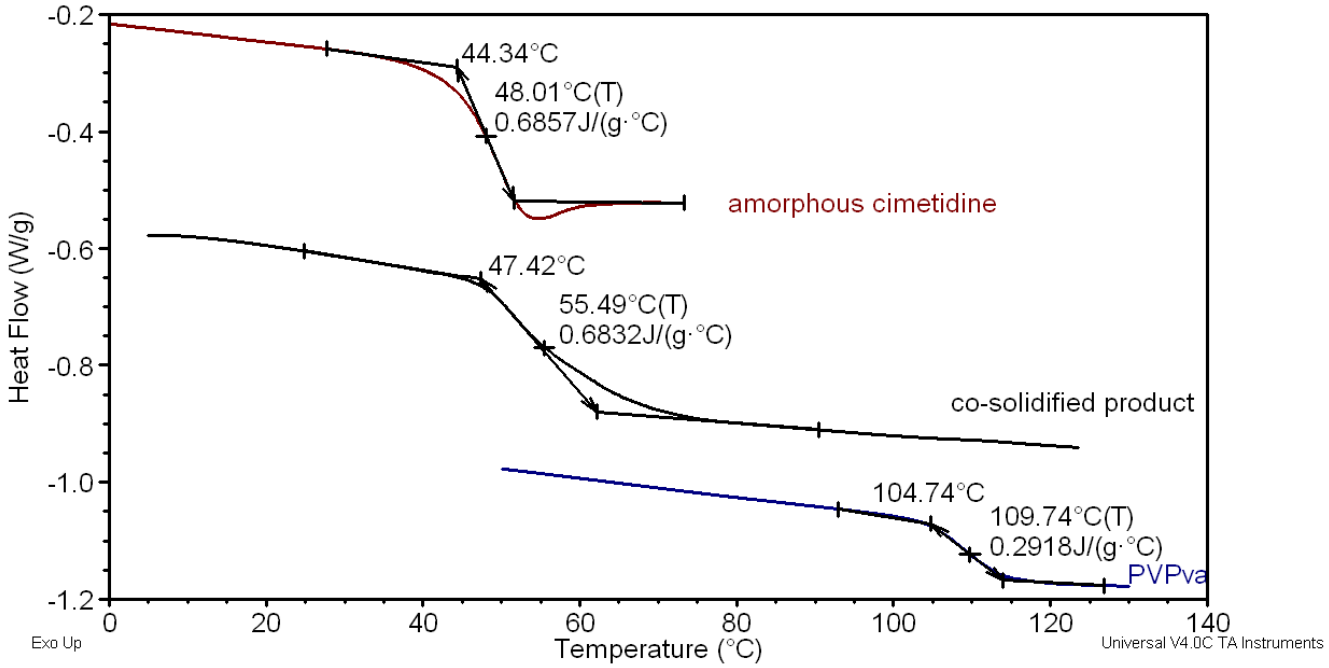

Figure C.13. The DSC thermograms of cimetidine:PVPva systems showing the glass transition event for the individual components and co-solidified product (as labeled) , where $T_{g,CK}$ = 69.9 °C. The single, detectable T_g in the co-solidified product is similar to that of amorphous cimetidine and therefore, not definitively interpretable.

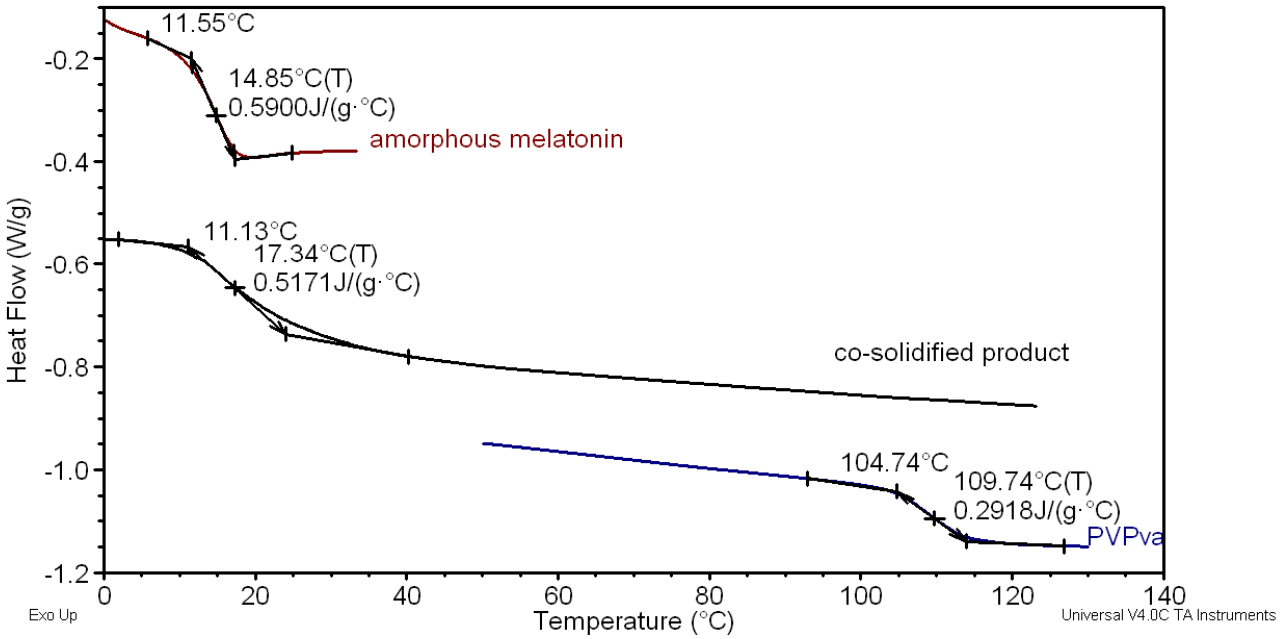

Figure C.14. The DSC thermograms of melatonin:PVPva systems showing the glass transition event for the individual components and co-solidified product (as labeled) , where $T_{g,CK}$ = 47.6 °C. The single, detectable T_g in the co-solidified product is similar to that of amorphous melatonin and therefore, not definitively interpretable

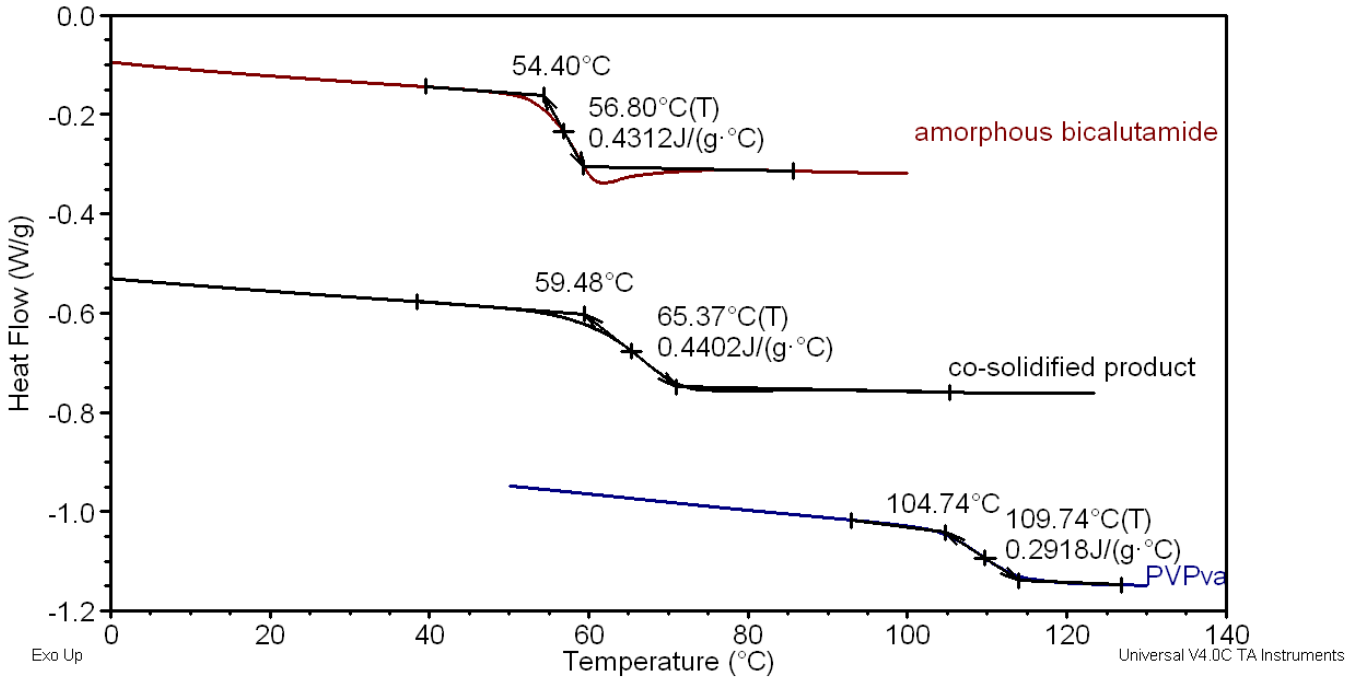

Figure C.15. The DSC thermograms of bicalutamide:PVPva systems showing the glass transition event for the individual components and co-solidified product (as labeled) , where $T_{g,CK}$ = 70.3 °C. The single, detectable T_g in the co-solidified product is similar to that of amorphous bicalutamide and therefore, not definitively interpretable

Bibliography

1. Amidon GL, Lennernaes H, Shah VP, Crison JR 1995. A theoretical basis for a biopharmaceutic drug classification: the correlation of in vitro drug product dissolution and in vivo bioavailability. Pharmaceutical Research 12(3):413 - 420.
2. Sinko PJ. 2006. Martin's physical pharmacy and pharmaceutical sciences. Fifth ed.: Lippincott Williams & Wilkins.
3. Fleisher D, Bong R, Stewart BH 1996. Improved oral drug delivery: solubility limitations overcome by the use of prodrugs. Advanced Drug Delivery Reviews 19:115 - 130.
4. Serajuddin ATM 2007. Salt formation to improve drug solubility. Advanced Drug Delivery Reviews 59:603 - 613.
5. Morris KR, Fakes MG, Thakur AB, Newman AW, Singh AK, Venit JJ, Spagnuolo CJ, Serajuddin ATM 1994. An integrated approach to the selection of optimal salt form for a new drug candidate. International Journal of Pharmaceutics 105(3):209 - 217.
6. Krise JP, Narisawa S, Stella VJ 1999. A novel prodrug approach for tertiary amines. 2. Physicochemical and in vitro enzymatic evaluation of selected N-phosphonooxymethyl prodrugs. Journal of Pharmaceutical Sciences 88(9):922 - 927.
7. Noyes AA, Whitney WR 1897. The rate of dissolution of solid substances in their own solutions. Journal of American Chemical Society 19:930 - 934.
8. Byrn SR, Pfeiffer RR, Stowell JG. 1999. Solid State Chemistry of Drugs. 2 ed., West Lafayette: SSCI, Inc.
9. Wildfong PLD, Morris KR, Anderson CA, Short SM 2007. Demonstration of a Shear-Based Solid-State Phase Transformation in a Small Molecular Organic System: Chlorpropamide. Journal of Pharmaceutical Sciences 96(5):1100 - 1113.
10. Lin Y, Cogdill RP, Wildfong PLD 2009. Informatic calibration of a materials properties database for predictive assessment of mechanically activated disordering potential for small molecule organic solids. Journal of Pharmaceutical Sciences 98(8):2696 - 2708.
11. Wildfong PLD, Hancock BC, Moore MD, Morris KR 2006. Towards an understanding of the structurally based potential for mechanically activated disordering of small molecule organic crystals. Journal of Pharmaceutical Sciences 95(12):2645 - 2656.
12. Zhang GGZ, Law D, Schmitt EA, Qiu Y 2004. Phase transformation considerations during process development and manufacture of solid oral dosage forms. Advanced Drug Delivery Reviews 56:371 - 390.
13. Loftsson T, Brewster ME 1996. Pharmaceutical applications of cyclodextrins. 1. Drug solubilization and stabilization. Journal of Pharmaceutical Sciences 85(10):1017 - 1025.
14. Li P, Zhao L 2007. Developing early formulations: Practice and perspective. International Journal of Pharmaceutics 341:1 - 19.
15. Kaushal AM, Gupta P, Bansal AK 2004. Amorphous Drug Delivery Systems: Molecular Aspects, Design, and Performance. Critical Reviews in Therapeutic Drug Carrier Systems 21:133 - 193.

16. Porter DA, Easterling KE. 1981. Phase Transformations in Metals and Alloys. ed.: Van Nostrand Reinhold.
17. Askeland DR, Phule PP. 2006. The Science and Engineering of Materials. 5 ed.
18. Woolliams ER, Machin G, Lowe DH, Winkler R 2006. Metal (carbide)-carbon eutectics for thermometry and radiometry: a review of the first seven years. Metrologia 43:R11 - R25.
19. Bansal SS, Kaushal AM, Bansal AK 2007. Molecular and Thermodynamic Aspects of Solubility Advantage from Solid Dispersions. Molecular Pharmaceutics 4(5):794 - 802.
20. Jenkins R, Snyder RL. 1996. Introduction to X-ray powder diffractometry. ed., New York: Wiley-Interscience. p 403.
21. Zevin LS, Kimmel G. 1995. Quantitative X-ray Diffractometry. ed., New York: Springer. p 372.
22. Misture ST, Chatfield L, Snyder RL 1994. Accurate powder diffraction patterns using zero background holders. Powder Diffraction 9:172 - 179.
23. Cullity BD, Stock SR. 2001. Elements of X-ray Diffraction. Third ed., Upper Saddle River: Prentice Hall. p 664.
24. Goehner RP 1978. Background subtract subroutine for spectral data. Analytical Chemistry 50(8):1223 - 1225.
25. Guinier A. 1994. X-ray diffraction in crystals, imperfect crystals, and amophous bodies. ed.: Dover Publications, Inc.
26. Alexander L, Klug HP 1948. Basic aspects of X-ray absorption. Analytical Chemistry 20(10):886 - 889.
27. Shah B, Kakumanu VK, Bansal AK 2006. Analytical techniques for quantification of amorphous/crystalline phases in pharmaceutical solids. Journal of Pharmaceutical Sciences 95(8):1641 - 1665.
28. Phadnis NV, Suryanarayanan R 1997. Simultaneous quantification of an enantiomer and the racemic compound of ibuprofen by X-ray powder diffraction. Pharmaceutical Research 14(9):1176 - 1180.
29. Suryanarayanan R, Herman CS 1991. Quantitative analysis of the active tablet ingredient by powder X-ray diffractometry. Pharmaceutical Research 8(3):393 - 399.
30. Tiwari M, Chawla G, Bansal AK 2007. Quantification of olanzapine polymorphs using powder X-ray diffraction technique. Journal of Pharmaceutical and Biomedical Analysis 43:865 - 872.
31. Rietveld HM 1967. Line profiles of neutron powder-diffraction peaks for structure refinement. Acta Crystallographica 22:151 - 152.
32. Rietveld HM 1969. A profile refinement method for nuclear and magnetic structures. Journal of Applied Crystallography 2:65 - 71.
33. Rietveld HM. 1995. The Rietveld Method. ed., New York: Oxford University Press.
34. Young RA. 1995. The Rietveld Method. ed., New York: Oxford University Press.
35. Will G. 2006. Powder Diffraction: The Rietveld Method and the Two-Stage Method. ed., New York: Springer.
36. Yamamura S, Momose Y 2001. Quantitative analysis of cyrstalline pharmaceuticals in powders and tablets by a pattern-fitting procedure using X-ray powder diffraction data. International Journal of Pharmaceutics 212:203 - 212.

37. Chen X, Bates S, Morris KR 2001. Quantifying amorphous content of lactose using parallel beam X-ray powder diffraction and whole pattern fitting. Journal of Pharmaceutical and Biomedical Analysis 26:63 - 72.
38. Egami T, Billinge SJL. 2003. Underneath the Bragg Peaks. Structural analysis of complex materials. ed., Oxford: Elsevier.
39. Billinge SJL, Kanatzidis MG 2004. Beyond crystallography: the study of disorder, nanocrystallinity and crystallographically challenged materials with pair distribution function. Chemical Communications:749 - 760.
40. Finbak C 1949. The Structure of Liquids. II. Acta Chemica Scandinavica 3:1293 - 1308.
41. Peterson PF, Bozin ES, Proffen T, Billinge SJL 2003. Improved measures of quality for the atomic pair distribution function. Journal of Applied Crystallography 36:53 - 64.
42. Bruhne S, Uhrig E, Luther K-D, Assmus W, Brunelli M, Masadeh AS, Billinge SJL 2005. PDF from X-ray powder diffraction for nanometer-scale atomic structure analysis of quasicrystalline alloys. Z Kristallogr 220:962 - 967.
43. Petkov V 2005. Atomic-scale structure of glassess using high-energy x-ray diffraction. Journal of the American Ceramic Society 88(9):2528 - 2531.
44. Petkov V, Qadir D, Shastri SD 2004. Rapid structure determination of disordered materials: study of GeSe2 glass. Solid State Communications (129):239 - 243.
45. Masadeh AS, Bozin ES, Farrow CL, Paglia G, Juhas P, Karkamkar A, Kanatzidis MG, Billinge SJL 2007. Quantitative size-dependent structure and strain determination of CdSe nanoparticles using atomic pair distribution function analysis. Condensed Matter 76(11):1 - 10.
46. Levashov VA, Billinge SJL, Thorpe MF 2005. Density fluctuations and the pair distribution function. Physical Review B 72(024111):1 - 6.
47. Jeong I-K, Proffen T, Mohiuddin-Jacobs F, Billinge SJL 1999. Measuring correlated atomic motion using X-ray diffraction. Journal of Physical Chemistry A (103):921 - 924.
48. Sheth AR, Bates S, Muller FX, Grant DJW 2005. Local structure in amorphous phases of piroxicam from powder x-ray diffractometry. Crystal Growth & Design 5(2):571 - 578.
49. Sheth AR, Bates S, Muller FX, Grant DJW 2005. Polymorphism in piroxicam. Crystal Growth & Design 4(6):1091 - 1098.
50. Bates S, Zografi G, Engers D, Morris K, Crowley K, Newman A 2006. Analysis of amorphous and nanocrystalline solids from their X-ray diffraction patterns. Pharmaceutical Research 23(10):2333 - 2349.
51. Bates S, Kelly RC, Ivanisevic I, Schields P, Zografi G, Newman AW 2007. Assessment of defects and amorphous structure produced in raffinose pentahydrate upon dehydration. Journal of Pharmaceutical Sciences 96(5):1418 - 1433.
52. Newman A, Engers D, Bates S, Ivanisevic I, Kelly RC, Zografi G 2008. Characterization of amorphous API:Polymer mixtures using X-ray powder diffraction. Journal of Pharmaceutical Sciences 97(11):4840 - 4856.
53. Wunderlich B 1989. The detection of conformational disorder by thermal analysis. Pure and Applied Chemistry 61(8):1347 - 1351.

54. Yu L 2001. Amorphous pharmaceutical solids: preparation, characterization and stabilization. Advanced Drug Delivery Reviews 48:27 - 42.
55. Gaskell PH 1997. Structure and properties of glasses - how far do we need to go? Journal of Non-Crystalline Solids 222:1 - 12.
56. Hancock BC, Zografi G 1997. Characteristics and significance of the amorphous state in pharmaceutical systems. Journal of Pharmaceutical Sciences 86(1):1 - 12.
57. Hilden LR, Morris KR 2004. Physics of amorphous solids. Journal of Pharmaceutical Sciences 93(1):3 - 12.
58. Hancock BC, Parks M 2000. What is the true solubility advantage for amorphous pharmaceuticals? Pharmaceutical Research 17(4):397 - 404.
59. Konno H, Taylor LS 2006. Influence of Different Polymers on the Crystallization Tendency of Molecularly Dispersed Amorphous Felodipine. Journal of Pharmaceutical Sciences 95(12):2692 - 2705.
60. Miyazaki T, Yoshioka S, Aso Y, Kojima S 2004. Ability of polyvinylpyrrolidone and polyacrylic acid to inhibit the crystallization of amorphous acetaminophen. Journal of Pharmaceutical Sciences 93:2710 - 2717.
61. Tang XC, Pikal MJ, Taylor LS 2002. A spectroscopic investigation of hydrogen bond patterns in crystalline and amorphous phases in dihydropyridine calcium channel blockers. Pharmaceutical Research 19:477 - 483.
62. Taylor LS, Zografi G 1997. Spectroscopic characterization of interactions between PVP and indomethacin in amorphous molecular dispersions. Pharmaceutical Research 14:1691 - 1698.
63. Waard Hd, Hinrichs WLJ, Visser MR, Bologna C, Frijlink HW 2008. Unexpected Differences in Dissolution Behavior of Tablets Prepared from Solid Dispersions with a Surfactant Physically Mixed or Incorporated. International Journal of Pharmaceutics 349:66-73.
64. Craig DQM 2002. The Mechanisms of Drug Release from Solid Dispersions in Water-Soluble Polymers. International Journal of Pharmaceutics (231):131-144.
65. Karavas E, Georgarakis E, Sigalas MP, Avgoustakis K, Bikiaris D 2007. Investigation of the release mechanism of a sparingly water-soluble drug from solid dispersions in hydrophilic carriers based on physical state of drug, particle size distribution and drug-polymer interactions. European Journal of Pharmaceutics and Biopharmaceutics 66:334 - 347.
66. Sekiguchi K, Obi N 1961. Studies on absorption of eutectic mixtures. I. A comparison of the behavior of eutectic mixtures of sulphathiazole and that of ordinary sulphathiazole in man. Chemical and Pharmaceutical Bulletin 9:866 - 872.
67. Tachibana T, Nakamura A 1965. A method for preparing an aqueous colloidal dispersion of organic materials by using water-soluble polymers: dispersion of beta-carotene by polyvinylpyrrolidone. Colloid and Polymer Science 203:130 - 133.
68. Friesen DT, Shanker R, Crew M, Smithey DT, Curatolo WJ, Nightingale JAS 2008. Hydroxypropyl Methylcellulose Acetate Succinate-Based Spray-Dried Dispersions: An Overview. Molecular Pharmaceutics 5(6):1003 - 1019.
69. Janssens S, Roberts C, Smith EF, Mooter GVd 2008. Physical stability of ternary solid dispersions of itraconazole in polyethyleneglycol 6000/hydroxypropylmethylcellulose 2910 E5 blends. International Journal of Pharmaceutics 355:100 - 107.

70. Zhang X, Sun N, Wu B, Lu Y, Guan T, Wu W 2008. Physical characterization of lansoprazole/PVP solid dispersion prepared by fluid-bed coating technique. Powder Technology 182:480 - 485.
71. Andrews GP, Abudiak OA, Jones DS 2010. Physicochemical Characterization of Hot Melt Extruded Bicalutamide–Polyvinylpyrrolidone Solid Dispersions. Journal of Pharmaceutical Sciences 99(3):1322 - 1335.
72. Chokshi R, Zia H 2004. Hot-Melt Extrusion Technique: A Review. Iranian Journal of Pharmaceutical Research 3:3 - 16.
73. Janssens S, Zeure AD, Paudel A, Humbeeck JV, Rombaut P, Mooter GVd online March 2010. Influence of Preparation Methods on Solid State Supersaturation of Amorphous Solid Dispersions: A Case Study with Itraconazole and Eudragit E100. Pharmaceutical Research.
74. Papadimitriou SA, Bikiaris D, Avgoustakis K 2008. Microwave-induced enhancement of the dissolution rate of poorly water-soluble tibolone from poly(ethylene glycol) solid dispersions. Journal of Applied Polymer Science 108:1249 - 1258.
75. Xu L, Li SM, Sunada H 2007. Preparation end evaluation of ibuprofen solid dispersion systems with Kollidon particles using a pulse combustion dryer system. Chemical and Pharmaceutical Bulletin 55(11):1545 - 1550.
76. Sethia S, Squillante E 2004. Solid dispersion of carbamazepine in PVP K30 by conventional solvent evaporation and supercritical methods. International Journal of Pharmaceutics 272:1 - 10.
77. Dong Z, Chatterji A, Sandhu H, Choi DS, Chokshi H, Shah N 2008. Evaluation of solid state properties of solid dispersions prepared by hot-melt extrusion and solvent co-precipitation. International Journal of Pharmaceutics 355:141 - 149.
78. Hancock BC, Zografi G 1994. The relationship between the glass transition temperature and the water content of amorphous pharmaceutical solids. Pharmaceutical Research 11(4):471 - 477.
79. Rumondor ACF, Taylor LS 2010. Effect of polymer hygroscopicity on the phase behavior of amorphous solid dispersions in the presence of moisture. Molecular Pharmaceutics:available online January 2010.
80. Zhou D, Grant DJW, Zhang GGZ, Law D, Schmitt EA 2007. A calorimetric investigation of thermodynamic and molecular mobility contributions to the physical stability of two pharmaceutical glasses. Journal of Pharmaceutical Sciences 96(1):71 - 83.
81. Mooter GVd, Wuyts M, Blaton N, Busson R, Grobet P, Augustijns P, Kinget R 2001. Physical stabilisation of amorphous ketoconazole in solid dispersions with polyvinylpyrrolidone K25. European Journal of Pharmaceutical Sciences 12:261 - 269.
82. Marsac PJ, Konno H, Rumondor ACF, Taylor LS 2007. Recrystallization of nifedipine and felodipine from amorphous molecular level solid dispersions containing poly(vinylpyrrolidone) and sorbed water. Pharmaceutical Research 25(3):647 - 656.
83. Huang J, Wigent RJ, Schwartz JB 2008. Drug-polymer interaction and its significance on the physical stability of nifedipine amorphous dispersion in microparticles of an ammonio methacrylate copolymer and ethylcellulose binary blend. Journal of Pharmaceutical Sciences 97(1):251 - 262.
84. Gordon M, Taylor JS 1952. Ideal copolymers and the second-order transitions of synthetic rubbers. I. Noncrystalline copolymers. Journal of Applied Chemistry 2:493 - 500.

85. Couchman PR, Karasz FE 1978. A classical thermodynamic discussion of the effect of composition on glass-transition temperatures. Macromolecules 11(1):117 - 119.
86. Katkov II, Levine F 2004. Prediction of the glass transition temperature of water solutions: comparison of different models. Cryobiology 49:62 - 82.
87. Janssens S, Mooter GVd 2009. Review: physical chemistry of solid dispersion. Journal of Pharmacy and Pharmacology 61:1571 - 1586.
88. Rumondor ACF, Ivanisevic I, Bates S, Alonzo DE, Taylor LS 2009. Evaluation of drug-polymer miscibility in amorphous solid dispersion systems. Pharmaceutical Research:published online September 22, 2009.
89. Marsac PJ, Shamblin SL, Taylor LS 2006. Theoretical and practical approaches for prediction of drug-polymer miscibility and solubility. Pharmaceutical Research 23(10):2417 - 2426.
90. Shibata Y, Fujii M, Kokudai M, Noda S, Okada H, Kondoh M, Watanabe Y 2007. Effect of Characteristics of Compounds on Maintenance of an Amorphous State in Solid Dispersion With Crospovidone. Journal of Pharmaceutical Sciences 96(6):1537 - 1547.
91. Martens H, Naes T. 1989. Multivariate Calibration. ed., New York, N.Y., USA: John Wiley and Sons.
92. Suda M, Takayama K, Otsuka M 2008. An accurate quantitative analysis of polymorphic content by chemometric X-ray powder diffraction. Analytical Sciences 24:451 - 457.
93. Jorgensen AC, Miroshnyk I, Karjalainen M, Jouppila K, Siiria S, Antikainen O, Rantanen J 2006. Multivariate data analysis as a fast tool in evaluation of solid state phenomena. Journal of Pharmaceutical Sciences 95(4):906 - 916.
94. Nassab PR, Rajko R, Szabo-Revesz P 2006. Physicochemical charaterization of meloxicam-mannitol binary systems. Journal of Pharmaceutical and Biomedical Analysis 41:1191 - 1197.
95. Agatonovic-Kustrin S, Wu V, Rades T, Saville D, Tucker IG 2000. Ranitidine hydrochloride X-ray assay using a neural network. Journal of Pharmaceutical and Biomedical Analysis (22):985 - 992
96. Okumura T, Nakazono M, Otsuka M, Takayama K 2006. An accurate quantitative analysis of polymorphs based on artificial neural networks. Colloids and Surfaces B Biointerfaces 49:153 - 157.
97. Moore MD, Cogdill RP, Short SM, Hair CR, Wildfong PLD 2008. The use of net analyte signal orthogonalization in the separation of multi-component diffraction patterns obtained from X-ray powder diffraction of intact compacts. Journal of Pharmaceutical and Biomedical Analysis 47:238 - 247.
98. Delhez R, Mittemeijer EJ 1975. An improved alpha$_2$ elimination. Journal of Applied Crystallography 8:609 - 611.
99. Haaland DM, Thomas EV 1988. Partial least-squares methods for spectral analyses. 1. Relation to other quantitative calibration methods and the extraction of qualitative information. Analytical Chemistry 60:1193 - 1202.
100. Hotelling H 1933. Analysis of a complex of statistical variables in principal components. Journal of Educational Psychology 24:417 - 441, 498 - 520.
101. *LAPACK User's Guide*, 1999,
102. Gabrielsson J, Lindberg N-O, Lundstedt T 2002. Multivariate methods in pharmaceutical applications. Journal of Chemometrics 16:141 - 160.

103. Helland IS 2001. Some theoretical aspects of partial least squares regression. Chemometrics and Intelligent Laboratory Systems 58(2):97 - 107.
104. de Jong S 1993. SIMPLS: an alternative approach to partial least squares regression. Chemometrics and Intelligent Laboratory Systems 18:251 - 263.
105. Cao W, Bates S, Peck GE, Wildfong PLD, Qiu Z, Morris KR 2002. Quantitative determination of polymorphic composition in intact compacts by parallel-beam X-ray powder diffractometry. Journal of Pharmaceutical and Biomedical Analysis 30(4):1111-1119.
106. Wildfong PLD, Morley NA, Moore MD, Morris KR 2005. Quantitative determination of polymorphic composition in intact compacts by parallel-beam X-ray powder diffractometry II. Data correction for analysis of phase transformations as a function of pressure. Journal of Pharmaceutical and Biomedical Analysis 39:1 - 7.
107. Challenge and opportunity on the critical path to new medical products, 2004, http://www.fda.gov/oc/initiatives/criticalpath/
108. Phadnis NV, Cavatur RK, Suryanarayanan R 1997. Identification of drugs in pharmaceutical dosage forms by X-ray powder diffractometry. Journal of Pharmaceutical and Biomedical Analysis 15:929 - 943.
109. Martens H, Hoy M, Wise BM, Bro R, Brockhoff PB 2003. Pre-whitening of data by covariance-weighted pre-processing. Journal of Chemometrics (17):153 - 165.
110. Jeong IK, Mohiuddin-Jacobs F, Petkov V, Billinge SJL 2001. Local structure of In Ga As semiconductor alloys by high-energy synchrotron x-ray diffraction. Physical Review B 63(205202):1 - 9.
111. Warren BE. 1990. X-ray Diffraction. ed., New York: Dover Publications, Inc.
112. Wold S, Esbensen K, Geladi P 1987. Principal component analysis. Chemometrics and Intelligent Laboratory Systems 2(1-3):37 - 52.
113. Toby BH, Egami T, Jorgensen JD, Subramanian MA 1990. Observation of a Local Structural Change at T_c for $Tl_2Ba_2CaCu_2O_8$ by Pulsed Neutron Diffraction. Physical Review Letters 64(20):2414-2417.
114. Norrman M, Stahl K, Schluckebier G, Al-Karadaghi S 2006. Characterization of insulin microcrystals using powder diffraction and multivariate data analysis. Journal of Applied Crystallography (39):391 - 400.
115. Atassi F, Mao C, Masadeh AS, Byrn SR 2009 online. Solid-State Characterization of Amorphous and Mesomorphous Calcium Ketoprofen. Journal of Pharmaceutical Sciences.
116. Heinz A, Strachan CJ, Atassi F, Gordon KC, Rades T 2008. Characterizing an Amorphous System Exhibiting Trace Crystallinity: A Case Study with Saquinavir. Crystal Growth & Design 8(1):119 - 127.
117. Moore MD, Steinbach AM, Buckner IS, Wildfong PLD 2009. A Structural Investigation into the Compaction Behavior of Pharmaceutical Composites Using Powder X-ray Diffraction and Total Scattering Analysis. Pharmaceutical Research 26(11):2429 - 2437.
118. Ivanisevic I, Bates S, Chen P 2009. Novel methods for the assessment of miscibility of amorphous drug-polymer dispersions. Journal of Pharmaceutical Sciences 98(9):3373 - 3386.
119. Nollenberger K, Gryczke A, Meier C, Dressman J, Schmidt MU, Bruhne S 2009. Pair Distribution Function X-ray Analysis Explains Dissolution Characteristics of

Felodipine Melt Extrusion Products. Journal of Pharmaceutical Sciences 98(4):1476 - 1486.
120. Toby BH, Billinge SJL 2004. Determination of standard uncertainties in fits to pair distribution functions. Acta Crystallographica A 60:315 - 317.
121. Toby BH, Egami T 1992. Accuracy of Pair Distribution Function Analysis Applied to Crystalline and Non-Crystalline Materials. Acta Crystallographica A 48:336 - 346.
122. Metropolis N, Ulam S 1949. The Monte Carlo Method. Journal of the American Statistical Association 44(247):335 - 341.
123. Prince E. 2004. Mathematical Techniques in Crystallography and Materials Science. 3rd ed., New York: Springer.
124. Yoo S-U, Krill SL, Wang Z, Telang C 2009. Miscibility/Stability Considerations in Binary Solid Dispersion Systems Composed of Functional Excipients towards the Design of Multi-Component Amorphous Systems. Journal of Pharmaceutical Sciences 98(12):4711 - 4723.
125. Waterbeemd Hvd, Gifford E 2003. ADMET in silico modelling: towards prediction paradise? Nature Reviews: Drug Discovery 2:192 - 204.
126. Estrada E 1996. Spectral moments of the edge adjacency matrix in molecular graphs. 1. Definition and applications to the prediction of physical properties of alkanes. Journal of Chemical Information Computer Science 36:844 - 849.
127. Gramatica P, Corradi M, Consonni V 2000. Modelling and prediction of soil sorption coefficients of non-ionic organic pesticides by molecular descriptors. Chemosphere 41:763 - 777.
128. Mihalic Z, Trinajstic N 1992. A graph-theoretical approach to structure-property relationships. Symposium on Graph Theory in Chemistry 69(9):701 - 712.
129. Codessa Pro Software, University of Florida, 2002, www.codessa-pro.com
130. VCCLAB, Virtual Computational Chemistry Laboratory, 2005, http:\\www.vcclab.org
131. Tetko IV, Gasteiger J, Todeschini R, Mauri A, Livingstone D, Ertl P, Palyulin VA, Radchenko EV, Zefirov NS, Makarenko AS, Tanchuk VY, Prokopenko VV 2005. Virtual computational chemistry laboratory - design and description. Journal of Computer-Aided Molecular Design 19:453 - 463.
132. Allen FH 2002. The Cambridge Structural Database: a quarter of a million crystal structures and rising. Acta Crystallographica B58:380 - 388.
133. Thomas IR, Bruno IJ, Cole JC, Macrae CF, Pidcock E, Wood PA 2010. WebCSD: the online portal to the Cambridge Structural Database. Journal of Applied Crystallography 43:362 - 366.
134. Kleinbaum DG, Klein M. 2002. Logistic Regression. 2nd ed.: Springer.
135. Pampel FC. 2000. Logistic Regression: A Primer. ed.: Sage Publications.
136. Pregibon D 1981. Logistic Regression Diagnostics. The Annals of Statistics 9(4):705 - 724.
137. Todeschini R, Consonni V. 2002. Handbook of molecular descriptors. ed.: Wiley-VCH.
138. Yu L, Mishra DS, Rigsbee DR 1998. Determination of the Glass Properties of D-Mannitol Using Sorbitol as an Impurity. Journal of Pharmaceutical Sciences 87(6):774 - 777.

139. Six K, Verreck G, Peeters J, Brewster M, Mooter GVD 2004. Increased Physical Stability and Improved Dissolution Properties of Itraconazole, a Class II Drug, by Solid Dispersions that Combine Fast- and Slow-Dissolving Polymers. Journal of Pharmaceutical Sciences 93(1):124 - 131.
140. Consonni V, Todeschini R, Pavan M 2002. Structure/response correlations and similarity/diversity analysis by GETAWAY descriptors. 1. Theory of the novel 3D molecular descriptors. Journal of Chemical Information Computer Science 42:682 - 692.
141. Consonni V, Todeschini R, Pavan M, Gramatica P 2002. Structure/response correlations and similarity/diversity analysis by GETAWAY descriptors. 2. Application of the novel 3D molecular descriptors to QSAR/QSPR. Journal of Chemical Information Computer Science 42:693 - 705.
142. Marsac PJ, Konno H, Taylor LS 2006. A comparison of the physical stability of amorphous felodipine and nifedipine systems. Pharmaceutical Research 23(10):2306-2316.
143. Kukushkin SA, Grigoriev DA 2000. Theory of the late-stage crystallization of eutectic composition melts. Journal of Physics and Chemistry of Solids 61:1337 - 1343.
144. Margarit MV, Marin MT, Contreras MD 2001. Solubility of solid dispersions of pizotifen malate and povidone. Drug Development and Industrial Pharmacy 27(6):517 - 522.
145. Nazzal S, Smalyukh II, Lavrentovich OD, Khan MA 2002. Preparation and in vitro characterization of a eutectic based semisolid self-nanoemulsified drug delivery system (SNEDDS) of ubiquinone: mechanism and progress of emulsion formation. International Journal of Pharmaceutics 235:247 - 265.
146. Rombach E, Ulrich J 2007. Self-controlled coating process for drugs. Crystal Growth & Design 7(9):1618 - 1622.
147. Sakata Y, Tanabe E, Sumikawa T, Shiraishi S, Tokudome Y, Otsuka M 2007. Effects of solid-state reaction between paracetamol and cloperastine hydrochloride on the pharmaceutical properties of their preparations. International Journal of Pharmaceutics 335:12 - 19.
148. Meng G, Lin X, Huang W 2008. The relationship between effective entropy change and volume fraction of the eutectic phases in eutectic microstructures. Materials Letters 62:984 - 987.
149. Hunt JD, Jackson KA 1966. Binary eutectic solidification. Transactions of the Metallurgical Society of AIME 236(6):843 - 852.
150. Yong CS, Oh Y-K, Jung SH, Rhee J-D, Kim H-D, Kim C-K, Choi H-G 2004. Preparation of ibuprofen-loaded liquid suppository using eutectic mixture system with menthol. European Journal of Pharmaceutical Sciences 23:347 - 353.
151. Lacoulonche F, Chauvet A, Masse J 1997. An investigation of flurbiprofen polymorphism by thermoanalytical and spectroscopic methods and a study of its interactions with poly-(ethylene glycol) 6000 by differential scanning calorimetry and modelling. International Journal of Pharmaceutics 153:167 - 179.
152. Lacoulonche F, Chauvet A, Masse J, Egea MA, Garcia ML 1998. An investigation of FB interactions with poly(ethylene glycol) 6000, poly(ethylene glycol) 4000, and poly-e-carpolactone by thermoanalytical and spectroscopic methods and modeling. Journal of Pharmaceutical Sciences 87(5):543 - 551.

153. Law D, Wang W, Schmitt EA, Qiu Y, Krill SL, Fort JJ 2003. Properties of Rapidly Dissolving Eutectic Mixtures of Poly(ethylene glycol) and Fenofibrate: The Eutectic Microstructure. Journal of Pharmaceutical Sciences 92(3):505 - 515.
154. Lheritier J, Chauvet A, Abramovici B, Masse J 1995. Improvement of the dissolution kinetics of SR 33557 by means of solid dispersions containing PEG 6000. International Journal of Pharmaceutics 123:273 - 279.
155. Naima Z, Siro T, Jaun-Manuel G-D, Chantal C, Rene C, Jerome D 2001. Interactions between carbamazepine and polyethylene glycol (PEG) 6000: characterisations of the physical, solid dispersed and eutectic mixtures. European Journal of Pharmaceutical Sciences 12:395 - 404.
156. Stott PW, Williams AC, Barry BW 1998. Transdermal delivery from eutectic systems: enhanced permeation of a model drug, ibuprofen. Journal of Controlled Release 50:297 - 308.
157. Harding LJ, Reading M, Craig DQM 2008. The development of thermally assisted particle manipulation and thermal nanointeraction studies as a means of investigating drug-polymer interactions. Journal of Pharmaceutical Sciences 97(4):1551 - 1563.
158. Chen Y, Zhang GGZ, Neilly J, Marsh K, Mawhinney D, Sanzgiri YD 2004. Enhancing the bioavailability of ABT-963 using solid dispersion containing Pluronic F-68. International Journal of Pharmaceutics 286:69 - 80.
159. Stott PW, Williams AC, Barry BW 2001. Mechanistic study into the enhanced transdermal permeation of a model beta-blocker, propranolol, by fatty acids: a melting point depression effect. International Journal of Pharmaceutics 219:161 - 176.
160. Yuan X, Capomacchia AC 2005. The binary eutectic of NSAIDs and two-phase liquid system for enhanced membrane permeation. Pharmaceutical Development and Technology 1:1 - 10.
161. Larrea A, Orera VM 2007. Porous crystal structures obtained from directionally solidified eutectic precursors. Journal of Crystal Growth 300:387 - 393.
162. Mullen JW. 2001. Crystallization. Fourth ed., Woburn: Reed Educational and Professional Publishing Ltd.
163. Osborn JC, York P, Rowe RC, Roberts RJ. Cambridge, UK, 1999, pp 1166 - 1174.
164. Bi M, Hwang S-J, Morris KR 2003. Mechanism of eutectic formation upon compaction and its effects on tablet properties. Thermochimica Acta 404:213 - 226.
165. Law D, Wang W, Schmitt EA, Long MA 2002. Prediction of Poly (Ethylene) Glycol-Drug Eutectic Compositions Using an Index Based on the van't Hoff Equation. Pharmaceutical Research 19(3):315 - 321.
166. Craig DQM 1995. A review of thermal methods used for the analysis of the crystal form, solution thermodynamics and glass transition behaviour of polyethylene glycols. Thermochimica Acta 248:189 - 203.
167. West AR. 1999. Basic Solid State Chemistry. 2 ed., Hoboken: John Wiley & Sons Ltd.